Experimental characterization of fundamental four-wave mixing : discovering the idealized nonlinear dynamics

Anastasiia Sheveleva

Doctoral thesis of THE UNIVERSITY OF BURGUNDY-FRANCHE-COMTÉ
prepared at THE UNIVERSITY OF BURGUNDY

Doctoral School n°553
CARNOT PASTEUR

For a qualification of Doctor of Physics
Speciality DILUTED AND OPTICAL MEDIA

By
Anastasiia SHEVELEVA

Experimental characterization of fundamental four-wave mixing: discovering the idealized nonlinear dynamics

Thesis presented and defended at the UNIVERSITY OF BURGUNDY (Dijon), 15th of September 2023

Committee members :

M. Arnaud MUSSOT	Professor, University of Lille	Referee
M. Stefan WABNITZ	Professor, University of Rome "La Sapienza"	Referee
M. John M. DUDLEY	Professor, University of Franche-Compté	Examiner, Committee President
M. Benjamin WETZEL	Research Fellow, CNRS, University of Limoges	Examiner
M. Christophe PEUCHERET	Professor, University of Rennes	Examiner
Mme. Sonia BOSCOLO	Research Fellow, University of Aston	Examiner
M. Christophe FINOT	Professor, University of Burgundy	Thesis supervisor
M. Pierre COLMAN	Research Fellow, CNRS, University of Burgundy	Thesis co-supervisor

THÈSE DE DOCTORAT DE L'ÉTABMISSEMENT UNIVERSITÉ BOURGOGNE-FRANCHE-COMTÉ
PRÉPARÉ À L'UNIVERSITÉ DE BOURGOGNE

Ecole doctorale n°553
CARNOT PASTEUR

Doctorat de spécialité Physique
MILIEUX DILUÉS ET OPTIQUE

Par
Anastasiia SHEVELEVA

Caractérisation expérimentale du mélange fondamental à quatre ondes : découverte de la dynamique non-linéaire idéalisée

Thèse présentée et soutenue à UNIVERSITÉ DE BOURGOGNE (Dijon), le 15 Septembre 2023

Composition du jury :

M. Arnaud MUSSOT	Professeur, Université de Lille	Rapporteur
M. Stefan WABNITZ	Professeur, Université de Rome "La Sapienza"	Rapporteur
M. John M. DUDLEY	Professeur, Université de Franche-Comté	Examinateur, Président du jury
M. Benjamin WETZEL	Chargé de Recherche, CNRS, Université de Limoges	Examinateur
M. Christophe PEUCHERET	Professeur, Université de Rennes	Examinateur
Mme. Sonia BOSCOLO	Chargée de Recherche, Université d'Aston	Examinatrice
M. Christophe FINOT	Professeur, Université de Bourgogne	Directeur de thèse
M. Pierre COLMAN	Chargé de Recherche, CNRS, Université de Bourgogne	Codirecteur de thèse

ECOLE DOCTORALE
CARNOT - PASTEUR

Titre : **Caractérisation expérimentale du mélange fondamental à quatre ondes : découverte de la dynamique non-linéaire idéalisée**

Mots clés : Optique non-linéaire fibrée, instabilité de modulation, récurrence de Fermi-Pasta-Ulam-Tsingou, mélange à quatre ondes, guides d'ondes optiques couplés, non-adiabaticité

Résumé : Cette thèse est consacrée à l'étude du mélange fondamental dit à quatre ondes dans un régime non-linéaire induit par l'instabilité de modulation , où l'interaction est limitée à seulement trois ondes. En développant un nouveau type de dispositif expérimental basé sur l'itération des conditions initiales dans un court segment de fibre, je confirme les caractéristiques théoriques de la dynamique : évolution suivant des orbites fermées interprétées comme la récurrence de Fermi-Pasta-Ulam-Tsingou, existence de deux types de solutions divisées par une séparatrice et apparition de points stationnaires. Afin d'interpoler les résultats et de mettre en lumière le modèle physique qui gouverne l'expérience, j'utilise des méthodes d'intelligence artificielle. Enfin, je mets en place une méthode pour induire une transition contrôlée d'un état arbitraire à un autre. Par un brusque changement de puissance, nous sommes capable de relier deux états qui n'appartiennent pas à la même orbite.
Une autre partie de la thèse s'est intéressée à l'étude des guides d'ondes couplés. Tout d'abord, j'étudie comment l'inclusion de l'effet de champ local et du fond effectif permet d'améliorer les méthodes perturbatives pour l'estimation des paramètres des guides d'ondes couplés. Puis, inspirés par des analogies entre l'optique guidée et la mécanique quantique, je développe une technique de contrôle non adiabatique, où la transition lumineuse est déclenchée par l'excitation des supermodes. Je recherche les principes sous-jacents de la transition et les appliquons à l'optimisation d'une puce photonique dense, où de multiples transitions lumineuses asymétriques sont réalisées.

Title : **Experimental characterization of fundamental four-wave mixing: discovering the idealized nonlinear dynamics**

Key words : Nonlinear fiber optics, modulation instability, Fermi-Pasta-Ulam-Tsingou recurrence, four-wave mixing, coupled optical waveguides, non-adiabaticity

Abstract : This thesis is devoted to the investigation of a fundamental four-wave mixing in a nonlinear regime induced by the modulation instability , where the interaction is limited to only three waves. By developing a new type of experimental setup based on iteration of initial conditions in a short segment of fiber, I confirm theoretical features of the dynamics : evolution following closed orbits interpreted as the Fermi-Pasta-Ulam-Tsingou recurrence, existence of two types of solutions divided by a separatrix and appearance of stationary points. In order to interpolate the results and to reveal a model that drives the experiment, I use artificial intelligence methods. Finally, I study a method to induce a controlled transition from one arbitrary state to another. By an abrupt change of power, I am able to connect two states that do not belong to the same orbit.
Another part of the thesis is dedicated to study of coupled waveguides. First, I investigate how inclusion of the local field effect and the effective background allows to improve the perturbative methods for estimation of the coupled waveguides parameters. Then, inspired by analogies between guided optics and quantum mechanics, I develop a non-adiabatic control technique, where light transition is triggered by excitation of the supermodes. I investigate the underlying principles of the transition, and apply them to optimization of a densely packed photonic chip, where multiple asymmetric light transitions are fulfilled.

UBFC
UNIVERSITÉ
BOURGOGNE FRANCHE-COMTÉ

Université Bourgogne Franche-Comté
32, avenue de l'Observatoire
25000 Besancon

Acknowledgments

I would like to express my deepest gratitude to the University of Burgundy and the EIPHI-BFC graduate school who has been supporting my studies and research. I also thank the Carnot Pasteur doctoral school for hosting me during these three years. This endeavor would not have been possible without the Laboratoire Interdisciplinaire Carnot de Bourgogne and the SAFIR (previously SCLO) team part of which I was.

I would like to extend my sincere thanks to Professor Arnaud MUSSOT from the University of Lille and to Professor Stefan WABNITZ from the University of Rome "La Sapienza" who has devoted their time to thoroughly study the manuscript and provide their valuable feedbacks. Many thanks to John M. DUDLEY, Professor of the University of Franche-Comté, Benjamin WETZEL, Researcher in the University of Limoges, Christophe PEUCHERET, Professor of the University of Rennes, Sonia BOSCOLO, Researcher in the University of Burgundy, who have kindly agreed to be a part of the jury.

I could not have undertaken this journey without my supervisors, Christophe FINOT and Pierre COLMAN, who have conveyed their experience and have provided everything for success of the subject and my personal growth. Your diametrically different approaches to work have helped me to maintain the scientific curiosity while still achieving results. You have walked this path alongside with me and I am grateful for your support.

I would like to thank all members of the SAFIR team for collaborations and everyday interactions. Special thanks to Olivier MUSSET, Guy MILLOT and Olivier FAUCHER for fascinating discussions about books, adventures, wines and politics. Many thanks to Ibtissam EL BAKKOUCHI, Claire PRIOU and Coralie FEVRE, without whom I would not have managed to pass the "french administration". Special thanks to Andrei ERMOLAEV and Andrey GELASH (and his family) for fruitful discussions both about science and everyday life.

Last but not least I would like to thank my family for their support and understanding. I am grateful to Dr Kirill VASILEV who has motivated me to begin the scientific path back in Tomsk and has always been nourishing and supporting my personal growth. Without you I would not have been able to pursue the scientific carrier and I am thankful for you being on my side.

Contents

Introduction

Wave evolution in a dispersive medium that experiences intensity-dependent nonlinear phase shift is described by the nonlinear Schrödinger equation (NLSE) which is one of the seminal equations in science. It is applied to many different domains including plasma physics, hydrodynamics, Bose-Einstein condensates, and propagation in optical fibers [1–3]. The study of the NLSE have yielded major advances in our understanding of the symmetry-breaking processes [4], modulation instability (MI) [3] and the Fermi-Pasta-Ulam-Tsingou (FPUT) recurrence [5] which is one of the most important discoveries of the last century. Here the authors studying an energy transfer between the modes of a nonlinearly coupled oscillators chain have revealed that this system experiences a reversible behavior : it progressed until the thermalization stage and then the system follows the reversed dynamics until, after some time, it returns to its initial condition. This unexpected phenomenon has created a great interest in other fields of nonlinear optics.

The MI process is an effect resulting from the Kerr nonlinearity of the fiber in conjunction with anomalous chromatic dispersion. It is manifested in a form of amplification of spectral sidebands that eventually leads to breakup of the wave to a train of pulses [6]. This process is a key of the rogue wave formation [7] and the supercontinuum generation [8]. The stage of amplification is followed by decay which leads the system into its initial condition. Such a dynamics can be characterized by breather dynamics [9]. For the case of a seeded MI, the dynamics reveals the spectral broadening into a triangular shape frequency comb in the spectral domain [10]. This process can be described in terms of the nonlinear four-wave mixing (FWM).

To characterize the FWM process, one considers two pump waves and two sidebands with upshifted and downshifted frequencies which are separated by a fixed frequency, so and the evolution is described as an exchange of spectral amplitudes and phases between these lines. The FWM evolution allows to generate many spectral lines starting from just four, and it also has a recurrent nature : the spectrum growth is followed by a saturation phase, then the energy flows back to the pump.

The breakthrough in understanding the FWM process has happened in 1991 with works of Stefano Trillo and Stefan Wabnitz [11, 12], where the evolution of amplitudes and phases between three spectral lines (FWM in its degenerate case) was described in terms of exact differential equations. This truncated three-wave model have revealed the recursive dynamics of the FWM, as well as existence of different types of energy conversion depending on phase behavior. The evolution of spectral amplitudes and phases was described in terms of reduced variables, which has allowed to display the process on a phase-space diagram - a plot typical for nonlinear oscillators (for instance, a nonlinear pendulum). The degenerate case was later expanded to four different spectral lines [13], where similar features were revealed.

This discovery has advanced the understanding of fundamental nonlinear processes. However, experimental demonstration of this process in fiber optics has its challenges. Unlike the hydrodynamics, where direct observation of the FPUT recurrence in water waves is possible [14], its demonstration in fiber optics requires to solve problems of distributed measurements.

One approach may consist in using the cut-back approach [10,15,16], where the measurements are made in pieces of fiber of different lengths and are concatenated after each other reconstructing the distributed spectral evolution. This method, however, lacks in flexibility and convenience. The state of the art of experimental demonstration of the FPUT dynamics and recurrence was developed in works of A. Mussot [4, 17–19]. Here the authors developed an original non-invasive experimental setup which is based on the optical time domain reflectometer and a multiheterodyne detection, with the help of which they record the distributed measurements of phases and amplitudes of evolving spectral lines. The effects of losses are mitigated with an active Raman amplification.

The demonstrated results have revealed the cascaded FWM process where generation of residual sidebands is unlimited, an experimental study of the ideal FWM process, however, was never made. In the full NLSE propagation, as soon as the sidebands' amplitudes grow, they start to act as pumps themselves, so the process is cascaded, and more spectral lines are generated. Here with this thesis, we seek to reveal the idealized dynamics where only interaction between three spectral lines is considered. The goal of the work is to make a link between the theory and the light propagation in an optical fiber. We discuss limits and residual effects that prevent the differential equations to work in the real system, and demonstrate an experimental approach removing these limitations. Then we study features of the experimental technique in details, and reveal interesting nonlinear effects linked to asymmetric spectral lines propagation and Hamiltonian conservation. The thesis is composed of five chapters that are dedicated to the experimental demonstration of the ideal FWM.

The Chapter 1 describes basics of light propagation in optical fibers : the propagation equation is derived from Maxwell's equations, and then the effects of dispersion and nonlinearity are discussed. The ideal FWM model is derived for the degenerate case, and effects limiting its experimental demonstration are described.

The Chapter 2 provides a detailed description of the experimental setup. Its idea is based on iterative propagation of the frequency components. The setup was built from scratch with a help of a knowledge obtained during my Master internship on shaping of optical waveforms [20,21]. Here we discuss the concept, calibration, stability and estimation of impact of the unwanted effects in the experimental setup. We estimate as well the level of errors and discuss their potential sources.

The Chapter 3 is dedicated to experimental demonstration of the ideal FWM dynamics. We provide a full investigation of the phase-space map for different values of gain, that reveals typical FWM features such as the existence of two types of solutions divided by a separatrix, and the FPUT recurrence profiles [22]. Then we investigate different aspects of the dynamics such as propagation of an asymmetric spectrum and conservation of a Hamiltonian. The results of the experimental approach, different from the ideal FWM, are analyzed and explained.

The Chapter 4 discusses implementation of advanced numerical tools such as neural networks (NN) and data-driven approaches to complete or analyze the experimental results. Here we provide an approach to efficient training of a NN on a limited set of experimental data impaired by inaccuracies [23]. Then we use a sparse identification of nonlinear dynamics (SINDy) [24] to retrieve a set of differential equations that governs the experimental dynamics.

As a continuation of the subject related to use of advanced numerical tools and artificial intelligence methods, we explore the Dynamic Mode Decomposition (DyMD) technique which aims in extraction of modes and their evolution from a dataset. As it is detailed in the Appendix C, we applied it to the Dispersive Fourier Transform dataset (DFT) which has recorded the soliton molecule (SM) evolution in a laser cavity [25]. With the DyMD, we reveal multiple vibrational modes and observe their interplay in a three-soliton molecule.

In the Chapter 5 we present a method of dynamics control : with an abrupt change of the input power we

are able to transform the incoming state to the desired one in a controlled and optimal manner [26].

We believe that the developed work will serve to design and development of high-speed optical networks. Indeed, the FWM process strongly depends on a phase-matching between the pump and the signal. This feature allows to build wavelength conversion devices where, for instance, the waveguide dispersion is engineered to optimize the phase-matching [27] or to make a mode selection based on the guiding media properties [28]. Since the gain in the system depends so strongly on the phase, it was possible to develop the phase-sensitive amplifiers [29,30]. Also study of nonlinear processes where the interaction is brought by variation of parameters has lead to development of parametric amplification [31,32] which can be done in phase-sensitive or insensitive manner [33, 34]. However, from the fundamental point of view, the FWM process is not trivial, and there is a room for discussions and investigations of the underlying principles of the FWM in order to improve the existing techniques or to develop the new ones especially in the non-degenerate case.

Another part of my work is dedicated to development of new techniques of light coupling in integrated photonics devices. In order to not disrupt an integrity of the thesis, this study is put to Appendices A and B.

When two waveguides are coupled, light can flow between them which is the basis in design of optical couplers. To estimate the coupling strength, one derives the coupling constant from the Maxwell's equations using the perturbative theory [35]. However, this approach fails to reproduce the coupling constant precisely, leading to poor approximation of the parameter variation with inter-waveguide spacing and the wavelength dependence. In Appendix A we demonstrate that inclusion of the local field effect (LFE) and the effective background in case of an inhomogeneous cladding allows to retrieve an acceptable level of accuracy. In this theoretical and numerical work, we first remind the basis of the perturbative method, then apply it onto two waveguides configurations based on SiN and SiO_2 rib waveguides, and demonstrate the improvement of the previous theoretical models.

Analogies between quantum and guided optics [36] have stimulated a growing interest in theoretical and experimental implementation of quantum strategies to control light flow in an array of coupled waveguides. However, the focus has been made on adiabatic coupling [37, 38] which provides robust and broadband light transition but limited to symmetric waveguides and is not adapted to densely packed arrays of waveguides. Therefore, in Appendix B, we investigate non-adiabatic transitions in coupled waveguides, where we discover that a small periodic modulation that fulfills frequency-matching condition allows to couple the supermodes (eigensolutions of the system representing the reciprocal space). We demonstrate that the non-adiabatic strategy can be successfully applied in design of complex densely packed photonics chips that fulfill multiple non-symmetric transitions [39]. Discussions regarding optimal shape maximizing the supermodes coupling lead to fundamental links with light propagation in periodic medium.

Parts of the thesis have been supported by the French Agence Nationale de la Recherche (ANR) project OPTIMAL and by the CNRS-funded project Fourier (Chapter 4 and Appendix C). The Appendices A and B have been supported by the ANR NAC-NIP.

Chapter 1

Light Propagation in Fibers

In this Chapter, we review light propagation equations in guided media. Starting from Maxwell's equations, we develop a pulse-propagation equation where the effects of dispersion and nonlinearity manifest themselves. Then we formulate the four-wave mixing (FWM) equations where the interaction is limited to three waves (in the degenerate case) and introduce a concept of a phase-space plane. In the end, we discuss the potential obstacles to experimental demonstration of the ideal FWM dynamics.

1.1 Pulse-propagation equation

Optical fields propagation, as any other electromagnetic phenomena in a dispersive nonlinear media, is governed by Maxwell's equations [40]:

$$\begin{aligned} \bigtriangledown \cdot \boldsymbol{D} &= \rho \qquad \bigtriangledown \times \boldsymbol{E} = -\frac{\partial \boldsymbol{B}}{\partial t} \\ \bigtriangledown \cdot \boldsymbol{B} &= 0 \quad \bigtriangledown \times \boldsymbol{H} = \boldsymbol{J} + \frac{\partial \boldsymbol{D}}{\partial t}, \end{aligned} \tag{1.1}$$

with $\boldsymbol{E}$ and $\boldsymbol{H}$ being electric and magnetic field, respectively, and $\boldsymbol{D}$ and $\boldsymbol{B}$ - electric displacement field and total magnetic field. In optical fibers, due to absence of free charges, the current density $\boldsymbol{J}$ and the charge density ρ are set to zero [41].

The $\boldsymbol{D}$ and $\boldsymbol{B}$ are related to the electric and magnetic field through :

$$\begin{aligned} \boldsymbol{D} &= \epsilon_0 \boldsymbol{E} + \boldsymbol{P} \\ \boldsymbol{B} &= \mu_0 \boldsymbol{H} + \boldsymbol{M}. \end{aligned} \tag{1.2}$$

Here the vacuum permittivity is denoted as ϵ_0 and the vacuum permeability is μ_0, and the relation for the speed of light $\mu_0 \epsilon_0 = 1/c^2$ holds. The magnetic polarization $\boldsymbol{M}$ equals to zero for a non-magnetic medium such as optical fiber. The induced polarization is denoted as $\boldsymbol{P}$.

To obtain a wave equation that describes light propagation in optical fiber, one takes a curl of $\bigtriangledown \times \boldsymbol{E}$ and uses the equation for $\bigtriangledown \times \boldsymbol{H}$ as well as the definition of $\boldsymbol{D}$, which results in:

$$\bigtriangledown \times \bigtriangledown \times \boldsymbol{E} = -\frac{1}{c^2}\frac{\partial^2 \boldsymbol{E}}{\partial t^2} - \mu_0 \frac{\partial^2 \boldsymbol{P}_L}{\partial t^2} - \mu_0 \frac{\partial^2 \boldsymbol{P}_{NL}}{\partial t^2}. \tag{1.3}$$

The estimation of the induced electric polarization $\boldsymbol{P}$ requires, in general, a quantum-mechanical approach. However, if the considered wavelength range ($0.5 - 2\mu$m for optical fibers) is far from medium resonances, the two quantities can be linked by a phenomenological relation $\boldsymbol{P} = \epsilon_0 \sum_{i=1}^{N} \chi^{(i)} \boldsymbol{E}^i$ [42], where $\chi^{(i)}$ is an optical susceptibility of i-th order. The linear susceptibility $\chi^{(1)}$ contributes the most to $\boldsymbol{P}$. The nonlinear change in the refractive index is around 10^{-6}, so the nonlinear part of the induced polarization is treated as a perturbative term. As for the second-order effect $\chi^{(2)}$, that corresponds to the processes of second-order or sum-frequency generation, it arises from media with no inversion symmetry at a molecular level. In SiO_2 glass, the lattice has no determined macroscopic orientation (there is no long range correlation), hence it is a symmetric structure. Thus, a fiber made of silica glasses experiences no second-order nonlinear effects. As a result, the first nonlinear effect of importance comes from the third-order $\chi^{(3)}$ process. Now we can separate linear and nonlinear contributions to the induced polarization:

$$\begin{gathered} \boldsymbol{P} = \epsilon_0 \int_{-\infty}^{t} \chi^{(1)}(t-t')\boldsymbol{E}(\boldsymbol{r},t')dt' + \\ \epsilon_0 \int_{-\infty}^{t} dt_1 \int_{-\infty}^{t} dt_2 \int_{-\infty}^{t} dt_3 \times \chi^{(3)}(t-t_1, t-t_2, t-t_3) \vdots \boldsymbol{E}(\boldsymbol{r},t_1)\boldsymbol{E}(\boldsymbol{r},t_2)\boldsymbol{E}(\boldsymbol{r},t_3) \\ = \boldsymbol{P}_L + \boldsymbol{P}_{NL}. \end{gathered} \tag{1.4}$$

If the nonlinear response is assumed to be instantaneous, the time dependence of $\chi^{(3)}$ is given by the product of three Dirac's delta functions $\delta(t - t_1)$, therefore the expression can be simplified:

$$\boldsymbol{P}_{NL} = \epsilon_0 \chi^{(3)} \vdots \boldsymbol{E}(\boldsymbol{r},t)\boldsymbol{E}(\boldsymbol{r},t)\boldsymbol{E}(\boldsymbol{r},t) \tag{1.5}$$

Here, $\chi^{(3)}$ is the third-order susceptibility tensor (rank 2). Note that, unlike in birefringent materials, in isotropic ones, the tensor has an inversion symmetry, so it is represented as a diagonal matrix. Therefore, the induced polarization will be proportional to the electric field that creates it. To solve Eq. 1.3 it is necessary to make several simplifying assumptions.

First, we consider that the field polarization is maintained along the fiber length, which is true if bending or defects are avoided (otherwise, a polarization-maintaining fiber can be used). However, the used scalar approach gives a good approximation in practice. Also, since the silica glass is an isotropic material, the $\chi^{(1)}$ and $\chi^{(3)}$ can be simplified to a single component if the field is polarized along the same direction $\hat{x}$: $\chi^{(1)}_{xx}$ and $\chi^{(3)}_{xxxx}$.

Second, we assume the field to be quasi-monochromatic, hence the spectrum of width $\Delta\omega$ is centered around ω_0, while $\Delta\omega/\omega \ll 1$. Since $\omega_0 \sim 10^{15}$ s^{-1}, this assumption is valid for pulses as short as 0.1 ps.

Following the slowly varying envelope assumption, the rapidly varying part of the field can be separated:

$$\boldsymbol{E}(\boldsymbol{r},t) = \frac{1}{2}\hat{x}\left[E(\boldsymbol{r},t)\exp(-i\omega_0 t) + \text{c.c.}\right], \tag{1.6}$$

where $\hat{x}$ is the polarization unit vector, $E(\boldsymbol{r},t)$ is a slowly varying function of time. Using the same notations the induced polarization components can be rewritten as :

$$\boldsymbol{P}_L(\boldsymbol{r},t) = \frac{1}{2}\hat{x}\left[P_L(\boldsymbol{r},t)\exp(-i\omega_0 t) + \text{c.c.}\right] \tag{1.7}$$

$$\boldsymbol{P}_{NL}(\boldsymbol{r},t) = \frac{1}{2}\hat{x}\left[P_{NL}(\boldsymbol{r},t)\exp(-i\omega_0 t) + \text{c.c.}\right] \tag{1.8}$$

In this case the linear polarization is transformed by substituting Eq. 1.7 to the first part of Eq. 1.4:

$$\begin{aligned} P_L(\boldsymbol{r},t) &= \epsilon_0 \int_{-\infty}^{\infty} \chi^{(1)}_{xx}(t-t')E(\boldsymbol{r},t')\exp(-i\omega_0(t-t'))dt' \\ &= \tfrac{\epsilon_0}{2\pi} \int_{-\infty}^{\infty} \chi^{(1)}_{xx}(\omega)\tilde{E}(\boldsymbol{r},\omega-\omega_0)\exp(-i(\omega-\omega_0)t)d\omega \end{aligned} \tag{1.9}$$

Eq. 1.8 can be expanded by substituting Eq. 1.6 in the Eq. 1.5 one obtains a term oscillating at ω_0 and another term at $3\omega_0$. The latter can be omitted since the third-harmonic generation requires a phase matching and is usually neglected in optical fibers. Taking into account Eq. 1.8, the nonlinear response is approximated as :

$$P_{NL}(\boldsymbol{r},t) = \epsilon_0 \frac{3}{4}\chi^{(3)}_{xxxx} |E(\boldsymbol{r},t)|^2 E(\boldsymbol{r},t) = \epsilon_0 \epsilon_{NL} E(\boldsymbol{r},t) \tag{1.10}$$

For further development we will translate this equation to the frequency domain by making a Fourier transform $\boldsymbol{E}(\boldsymbol{r},t) \rightarrow \tilde{\boldsymbol{E}}(\boldsymbol{r},\omega)$, $\chi^{(i)}(t) \rightarrow \tilde{\chi}^{(i)}(\omega)$:

$$\begin{aligned} \mathcal{F}.\mathcal{T}.\left(\frac{\partial^2 \boldsymbol{E}(\boldsymbol{r},t)}{\partial t^2}\right) &= -\omega^2 \tilde{\boldsymbol{E}}(\boldsymbol{r},\omega) \\ \mathcal{F}.\mathcal{T}.\left(\frac{\partial^2 \boldsymbol{P}_L(\boldsymbol{r},t)}{\partial t^2}\right) &= -\epsilon_0 \omega^2 \tilde{\chi}^{(1)}(\omega)\tilde{\boldsymbol{E}}(\boldsymbol{r},\omega) \\ \mathcal{F}.\mathcal{T}.\left(\frac{\partial^2 \boldsymbol{P}_{NL}(\boldsymbol{r},t)}{\partial t^2}\right) &= -\epsilon_0 \omega^2 \epsilon_{NL}\tilde{\boldsymbol{E}}(\boldsymbol{r},\omega). \end{aligned} \tag{1.11}$$

Here we use the following definitions : $\tilde{\boldsymbol{E}}(\boldsymbol{r},\omega) = \mathcal{F}.\mathcal{T}.(\boldsymbol{E}(\boldsymbol{r},t)) = \int_{-\infty}^{+\infty} \boldsymbol{E}(\boldsymbol{r},t)\exp(i\omega t)dt$ for the direct Fourier transform, and $\boldsymbol{E}(\boldsymbol{r},t) = \mathcal{F}.\mathcal{T}.^{-1}(\tilde{\boldsymbol{E}}(\boldsymbol{r},\omega)) = \frac{1}{2\pi}\int_{-\infty}^{+\infty} \tilde{\boldsymbol{E}}(\boldsymbol{r},\omega)\exp(-i\omega t)d\omega$ for the inverse one.

Substituting the Eq. 1.11 in Eq. 1.3 and using equality $\bigtriangledown \times \bigtriangledown \times \boldsymbol{E} = \bigtriangledown(\bigtriangledown \cdot \boldsymbol{E}) - \bigtriangledown^2 \boldsymbol{E} = -\bigtriangledown^2 \boldsymbol{E}$ one obtains :

$$\bigtriangledown^2 \tilde{\boldsymbol{E}} + \epsilon(\omega)\frac{\omega^2}{c^2}\tilde{\boldsymbol{E}} = 0, \tag{1.12}$$

where $\epsilon(\omega) = 1 + \tilde{\chi}^{(1)}(\omega) + \epsilon_{NL}$ is the dielectric constant including linear and nonlinear response. Note that $\epsilon(\omega)$ may change along the spatial coordinate giving $\epsilon(\boldsymbol{r},\omega)$, however, here we assume a homogeneous structure.

Neglecting for a moment ϵ_{NL}, with which we will deal later, the Eq. 1.12 becomes a usual wave equation-like (d'Alembert equation) in the frequency domain, which can be solved by separation of variables. Here we assume that the fiber is invariant along the $z-$ direction, so the general solutions of the linear problem Eq. 1.12 can be expressed as :

$$\tilde{E}(\boldsymbol{r},\omega-\omega_0) = F(x,y)\tilde{A}(z,\omega-\omega_0)\exp(i\beta_0 z), \tag{1.13}$$

where we assume that the spatial mode $F(x,y)$ with an eigenvalue k does not vary much with ω and follows a slowly varying function $\tilde{A}(z,\omega-\omega_0)$ [43]. Here a wave number β_0 will be defined later.

Substituting Eq. 1.13 to Eq. 1.12 and separating transverse $F(x,y)$ and longitudinal $\tilde{A}(z,\omega-\omega_0)$ parts:

$$\frac{\partial^2 F(x,y)}{\partial x^2} + \frac{\partial^2 F(x,y)}{\partial y^2} + \left[\epsilon(\omega)\frac{\omega^2}{c^2} - \tilde{\beta}^2\right]F(x,y) = 0, \tag{1.14}$$

$$2i\tilde{\beta}\frac{\partial \tilde{A}(z,\omega-\omega_0)}{\partial z} + \left(\tilde{\beta}^2 - \beta_0^2\right)\tilde{A}(z,\omega-\omega_0) = 0. \tag{1.15}$$

Under assumption of linear response so that $\epsilon_{NL} = 0$, the solutions of Eq. 1.14 correspond to eigenmodes supported by the fiber with $F(x,y)$ being a spatial distribution that satisfies given geometry and boundary

conditions, and k defining the eigenvalue. This is similar to the Helmholtz equation. Depending on fiber core size and the core-cladding difference, the fiber can support several modes and operate in a multimode regime [44]. For each mode there exists a cut-off frequency and with careful selection of parameters a fiber can operate in a single-mode regime, where only fundamental mode is supported. The shape of the fundamental mode can be approximately described by a Gaussian distribution of the form : $F(x,y) \approx \exp(-(x^2+y^2)/w^2)$ with w being a width parameter obtained from a curve fitting.

Note that here we have used a simplified approach that fits well the context of optical fibers, however, in waveguides in general, the considered simplifications in the Eq. 1.11 and, hence, in the Eq. 1.12 can result in missing some important nonlinear effects, for instance, the slow light effect [41]. In this case, it is better to use a generalized Poynting vector [40,43,45] in derivation of pulse propagation equation. Then instead of Eq. 1.14 and Eq. 1.15 one obtains:

$$\frac{\partial \tilde{A}(z,\omega-\omega_0)}{\partial z}\int \hat{z}\,[F_E \times F_H^* + F_E^* \times F_H]\,dxdy = i\omega \int F_E \exp(-i\beta_0 z)\boldsymbol{P}_{NL}(\boldsymbol{r},\omega)dxdy \tag{1.16}$$

with F_E, F_H being modes of the electric and the magnetic fields, respectively. Nevertheless, with the simplifications valid for optical fibers, the results of two approaches are identical.

If ϵ_{NL} is included, the refractive index n and the absorption coefficient α become intensity dependent, however, in silica the nonlinear contribution to α is small and usually ignored. In the first-order perturbation theory the dielectric constant becomes :

$$\epsilon(\omega) = (n+\Delta n)^2 \approx n^2 + 2n\Delta n, \tag{1.17}$$

with a small perturbation Δn denoted as:

$$\Delta n = \bar{n}_2 \left|E\right|^2 + \frac{i\alpha c}{2\omega}. \tag{1.18}$$

where we assume an equivalence between the power and the field intensity. Here we see an appearance of the linear losses term α that was neglected before.

This perturbation is small enough so that it does not modify solutions $F(x,y)$ of Eq. 1.14, however the eigenvalue becomes $\tilde{\beta} = \beta(\omega) + \Delta\beta(\omega)$. Then Eq.1.15 can be modified using $(\beta(\omega)+\Delta\beta(\omega))^2 - \beta_0^2 = 2\beta_0(\beta(\omega)+\Delta\beta(\omega)-\beta_0)$:

$$\frac{\partial \tilde{A}(z,\omega-\omega_0)}{\partial z} = i\left(\beta(\omega)+\Delta\beta(\omega)-\beta_0\right)\tilde{A}(z,\omega-\omega_0). \tag{1.19}$$

The exact form of $\beta(\omega)$ is rarely known, so one can expand both $\beta(\omega)$ and $\Delta\beta(\omega)$ in a Taylor series around the carrier frequency ω_0 [45]:

$$\beta(\omega) = \beta_0 + (\omega-\omega_0)\beta_1 + \frac{1}{2}(\omega-\omega_0)^2\beta_2 + \frac{1}{6}(\omega-\omega_0)^3\beta_3 + \cdots \tag{1.20}$$

$$\Delta\beta(\omega) = \Delta\beta_0 + (\omega-\omega_0)\Delta\beta_1 + \frac{1}{2}(\omega-\omega_0)^2\Delta\beta_2 + \frac{1}{6}(\omega-\omega_0)^3\Delta\beta_3 + \cdots . \tag{1.21}$$

In principle, the cubic and the higher-order terms in Eq. 1.20 can be neglected under the quasi-monochromatic assumption used in this thesis, however for specific values of ω_0 it may be necessary to include β_3 term [44]. Under the same assumptions value of $\Delta\beta(\omega)$ can be approximated as the first order term $\Delta\beta(\omega) \approx \Delta\beta_0$. Substituting Eq. 1.20 and Eq. 1.21 to Eq. 1.19 and making the Fourier transform, one receives an expression for $A(z,t)$:

$$\frac{\partial A(z,t)}{\partial z} + \beta_1\frac{\partial A(z,t)}{\partial t} + \frac{i\beta_2}{2}\frac{\partial^2 A(z,t)}{\partial t^2} - i\Delta\beta_0 A(z,t) = 0. \tag{1.22}$$

Here $\Delta\beta_0$ is defined as:

$$\begin{aligned}\Delta\beta_0 &= \frac{\omega^2 n(\omega)}{c^2\beta(\omega)}\frac{\int\int_{-\infty}^{\infty}\Delta n\left|F(x,y)\right|^2 dxdy}{\int\int_{-\infty}^{\infty}\left|F(x,y)\right|^2 dxdy} \\ &= \frac{i\alpha}{2}+\left|A(z,t)\right|^2\frac{\omega_0\bar{n}_2}{c}\frac{\int\int_{-\infty}^{\infty}\left|F(x,y)\right|^4 dxdy}{\int\int_{-\infty}^{\infty}\left|F(x,y)\right|^2 dxdy} \\ &= \frac{i\alpha}{2}+\left|A(z,t)\right|^2\gamma,\end{aligned} \tag{1.23}$$

where an approximation $\beta(\omega)\approx n(\omega)\omega/c$ and Eq. 1.18 are used to simplify the expression. Substituting Eq. 1.24 to Eq. 1.22 one obtains:

$$\frac{\partial A(z,t)}{\partial z}+\beta_1\frac{\partial A(z,t)}{\partial t}+\frac{i\beta_2}{2}\frac{\partial^2 A(z,t)}{\partial t^2}+\frac{\alpha}{2}A(z,t)-i\gamma\left|A(z,t)\right|^2 A(z,t)=0. \tag{1.24}$$

Equation 1.24 describes pulse propagation in single-mode optical fibers. It is referred to as the nonlinear Schrödinger (NLS or NLSE) equation (when the losses are neglected). This equation includes effects of losses where α is a measure of total power loss from all sources. The attenuation is expressed in m^{-1} or in dB/km and depends on the wavelength of light. Typical losses of silica fiber are about 0.2 dB/km near 1.55μm and it can be neglected for short propagation lengths. Chromatic dispersion effects are included through β_1 and β_2. Here the pulse envelope moves at the group velocity $v_g=1/\beta_1$ and, in the moving frame $t'=t-z/v_g$, β_1 can be omitted from Eq. 1.24. The β_2 coefficient includes effects of the group velocity dispersion (GVD), this parameter can be positive or negative for the given wavelength and linked to normal or anomalous dispersion regimes, respectively. The nonlinear effect of the self-phase modulation (SPM) are governed by the γ parameter. The effects of GVD and SPM are discussed in more details further.

1.2 Effects of dispersion and nonlinearity

Now consider propagation of a pulse in the framework of the NLSE. Depending on the initial pulse width and the peak power either dispersive or nonlinear effect may dominate the light propagation in fiber. So depending on the interplay between β_2 and γ, one or another phenomenon would develop over the distance. To characterize the propagation regime one may define dispersion and nonlinear lengths, which are defined as, respectively:

$$L_D=\frac{T_0^2}{|\beta_2|}, L_{NL}=\frac{1}{\gamma P_0}, \tag{1.25}$$

where T_0 is the input pulse width and P_0 is the peak power of the input pulse.

In the moving frame and neglecting the losses the Eq. 1.24 becomes the NLSE:

$$i\frac{\partial A(z,t)}{\partial z}-\frac{\beta_2}{2}\frac{\partial^2 A(z,t)}{\partial t^2}+\gamma\left|A(z,t)\right|^2 A(z,t)=0. \tag{1.26}$$

Here we assume that the pulse duration is of picosecond order, and that there is no other sources of scattering. This equation is the framework that will be used in the rest of this thesis.

In the following section the effect of GVD and SPM will be described.

1.2.1. Group-velocity dispersion

Consider a case where nonlinear effect is weak (which is true for at a typical dispersion-dominating case $z \ll L_{NL}$), so the propagation is considered purely linear and γ can be neglected. In this case the NLS equation becomes:

$$i\frac{\partial A(z,t)}{\partial z} - \frac{\beta_2}{2}\frac{\partial^2 A(z,t)}{\partial t^2} = 0. \tag{1.27}$$

This equation is equivalent to the paraxial approximation of the Helmholtz equation that governs light diffraction of a continuous wave when only a transverse direction is taken into account. If β_2 is replaced by $-\lambda/(2\pi)$, one can observe similar diffraction of light on temporal gratings which is evolving in the longitudinal direction. The observed effects have close analogy with diffraction-induced spatial effects [46–48].

The Eq. 1.27 can be solved in the frequency domain by making $\mathcal{F}.\mathcal{T}.(A(z,t))$:

$$i\frac{\partial \tilde{A}(z,\omega)}{\partial z} + \frac{1}{2}\beta_2\omega^2\tilde{A}(z,\omega) = 0. \tag{1.28}$$

The solution of Eq. 1.28 is :

$$\tilde{A}(z,\omega) = \tilde{A}(0,\omega)\exp\left(\frac{i}{2}\beta_2\omega^2 z\right), \tag{1.29}$$

where $\tilde{A}(0,\omega)$ is the Fourier transform of the input pulse $A(0,t)$. From here we see that each spectral line is dephased from another by the GVD effect, and the phase depends linearly on the propagation distance. The spectral amplitude, however, is not affected, nevertheless the pulse shape in temporal domain will be modified :

$$\tilde{A}(z,t) = \frac{1}{2\pi}\int_{-\infty}^{\infty}\tilde{A}(0,\omega)\exp\left(\frac{i}{2}\beta_2\omega^2 z - i\omega t\right)d\omega. \tag{1.30}$$

The spectral phase change caused by the GVD can be seen as an occurring difference in speed of spectral components as they travel along the fiber. In normal dispersion fiber ($\beta_2 > 0$) the red components travel faster, while it is the opposite in the anomalous-dispersion regime ($\beta_2 < 0$). Any time delay in arrival of spectral components leads to pulse broadening.

1.2.2. Self-phase modulation

The refractive index of optical fiber becomes intensity dependent which leads to occurrence of the self-phase modulation - an effect that leads to energy exchange between spectral lines provoking a spectral broadening.

Assuming a lossless fiber with $\alpha = 0$ and highly nonlinear medium so that $L_D \gg L > L_{NL}$, Eq. 1.26 becomes:

$$i\frac{\partial A(z,t)}{\partial z} + \gamma\left|A(z,t)\right|^2 A(z,t) = 0. \tag{1.31}$$

Let's look separately at change of amplitude and phase occurring during propagation by assuming $A(z,t) = |A(z,t)|\exp(i\phi_{NL})$. Since :

$$\begin{aligned}\tfrac{\partial|A(z,t)|^2}{\partial z} &= \tfrac{\partial A(z,t)}{\partial z}A^*(z,t) + A(z,t)\tfrac{\partial A^*(z,t)}{\partial z}\\ &= i\gamma\left|A(z,t)\right|^2 A(z,t)A^*(z,t) - iA(z,t)\gamma\left|A(z,t)\right|^2 A^*(z,t) = 0,\end{aligned} \tag{1.32}$$

the amplitude change is invariant along the fiber length. For the phase we obtain :

$$\frac{\partial |A(z,t)| \exp(i\phi_{NL})}{\partial z} = \frac{\partial |A(z,t)|}{\partial z} \exp(i\phi_{NL}) + |A(z,t)| \frac{\partial \exp(i\phi_{NL})}{\partial z}, \tag{1.33}$$

hence, the nonlinear phase evolves as:

$$\frac{\partial \phi_{NL}}{\partial z} = \gamma |A(z,t)|^2 . \tag{1.34}$$

Then the effect of the SPM at distance z is equal to $\phi_{NL}(z,t) = \gamma |A(0,t)|^2 z$, and the evolution of the field reads:

$$A(z,t) = A(0,t) \exp(i\gamma |A(0,t)|^2 z), \tag{1.35}$$

from which we can conclude that the phase-shift becomes intensity dependent and increases with distance, while the pulse shape remains unaffected. The spectral changes induced by SPM can be seen from temporal variation of the phase:

$$\delta\omega(t) = -\frac{\partial \phi_{NL}(z,t)}{\partial t} = -\gamma z \frac{\partial |A(z,t)|^2}{\partial t}. \tag{1.36}$$

The time dependence of $\delta\omega$ implies a frequency chirping, which magnitude increases with propagation length. Hence, for a given frequency component there are contributions from different times and depending on the exact frequency, these contributions may add up constructively or not [49]. If the initial pulse is not chirped, these SPM generated components make the spectrum broader.

1.2.3. Modulation instability

An interplay between dispersive and nonlinear effects results in a phenomena referred to as a modulation instability (MI). This effect manifests into breaking of a continuous wave (CW) into a train of ultrashort pulses under propagation in an anomalous dispersion media. This effect was observed and studied in other domains such as fluid dynamics, nonlinear optics and plasma physics [1–3].

To demonstrate the effect, we consider propagation of a CW inside of a fiber in the NLSE framework (Eq. 1.26). Under assumption that $A(z,t)$ remains time independent during propagation one obtains a steady-state solution $A(z,t) = \sqrt{P_0} \exp(i\phi_{NL}(z,t))$ which means that the light shall propagate unchanged only acquiring a power-dependent phase. However, this solution does not imply stability in presence of a small perturbation. To check that we consider an ersatz $A(z,t) = (\sqrt{P_0} + a(z,t)) \exp(i\phi_{NL}(z,t))$ to Eq. 1.26:

$$i\frac{\partial a(z,t)}{\partial z} - \frac{\beta_2}{2}\frac{\partial^2 a(z,t)}{\partial t^2} + \gamma P_0 \left(a(z,t) + a^*(z,t)\right) = 0. \tag{1.37}$$

This equation can be solved in the frequency domain, however, due to presence of $a^*(z,t)$ term, the Fourier components at ω and $-\omega$ are coupled, therefore the solution takes form:

$$a(z,t) = a_1 \exp[i(kz - \omega t)] + a_2 \exp[-i(k^* z - \omega t)], \tag{1.38}$$

with k and ω being the wave number and the frequency of the perturbation. Substituting Eq. 1.38 to Eq. 1.37 one obtains a set of two homogeneous equations that has a nontrivial solution when the determinant of:

$$\begin{vmatrix} -k + \omega^2 \frac{\beta_2}{2} + \gamma P_0 & \gamma P_0 \\ \gamma P_0 & k + \omega^2 \frac{\beta_2}{2} + \gamma P_0 \end{vmatrix} \tag{1.39}$$

is equal to zero. In result k and ω must satisfy the following relation:

$$k^2 = \frac{\omega^2 \beta_2^2}{4}\left(\omega^2 + \frac{4\gamma P_0}{\beta_2}\right), \tag{1.40}$$

here, because of the moving framework concept adopted earlier, the frequencies ω and the wave number k should be understood as $\omega_0 \pm \omega$ and $\beta_0 \pm k$. The dispersion relation Eq. 1.40 shows that if the dispersion is normal ($\beta_2 > 0$), then the wave number is real for any frequency, so the state is stable against perturbations. However, in case of anomalous dispersion ($\beta_2 < 0$), k becomes imaginary for $|\omega| < \frac{4\gamma P_0}{\beta_2}$ so the perturbation grows exponentially as it seen from Eq. 1.38, hence the CW solution is unstable for $\beta_2 < 0$. This phenomenon is called a modulation instability because the CW is spontaneously modified which leads to transformation of the CW to a train of short pulses.

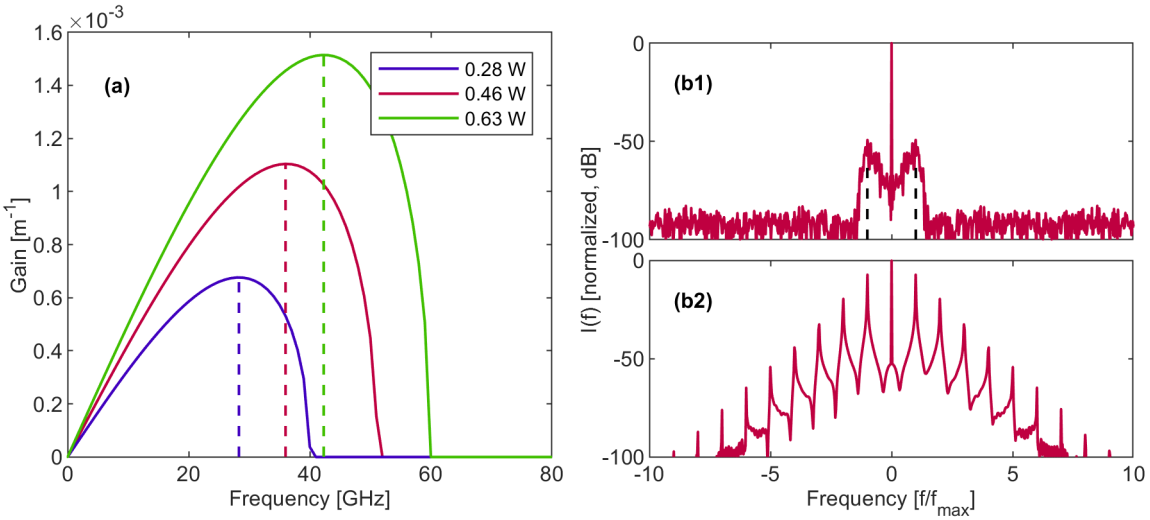

FIGURE 1.1: (a) Gain profiles obtained from Eq. 1.41 for an optical fiber with $\beta_2 = -21.4$ ps^2 km^{-1}, $\gamma = 1.2$ W^{-1} km^{-1} (parameters taken from [10]). Blue, red and green lines correspond to input powers of 0.28, 0.46 and 0.63 W, respectively, with dashed lines marking the maximum gain frequency. Output spectra of a CW seeded with 1% noise (b1) or seed at the maximum gain point of 36 GHz (b2) that propagated over 8 km in the given fiber with input power of $P_0 = 0.46$ W. Here (b1) and (b2) reveal spontaneous and induced modulation instability (and its cascading), respectively.

The gain spectrum is defined by $g(\omega) = 2\Im(k)$:

$$g(\omega) = |\omega\beta_2|\left(\frac{4\gamma P_0}{|\beta_2|} - \omega^2\right)^{1/2}, \tag{1.41}$$

here we denote $\omega_c^2 = 4\gamma P_0/\beta_2$. The gain is symmetric with respect to carrier frequency (hence ω_0) and the maximum appears at $\omega_{max} = \pm\omega_c/\sqrt{2}$ with a value of $2\gamma P_0$. Depending on the input power and fiber parameters, the gain curves have different area and position of the maximum, the shape, though, stays the same. A few examples of gain profiles are depicted in Figure 1.1 (a).

Due to the presence of noise, the MI occurs even when the pump propagates by itself, which will be amplified with frequency peaks located at $\pm\omega_{max}$. This effect is referred to as spontaneous MI [7, 50], and is depicted in Figure 1.1 (b1) where we observe an emergence of amplified sidebands as a result of propagation

of a 1% random noise in a fiber defined as random seeding in the temporal domain. We obtain this result from numerical simulations using a standard split-step Fourier algorithm (note that it is a result of a single run of the simulation without the averaging over several runs). The shape of the spectrum resembles the gain curves, and a position of the maximum coincides with ω_{max}.

If along with a pump wave one launches a probe which frequency located within the MI gain area, the amplitude of the wave is getting amplified with propagation. This phenomenon is called an induced MI [6] and is depicted in Figure 1.1 (b2), where a pump and a 1% seed located at ω_{max} is sent along. Due to MI the spectrum broadens with propagation resulting in a broad comb at ω_{max}. This rather simple process becomes less straightforward when the MI enters its nonlinear stage. In this case, when the second harmonic of initial modulation frequency falls into the MI gain, the breather structure is decomposed and split into two subpulses [51]. Then the process is generalized to an excitation of multiple instability modes that undergo a complex evolution.

MI can occur also if pump waves have different polarization states which can be applied to a case of birefringent fiber (even for the normally dispersive ones). In this case one writes coupled NLSE for each polarization state and derives linear equations in a presence of a small perturbation [52]. From these equations the presence of MI gain is evident, and exponential growth of polarized sidebands was observed [53–55]. In the present thesis both pump and the sidebands are considered polarized on a single axis, therefore effects of the polarization MI are neglected.

In the next part the modulation instability will be interpreted in terms of a four-wave mixing (FWM) process that is phase-matched by the SPM [3, 56].

1.3 Degenerate four-wave mixing (FWM)

The four-wave mixing (FWM) describes a process of interaction between waves at four different frequencies which are mixed by an action of the $\chi^{(3)}$ coefficient in the Kerr medium as light propagates in an optical fiber. The FWM has a myriad of practical applications in fibers including frequency-conversion devices and amplifiers [31, 32].

The FWM process requires two pumps with distinct frequencies, however the special case with a single pump beam can be considered as well [57]. In this case the process is degenerate and sometimes called three-wave mixing since only three frequencies are involved. Note that this process should not be confused with the second order nonlinearity, since silica glass doesn't have $\chi^{(2)}$. During the degenerate FWM two waves with upshifted and downshifted frequencies are generated due to nonlinear interaction.

To derive the FWM equations, we first consider propagation of three optical waves, that are assumed to be collinearly polarized and monochromatic, at frequencies ω_0, $\omega_0-\omega_m$ and $\omega_0+\omega_m$, with respective propagation constants $k_0 = k(\omega_0)$, $k_{-1} = k(\omega_0-\omega_m)$, $k_1 = k(\omega_0+\omega_m)$, and with complex electric field envelope denoted Ψ_0, Ψ_{-1} and Ψ_1, respectively [11]. The total field in this case reads as :

$$A(z,t) = \Psi_0(z)\exp(ik_0 z) + \Psi_{-1}(z)\exp(ik_{-1}z - i\omega_m t) + \Psi_1(z)\exp(ik_1 z + i\omega_m t). \tag{1.42}$$

The propagating waves are interacting through the Kerr nonlinearity of the fiber. A frequency separation between the waves is considered small (around dozens GHz), so the Raman effect does not impact the propagation [58], also the process is considered as nearly phase-matched, and the generation of higher order harmonics is neglected.

Substituting Eq. 1.42 in the Eq. 1.26 and separating terms at ω_0, $\omega_0 - \omega_m$ and $\omega_0 + \omega_m$, one receives a set of coupled equations, that are fundamental in many works [11, 59, 60]:

$$\begin{cases} -i\frac{d\Psi_0}{dz} = \gamma\left(|\Psi_0|^2 + 2|\Psi_{-1}|^2 + 2|\Psi_1|^2\right)\Psi_0 + 2\gamma\Psi_{-1}\Psi_1\Psi_0^*\exp(i\Delta kz) \\ -i\frac{d\Psi_{-1}}{dz} - \frac{1}{2}\omega_m^2\beta_2\Psi_{-1} = \gamma\left(|\Psi_{-1}|^2 + 2|\Psi_1|^2 + 2|\Psi_0|^2\right)\Psi_{-1} + \gamma\Psi_1^*\Psi_0^2\exp(-i\Delta kz) \\ -i\frac{d\Psi_1}{dz} - \frac{1}{2}\omega_m^2\beta_2\Psi_1 = \gamma\left(|\Psi_1|^2 + 2|\Psi_{-1}|^2 + 2|\Psi_0|^2\right)\Psi_1 + \gamma\Psi_{-1}^*\Psi_0^2\exp(-i\Delta kz) \end{cases} \tag{1.43}$$

where $\Delta k = k_1 + k_{-1} - 2k_0$ is the propagation constant mismatch.

This system should be solved numerically, if one wants to obtain the evolution equations for three waves. An approximate solution can be obtained when specific assumptions are made, for instance, if the pump wave is strong enough, so it can be considered as undepleted.

1.3.1. Undepleted pump approximation

In the undepleted pump approximation, the pump is assumed to be much more intense than any other waves participating in the interaction, so the FWM is considered undepleted [44]. In this case, $|\Psi_0| \gg |\Psi_{-1}|, |\Psi_1|$ so the Eqs. 1.43 are modified as :

$$\begin{cases} -i\frac{d\Psi_0}{dz} = \gamma|\Psi_0|^2\Psi_0 \\ -i\frac{d\Psi_{-1}}{dz} = 2\gamma|\Psi_0|^2\Psi_{-1} + \gamma\Psi_1^*\Psi_0^2\exp(-i\Delta kz) \\ -i\frac{d\Psi_1}{dz} = 2\gamma|\Psi_0|^2\Psi_1 + \gamma\Psi_{-1}^*\Psi_0^2\exp(-i\Delta kz) \end{cases} \tag{1.44}$$

The first equation can be readily solved :

$$-i\frac{d\Psi_0}{dz} = \Psi_0(0)\exp(i\gamma|\Psi_0|^2 z), \tag{1.45}$$

where $\Psi_0(0) = \Psi_0(z=0)$ is initial pump power. We see that the pump experiences only phase changes due to the SPM during the propagation.

Denote $P_0 = |\Psi_0|^2$, and substitute Eq. 1.45 in Eqs. 1.44 with making a conjugate of the last equation :

$$\begin{cases} -i\frac{d\Psi_{-1}}{dz} = 2\gamma P_0\Psi_{-1} + \gamma\Psi_1^*\Psi_0^2(0)\exp(-i\Delta kz + i2\gamma P_0 z) \\ i\frac{d\Psi_1^*}{dz} = 2\gamma P_0\Psi_1^* + \gamma\Psi_{-1}\Psi_0^2(0)\exp(i\Delta kz - i2\gamma P_0 z). \end{cases} \tag{1.46}$$

Denote $B_j = \Psi_j\exp(-i2\gamma P_0 z)$ with $j = \pm 1$ and transform the equations to :

$$\begin{cases} -i\frac{dB_{-1}}{dz} = \gamma B_1^*\Psi_0^2(0)\exp(-i\Delta kz + i2\gamma P_0 z) \\ i\frac{dB_1^*}{dz} = \gamma B_{-1}\Psi_0^{*2}(0)\exp(i\Delta kz - i2\gamma P_0 z). \end{cases} \tag{1.47}$$

After differentiating these equations for the second time and making simplifications, one receives :

$$\begin{cases} \frac{d^2B_{-1}}{dz^2} + i(\Delta k + 2\gamma P_0)\frac{dB_{-1}}{dz} - \gamma P_0^2 B_{-1} = 0 \\ \frac{d^2B_1^*}{dz^2} - i(\Delta k + 2\gamma P_0)\frac{dB_1^*}{dz} - \gamma P_0^2 B_1 = 0. \end{cases} \tag{1.48}$$

General solutions of these equation are :

$$B_{-1} = \left(a_{-1}\exp(\sqrt{\gamma P_0^2-(\Delta\kappa/2)^2}z)+b_{-1}\exp(-\sqrt{\gamma P_0^2-(\Delta\kappa/2)^2}z)\right)\exp(-i\Delta\kappa/2z), \quad (1.49)$$

$$B_1 = \left(a_1\exp(\sqrt{\gamma P_0^2-(\Delta\kappa/2)^2}z)+b_1\exp(-\sqrt{\gamma P_0^2-(\Delta\kappa/2)^2}z)\right)\exp(i\Delta\kappa/2z), \quad (1.50)$$

where $\Delta\kappa = (\Delta k + 2\gamma P_0)$ denotes an effective phase mismatch, a_j, b_j with $j = \pm 1$ are determined based on boundary conditions. Here value of $\sqrt{\gamma P_0^2-(\Delta\kappa/2)^2}$ denotes the parametric gain, which has a similar shape as the MI gain when plotted with respect to the mismatch $\Delta\kappa$. The results of these equations are fully consistent with the MI approach derived in the Section 1.2.3., which shows that the linear stage of the MI and the FWM in the undepleted regime are identical.

The derived equations give an approximate solution to the FWM problem, however, the undepleted pump approximation is a very strong assumption and holds only in very special situations in practice. Therefore, we develop another set of governing equations that would work in any configuration.

1.3.2. General governing equations

We continue from the Eqs. 1.43. Next step is to separate the phase and the amplitude of each spectral component : $\Psi_i = \psi_i \exp i\phi_i$, where $\psi_i = |\Psi_i|$ and $\phi_i = angle(\Psi_i)$. After separating real and imaginary parts of Eq. 1.43 one receives:

$$\begin{cases} \frac{d\phi_0}{dz} = \gamma\left(\psi_0^2+2\psi_{-1}^2+2\psi_1^2\right)+\gamma\psi_{-1}\psi_1\cos\phi \\ \frac{d\phi_{-1}}{dz}-\frac{1}{2}\omega_m^2\beta_2 = \gamma\left(\psi_{-1}^2+2\psi_1^2+2\psi_0^2\right)+\gamma\psi_{-1}^{-1}\psi_1\psi_0^2\cos\phi \\ \frac{d\phi_1}{dz}-\frac{1}{2}\omega_m^2\beta_2 = \gamma\left(\psi_1^2+2\psi_{-1}^2+2\psi_0^2\right)+\gamma\psi_1^{-1}\psi_{-1}\psi_0^2\cos\phi \\ \psi_0\frac{d\psi_0}{dz} = -2\gamma\psi_{-1}\psi_1\psi_0^2\sin\phi \\ \frac{d\psi_{-1}}{dz} = \gamma\psi_1\psi_0^2\sin\phi \\ \frac{d\psi_1}{dz} = \gamma\psi_{-1}\psi_0^2\sin\phi \end{cases} \quad (1.51)$$

Here $\phi(z) = \Delta kz + \phi_{-1} + \phi_1 - 2\phi_0$ represents a phase mismatch between the pump and the sidebands. Under assumption that the energy exchange is restricted solely to the three waves interaction with no losses, the total power $P_0 = |\psi_0|^2 + |\psi_{-1}|^2 + |\psi_1|^2$ is conserved, hence, we can normalize the amplitudes denoting $\eta = \psi_0^2/P_0$, $\psi_{-1,1} = \psi_{-1,1}/\sqrt{P_0}$. In this case equations Eqs. 1.51 become:

$$\begin{aligned} \frac{d\eta}{dz} &= -4\gamma P_0\psi_{-1}\psi_1\eta\sin\phi, \\ \frac{d\psi_{-1}}{dz} &= \gamma P_0\psi_1\eta\sin\phi, \\ \frac{d\psi_1}{dz} &= \gamma P_0\psi_{-1}\eta\sin\phi, \\ \frac{d\phi}{dz} = \omega_m^2\beta_2 &+ \gamma P_0\left(-\psi_1^2-\psi_{-1}^2+2\eta\right)+\gamma P_0\left[\eta\left(\frac{\psi_{-1}}{\psi_1}+\frac{\psi_1}{\psi_{-1}}\right)-4\psi_{-1}\psi_1\right]\cos\phi. \end{aligned} \quad (1.52)$$

To achieve a phase-matching one has to fulfill :

$$\Delta k_M + \Delta k_W + \Delta k_{NL} = 0, \quad (1.53)$$

where the three terms represent the mismatch induced by material, waveguide dispersion and nonlinear contribution, respectively. General technique of phase-matching include working near the zero-dispersion point for

small frequency detuning at low power [61] In our case, the linear mismatch, that includes $\Delta k_M + \Delta k_W$ is defined as

$$\Delta k_M + \Delta k_W = \omega_m^2 \beta_2. \tag{1.54}$$

The nonlinear contribution :

$$\Delta k_{NL} = \gamma P_0 \left(|\psi_1|^2 - |\psi_{-1}|^2 + 2\eta \right) \tag{1.55}$$

can be approximated as $\approx 2\gamma P_0$ if one considers propagation of a strong pump and small sidebands.

Therefore, to achieve a phase-matching one can work in anomalous dispersion regime, so that the linear contribution is compensated by the nonlinear one: $\Delta k_M + \Delta k_W = -\Delta k_{NL}$. By substituting Eqs. 1.55 and 1.54 to 1.53, one obtains $\omega_m = \sqrt{(\frac{2\gamma P_0}{|\beta_2|})}$. The given detuning corresponds to a positive frequency ω_{max} at which the maximum modulation instability gain is achieved, which is consistent with interpretation of induced MI through a FWM process [12]. To introduce a mismatch that characterizes the process we denote $\kappa = sgn(\beta_2)\frac{|\beta_2|\omega_m^2}{\gamma P_0}$. Note that, under specific conditions, the phase-matching can be achieved in the normal dispersion regime which results in manifestation of the modulation instability and the FWM [62, 63].

1.3.3. The system invariants and Hamiltonian approach

A pioneering interpretation of the FWM was proposed in 1991 by S. Trillo, S. Wabnitz and G. Cappellini [11, 12], where the Hamitonian formulation and the phase-space plane were used to characterize the dynamics. Below we give an overview of the system's interpretation.

In addition to the total power, the considered system is characterized by another two invariants. From the second and third equations of Eqs. 1.52 one obtains the first invariant:

$$\rho = |\psi_{-1}|^2 - |\psi_1|^2. \tag{1.56}$$

This parameter characterizes an asymmetry between two sidebands, and is conserved during propagation if the interaction is limited to three spectral lines only.

The last invariant is obtained from the first and the fourth equations of 1.52 using Eq. 1.56 :

$$H(\eta, \phi) = 2\eta \left[(1-\eta)^2 - \rho^2 \right]^{1/2} \cos\phi - (\kappa - 1)\eta - \frac{3}{2}\eta^2. \tag{1.57}$$

This one dimensional conservative Hamiltonian represents the conservation of the time-averaged energy of the field. This formulation allows to reduce the set of equations to :

$$\begin{cases} \frac{1}{\gamma P_0}\frac{d\eta}{dz} = \frac{dH(\eta,\phi)}{d\phi} = -2\eta \left[(1-\eta)^2 - \rho^2 \right]^{1/2} \sin\phi \\ \frac{1}{\gamma P_0}\frac{d\phi}{dz} = -\frac{dH(\eta,\phi)}{d\eta} = (\kappa - 1) + 3\eta - 2\frac{1+2\eta^2-3\eta-\rho^2}{\left[(1-\eta)^2-\rho^2\right]^{1/2}} \cos\phi. \end{cases} \tag{1.58}$$

To analyze dynamics of FWM first, consider a case when the sidebands are equal, hence $\rho = 0$. In this case the Eq. 1.58 are modified:

$$\begin{cases} \frac{1}{\gamma P_0}\frac{d\eta}{dz} = \frac{dH(\eta,\phi)}{d\phi} = -2\eta\,(1-\eta)\sin\phi \\ \frac{1}{\gamma P_0}\frac{d\phi}{dz} = -\frac{dH(\eta,\phi)}{d\eta} = (\kappa - 1) + 3\eta - 2\,(1-2\eta)\cos\phi. \end{cases} \tag{1.59}$$

This system will be a great help throughout the manuscript and will constitute a major of the work.

1.3.4. The eigensolutions and phase-space portraits

The dynamical exchange of amplitude and phase between the three lines can be analyzed with the help of phase-space portrait where we adopt polar coordinates $X = \eta\cos\phi, Y = \eta\sin\phi$ to display evolution of η, ϕ with distance. Depending on value of κ the portraits would experience different patterns and eigensolutions described above may become unstable. Further we characterize the features and types of observed dynamics with the help of the phase-space plane.

The eigensolutions of this system represent the input conditions η_0, ϕ_0 that propagate unchanged along the fiber, i.e. stationary solutions. Starting from $\frac{dH(\eta,\phi)}{d\phi} = 0$ and using $\frac{dH(\eta,\phi)}{d\eta} = 0$, one obtains the following eigensolutions.

- $\eta_0 = 0$ with $\phi_0 = \cos^{-1}[(\kappa-1)/2]$ which corresponds to interaction of two waves in the absence of pump. This solution is stable for the values of $\kappa \notin [-1:3]$. Formally, even if the phase relation is not fulfilled, no power exchange occurs among the waves, so the solution still holds and we remain on that fixed point.
- $\eta_0 = 1$ with $\phi_0 = \cos^{-1}[-(\kappa+2)/2]$ displays propagation of the central line (pump) in the absence of sidebands.
- $\phi_{fp} = 0$ or π with $\eta_{fp} = (3-\kappa)/7$ or $\eta_{fp} = 1+\kappa$, for the values of κ that satisfy $0 < \eta < 1$.

For large absolute values of κ only solutions $\eta_0 = 0$ or 1 are stable, however, as soon as κ is within $[-4, 3]$ these solutions loose their stability giving priority to η_{fp} and ϕ_{fp}. When value of κ corresponds to existence of unstable solutions the phase-space portrait consists of two regions of periodic orbits divided by the unstable solution at $\eta_0 = 1$. This solution is referred to as a homoclinic or a separatrix trajectory. In Figure 1.2 (b) one observes a phase-space portrait at $\kappa = -2$ (the value that corresponds to maximum MI gain) obtained by plotting dynamics with different input conditions on one graph. The dashed black line marks position of the separatrix. Panels (a) and (c) of Figure 1.2 depict other phase portraits when eigensolutions $\eta_0 = \{0, 1\}$ are stable, so the separatrix position is not defined.

In case of intermediate values of $\kappa \in [-4, 3]$ the fixed point η_{fp} emerges. Panels (a1) and (a2) in Figure 1.3 display propagation and the distinctive shape of the fixed point (red solid line). In the focusing NLSE exists a class of stationary solutions known as dnoidal (dn-) and cnoidal (cn-) waves [15], where dn-wave corresponds to a solution with a carrier frequency included, hence, resembling the degenerate FWM. For comparison this shape is plotted in gray solid line in Figure 1.3 (a2), from which we can conclude that the fixed point is a unique solution that is not included into other class of stationary solutions. Panel (b) in Figure 1.3 displays change in characteristic shapes on two sides of the separatrix. With variation of κ one observes growth of left or right parts, shifts of positions of the separatrix and the fixed point [12].

Depending on the initial phase, the dynamics belongs to either the left or right sides. These trajectories may have different shapes and speed of rotation. An example of the dynamics with input $\eta = 0.90$ or 0.30 for the phases $\phi_0 = 0$ or π, respectively, is depicted in panels (b) of Figure 1.4. The temporal intensity experiences a recurrence pattern known as FPUT recurrence [16] - a fundamental phenomenon observed in many domains including hydrodynamics, plasma physics [64–66]. For the right-side trajectories, the recurrence pattern has a regular periodicity period and is symmetric, while for the left ones the period is doubled revealing a broken symmetry [67]. These features can be explained by the phase behavior that is behind the two regimes : close trajectories on the right side have the phase which is bounded, hence, oscillating around an average value. On the contrary, on the left side the phase growth with propagation experiencing unbounded nature (Figure 1.4 (c)).

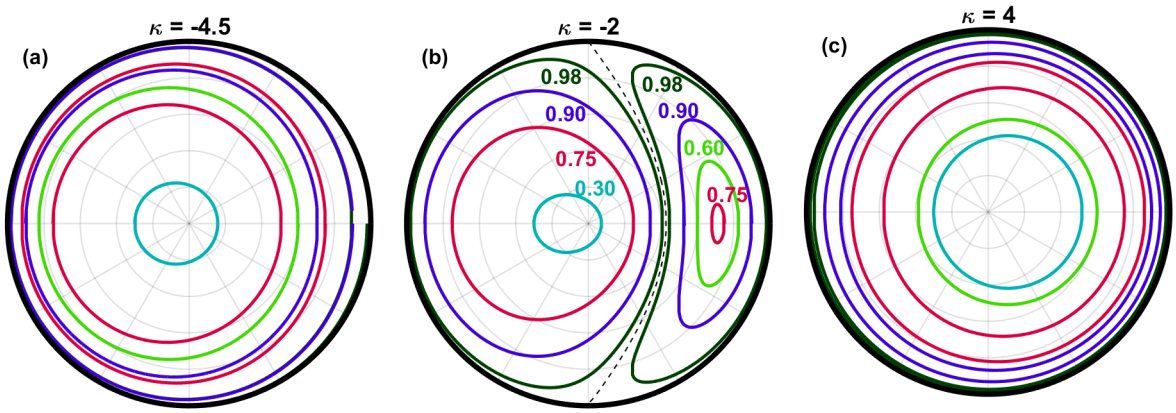

FIGURE 1.2: (a-c) Phase-space portraits displaying evolution of relative amplitude η and phase ϕ of three spectral lines over a distance of 25 km in a fiber with $\gamma = 1.7\ \mathrm{W^{-1}km^{-1}}$, $\beta_2 = -8\ \mathrm{ps^2m^{-1}}$ and input wave of average powers $P_0 = 67, 150, 75$ mW (18.22, 21.7, 18.75 dBm) corresponding to $\kappa = -4.5, -2, 4$, respectively. Case (c) corresponds to normal dispersion of $\beta_2 = 8\ \mathrm{ps^2m^{-1}}$. Dashed line marks the separatrix position. In panel (b) trajectories on the left correspond to the input phase of π, while the right ones to 0. Input values of η are denoted on the panel (b).

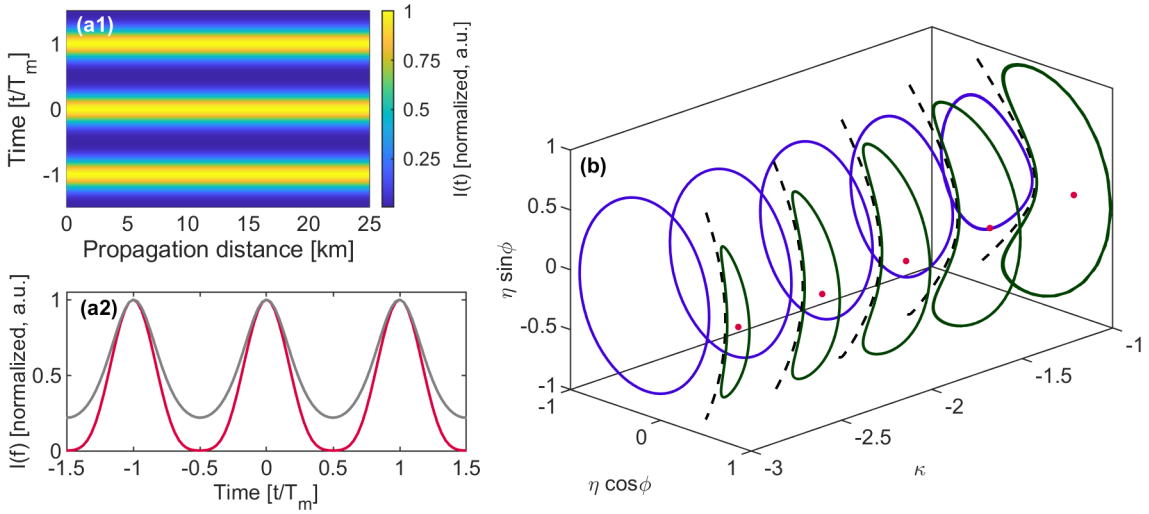

FIGURE 1.3: (a1) Evolution of temporal intensity of a fixed point input condition for $\kappa = -2$. (a2) Comparison of the intensity profile of the fixed point (red solid line) with the dn-periodic wave (Eq. (3) in [15]) with $k = 0.78$ (gray solid line). Here $T_m = 2\pi/\omega_m$ is the modulation period. (b) Phase-space portraits for $\eta_0 = 0.98, \phi_0 = 0$ and $\eta_0 = 0.90, \phi_0 = \pi$ in blue and green solid lines, respectively, for varying value of κ. Red markers denote position of a fixed point according to $(3 - \kappa)/7$. Black dashed lines mark position of the separatrix for each value of κ.

Impact of the phase dynamics on the recurrence periodicity can be readily seen if the intensity profile is represented as an interference of three spectral lines:

$$\begin{aligned} I(t,z) &= |\psi_{-1}(z)\exp(-i\omega t + i\phi_{-1}(z)) + \psi_0(z)\exp(i\phi_0(z)) + \psi_1(z)\exp(-i\omega t + i\phi_1(z))|^2 \\ &= 1 + (1-\eta(z))\cos(2\omega t) + 4\sqrt{\tfrac{\eta(z)(1-\eta(z))}{2}}\cos(\omega t)\cos\tfrac{\phi(z)}{2}. \end{aligned} \tag{1.60}$$

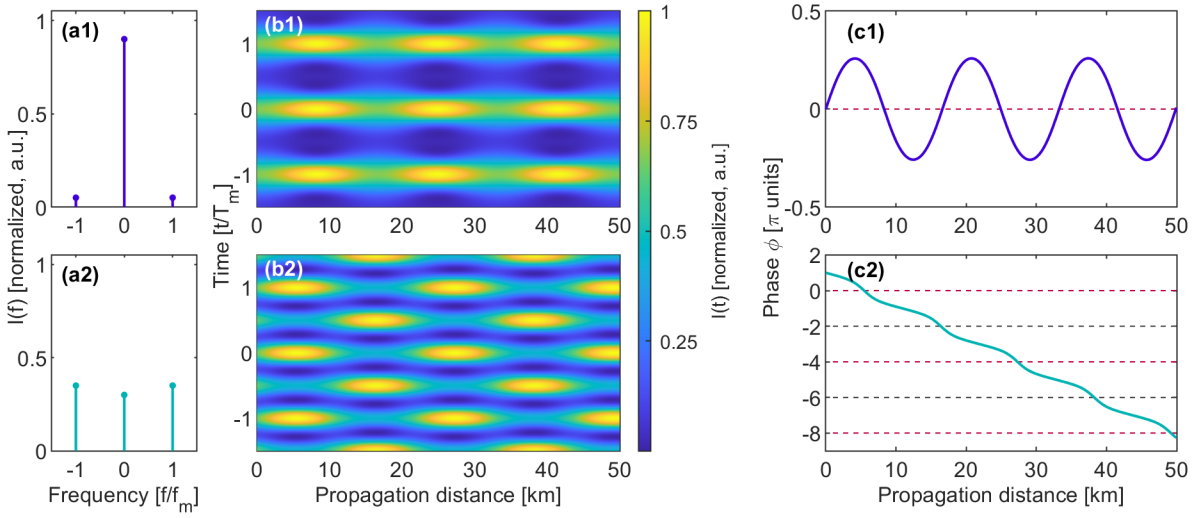

FIGURE 1.4: Evolution of temporal intensity of the spectra depicted in panels (a) with input parameters $\eta_0 = 0.90, \phi_0 = 0$ and $\eta_0 = 0.30, \phi_0 = \pi$, respectively, is displayed in (b1) and (b2). Solid lines in panels (c1), (c2) display evolution of phase for the given input conditions. Dashed red and gray lines mark values of phase that correspond, respectively, to maximum and minimum of intensity at $t = 0$.

In this case intensity in the center of the time axis $t = 0$ can be described as:

$$I(t = 0, z) = 2 - \eta(z) + 4\sqrt{\frac{\eta(z)(1 - \eta(z))}{2}} \cos\frac{\phi(z)}{2}. \tag{1.61}$$

Hence, the maximum of intensity is observed at positions where $\phi(z) = 4\pi(n - 1)$, while the minimum at $\phi(z) = 2\pi(2n - 1)$ where $n = 1, 2, \ldots N$ is an integer number. Marking these positions with red and gray dashed lines, respectively, in Figure 1.4 (c), one observes that for trajectories on the right the phase oscillates around zero, which corresponds to the maximums appearing. In case of the unbounded phase evolution, the maximum and minimum at central position are alternated and we observe period doubling and shift of periodicity.

To display the phase features typical for the left and right sides on the phase-space portraits more straightforwardly, there exist other possibilities in axis definitions. Other approaches seen in the literature include the use of $X = \phi, Y = \eta$ axis directly (hence, the genuine phase portrait representation) [68, 69] or adopt $X = (1 - \eta)\cos(\phi/2), Y = (1 - \eta)\sin(\phi/2)$ [4, 70]. In these cases the unbounded phase feature is presented in form of continuous trajectories or larger orbits outside the separatrix as it is presented in Figure 1.5 (a) and (b), respectively. Another possible notations include movement of trajectories using analogies with a Poincare sphere [71].

Here the focus is on the degenerate FWM, however similar equations and features of the dynamics can be drawn in the dual pump case [13].

1.4 Conclusion

We have provided a development of the light propagation starting from Maxwell's equations. After specifying the effects of dispersion and nonlinearity on light propagating in a fiber, we provide an insight into the MI

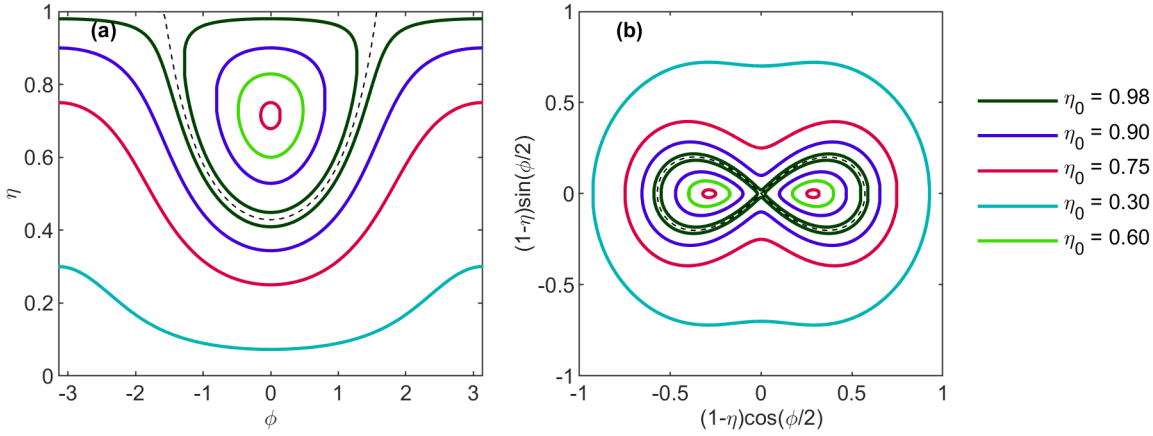

FIGURE 1.5: Other notations used to describe the FWM phase diagram. (a) Phase-space portrait in $X = \phi, Y = \eta$, (b) in $X = (1-\eta)\cos(\phi/2), Y = (1-\eta)\sin(\phi/2)$ coordinates.

phenomenon. Then we give a reminder on the FWM equations for the degenerate case in optical fiber. The FWM dynamics results in recurrence patterns that, following the formalism developed by S. Trillo, S. Wabnitz and G. Cappellini in 1991 [11, 12], can be displayed on the phase-space plane in terms of closed orbits. The orbits shape depends on a value of the mismatch parameter κ that includes properties of the system (nonlinearity, dispersion, input average power) and light (frequency, initial relative amplitude and phases). There exist two types of trajectories : one with bounded and another with unbounded phases which is reflected in different types of recurrence. Further we seek for an experimental technique that would allow to demonstrate the ideal FWM experimentally.

Chapter 2

Experimental setup

This chapter is dedicated to a detailed description of the idea, practical implementation and accuracy estimation of the developed experimental setup. First we give the description of the state of the art in the experimental demonstration of the FWM. Then we discuss obstacles and limitations to demonstrate experimentally the ideal FWM. In order to counteract these effects, we proposed the setup based on iterative propagation. We explain how it is used to reconstruct the ideal FWM orbits. The errors, stability and level of residual sidelobes are characterized, as well as other detrimental experimental effects.

2.1 State of the art of wave mixing in the NLSE framework

As it was shown in the previous chapter, the FWM occurs between the spectral lines when the phase-matching is fulfilled. We have shown the general set of differential equations that describes fundamental interaction between three waves. However, in practice, when light propagates in a fiber according to the NLSE, the dynamics becomes more complex and nontrivial. As soon as energy exchange happens between the three waves and the sidelobes amplitudes start to grow, more spectral lines start to generate from the latter which leads to growth of spectral harmonics. This process can be described as a cascaded FWM, and it was demonstrated numerically and experimentally [51, 72, 73]. In this case, the interaction between the waves becomes of more complex nature, and the description in terms of differential equations may become lengthy and complicated [74]. So the wave evolution can be easier retrieved from direct numerical simulation of the NLSE propagation. However, the features of the FWM, such as two types of dynamics and the FPUT recurrence, are preserved [75].

In this section we review the existing approaches to demonstrate the FWM experimentally in fiber optics. We describe different techniques and recall the scientific results.

Experimental demonstration of the FWM process is a challenging task. Note that due to analogy with other domains, demonstration of the recurrence and other features is also feasible. For instance, in case of hydrodynamics, the distributed measurements are readily available which makes the FPUT recurrence observed easier, however, it can be impaired by effects of damping or forcing [14, 69, 76]. In fiber optics, first, the evolution is impaired by loss of the fiber. In this case, the total power drops and the recurrence is broken which leads to the trajectories falling to the phase-shifted type of dynamics [70]. To avoid this effect, either a short piece of fiber can be used, or the fiber loss is compensated by a counter-propagating Raman pump [4, 17–19, 70]. This scheme consists in pumping the fiber with a Raman laser source in the backward direction, so the Raman gain is distributed along the fiber length [77], and it minimizes the relative intensity noise transfer from the

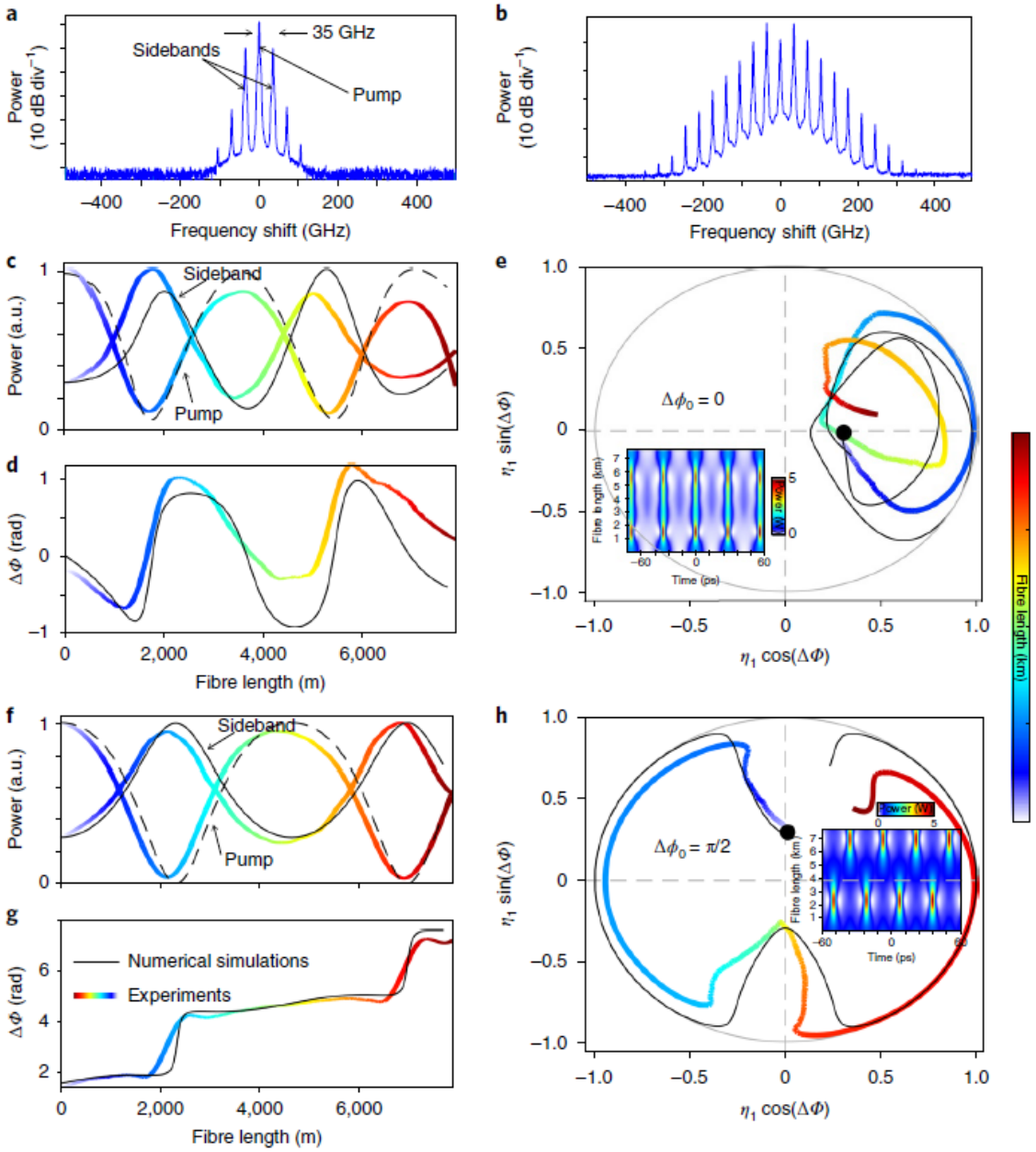

FIGURE 2.1: Observed recurrences and their phase-plane projections. Spectra at the input of the SMF28 (a) and the fiber output recorded with an optical spectrum analyser by slightly decreasing the sideband amplitude to shift the maximal compression point at the fiber output (b). Evolution along the fiber length of the pump power (dashed lines) and the first sideband pair power (dotted lines) in (c,f), and the relative phase $\Delta\phi = \phi/2$ (d,g). (e,h) Projections of the evolutions in the 3WM phase plane (the insets show the corresponding evolutions obtained numerically from the NLSE). Numerical simulations are depicted in black lines and experiments in solid rainbow lines. (c-e) and (f-h) differ only in the initial relative phase of the modulation, $\Delta\phi = 0$ and $\Delta\phi = \pi/2$, respectively. *Source : Mussot et al. Nature Photonics, 12, 2018* [70].

pump to signal. With such a technique, the recurrence can be kept stable.

Another effect that impairs the FPUT recurrence is the noise. Due to spontaneous MI the quantum noise

background is amplified after a few recurrence cycles that leads the field to break-up into an irregular structure with high intensity peaks at different points of space and time [78, 79]. This leads to irreversible evolution and breaking of the FPUT recurrence patterns.

Therefore, both effects of loss and noise unavoidably affect light propagation in fiber, however, they can be mitigated depending on the selected experimental technique.

Experimental approaches to demonstrate the reversibility of the MI and the FPUT recurrence in fiber optics can be split into two groups: a cutback method, where the results of propagation in different fiber lengths are concatenated to construct the complete evolution, and distributed measurements, where the dynamics is recorded as light propagates in a fiber.

The cutback (or cutting-back) method consists in measuring the output signal resulting from propagation in fiber segments of different lengths. If the input signal for each segment is the same, we can observe how it evolves with gradually growing propagation length. Usually the evolution is observed in terms of the spectral amplitudes that can be measured with a commercially available spectrum analyzer. As such, the FPUT recurrence was experimentally demonstrated in optical fibers in [80], where the stage of spectral broadening measured each 250 m was followed by compression. This method allows to investigate dynamics of different types of waves by just changing the input conditions, for instance, in [15] the authors observe evolving spectra of cnoidal (cn-) and dnoidal (dn-) waves. Since evolution of residual lines is unlimited in this approach, it is also possible to investigate higher-order MI [10] or multi-wave mixing in the nonlinear stage of MI [81]. Another way to observe the evolving dynamics is to vary the input power with the fixed fiber length, hence, the normalized distance $\gamma P_0 L$ is changed [82], which is similar to some extend to the previously described process. Overall the cutback approach is quite simple and reliable, however, the preparation and the measurements are time-consuming, and usually the phase evolution is not accessible.

Performing distributed measurements of phase and amplitude on a picosecond timescale is another challenge. One way is the Rayleigh scattering, where the scattered light envelope is proportional to the power evolution along the fiber. Therefore, in order to record the FPUT recurrence, one can measure the Rayleigh signals of various sidebands, and then reconstruct the spectral evolution along the propagation distance [80].

Another non-destructive approach relies on recirculating fiber loop with periodic amplification [83]. Here, with synchronized acousto-optical modulators, the input long pulses are recirculated inside of a 75 km fiber in a controlled manner : the number of spans can be manipulated from 0 to 120, allowing to simulate an effective propagation over 9000 km. Both real and imaginary parts of the waveforms are recorded with an intradyne coherent receiver, so the FPUT dynamics was demonstrated both in spectral phases and amplitudes.

A breakthrough in the experimental FPUT investigation was made in 2018 in the group of A. Mussot, where a setup based on a vector heterodyne time-domain reflectometer was developed [70]. Starting from the CW laser, a pump and a pair of sidebands propagate in the SMF fiber of 7.7 km, where the MI dynamics manifests itself. Then the backscattered signal is recirculated and analyzed via heterodyning (beating with the local oscillator), and the amplitudes and phases of each spectral line are extracted through filtering. With the help of this technique the FPUT recurrence has been demonstrated : in Figure 2.1 one observes how pump and sidebands grow and decay over multiple cycles with phase-space portraits following the recurrence orbits. Here, since the fiber length is rather long, the loss impact is counterbalanced by the Raman amplification described earlier.

The following works have demonstrated longitudinal profiles and orbits that correspond to two different types of dynamics : with normal and period-shifted symmetry (Figures 2.2 and 2.3, respectively) [17], that are sometimes referred to as the A and B-types of periodic solutions of the NLSE [19, 84]. The retrieved dynamics

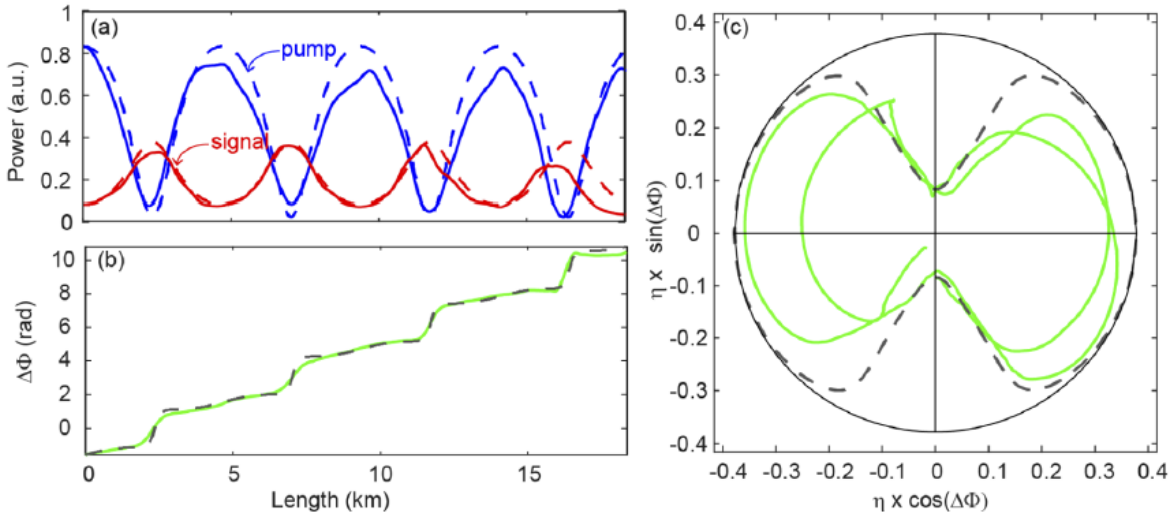

FIGURE 2.2: Longitudinal evolution of (a) the pump (blue line) and signal/idler (red line) powers and (b) their relative phase for $\Delta\phi = \phi/2 = -\pi/2$; (c) Phase-plane representation. Here η is the signal power normalized to the total power (therefore $1-\eta$ in the adopted notations). Solid and dashed lines stand for experimental results and numerical simulations from NLSE, respectively. *Source : Vanderhaegen et al. Opt.Express, 28, 2020* [18].

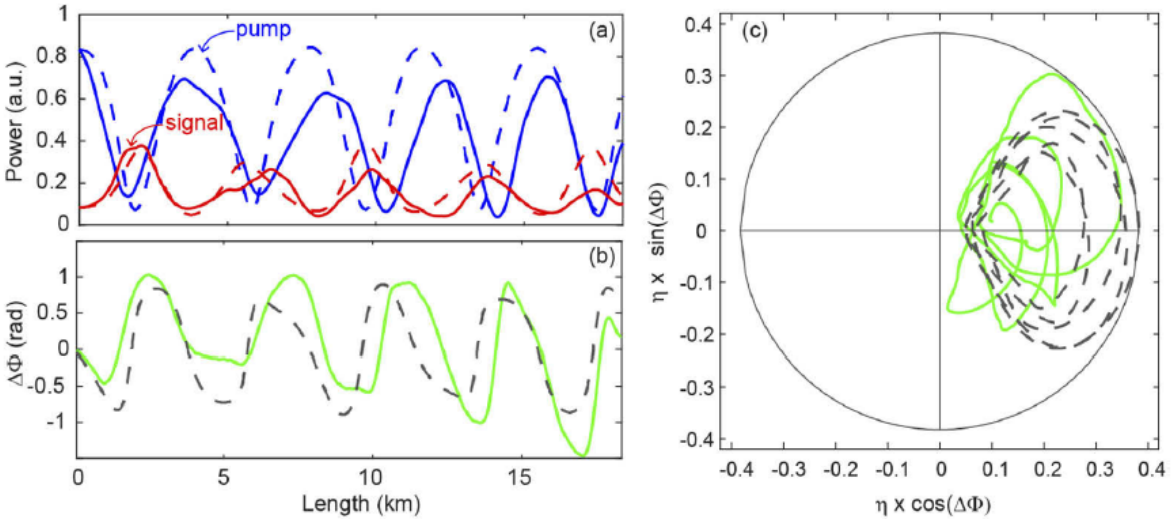

FIGURE 2.3: Same as Figure 2.2 with $\Delta\phi = \phi/2 = 0$. *Source :Vanderhaegen et al. Opt.Express, 28, 2020* [18].

follows well the predicted periodic orbits and the phase features are reproduced.

In order to retrieve more recurrence cycles, the study was repeated in an ultra-loss fiber [18]. Here not only the measurements agree perfectly with numerical simulations, but the study also demonstrates two different types of dynamics over multiple cycles.

Another set of studies were made to characterize the FPUT dynamics in terms of its stability and impact of other effects. For instance, a separatrix crossing is demonstrated in [4], where the impact of relative phase and amplitudes of the sidelobes on the latter was investigated. In [85], the authors introduce a weak damping in the governing equation, and then confirm that the FPUT recurrence becomes unstable which is pronounced

as separatrix crossing and broken symmetry. A multiple values of critical linear attenuation are obtained with experimental confirmation. Finally, an interplay between the seeded and the induced MI and the consequent impact on the FPU recurrence was discussed in [79]. Here the authors report a thermalization of the FPUT process, where a transition to an irreversible state was observed.

Overall the state of the art experimental demonstration of the FWM process and the FPUT recurrence consists in observation of spectral and temporal changes as a seeded pump propagates in an optical fiber. However, in this case, the model governing the system is out of the scope of the fundamental FWM process due to generation of additional sidebands. Another restriction impacting the results demonstrated previously is the limited number of initial conditions, hence, the phase portrait is not complete. Therefore, the motivation of the thesis is to lift-off the restrictions and investigate experimentally the complete phase portrait of the fundamental FWM process.

2.2 Ideal FWM

The ideal FWM model described in Chapter 1.3 implies several strict limitations such as interaction of three spectral lines only, collinear polarization of lines, the omission of third-order dispersion and higher order nonlinear effects. This makes the model relatively simple and well-formulated mathematically, however, its experimental demonstration can be problematic since one has to diminish impact of any other, and sometimes unavoidable, effects. This brings the question whether the ideal FWM is a pure theoretical model or it can be reproduced in practice. This section aims to discuss potential effects and experimentally induced discrepancies that could limit experimental demonstration of the ideal FWM.

2.2.1. Main obstacles to experimental demonstration

Fiber losses

The main limitation in experimental demonstration of the FPUT recurrence is the impact of fiber losses. With linear attenuation, the average power drops, so the trajectories deviate from the initial κ parameter, and dynamics starts to follow a different trajectory shifting from the initial one with propagation distance. As it was demonstrated in [85], the damping can result in the separatrix crossing and the symmetry breaking. Similar effects were observed in hydrodynamics [68, 86] where the damped water-waves deviate from ideal orbits. The strategies to counterbalance this effect may include using a low-loss fiber [18] or to implement active Raman amplification [70, 87].

Cascaded FWM

As it is discussed in the previous chapter, as soon as the sidebands grow, the cascaded FWM process is triggered, which results in growth of extra lines outside the ideal FWM approximation. In real fiber it's very hard to limit interaction to only three spectral lines, which becomes a fundamental restriction in practical application of the theory. However, if we imagine a system with distributed spectral filters, that cut out the residual harmonics, along the propagation length, the full NLSE dynamics can be approximated by interaction of just three waves. As an example consider a propagation of the input waves shaped according to $\eta = 0.90, \phi = 0$ in a fiber with $\beta_2 = -8$ ps^2/km, $\gamma = 1.7$ /W/km over 50 km at $P_0 = 22.6$ dBm, in a system where each $0.5, 1, 2.5$ or 5 km the residual lines are filtered out, and the signal is reamplified (Figure 2.4). From panel (a) one can conclude that at

short segment length the trajectory resembles the ideal FWM portrait, and degrades as the length grows. This behavior is directly linked with growth of residual sidelobes that is unlimited within a single segment : panel (b) depicts spectral amplitudes after three rounds of propagation. Therefore, the ideal FWM demonstration is possible if the growth of cascaded FWM is limited.

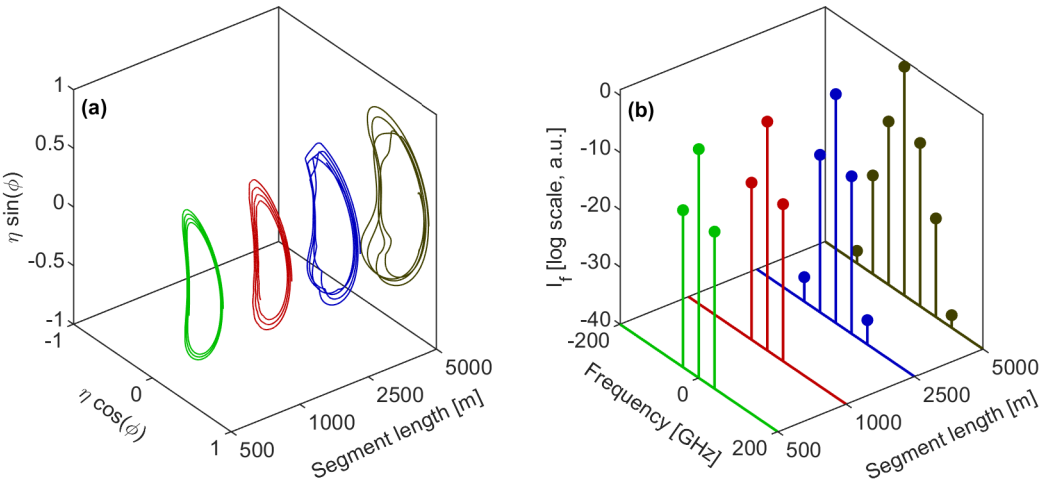

FIGURE 2.4: (a) Trajectories retrieved from the NLSE propagation where the residual harmonics outside the FWM are filtered out each $0.5, 1, 2.5, 5$ km (green, red, blue, dark green lines, respectively). (b) Spectrum resulting after three rounds of propagation in the given artificial system for each segment length.

2.2.2. Second-order effects

Raman effect

In any medium spontaneous Raman scattering can transfer a fraction of energy from one field to another, where the frequency of the latter is downshifted by an amount determined by the vibrational modes of the medium. This phenomenon is referred to as Raman effect and can be interpreted as conversion of a photon by a molecule as it makes transition to a vibrational excited state. In order to include this high-order nonlinear effect one modifies Eq. 1.26 to obtain a generalized NLSE [88] :

$$\frac{\partial A(z,t)}{\partial z} - i\frac{\beta_2}{2}\frac{\partial^2 A(z,t)}{\partial t^2} + i\gamma\left(1 + i\tau_{shock}\frac{\partial}{\partial t}\right)\left(A(z,t)\int_{-\infty}^{+\infty} R(t')\left|A(z,t-t')\right|^2 dt'\right) = 0, \tag{2.1}$$

where $\tau_{shock} = \lambda/(2\pi c)$ describes the dispersion of the nonlinearity, and the nonlinear response

$$R(t) = (1 - f_R)\delta(t) + f_R h_R(t), \tag{2.2}$$

includes both instantaneous and delayed Raman contributions. $f_R = 0.18$ is the fractional contribution of the Raman response for a fused silica [89]. Here $h_R(t)$ is a Raman response function exhibiting complex dynamics due to amorphous nature of glass. If we assume that a single vibrational frequency is included in the process, the response function can be approximated as:

$$h_R(t) = \left(\tau_1^{-2} + \tau_2^{-2}\right)\tau_1 \exp(-t/\tau_2)\sin(t\tau_1), \tag{2.3}$$

where τ_1 and τ_2 are fitting parameters for the experimentally measured Raman-gain spectrum, which are equal to $\tau_1 = 12.2$ fs and $\tau_2 = 32$ fs [90].

Main effects of Raman scattering contain an emergence of a broad band gain with a peak value around 13.2 THz, so an indication of the Raman effect presence is an emergence of a downshifted signal [91]. This effect affects the propagation of ultrashort pulses considerable, however, for long pulses > 5 ps it can be neglected. There is an another secondary effect when the intrapulse Raman scattering leads to a continuous frequency shift, which, however, mainly impairs pulses with width below the ps range. If the Raman effect is combined with parametric gain, and the phase matching is achieved, the gain profile changes significantly [92].

The spontaneous Raman scattering (Raman effect) is typical for low-intensity light, however, at higher intensity this effect leads to a stimulated Raman scattering [93] that enhances the process due to mixing of incoming wave with the scattered signal. Stimulated Raman scattering has rather a high threshold to manifest (in comparison with stimulated Brillouin scattering), which can be around ≈ 1 W.

Stimulated Brillouin scattering

Stimulated Brillouin scattering is another nonlinear process occurring in optical fiber that can be summed up in an interaction between the initial light wave and a thermally excited acoustic wave. It originates from electrostriction - a phenomena when the medium's density is varied in a presence of light, hence, modifying a refractive index of the medium. Therefore, when light propagates in a fiber, it creates a moving density that acts as a grating, resulting in pump scattering through Bragg diffraction in the backward direction [94]. This phenomena exhibits a threshold-like behavior, hence it manifests only when pump power exceeds a certain level [95]. The Brillouin threshold depends on the fiber characteristics and length : the longer the fiber, the lower is the threshold [96]. Unwanted effects of the Brillouin scattering are depletion of energy and a risk of damaging the equipment with the back-scattered light. That said, note that, there are applications of this effect in lasers [97], amplifiers [98] ans sensors [99].

Third-order dispersion

The dispersion induced pulse broadening was discussed in section 1.2.1. with a focus on the second-order dispersion β_2. Although its contribution dominates in many cases, the third-order dispersion effects may come into play, especially in a case of working near the zero-dispersion wavelength [100]. The β_3 shall be included in propagation of ultra-short pulses, it would result in temporal pulse broadening with oscillatory structures, called dispersive waves, appearing near the leading ($\beta_3 < 0$) and the trailing ($\beta_3 > 0$) edges of the pulse [101]. The third-order dispersion can be also a source of instabilities and symmetry-breaking of the modulation instability spectrum [102, 103].

2.2.3. Proposed experimental architecture : overview of the system

The main goal of the developed setup and idea is to be able to demonstrate the fundamental FWM process (Section 1.3) that includes interaction of only three spectral lines (in the degenerate pump case). The setup should be flexible and robust enough to demonstrate several recurrence cycles for any initial point on the phase portrait (Figure 1.2).

The key idea of the setup is based on iterative propagation of light with a continuous update of input conditions. The setup concept is depicted in Figure 2.5: the input spectrum, which is tailored to match required

relative amplitude and phase ϕ_0, η_0, propagates in a piece of fiber. If the segment is sufficiently short, the lateral sidebands located at $\pm 2 f_m$ (and further) will not be developed, hence light evolution stays within the fundamental FWM model. After measuring output values ϕ_1, η_1, the input three lines are updated accordingly, and the process is repeated in a loop $N-$times until the trajectory is completed. This way with a continuous update of input conditions, the dynamics can be reconstructed over required propagation distance.

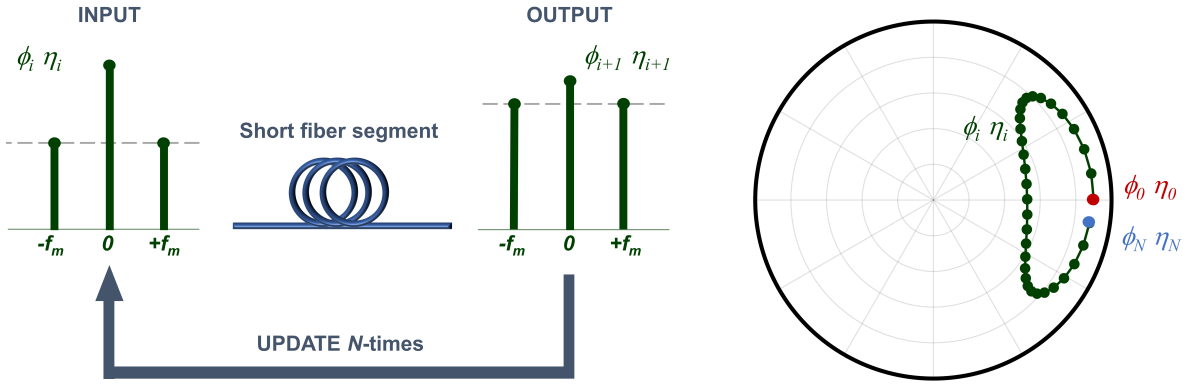

FIGURE 2.5: The setup concept is based on iterated initial conditions : input spectra shaped according to η_i, ϕ_i propagates in a short segment of fiber, the output η_{i+1}, ϕ_{i+1} are measured, and the input spectra is updated. With subsequent update of initial conditions and light evolution in fiber, complete recurrence profile is reconstructed (left).

Difference between the ideal FWM, segmented approach and full NLSE propagation (hence, cascaded FWM) can be drawn from Figure 2.6. Here initial condition $\eta_0 = 0.90, \phi_0 = 0$ at $\kappa = -2$ ($P_0 = 150$ mW $= 21.76$ dBm) has propagated in a 50 km anomalous dispersion fiber ($\beta_2 = -8$ ps^{2}km^{-1}, $\gamma = 1.7$ W^{-1}km^{-1}) following three different models. On the phase-space portraits (panel (a1)) one observes that full NLSE model does not follow the ideal FWM dynamics due to development of additional sidebands : energy of the pump is depleted stronger and relative amplitudes of spectral lines at $\pm 2 - 3 f_m$ are stronger than in case of ideal FWM and segmented approaches (panels (a2) and (a3)). The NLSE trajectory crosses the separatrix of the ideal model. Note that the separatrix of the NLSE itself is different and is formally linked to the Akhmediev breather (AB).

If power is increased (while keeping fiber characteristics the same), the process becomes more nonlinear and the normalized mismatch parameter increases $\kappa = -1.2$ ($P_0 = 150$ mW $= 24$ dBm) - panels (b). The segmented approach now deviates a bit stronger from the ideal FWM, which results from the fact that even at short segment length some energy flows to the sidebands, hence the deviations are accumulated faster (compare cyan and red lines amplitudes in panels (a3) and (b3)). Nevertheless, the segmented approach dynamics still follows closely the ideal FWM, and several recurrence cycles can be reproduced.

To implement the described concept which is based on iteration of initial conditions, an experimental setup depicted in Figure 2.7 is realized. It is based on commercially-available telecommunications components. We work at telecom wavelength 1550 nm in order to benefit from high level devices. The setup is fully fibered to achieve a better stability.

The setup can be divided into several stages with the following functionality :

- comb generation - a CW laser operating at 1550 nm is sent through a phase modulator that imprints a sinusoidal phase profile converting the monochromatic spectrum into a set of equally spaced spectral

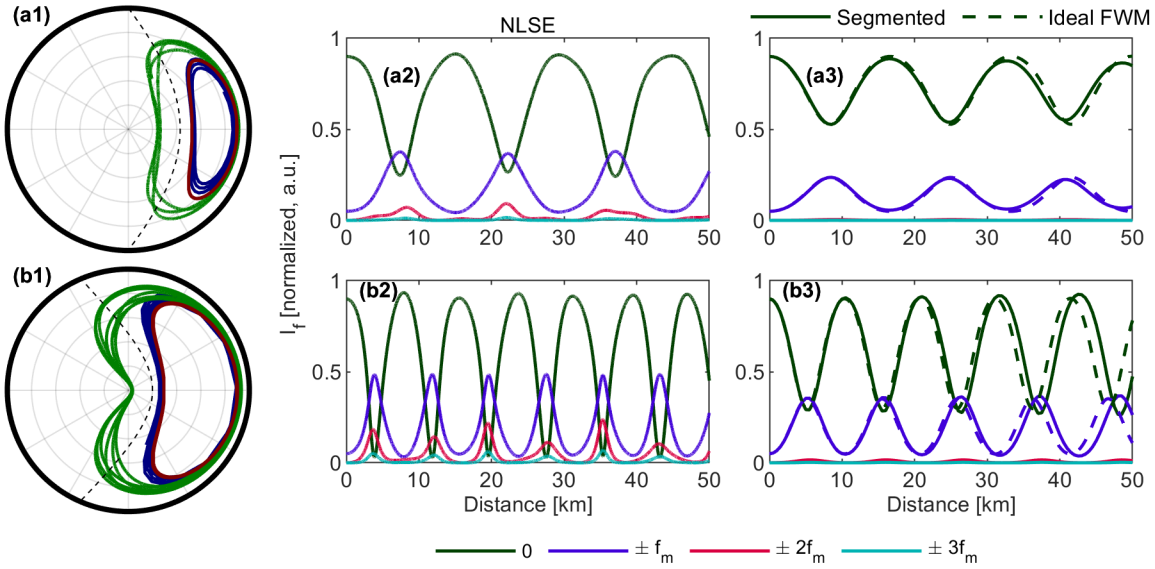

FIGURE 2.6: Comparison between the models for $\kappa = -2$ and $\kappa = -1.2$, and $\eta_0 = 0.90, \phi_0 = 0$ is shown in panels (a) and (b), respectively. Phase-space portraits are depicted in panels 1 for : green - full NLSE propagation, blue - segmented approach (500 m fiber), red - ideal FWM model, dashed black line marks the separatrix. Panels 2 and 3 show evolution of spectral sidebands located at $\pm 0 - 3f_m$ for the NLSE and segmented (ideal FWM), respectively.

lines with frequency of the radio-frequency (RF) clock (40 GHz);

- spectral shaping - the resulting spectrum is tailored by a programmable spectral filter (Finisar WaveShaper 4000) to match the required η_i, ϕ_i and then amplified by the erbium-doped fiber amplifier (EDFA) to reach P_0, the polarization controller is required to adjust the input polarization state since it is not maintained before;

- nonlinear propagation - the shaped spectrum then propagates in a 500 m segment of fiber with $\beta_2 = -8$ ps^{2}km^{-1}, $\gamma = 1.7$ W^{-1}km^{-1};

- phase and amplitude detection - the resulting relative amplitude is measured with an optical spectrum analyzer (OSA), the relative phase is retrieved from the temporal delay between central and lateral sidebands as measured with the high-speed sampling oscilloscope;

- control - the WaveShaper 4000, OSA and the sampling oscilloscope are linked under a home-made Matlab script, so the process of continous update and measurement is automatized.

With the given setup, light dynamics can be reproduced over 100 iterations resulting in 50 km total propagation length, which corresponds to several recurrence cycles. The details about each stage and error margins of each stage of the experiment are provided later in this manuscript.

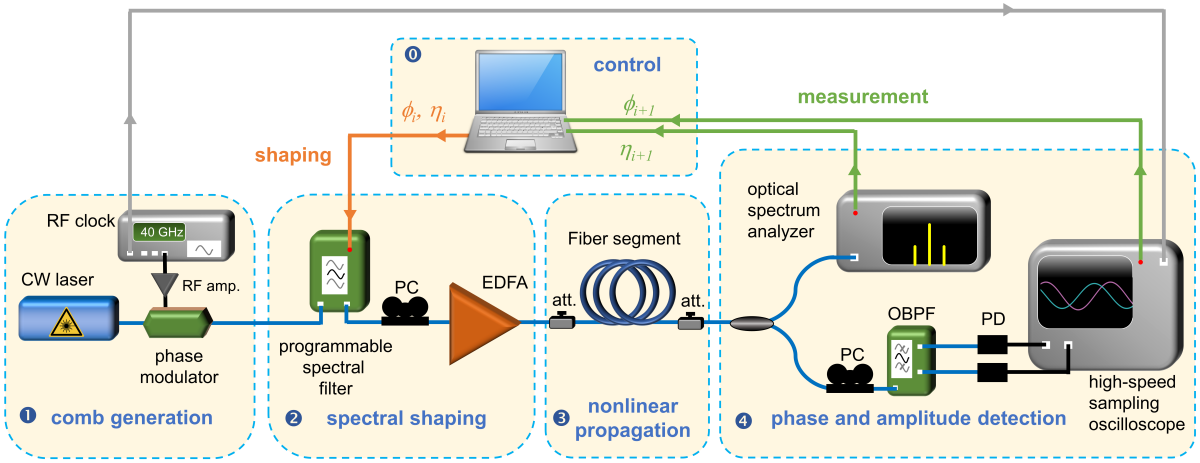

FIGURE 2.7: Experimental setup. CW laser - continuous wave laser; RF clock - radio-frequency clock; RF amp. - radio-frequency amplifier; PC - polarization controller; EDFA - erbium-doped fiber amplifier; att. - tunable attenuator; OBPF - optical band-pass filter; PD - photodiode.

2.3 Details of the experimental setup

2.3.1. Comb generation

Consider a CW laser (Yenista Optics ECL 1560/P6 external cavity laser with a range of 1520-1600 nm) with an arbitrary carrier angular frequency ω_0 and amplitude a_0 which is modulated by a temporal sinusoidal phase : $\Psi(t) = a_0 \exp(i\omega_0 t) \exp(iA_m \cos(\omega_m t))$, where A_m and ω_m are modulation amplitude and frequency, respectively. As the result of this temporal phase modulation, the spectrum of a CW is transformed into a series of discrete spectral lines evenly spaced by ω_m with amplitudes of each n^{th} component given by $J_n^2(A_m)$ where $J_n(x)$ is the Bessel function of the first kind of order n [20, 104]. Due to shaping constraints that will be described below, we work at modulation frequency of 40 GHz. In Figure 2.8 (a) a typical experimental spectrum resulting after a phase modulation with $A_m = 1.05$ rad at 40 GHz is compared with a theoretical spectrum (red dots).

In order to generate the spectrum that would correspond to a range of relative amplitudes η from 0 to 1, one is interested in generation of input spectra with equalized spectral lines that corresponds ideally to $A_m = 1.45$ rad. However, the phase modulators (PM), in general, are limited in performance when it comes to modulations at high frequencies such as 40 GHz, and the price of such components growth significantly. We are using the EOspace PM that supports frequencies from 20 to 40 GHz. At the same time, the power provided by the RF signal generator is limited, so in order to generate a broad spectrum with nearly equalized amplitudes, we use a RF amplifier to provide enough power to the PM. This typically enables us to reach $A_m = 1.05$ rad.

This first part of the setup is polarization maintaining, which allows to avoid extra phase deviations between the lines that input the shaping part. In case if polarization is not maintained, the spectral lines may exchange some energy, so the comb becomes less stable.

The obtained spectrum has an intrinsic $\pi/2$ phase shift between successive frequency components that appears due to Jacobi-Anger expansion [20, 21, 105]. In order to control the phase difference between the lines correctly, this phase shift shall be taken into account at the stage of spectral shaping.

After the spectrum is generated, only three lines are kept and shaped according to the relative amplitude

and phase. Panels (c1) and (c2) of Figure 2.8 display three harmonics with compensated $\pi/2$ phase in spectral and temporal domains, respectively.

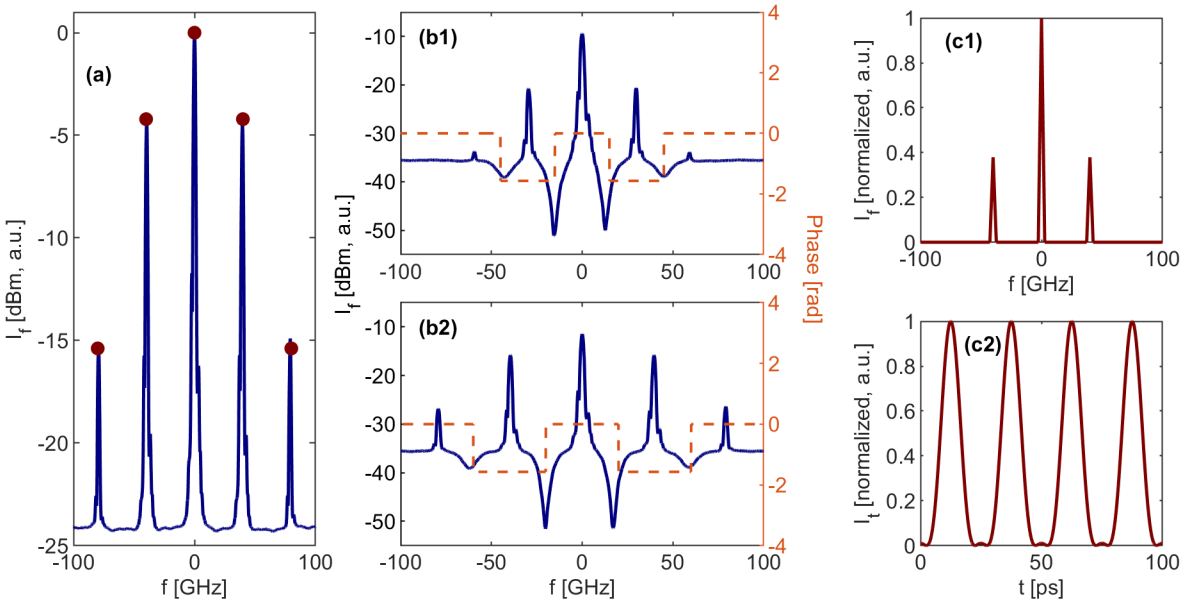

FIGURE 2.8: (a) Spectrum resulting after the sinusoidal PM experimentally (blue solid line) and theoretically (red dots) at 40 GHz and $A_m = 1.05$ rad. PM-spectrum at 30 GHz (b1) and 40 GHz (b2) combined with ASE and shaped with a step-like phase profile of a depth $\pi/2$ (dashed orange line). (c) Three spectral lines with compensated phase profile in spectral (c1) and temporal (c2) domains.

2.3.2. Spectral shaping

To shape the input spectrum to match required η, ϕ the WaveShaper 4000 (Finisar) was used [106]. It is based on a diffraction grating combined with a liquid-crystal-on-silicon optical processor and polarization optics, that controls the phase of light at each pixel to obtain an electrically programmable grating. Such technology allows to control amplitude and phase of each spectral line, and to imprint complex attenuation and phase profiles.

Phase shaping seems quite straightforward at first glance, however, there are several tricks that one should keep in mind in order to achieve very precise amplitude and phase sculpturing.

One issue that may emerge during masks implementation is the phase-intensity coupling which appears when a discrete spectral phase shift creates a notch filter at the transition point due to destructive interference of phase shifted spectral lines [107]. To avoid impact of notch filters on spectral amplitudes one has to select the modulation frequency so the spectral lines are separated enough. To do so, the modulated CW at different frequencies was combined with amplified spontaneous emission (ASE) and then a $\pi/2$ step-like phase profile was imprinted on the sidebands. In Figure 2.8 (b) one observes an emergence of the notch filters in between harmonics. In case of 30 GHz modulation (b1) the pedestals around harmonics are smoothed, and the amplitudes are more affected than in case of 40 GHz modulation (b2), where the lines are better separated. It motivates us to continue working at 40 GHz modulation.

We use a step-like phase profile imprinting phase values in radians for each spectral line (similar to the orange line in Figure 2.8 (b)). What is important in the definition of ϕ is the relative phase, therefore, after $\pi/2$

correction, all lines are in phase, and then we assume that $\phi_{-1} = \phi_1 = 0$, hence $\phi = -2\phi_0$ (ϕ_i being phases of each spectral line). In this case the required ϕ value can be imprinted just by phase shaping of the central line.

In order to shape the spectral amplitudes we design attenuation masks that are step-like profiles for each harmonic with values corresponding to the desired η. Since the spectral lines have equal spectral amplitudes after the phase modulation stage, we measure the initial relative amplitude $\Delta B = (|\psi_{-1}|^2 + |\psi_1|^2)/2|\psi_0|^2$, where $|\psi_i|^2$ are the amplitudes just after the comb generation stage. This initial power distribution must be taken into account when computing the attenuation masks.

To equalize the lines one must first attenuate the central line $|\psi_0|^2$ by ΔB, in this case the η and ρ definitions introduced in Section 1.3 become :

$$\begin{cases} \eta = \frac{\Delta B|\psi_0|^2}{\Delta B|\psi_0|^2+|\psi_{-1}|^2+|\psi_1|^2} \\ |\psi_{-1}|^2 - |\psi_1|^2 = \rho\left(\Delta B|\psi_0|^2 + |\psi_{-1}|^2 + |\psi_1|^2\right). \end{cases} \tag{2.4}$$

Then we must find the attenuation B_i imprinted on each spectral line $i = 0, \pm 1$ to shape them according to η and ρ. In order to preserve the total power at best, we minimize the imprinted attenuation by maximizing the $B_0|\psi_0|^2 + B_{-1}|\psi_{-1}|^2 + B_1|\psi_1|^2$ sum. In order to achieve that, the Eqs. 2.4 are solved for cases when one of the three lines is the maximum and it's spectral intensity is not attenuated. All the resulting cases are summarized below:

- if $2\eta > \Delta B\,(1 - \eta + |\rho|)$, then $B_0 = 0$, $B_{-1} = \Delta B\frac{1-\eta+\rho}{2\eta}$, $B_1 = \Delta B\frac{1-\eta-\rho}{2\eta}$, which is referred to a case where the central line is higher than the sidelobes, and $\eta > 0.33$;
- if $2\eta \leq \Delta B\,(1 - \eta + |\rho|)$ and $\rho > 0$, then $B_{-1} = 0$, $B_0 = \frac{2\eta}{\Delta B(1-\eta+\rho)}$, $B_1 = \frac{1-\eta-\rho}{1-\eta+\rho}$, which corresponds to cases with $\eta \leq 0.33$ and the $-f_m$ (left) line being higher than the right one;
- if $2\eta \leq \Delta B\,(1 - \eta + |\rho|)$ and $\rho \leq 0$, then $B_1 = 0$, $B_0 = \frac{2\eta}{\Delta B(1-\eta+\rho)}$, $B_{-1} = \frac{1-\eta-\rho}{1-\eta+\rho}$, which is similar to the situation above but the $+f_m$ (right) line is higher than the left one.

The resulting values B_{-1}, B_0, B_1 are translated to attenuation in dB by $10\log_{10}(B_i)$ and then imprinted on the respective harmonics. For example, if the input spectra is the one displayed in Figure 2.8 (a), then $\Delta B = 0.37$, and if one wants to obtain $\eta = 0.90$ with $\rho = 0$, then the attenuation mask shall imprint $B_0 = 0$ dB on the central line and $B_{\pm 1} = 16.87$ dB on the sidelobes.

To verify that the WaveShaper is able to imprint correctly values of η we first check the output spectra directly with no fiber included by imprinting random values of η with $\phi = 0$. In contrast with monotonous variation of η, this procedure allows to conclude on reproducibility of the results. From Figure 2.9 (a1) we see that the shaped spectra corresponds to the imprinted η, however the errors are quite systematic and not negligible with values from -5 to 15 %. Stronger deviations are present for $\eta = [0 : 0.20] \cup [0.40 : 1]$ (Figure 2.9 (a2)). It can be explained by the fact that at these values the relative amplitude on either central line ($\eta = [0 : 0.20]$) or the sidebands ($\eta = [0.40 : 1]$) reaches the accuracy limits of the device : ± 1.0 dB from 0 to 10 dB, ± 10 % from 10 to 30 dB [106]. Here, since the measurement on the OSA was tested in the averaging regime, and the result was reproduced, we assign the deviations mainly to the WaveShaper.

Figure 2.9 (b1,b2) displays an error on η : $\delta\eta(\text{dB}) = 10\log_{10}\left(\frac{\eta_{in}}{1-\eta_{in}} \cdot \frac{1-\eta_{out}}{\eta_{out}}\right)$, which results from attenuation of the sidelobes (hence, $\psi_0 = 1$) and the central line (hence, $\psi_{\pm 1} = 1$), respectively, depending on the imprinted attenuation value. We see that indeed below 10 dB attenuation the deviation is less than 1 dB, and it growth for values higher than 10 dB. Since the errors seem to be reproduced and not fully random, we make a

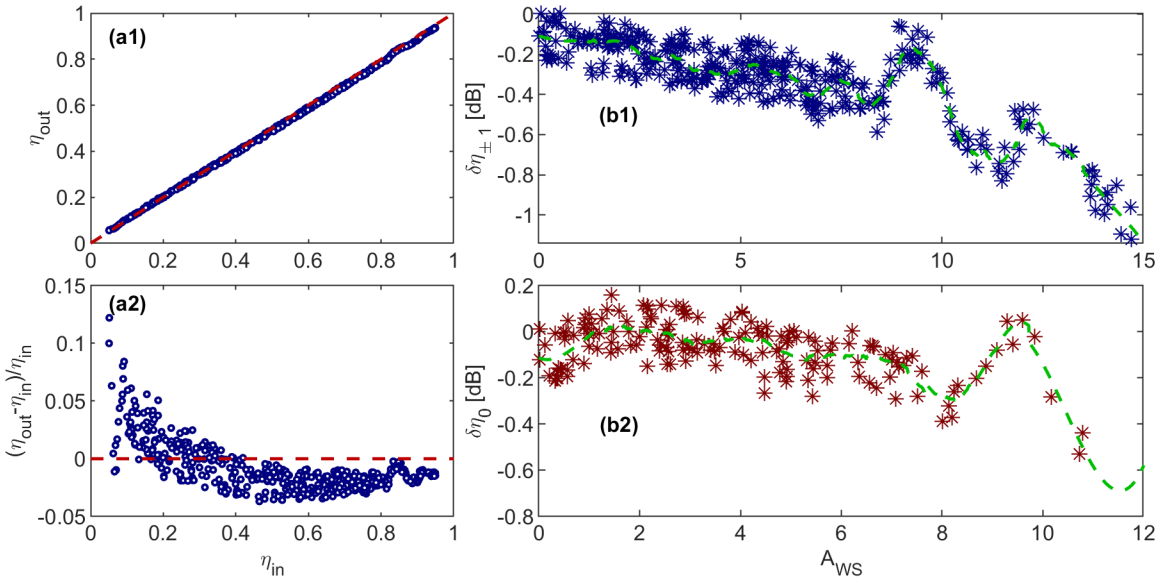

FIGURE 2.9: (a1) Imprinted values of η vs the output ones (directly after the WaveShaper) and (a2) the relative error (blue dots - experimental values, red line - ideal prediction). Error on the attenuation vs the command values A_{WS} for (b1) sidelobed and (b2) central line. Stars - experimental values, green dashed line - interpolated polynomial used as a calibration curve.

fit of the deviation and use it as a calibration to correct the imprinted attenuation to match η more precisely at the shaping stage. Nevertheless, the thickness of the calibration curve allows to put a global offset if the errors accumulate too fast.

The imprinting of phase, however, does not require additional calibrations, as we have checked in the phase measurements described later.

2.3.3. Nonlinear propagation : fiber selection and space of explored parameters

Before going inside of a fiber, the spectrum has to be amplified in order to reach a controlled average power. We use the CEFA-C-PB-HP EDFA (Keopsys by Lumibird) that can operate with a weak signal down to -20 dBm (thanks to a pre-amplification stage) and amplify the signal up to 20-33 dBm (with a saturated output power up to 42 dBm).

Next, we have to select a fiber with appropriate characteristics. As it was demonstrated in Section 1.2.3. the MI gain depends on fiber's non-linearity, dispersion (sign and absolute value) and input average power. In the experiment we would like to rely on commercially available fibers with anomalous dispersion. The following fibers were tested :

- single mode fiber - SMF : $\beta_2 = -20$ ps^2/km, $\gamma = 1.1$ /W/km, L = 300 m;
- highly-nonlinear fiber - HNLF manufactured by OFS: $\beta_2 = -0.88$ ps^2/km, $\gamma = 10$ /W/km, L = 720 m;
- TeraLight - TL manufactured by Alcatel: $\beta_2 = -8$ ps^2/km, $\gamma = 1.7$ /W/km, L = 300 m and 500 m.

The fiber parameters are not the only criteria to select the fiber. One important other criteria is the maximum power that can be launched into the fiber. This parameter can be either limited by the high power erbium doped fiber amplifier that is used before the fiber or by higher-order nonlinear effects such as Brillouin or Raman scattering that may deplete the pump.

The Raman scattering, manifesting itself in emergence of gain with a peak around 13.2 THz, was not observed in the experimental measurements. And the Brillouin scattering, emerging at a lower threshold and resulting in the pump scattering backwards, was kept to a minima by estimation of the maximum input power level at which the back-scattered power starts to be pronounced. This point can be estimated from measuring the output power with gradually increasing input power. The results are presented in Figure 2.10 (b): when the output power starts to deviate from the input one (connection and propagation losses are taken into account) the maximally available power is defined. The resulting maximum powers are 630 mW (28 dBm), 63 mW (18 dBm), 630 mW (28 dBm) and 398 mW (26 dBm) for the SMF, HNLF, TL of 300 m and 500 m, respectively.

Another approach in minimization of the Brillouin scattering impact is to put an additional phase modulation, that would redistribute the energy of each spectral line to small sidelobes. This method, however, would increase the difficulty of our detection setup, therefore we have not used it.

For the power sets determined from Figure 2.10 (b), the gain curves Eq. 1.41 are computed. Like this, we can check the gain range that is available for measurements at 40 GHz. Figure 2.10 (a) displays these gain regions for the considered fibers. In principle, in all the cases we can observe the FWM process at selected frequency for the range of power that is available. However, if we check the normalized mismatch parameter κ computed at each average power (Figure 2.11) we would see that the widest range corresponds to the TL fiber (blue area and lines in Figure 2.11). Note that it's always possible to reach more linear regimes with $\kappa << 0$ by decreasing the amplifier power or putting an attenuator. For HNLF (green) only a short range of strong nonlinear evolution is covered (here come the limits of the amplifier itself), while for the SMF (blue) a wider range of more linear propagation is obtained. In principle, one may replace a fiber if a certain range of κ is of interest. For the TL and HNLF we observe also that the next harmonic at 80 GHz lies within the MI range for higher powers. That will lead to amplification of the lateral sidebands that we would like to avoid in order to be within the ideal FWM model.

Additional drawback of the SMF fiber is that the supported powers are quite high, so the risk of damaging several components, for which the use of such powers is not validated, is more crucial than the range of available measurement points.

In order to reconstruct the phase-space portraits we shall propagate the light in a piece of fiber with continuous update of initial conditions. Depending on fiber parameters and length, the "step size" between the two consecutive η, ϕ on the phase plane will be different (for example, green dots in Figure 2.5). One must balance out dispersion and nonlinearity, so the changes on one parameter are not overpowering the evolution of the other. As an example, let's compare numerical simulations of the experimental process where three segments of fibers are tested : SMF 300 m, HNLF 720 m and TL 300 m. From the theory we know that depending on position on the phase space plane, the trajectories, hence, the relative changes of η, ϕ are different. If in Eq. 1.59 we take an infinitely-small $dz = \Delta z$, we obtain $\Delta\phi = f(\Delta z, \phi, \eta), \Delta\eta = f(\Delta z, \phi, \eta)$ where $\Delta\phi, \Delta\eta$ are the resulting small changes. Therefore, the "step size" described before may have different lengths. To have a global picture we sample initial conditions over the whole available space at equal distances and propagate each input point once. Hence, the full mapping is reconstructed and we can conclude on the potential effects of the fiber.

The mapping results at same $\kappa = -2$ for different fibers are presented in Figure 2.12. From here we can

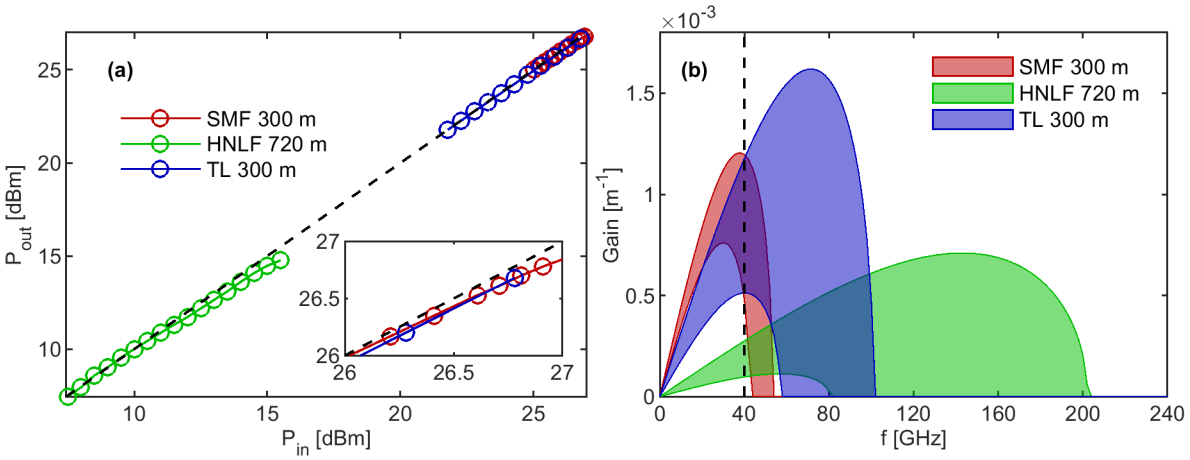

FIGURE 2.10: (a) Output versus input average power for selected fibers (losses are taken into account), black dashed line marks ideal case with no Brillouin back-scattering present. (b) Gain curves covering available power regions, black dashed line marks position of the operating frequency 40 GHz.

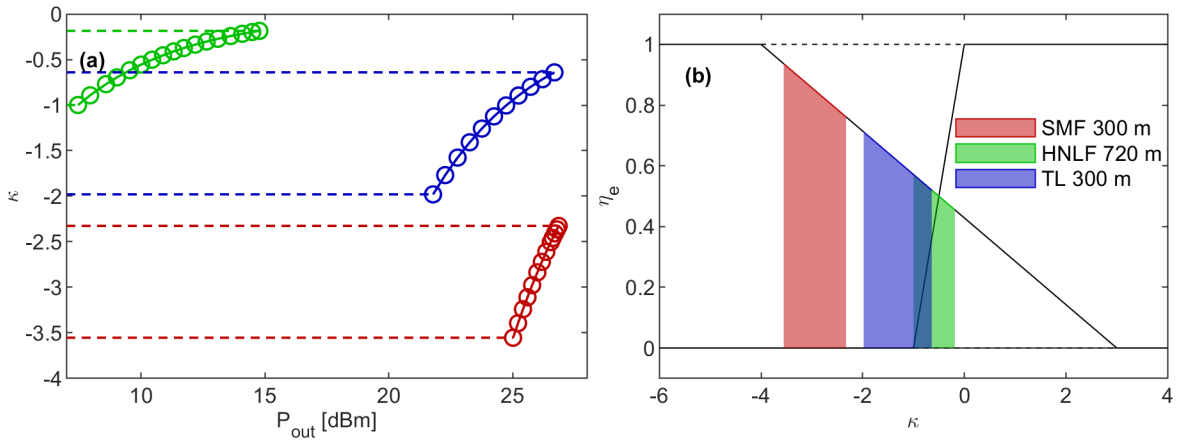

FIGURE 2.11: (a) Values of the normalized mismatch κ that are available for SMF, HNLF, TL fibers (red, green, blue lines, respectively). (b) Same as (a) but κ versus η_e - the eigen solutions of the three-wave system.

conclude that the "step size" of the SMF is too large due to high value of the dispersion coefficient. For the HNLF the situation is the opposite - the relative changes in both phase and amplitude are too small, therefore experimentally the errors may impact strongly the measurements (for instance, the WaveShaper accuracy discussed in the previous section), and the two subsequent points may appear indistinguishable. The TL 300 m fiber seems to be a good alternative : the "step size" is pronounced enough but not to high, so the shape of the trajectory can be reconstructed. Two pieces of the TL fiber were tested experimentally : 300 m and 500 m. An advantage of a shorter segment of fiber is that we can go deeper to the nonlinear regime since the Brillouin backscattering threshold is higher, however small step evolution, hence measurements of small changes, are more impaired by measurement noise and artifacts. The results of the mapping are presented in Figure 2.13 : colored solid lines with markers display the experimental measurements, while the dashed gray lines denote the numerical NLSE solving over the given segment of fiber (a) 300 m and (b) 500 m. The colors of the ex-

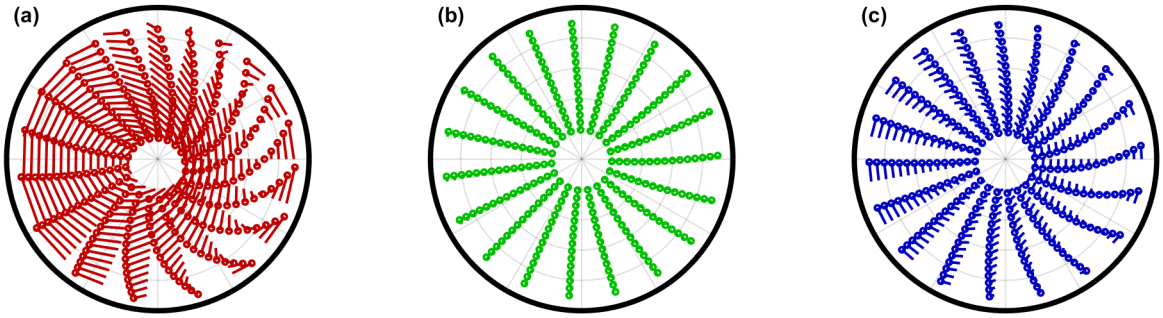

FIGURE 2.12: Numerical simulations of the experimental approach for regularly mapped values of $\eta = [0.2 : 0.05 : 0.90]$, $\phi = [0 : 0.33 : 2\pi]$ at $\kappa = -2$ for (a) SMF 300 m (b) HNLF 720 m (c) TL 300 m.

perimental results depict deviation from the numerical results : $Err = \sqrt{(x_{num} - x_{exp})^2 + (y_{num} - y_{exp})^2}$, with x, y being coordinates of the output points on the phase-space plane for the numerics and the experiment. Errors range for the TL 300 m fiber covers the range of $(6 \cdot 10^{-4} - 0.072)$ with the mean of 0.016, while for the TL 500 m these values are $(3 \cdot 10^{-4} - 0.025)$ and 0.008, respectively. Higher experimental errors in the TL 300 m fiber can be ascribed to the PMD effect (since the error on the phase is more pronounced), while for both measurements the shaping and the measurements accuracy is assumed to be the same. Even though the 300 m segment could be a nice candidate for the measurements, with such an error level propagation in a loop would accumulate the deviations too fast, therefore the TL 500 m is selected for the measurements.

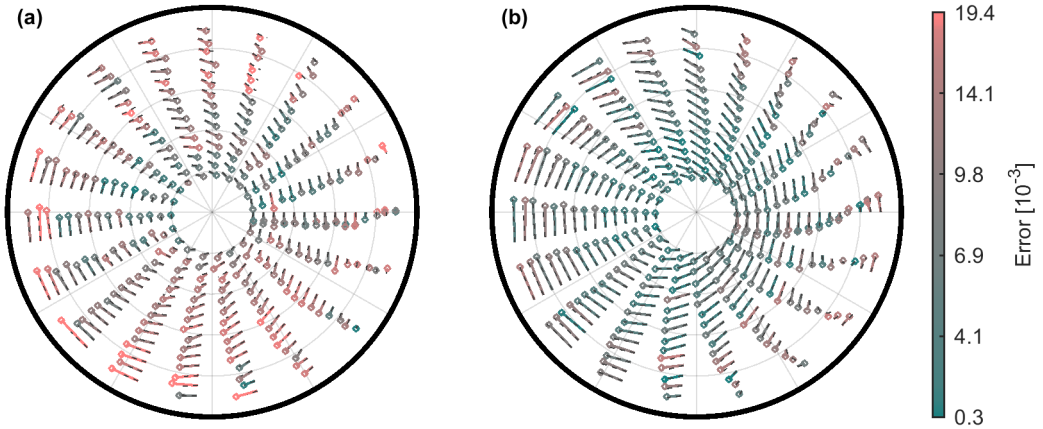

FIGURE 2.13: Phase-space map combining experimental measurements (solid line with a marker) and numerical predictions (dashed gray line) for the TL fiber of length (a) 300 m (b) 500 m. Red colorscale characterizes an error with respect to the numerical results.

For the selected TL 500 piece of fiber, the available power region is $P = 126 - 316$ mW $(21 - 24.5$ dBm) with κ from -2.51 to -1.0 (here we took the safest power margin).

2.3.4. Phase and amplitude measurement

The final stage of the setup before the next iteration is measurement of spectral phase and amplitude at the output of the fiber segment. We use the 50:50 splitter to redirect the power to the phase and amplitude measurements parts as depicted in Figure 2.7.

Measurement of the spectral lines power is quite straightforward : we use the OSA (Yokogawa AQ6370 [108]) to record the output spectra, then find the peaks amplitudes and convert in to the normalized spectral amplitude η. We keep the resolution of the OSA quite small 0.02 nm, and record just 2001 points over 2 nm space with a center at 1550 nm in order to speed up the process. Since the resolution is limited, an accuracy of the measurements can be impacted by deviations related to pixels presence. To counterbalance this effect we've tested four different strategies in measurement the peak spectral amplitude :

- fit peaks with Matlab function *'findpeaks'* on the log scaled signal;
- find maximum positions of each peak by simply taking *max(Spectrum)*;
- fit three points around the maximum value by a parabola and then interpolate a value of the maximum;
- integrate the power within each peak : instead of relative amplitudes we look at the total power contained in each line by taking a sum of 8 points around the maximum value.

To compare these four methods we measure the resulting η after the WaveShaper output while keeping previously developed calibration to zero in order to avoid any ambiguity. The results are presented in Figure 2.14. All methods provide an accurate estimation of η. The resulting RMS errors are $8{\cdot}10^{-3}$, $7.4{\cdot}10^{-3}$, $9.5{\cdot}10^{-3}$, $12.6{\cdot}10^{-3}$ for the fit peaks, find maximum, parabola fit and the integration methods, respectively. The find maximum approach is the simplest and the most reliable in practice, therefore we implement this one.

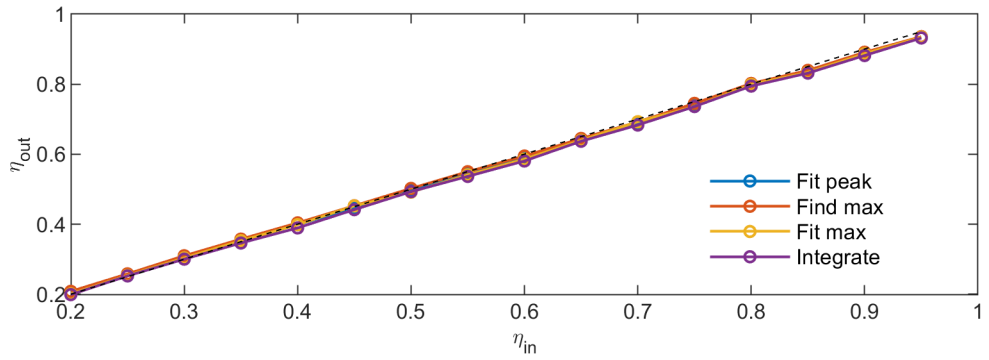

FIGURE 2.14: Measurements of normalized amplitude by different methods.

To measure the phase we split the output spectra into two parts : left - $\Psi_L = \Psi_{-1} + \Psi_0$ and right - $\Psi_R = \Psi_1 + \Psi_0$ (red and blue lines in panels (b2) and (b1) of Figure 2.15), which translates into the following equations :

$$\Psi_L = \psi_0 + \psi_{-1} \exp\left(-i\omega_m t + i\phi/2 + i\phi_x\right) \tag{2.5}$$

$$\Psi_R = \psi_0 + \psi_1 \exp\left(i\omega_m t + i\phi/2 + i\phi_y\right), \tag{2.6}$$

here we assume that the phases of the sidelobes are equal $\phi_{-1} = \phi_1$ and take into account only a relative phase between the respective spectral lines $\phi/2 = \phi_{-1} - \phi_0 = \phi_1 - \phi_0$. The phases ϕ_x and ϕ_y denote the global

phase offsets of each line linked to : different propagation paths, PMD-induced phase offsets for x- and y-axis, photodiode's trigger times.

Experimentally in order to implement efficient filters we use WaveShaper 2000s (COHERENT, Finisar) which allows to shape the x- and y- polarization directions of the input separately. For the signal to be pronounced in both directions we use the PC to adjust the input polarization to $\pi/2$. Then we shape the spectral lines to keep Ψ_L and Ψ_R on the x- and y-axis, respectively. The filter outputs then go through the PD and the temporal intensity profiles are measured by a high-speed sampling oscilloscope (panels (c1) and (c2) in Figure 2.15) :

$$|\Psi_L|^2 = \psi_0^2 + \psi_{-1}^2 + 2\psi_0\psi_{-1}\cos\left(\omega_m t - \phi/2 - \phi_x\right) \tag{2.7}$$

$$|\Psi_R|^2 = \psi_0^2 + \psi_1^2 + 2\psi_0\psi_1\cos\left(\omega_m t + \phi/2 + \phi_y\right). \tag{2.8}$$

The oscilloscope must have the bandwidth of at least 40 GHz. In our setup, we use 86100D Infiniium DCA-X Wide-Bandwidth oscilloscope with > 100 GHz bandwidth [109]. For a trigger, we use a 86107A Precision Timebase Reference Module that is synchronized on our 40 GHz RF clock.

From these equations we see that the phase between two lines can be extracted by making a fit by a $\cos(\omega_m t + \phi_{out})$ from where the measured phases are:

$$\phi_L = -\phi/2 - \phi_x \tag{2.9}$$

$$\phi_R = \phi/2 + \phi_y, \tag{2.10}$$

For instance, the experimental profiles presented in Figure 2.15 correspond to $\phi_L = 1.54$ rad and $\phi_R = 1.71$ rad. Therefore the output relative phase can be derived as:

$$\phi = (\phi_R - \phi_L) - (\phi_y - \phi_x) = (\phi_R - \phi_L) - \phi_{cal}, \tag{2.11}$$

here we see that a single unknown is left, which characterizes the offsets related to detrimental effects described before, as well as potential different lengths of fibers or electrical cables used in the detection stage. So it is not induced by the FWM process. It was checked indeed that experimentally $\phi_y \neq \phi_x$ and there is no simple way to correct it unless a prior calibration of the phase is made. Note that, if one measures first the ϕ_L and then ϕ_R with the use of a same filter, PD and connecting fibers, then $\phi_y = \phi_x$, and the output relative phase can be measured directly. However this approach implies inconveniences in a need to physically reconnect the fiber outputs for each iteration, therefore the phase calibration is justified.

The phase calibration can be done with a few different techniques which rely on comparison of fiber outputs with predicted numerical results (NLSE propagation over a fiber segment). In principle, the phase offset is the same for all points on the phase plane. However, knowing that, depending on a position in the phase plane, the amount of changes is different, hence some points may be more prone to experimental errors, therefore a selection of the calibration points is important. First, we've tested a calibration over selected small region with 12 points (Figure 2.16 (a)) - this approach would allow to precisely average the phase over a region where the changes are relatively pronounced, however outside the region the phase may be poorly adjusted. Second approach relies on selection of random points on the phase plane (Figure 2.16 (b), 20 points) - with this technique the phase is better averaged over the whole space, but may not fit for the loop we're interested in. In the third approach we select random point near the value of the input η (Figure 2.16 (c), 10 points) - in this case the phase is well calibrated for a single loop, but it may not be optimized for a complete mapping.

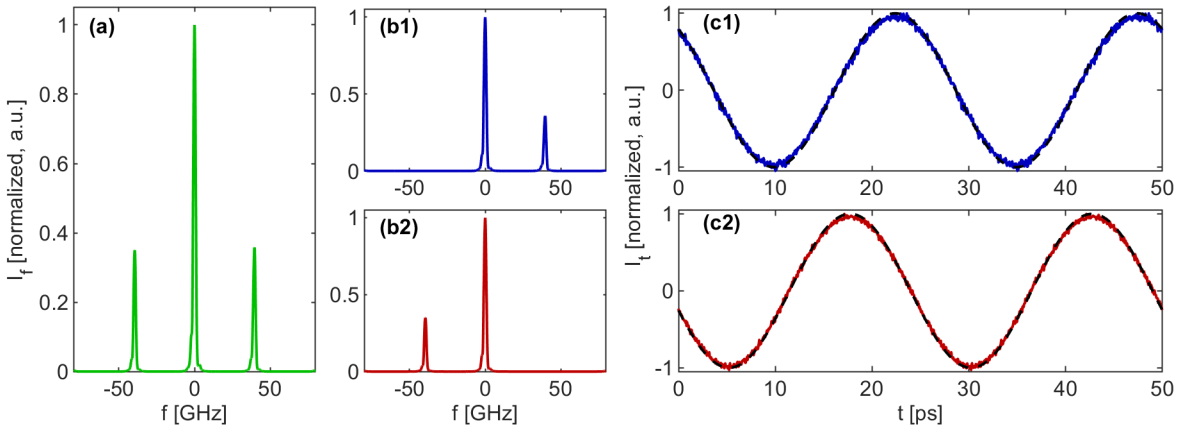

FIGURE 2.15: An example of the output spectra (a) for $\eta = 0.60$ and the correspondent Ψ_R (b1) and Ψ_L (b2). The temporal sinusoidal profiles corresponding to both filters are depicted in panels (c). Black dashed lines mark the fitted profiles with adjusted phase offsets.

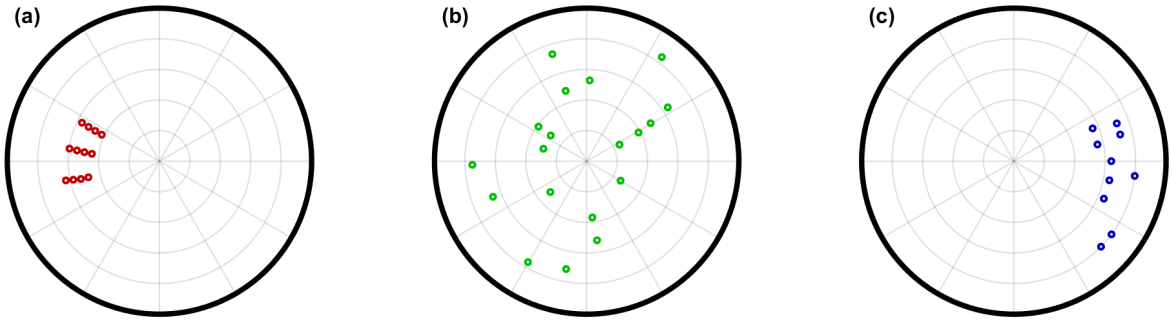

FIGURE 2.16: Points for phase calibration (a) pre-selected set, (b) random points distributed over the phase-space, (c) around $\eta_0 = 0.85$.

For all presented approaches the output phase is compared with numerical simulations for each point and then averaged over the measured values. Overall, these methods give comparable phase corrections and are robust, however, they rely heavily on numerical simulations and the calibration takes a lot of time due to the time required to change the input properties, measure the output and communicate between the different devices. So the alternative approach was taken : we know that the fixed point exists in our idealized FWM propagation, then if we measure the phase value at the fixed point, it would give the phase calibration offset directly, since $\Delta\phi = 0$ and $\phi_{fp} = 0$. This approach is quick and reliable the same way as the other methods. Experimental results in further chapters are obtained using this calibration method.

After both η and ϕ are measured, a home-made Matlab script gathers the data and updates the input, and the process is repeated until a complete loop is measured. A complete measurement of one point takes around 5 seconds (hence, 12 points in a minute). Here the main limitation is the OSO, which communicates with a computer through the Ethernet cable, so sending the traces point by point takes the most of time. Measurement of 100 points (hence, 50 km of effective propagation) takes about 6-7 minutes in total. The next subsection describes stability, robustness and residual effects that are present in the setup.

2.4 Setup stability and limits

As all experimental setups, our setup has unavoidable errors, noise or deviations. This section discusses the impact of different effects on the setup and gives an assessment of a stability.

2.4.1. Power calibration

First thing that was checked in the setup is a power level inside a fiber. A product γP_0 determines the nonlinearity level of the dynamics. Due to presence of several connectors and a tunable attenuator before the fiber, one may expect a certain level of losses. Moreover, the fiber's nonlinear parameter is only known approximately (since the exact design of fiber not being disclosed by the manufacturer), therefore, a product γP would be not exactly defined. The value to be corrected : either P_0 or γ, can be selected arbitrary. In our case we select to calibrate the average input power P_0. For that an experimental map of one-segment propagation is measured and then compared to numerical simulations at different values of input power. The measurement were done at 23 and 24.5 dBm values of power that were set on the amplifier (Figure 2.17 (a) and (b), respectively). As long as P_0 is unknown, the phase calibration cannot be performed, and numerically obtained values were taken instead. After comparison with numerics we observe clear decays of the RMS error at values corresponding to the real power, so the average attenuation level of -1.9 dB was determined. This value is comparable with -1.63 dB attenuation found with direct measurements of the fiber output.

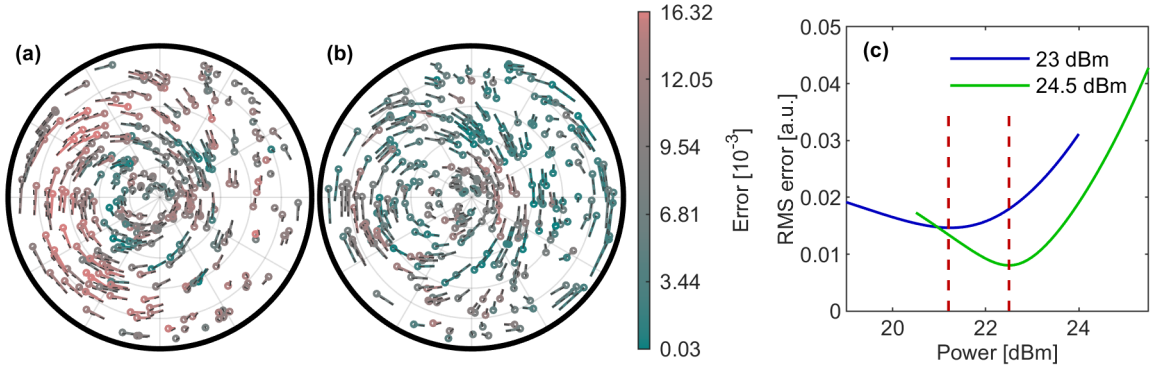

FIGURE 2.17: Phase-space maps recorded for (a) 23 dBm (b) 24.5 dBm input power (a value set on the amplifier). (c) RMS errors when the results are compared with numerical predictions indicate losses of 1.9 dB (red dashed lines mark the minimum error points).

2.4.2. Measurement errors and stability

Setup warm-up

The warm-up is typical for an experimental setup : the equipment may require some time running before the stabilization. In our case the WaveShapers and the amplifier must be on for at least 40 minutes before taking the measurements (not running actively, but at least with power supply on). This required time is consistent with technical documentation of the WaveShaper. However, another issue is that even if this requirement is fulfilled, the phase calibration fluctuates strongly around 1 hour after the laser is on. Figure 2.18 displays a phase-space map with 600 points selected on circles with $\eta = [0.20 : 0.05 : 0.90]$, which was taken right after beginning

of the measurements. In panel (a) the phase offset was calibrated with random points selected on the phase space which gives strong deviations on big area of the map. Then the phase offset of each circle was calibrated, panel (b) shows the resulting phase calibrations for each η. The phase offsets are varying by $0.15-0.33$ radians around an average value, and the fluctuations are not pronounced that much after the warm-up time is over. This behavior and need for the warm-up is reproduced from day to day, however, clear reasons are not identified.

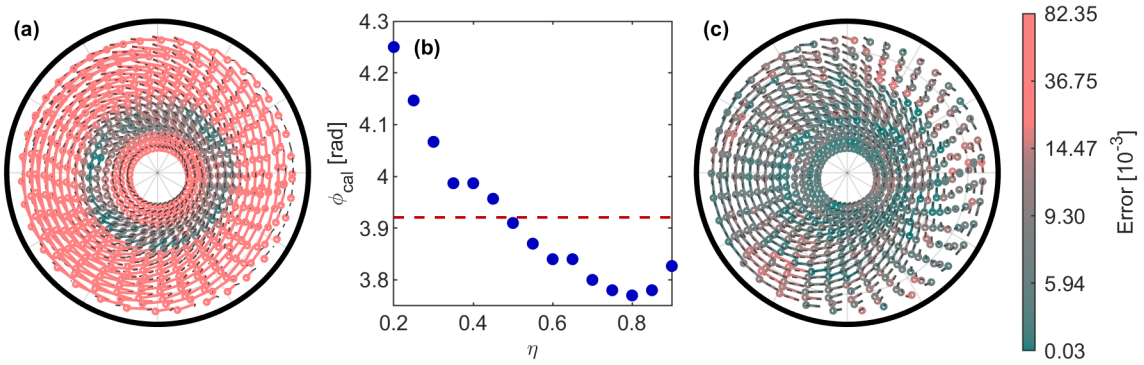

FIGURE 2.18: Experimental results during the warm-up period. (a) A phase space with 600 equally distributed points measured experimentally with a phase offset calibrated with random points. (b) Phase calibration that corresponds to each circle of $\eta = [0.20 : 0.05 : 0.90]$ (blue dots) and the average value (red dashed line). (c) The same experimental map but with phases corrected at each circle.

Measurement errors and stability

To estimate the setup stability, once the setup is conveniently warmed, a fixed point $\eta_{fp} = 0.599$, $\phi_{fp} = 0$ at $\kappa = -1.20$ was measured over 5 minutes sequentially and 50 minutes with an interval of 1 minute. Here we record values of the output relative amplitude η and phase ϕ, and the amplitude difference between the $\pm f_m$ spectral lines ρ (defined according to Eq. 1.56). The results are presented in Figure 2.19.

Fluctuations of η and ρ over time have random nature with errors not exceeding $\delta\eta = \pm 0.15$ dB at imprinted attenuation of 4.28 dB. The errors are within the range of the WaveShaper accuracy limits discussed in Section 2.3.2.

The phase, however, degrades more considerably with time: over 5 minutes the deviation reaches -0.03 radians, while at longer time it can climb up to -0.11 radians. The fluctuations seem random at short timescale, however, the phase clearly gradually degrades to a defined value over longer time. This behavior can be explained by change of polarization state of the waves propagating in the TL fiber that is not polarization maintaining due to temperature drifts or the polarization-mode dispersion (PMD).

Polarization-mode dispersion

In Section 1.1 an important assumption regarding field polarization was made : for single-mode fibers the polarization state is maintained along the propagation. However, a single-mode fiber can support two degenerate modes polarized in two orthogonal directions [110]. If the fiber is perfect, these two states never mix, however in real fibers random variations of core shape or anisotropic stress cause mixing between the modes polarized in x- and y-directions. Mathematically it means that the mode-propagation constant becomes slightly

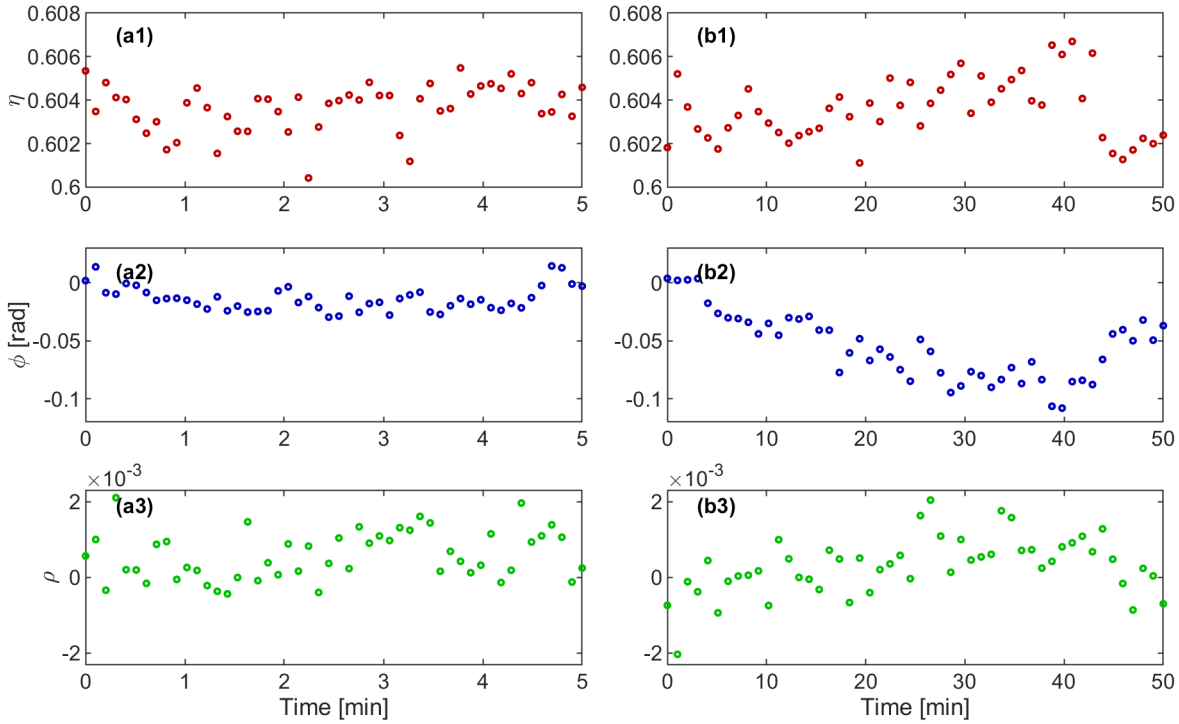

FIGURE 2.19: Values of the relative amplitude η and phase ϕ, and the asymmetry parameter ρ (panels 1, 2 and 3, respectively) measured over : (a) 5 minutes with 6 seconds interval (b) 50 minutes with 1 minute interval.

different for the two modes (let denote each as $\beta_{x,y}$, respectively), that can be characterized by a parameter $B_m = |\beta_x - \beta_y| / k_0$. In a standard fiber B_m is not a constant but changes randomly along the fiber length, so the group velocities of each polarized component would change randomly as well, so the pulse becomes broader. This effect is referred as polarization-mode dispersion (PMD) [44]. Since the changes induced by the PMD are random, the birefringence correlation length (at which the polarization state is maintained) is low, the dispersion effects may statistically cancel each other [111]. Nevertheless, the PMD impacts the FWM process by modifying the gain [112], and for proper investigation it shall be included into propagation equations.

Impact of the polarization on the phase calibration was measured with injecting the amplified spontaneous emission signal (ASE) to the fiber and changing the polarization state by adjusting the PM of either the input to the fiber (Figure 2.20 (a)) or the output (Figure 2.20 (b)) and measuring the output spectrum. In the result we observe dips at spectral amplitudes where two waves with different polarization and, hence, phase are recombined. If one of the PC's state is changed the oscillations are shifted, but the periodicity remains the same (≈369 GHz for both panels (a) and (b) in Figure 2.20). Therefore, with time the phase calibration could degrade and it's required to recalibrate the system. However, within one measurement of 50 points (25 km of propagation), which takes around 5-7 minutes, the phase remains stable.

2.4.3. Level of residual sidelobes

As it was discussed in Section 2.2, one of the main limits in the observation of ideal FWM is the growth of residual sidebands due to cascaded FWM process. The developed setup targets explicitly this problem which is

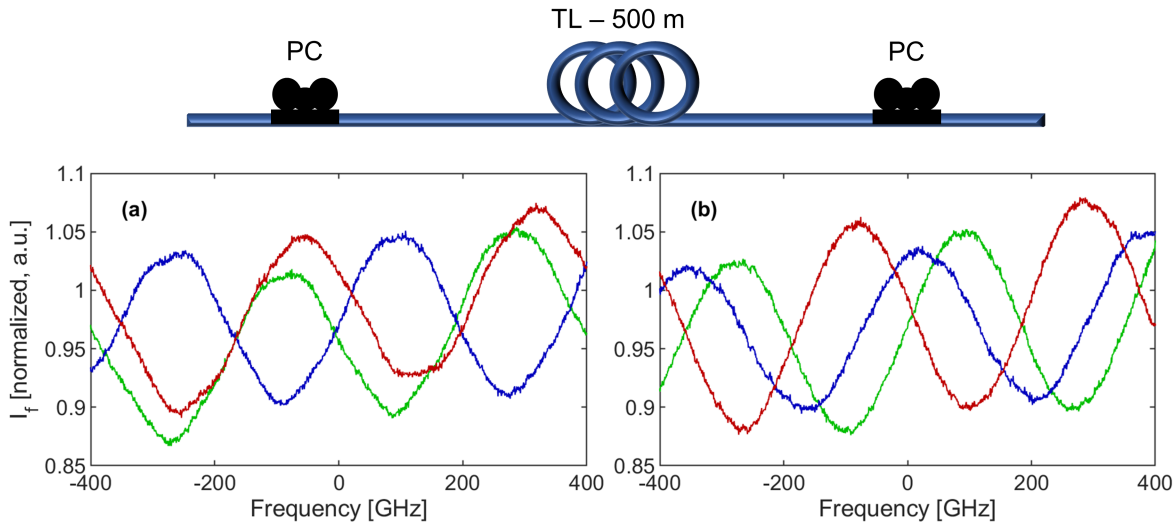

FIGURE 2.20: ASE output spectra at arbitrary configuration of PC at (a) input of the fiber (b) output of the fiber. Shifted oscillations confirm the phase dependence on the polarization state.

the main source of discrepancies and 'spiraling' of trajectories due to dissipation of energy as reflected in Figure 2.6. The level of sidelobes depending on a position on the map for two different levels of powers is displayed in Figure 2.21. In fact, it is the same dataset as for the Figure 2.17, where a normalized spectral intensity at $\pm 2f_m$: $I_f(\pm 2f_m)/\sum_{j=-1}^{1} I_f(jf_m)$, is depicted in color at positions of the output η, ϕ. Comparing the panels (a) and (b) one may conclude that for higher powers the extra sidelobes are more pronounced, because the process becomes more nonlinear, and the cascaded FWM is triggered even at small propagation lengths. The level of sidelobes is distributed similarly at both graphs : values of η where the spectral lines at $\pm f_m$ are comparable or stronger than the middle one (hence, $\eta < 0.40$), hence they act as pumps themselves amplifying the extra spectral lines.

Numerically obtained levels of the sidebands differ from the experimental ones by $1.2 \cdot 10^{-3} - 2.2 \cdot 10^{-3}$. Experimentally the level of the sidelobes can be affected by additional effects such as : the amplifier's power output fluctuations, small Raman amplification, a general inaccuracy of measurements. They may explain the difference with numerical simulations.

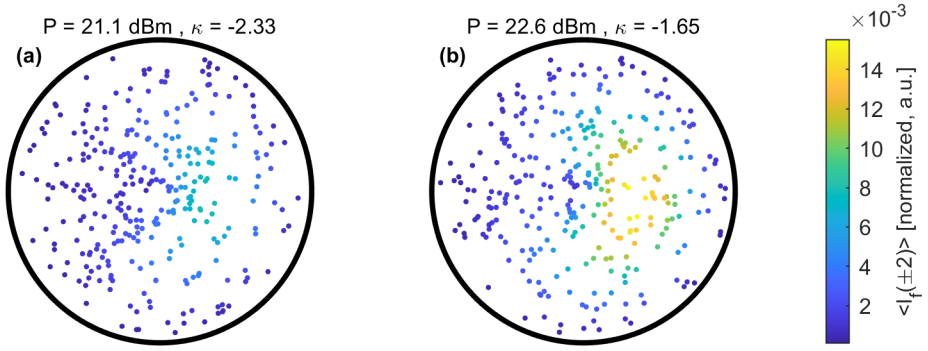

FIGURE 2.21: Phase-space maps recorded at (a) 21.1 dBm and (b) 22.6 dBm where only the output points are displayed. Color indicated normalized level of residual sidelobes : $I_f(\pm 2f_m)/\sum_{j=-1}^{1} I_f(jf_m)$.

2.4.4. Raman effect, losses, third-order dispersion

The last type of effects that could impact the experiment and induce discrepancies when comparing to the ideal FWM model are the higher-order nonlinear effects that include Raman effect, third-order dispersion $\beta_3 = 0.12$ ps^3/km and propagation losses $\alpha = 0.2$ dB/km.

First, in Figure 2.22 we compare two numerical simulations of the phase-space map with the mentioned effects turned on and off, computed at two different powers. The colorbar displays an RMS error, defined as $\sqrt{(\eta_1\cos(\phi_1) - \eta_2\cos(\phi_2))^2 + (\eta_1\sin(\phi_1) - \eta_2\sin(\phi_2))^2}$ with 1 and 2 being solutions with and without extra effects included. The error can go up to 0.02 on a very limited area on the right side of the map, while for majority of points the errors are negligible.

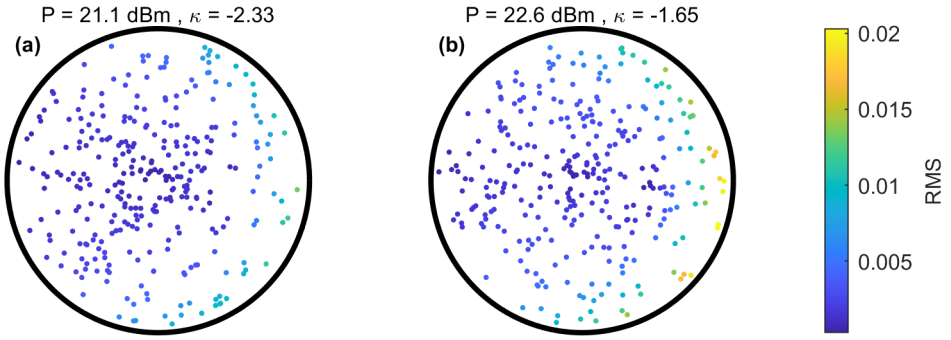

FIGURE 2.22: Phase-space maps recorded at (a) 21.1 dBm and (b) 22.6 dBm where only the output points are displayed. Color indicated RMS error comparing to numerical simulations without Raman amplification, $\beta_3 = 0.12$ ps^3/km and propagation losses $\alpha = 0.2$ dB/km.

For a more rigorous comparison we measure experimental sets consisting of 300 randomly selected points measured at different powers $P_0 = 21.8 : 0.5 : 24.3$ dBm , hence, 1800 points in total. These experimental results are compared with the ideal FWM theory. The same comparison is then done with numerical simulations where the Raman effect, β_3 and losses are "ON" and "OFF". From resulting RMS errors we draw statistics on each approach (Figure 2.23). We see that nominal NLSE with no losses has the least error, and the generalized NLSE creates a certain deviation. The experimental measurement has the highest errors. However, we cannot distinguish the measurement or shaping errors discussed above and the impact of higher order effects. Nevertheless, note that the selected power limits are below the stimulated Brillouin scattering (that was confirmed experimentally), and then well below the threshold for the stimulated Raman scattering. Moreover, the spectral measurements showed no indication of a downshifted spectral peak appearing. Therefore, judging from numerical simulations, we can conclude that the impact of Raman effect, third-order dispersion and losses is negligible.

The dispersion length for the second order dispersion is around 77 km, while for the third-order one, it is 130 208 km, which is well above the segment length. Therefore, the impact of β_3 can be neglected. The effect of β_2 is dominant on the system : compare $|\beta_2/\beta_3| = 6.7 \cdot 10^{13}$, which is another advantage to take a fiber with a dispersion coefficient that is quite high (in comparison to a zero-order dispersion fiber, where β_3 may become dominant).

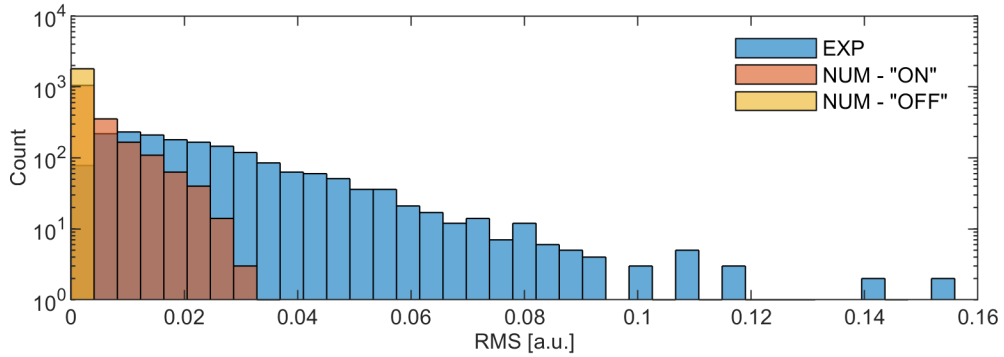

FIGURE 2.23: RMS error when comparing 1800 points at different powers ($P_0 = 21.8 : 0.5 : 24.3$ dBm) computed via ideal FWM model and : experimental results (blue), numerical generalized NLSE simulation with Raman effect, losses and β_3 (orange) and NLSE simulation (yellow).

2.5 Conclusion

We describe the experimental setup dedicated to demonstration of the ideal FWM dynamics. With the concept of iterative propagation in a short segment of fiber we can keep the residual effects to a minimum, while retaining the interaction between just three waves. The selected fiber is TL with $\beta_2 = -8$ ps^2/km, $\gamma = 1.7$ /W/km and length of 500 m. Level of extra harmonics is limited to $14 \cdot 10^{-3}$ relative amplitudes at highest input power. Main source of errors are identified as inaccuracies in shaping of the input signal : the WaveShaper has accuracy limits ± 1.0 dB which impacts fine tuning of the input conditions. Performed calibrations of power, imprinted attenuation and phase measurements are described and characterized in details.

In the next Chapter, we demonstrate how this newly developed experimental technique can be used to characterize the FWM dynamics in its ideal approximation. We explore the phase-space maps and demonstrate the fundamental features of the process, and discuss new characteristics of the interaction.

Chapter 3

Experimental demonstration of idealized FWM

The fundamental FWM interaction described by the truncated three-wave model [11,12] has never been demonstrated experimentally before. With a technique described in the previous Chapter, we are able to keep the system close to the three-waves model which results in idealized dynamics. Firstly, we target to demonstrate the typical FWM recurrent orbits which reproduce the FPUT recurrence. Since the setup allows to tune the initial conditions, we want to reconstruct a complete phase-space plane experimentally, where both types of dynamics are displayed, and the separatrix position is predicted. Second goal is to study the system behavior under gain variation: the orbits' shape and position of stationary solutions vary under the change of input average power. Thirdly, we aim to characterize differences between the ideal and the idealized dynamics by discussing the Hamiltonian conservation and the asymmetric spectra propagation in the experimental conditions.

3.1 Phase-space maps and recurrence dynamics

We first study the dynamics of the system at maximum gain which corresponds to $\kappa = -2$, i.e. for $P_0 = 21.5$ dBm. That corresponds to the case where the lateral sideband is located at the maximum of the gain profile and is the case that has been the most widely studied in the literature. The experimental phase space portraits obtained for different initial values η_0 and ϕ_0 are shown in Figure 3.1 with the orbits shown as circles connected by dotted lines. For each value of η_0, we examined the dynamics at two values of initial phase: $\phi_0 = 0$ and $\phi_0 = \pi$ which yielded trajectories on right and left sides of the separatrix, respectively. The dynamics is measured over 50 km (100 iterations) and the results yield immediate insight into the phase space topology. The experimental orbits are seen to be in very good agreement with the predictions from the ideal system which are shown as thick solid lines. Indeed, many fundamental features of the ideal FWM dynamics can be seen from these results. Specifically, we clearly confirm the importance of the separatrix dividing the phase-space plane into two well-defined regions, with the measurements for $\eta = 0.95$ in particular providing a very clear indication of its location. We also see that the different experimental trajectories are nearly closed orbits and do not intersect. The discrepancies between experiment and prediction here are attributed to the accumulation of small errors in the phase/intensity measurements and residual depolarization effects not included in our scalar model.

Significantly, with complete experimental knowledge of the spectral phase and intensity of the three in-

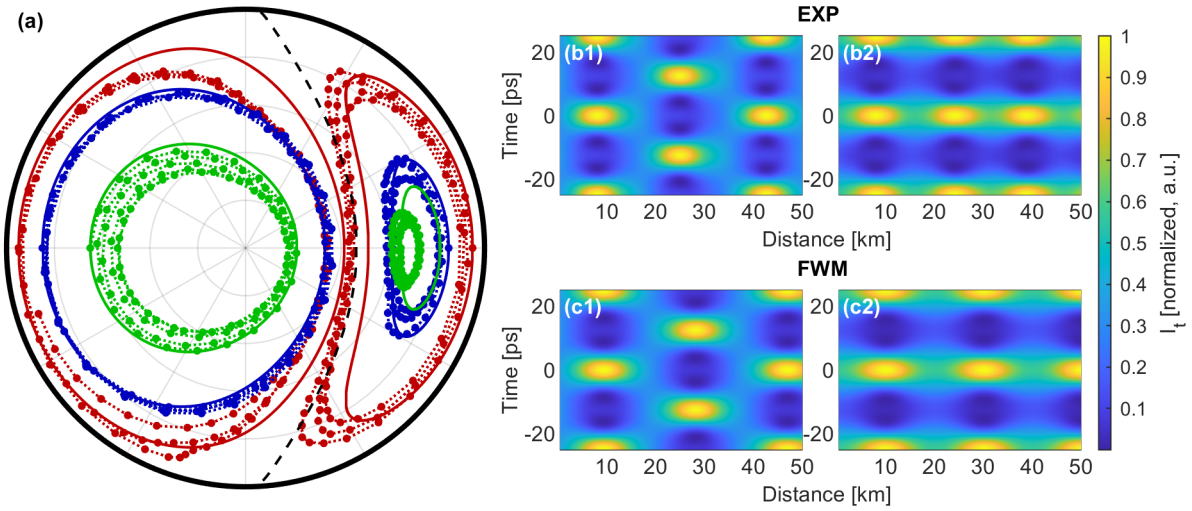

FIGURE 3.1: (a) Phase-space map recorded experimentally (dashed lines with markers) is compared to ideal FWM (solid lines) for $\eta_0 = 0.95, 0.85, 0.65$ (red, blue and green, respectively) at $\phi_0 = 0$ or π (left and right sides with respect to the separatrix denoted in dashed black line). The power level is $P_0 = 21.5$ dBm ($\kappa = -2$). Panels (b) display the temporal intensity profiles reconstructed from experimental measurements for $\eta_0 = 0.95$ and $\phi_0 = \pi$ (panel 1), $\phi_0 = 0$ (panel 2). The respective results of the ideal FWM are depicted in panels (c).

teracting frequency components of the evolving field, it is straightforward to fully reconstruct the evolving intensity profiles in the temporal domain using a simple inverse Fourier transform operation. Over a propagation distance of 50 km, Figure 3.1 (b) shows these results for initial values of $\eta_0 = 0.95$ and phase $\phi_0 = \pi, 0$ (panels 1 and 2, respectively). These results show the expected recurrence dynamics, and for the case of $\phi_0 = \pi$, also highlight the evolution phase shift of half temporal period, leading, as expected by theory to a period doubling [113]. A comparison with theoretical predictions displayed in the respective panels (c) reveals that the experimental evolution is "faster" than the desired one, however, it can be explained by experimental inaccuracies.

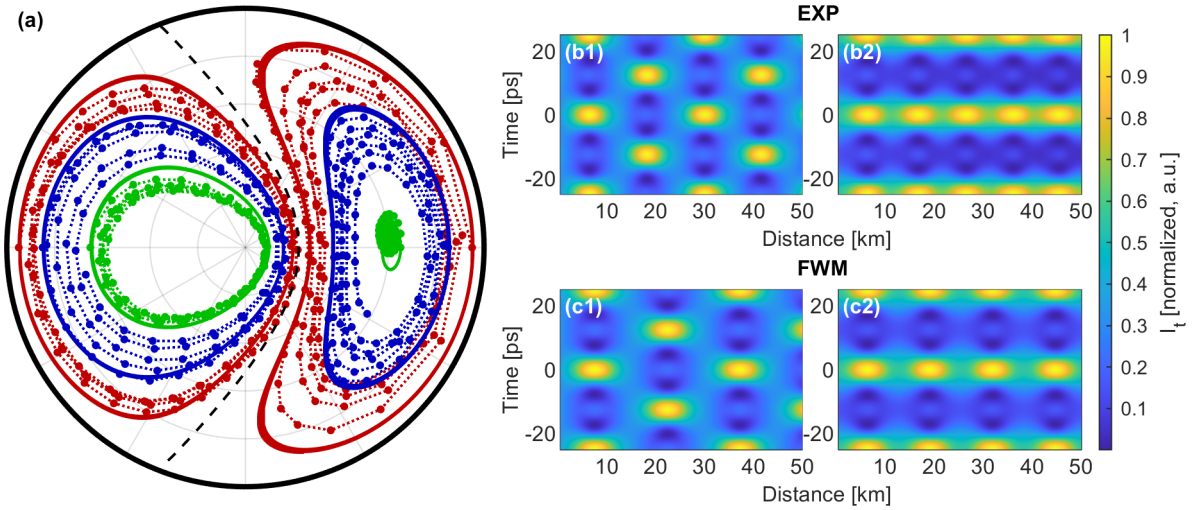

FIGURE 3.2: Same as in Figure 3.1 but for $P_0 = 23.7$ dBm ($\kappa = -1.28$).

Tuning the input power, we can also explore the modulationally unstable dynamics for higher values of gain. Phase space portraits obtained for $P_0 = 23.7$ dBm leading to $\kappa = -1.28$ are plotted in Figure 3.2. Once again, the experimental results are in good agreement with the theoretical predictions. And when comparing with Figure 3.1, we note how the dynamics at higher gain are associated with the change of the shape of the trajectories and the displacement of the separatrix. The discrepancies from ideal FWM propagation are more pronounced both in the phase-space map and in the longitudinal propagation. As it was discussed in Chapter 2.4.3. and demonstrated in Figure 2.6, the deviation from the ideal FWM is increased with the growth of power due to generation of residual sidebands located at $\pm 2f_m$. In Figure 3.3 we compare the normalized spectral amplitudes $< I_f(\pm 2f_m) > / \sum_{j=-1}^{1} I_f(jf_m)$ that are emerging when propagating $\eta_0 = 0.95$, $\phi_0 = 0, \pi$ at 21.5 and 23.7 dBm. We see that the sidebands are higher in the latter case, and even though in both cases they rest well below 3% the accumulated changes cause faster spiraling and deviation from the model.

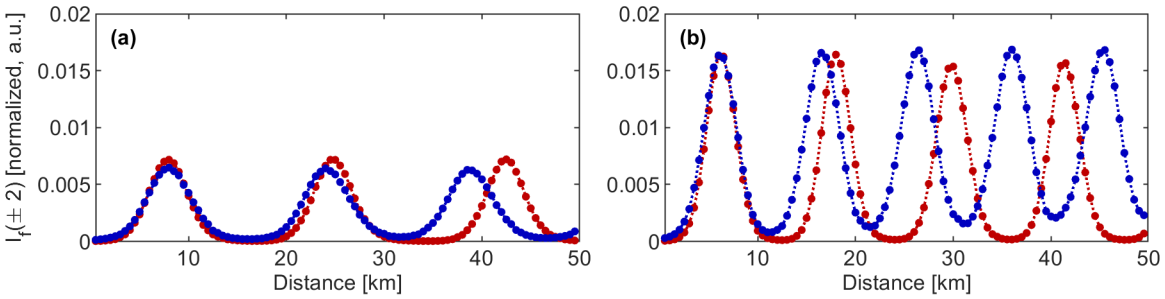

FIGURE 3.3: Normalized intensity of spectral lines located at $\pm 2f_{mod}$ for experimental curves at $\eta_0 = 0.95$, $\phi_0 = 0$ (blue) and $\phi_0 = \pi$ (red) for (a) $P_0 = 21.5$ dBm ($\kappa = -2$), (b) $P_0 = 23.7$ dBm ($\kappa = -1.28$).

To test the limits of how many recurrence cycles can be observed with the developed setup, we propagate the spectral lines over 100 km (200 iterations). The results are displayed in Figure 3.4. The phase-space portrait reveals a strong spiraling towards the fixed point, nevertheless, the temporal intensity profile shows many recurrence patterns that are resembling the ideal FWM predictions. The bounded phase behavior and normal recurrence periodicity is also maintained even during such a long propagation distance.

3.2 Gain dependence

An exhaustive study of the influence of the average power for a fixed value of $\eta_0 = 0.65, 0.90$ with phase offsets $\phi = 0, \pi$ is shown in Figure 3.5. Average powers between 19.7 and 23.7 dBm were tested, which corresponds to κ range between -3.22 and -1.28.

The measurements of the instability process achieved at $\eta = 0.90$ (panels 2) confirm that with increasing powers the separatrix progressively shifts: the intersection point between the separatrix and the horizontal axis continuously decreases. Consequently, the phase space available for the evolution of initial conditions $\phi_0 = 0$ (right side) gets larger, whereas initial conditions $\phi_0 = \pi$ (left side) evolve in more restricted areas. This shift of the separatrix with power helps to qualitatively understand the reported influence of the losses or gain on the FPUT recurrence [14, 113]. Indeed, for a lossy system, the dynamics gradually shifts towards lower powers with a simultaneous shift of the separatrix to the right side, therefore the FPUT recurrence started with $\phi_0 = 0$ crosses the "moving" separatrix and becomes broken. Consequently, phase shifts of half temporal period appear.

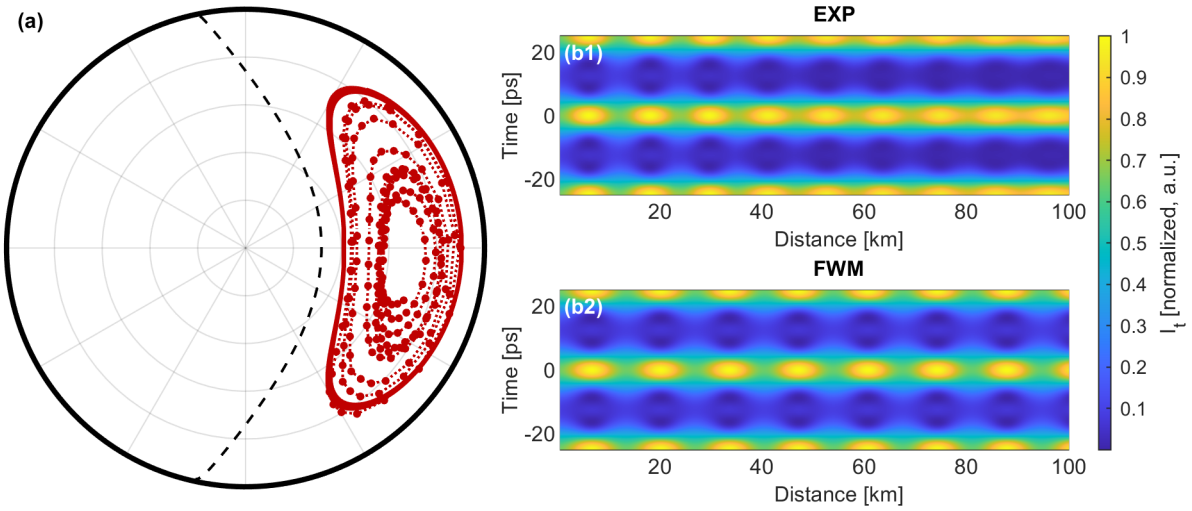

FIGURE 3.4: (a) Phase-space map displaying 100 km propagation (200 segments) for experimental input of $\eta_0 = 0.90$, $\phi_0 = 0$ at $P_0 = 22.7$ dBm ($\kappa = -1.61$), and the corresponding temporal intensity profiles (b1) reconstructed from the experiment, (b2) ideal FWM.

In presence of gain instead of losses, the separatrix would move to the other direction, the in-phase recurrence cycles would be preserved.

Further measurements at $\eta = 0.65$ (panels 1) are also of interest, especially for $\phi_0 = 0$. Indeed, we note that for the lowest powers (19.7 and 20.2 dBm), the initial condition $\eta = 0.65$ and $\phi_0 = 0$ corresponds to solutions located on the left side from the separatrix. For these powers, the trajectory obtained for $\phi_0 = \pi$ is therefore enclosed within the trajectory at $\phi_0 = 0$. When increasing the power, this initial condition evolves on a opposite sides of the phase plane. For powers between 20.7 and 22.7 dBm, the orbits get smaller and smaller up to the stage where they reach a fixed point for 22.7 dBm. When further increasing the average power, the orbit becomes increasingly open.

3.3 Observation of a fixed point

Another property of the ideal FWM is the existence of the fixed point. Within the given experimental limits, only the fixed point located at $\eta_{fp} = (3 - \kappa)/7$, $\phi_{fp} = 0$ is reachable in our configuration. We investigate the fixed points positions and behavior depending on value of normalized mismatch κ. Figure 3.6 (a) displays results of the measurements which start at position of the fixed point for the given power and propagate for 25 km (50 iterations). The drift observed in wave dynamics of the phase-space plane characterizes an importance of errors accumulations, especially at low powers (below 22 dBm), which was noted during experimental measurements in general, and can be explained by excessive linear effects (hence, the phase deviations) over the nonlinear ones. Nevertheless, taking into account experimental errors and its accumulation, the results show that the wave propagates within a very limited area of the phase plane.

The longitudinal evolution of the temporal intensity reconstructed from the spectral measurements at $P_0 = 22.7$ dBm is plotted in Figure 3.6 (b1). We clearly see in this case that the temporal profile is invariant with propagation. Panel (b2) explicitly compares these results (red solid line) with temporal measurements made with a picosecond-resolution optical sampling oscilloscope that were made at the input (blue dotted line) and

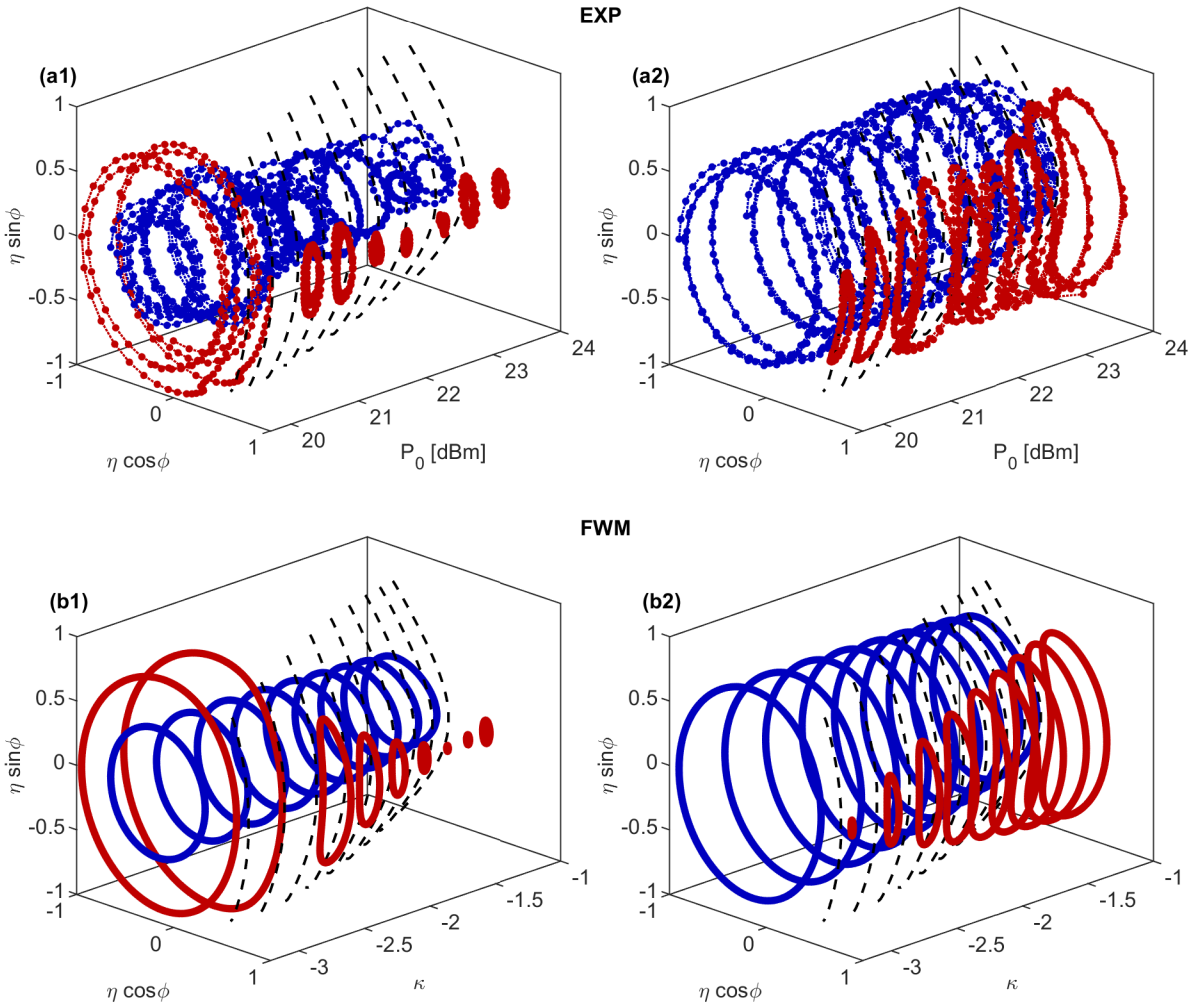

FIGURE 3.5: Phase-space portraits with $\eta_0 = 0.65$ and 0.90 (panels 1 and 2) at varying power ($P_0 = 19.7 : 0.5 : 23.7$ dBm or $\kappa = -3.22 : -1.28$) obtained experimentally (panels a) and from the ideal FWM model (panels b). Red and blue denote orbits with $\phi_0 = 0$ and π, respectively. The black dashed line marks position of the separatrix at the given average power.

at the output (green dashed line) of the fiber. The agreement between these experimental is visually indistinguishable.

The experimental results of the of the fixed point propagation at different powers are compared to the theoretical formula : $\eta_{fp} = (3 - \kappa)/7$. To estimate the experimental errors, an average deviation of η along the propagation was defined. The results are presented in 3.6 (c). The agreement between the theory (black dashed line) and the experiment (red) is excellent.

3.4 Asymmetric spectrum propagation

Propagation of an asymmetric spectral profile where the sidebands' amplitudes are not equal can be important in the context of amplification systems [30, 33, 34] or as an evaluation of system's stability. The asymmetry is usually induced from the third-order dispersion which results in appearance of instabilities and symmetry-

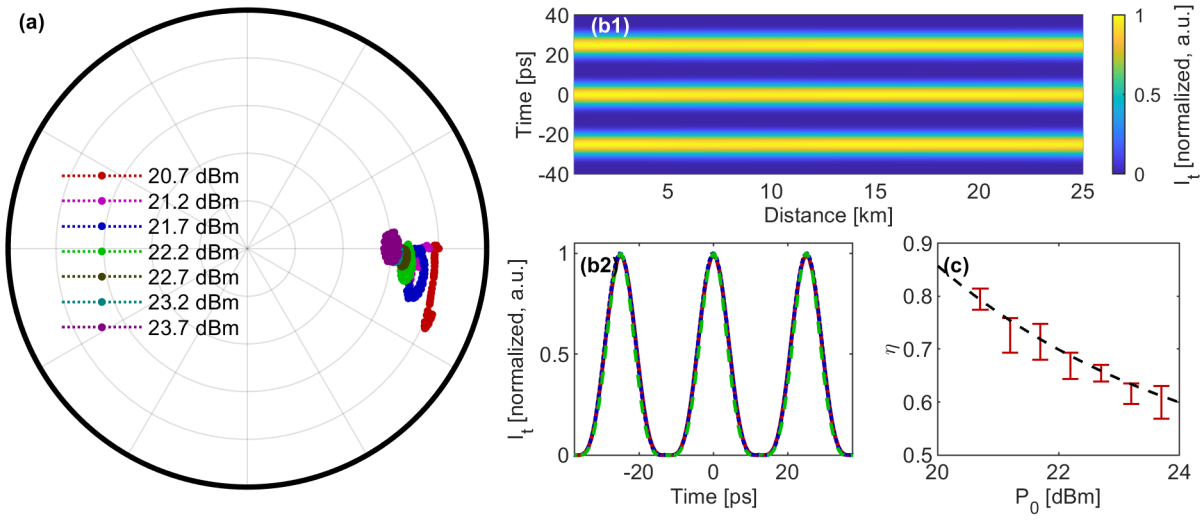

FIGURE 3.6: (a) Propagation of η_{fp} over 25 km is recorded for different values of power. (b1) Longitudinal propagation of the temporal intensity profile at $\eta = 0.65, \phi_{fp} = 0$ and $P_0 = 22.7$ dBm reconstructed from the experimental results. (b2) The shape of the reconstructed temporal profile (red solid line) is compared to direct measurements with a picosecond-resolution optical sampling oscilloscope at the input (blue dotted line) and at the output (green dashed line) of the fiber. (c) Experimentally measured position of the fixed points (red) is compared to theoretical predictions (dashed black line).

breaking of the generated spectrum [102]. Here we discuss how the asymmetric propagation is different in the ideal FWM case, the full NLSE propagation and the developed closely idealized FWM process. The numerical simulations are confirmed with experimental results.

3.4.1. Comparison between the models

Ideal four-wave mixing

In the ideal FWM case, the asymmetry between the sidebands at $\pm f_m$ is defined as $\rho = |\psi_{-1}|^2 - |\psi_1|^2$ (Eq. 1.56). As explained in section 1.1.3 of chapter 1.3, it is defined as one of the invariants, namely the asymmetry, is preserved with distance, while the dynamics still follows similar closed orbits [11]. Figure 3.7 (a) depicts the trajectories where $\rho = 0.20$ is present or not (solid and dashed lines, respectively). The shape of orbits differs, however, the main recurrence features are preserved (Figure 3.7 (c)). The spectral amplitudes depicted in Figure 3.7 (b) reveal that the spectrum can evolve significantly even in presence of the asymmetry between the lateral sidebands.

Since the spectral amplitudes of three lines are normalized, the values of η are limited to $1 - |\rho|$. The eigensolution at $\eta_0 = 1$ no longer exists, since it does not fulfill $\eta_0 = 1 - |\rho|$ with $|\rho| \neq 0$, however the one with $\eta_0 = 0$ is still valid. Other fixed points where $d\phi/dz = 0$ are present, their exact positions can be found in [11].

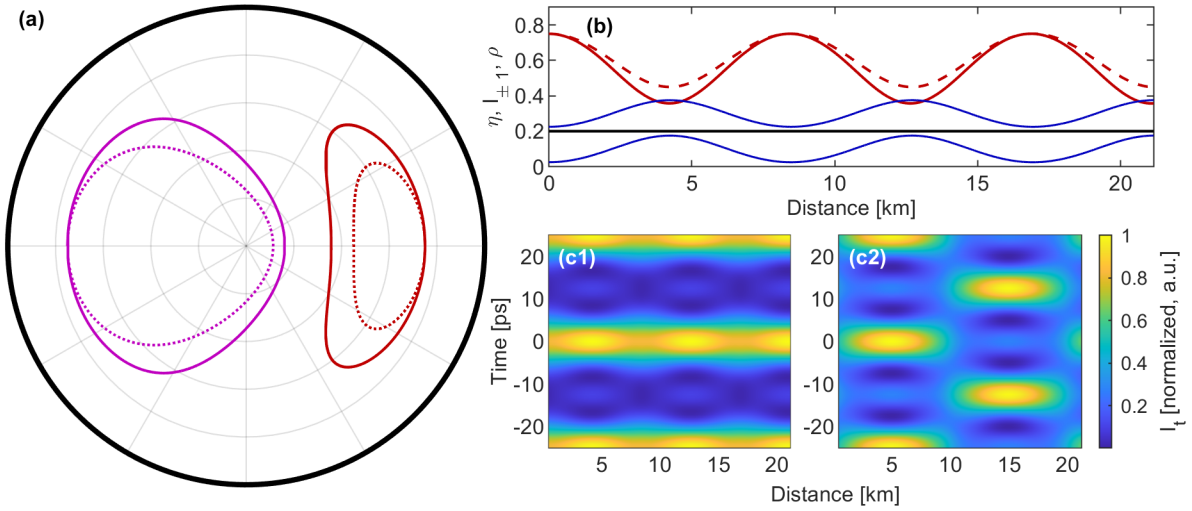

FIGURE 3.7: (a) Phase-space portraits for initial values of $\eta_0 = 0.75$ and $\phi = 0, \pi$ (red and magenta lines, respectively) at $\kappa = -1.2$. Dashed and solid lines denote cases with $\rho = 0$ and $\rho = 0.20$, respectively. (b) Evolution of η (red solid and dashed lines), lateral sidelobes I_{-1} and I_1 (top and bottom blue solid lines, respectively) and α (black line) with distance. (c) Temporal profiles for $\eta_0 = 0.75, \phi_0 = 0, \rho = 0.20$ and $\eta_0 = 0.75, \phi_0 = \pi, \rho = 0.20$ are presented in panels 1 and 2.

Full NLSE - cascaded FWM

In case of the full NLSE evolution, where the lateral sidebands are not limited in growth, and the cascaded FWM is triggered, the evolution looks completely different. Such configuration is of experimental relevancy: for instance, it has been used in the framework of the wavelength conversion or single-sided process. At short propagation length, the asymmetry is conserved [114], however at longer propagation length, the asymmetry parameter ρ is no longer a constant: energy from the spectral lines located at $\pm f_m$ flows to the lateral ones, where the strongest sideband amplifies the residual ones more. One can observe a created asymmetry between the spectral lines around 4 km propagation length in Figure 3.8 (b1) as well as in panel (a2) depicting the longitudinal evolution of the ρ parameter. Then at some point the energy between $\pm f_m$ lines is equalized, and the process is reversed : now the line that had less energy is amplified more strongly. It can be seen in Figure 3.8 (b1) from 4 to 7 km or in Figure 3.9 (a2) (blue dashed and solid line are reversed). The extra sidebands's amplitudes, for instance the ones at $\pm 2 f_m$ are depicted in green in Figure 3.9 (a2), follow the growth or decay of the neighboring lines.

The phase difference between the spectral lines becomes asymmetric as well. The exact phase difference evolution is depicted in Figure 3.9 (a1). With distance the difference between ϕ_{-1} and ϕ_1 is growing following a complex pattern. If one takes a direct Fourier transform of the full spectrum, a temporal profile reveals a shift of the pulses (Figure 3.8 (c1)) that can be approximated with a linear trend (dashed line). The pulse train is now traveling with a certain group velocity (note that the NLSE simulations were done in the moving frame), that is not there when no asymmetry is present (Figure 3.8 (c2)).

The corresponding asymmetry ρ oscillates from positive to negative values. It is hard to identify the exact parameter that forces the asymmetry to be reversed. From the correlation coefficient (Figure 3.9 (c)) one can conclude that the growth of spectral lines on the side which was amplified at first ($I_f(-f_m)$ in our case) has the

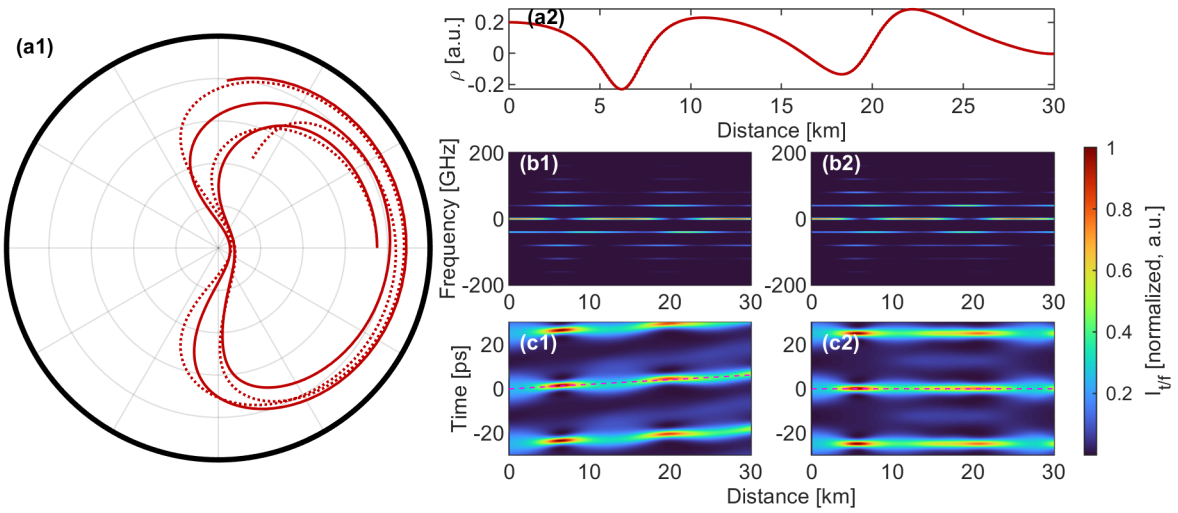

FIGURE 3.8: (a1) Phase-space portrait with full NLSE propagation (cascaded FWM) at $\eta_0 = 0.75, \phi_0 = 0$ and $\rho = 0.20$ (red solid line) or $\rho = 0$ (red dashed line). (a2) Evolution of the asymmetry parameter. The corresponding spectral amplitudes and temporal profiles longitudinal evolution is displayed in (b) and (c) with panels 1 and 2 dedicated to $\rho = 0.20$ and $\rho = 0$, respectively.

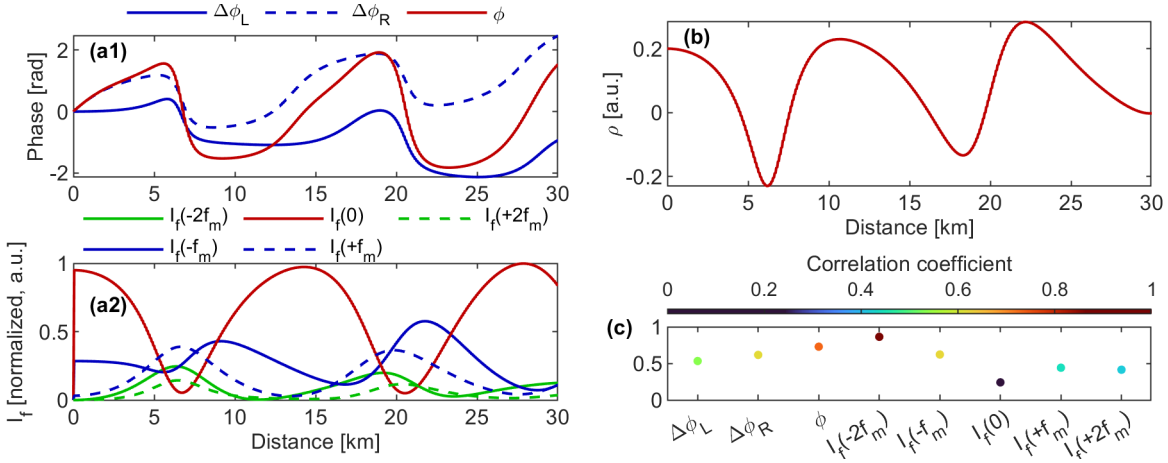

FIGURE 3.9: Longitudinal evolution of (a1) relative phases $\Delta\phi_L = \phi_{-1} - \phi_0$, $\Delta\phi_R = \phi_1 - \phi_0$, $\phi = \phi_1 + \phi_{-1} - 2\phi_0$ and (a2) spectral amplitudes for full NLSE propagation with $\eta_0 = 0.75, \phi_0 = 0$ and $\rho = 0.20$. (b) Evolution of the asymmetry parameter ρ. (c) Correlation coefficient when comparing ρ with listed values.

highest correlation with the asymmetry parameter fluctuations. Note that if the initial conditions are reversed, hence $I_f(+f_m) > I_f(-f_m)$ and $\rho < 0$, then the correlation with $I_f(+f_m)$ is the highest. This behavior is confirmed on both sides of the separatrix.

Idealized FWM

Unlike the full NLSE evolution, the segmented approach with a 500 m segment presented experimentally assumes that the residual spectral components are cut after each propagation round. At the same time, even though the normal propagation shows the results close to the ideal FWM model, in case of asymmetric spectral amplitudes the behavior becomes different.

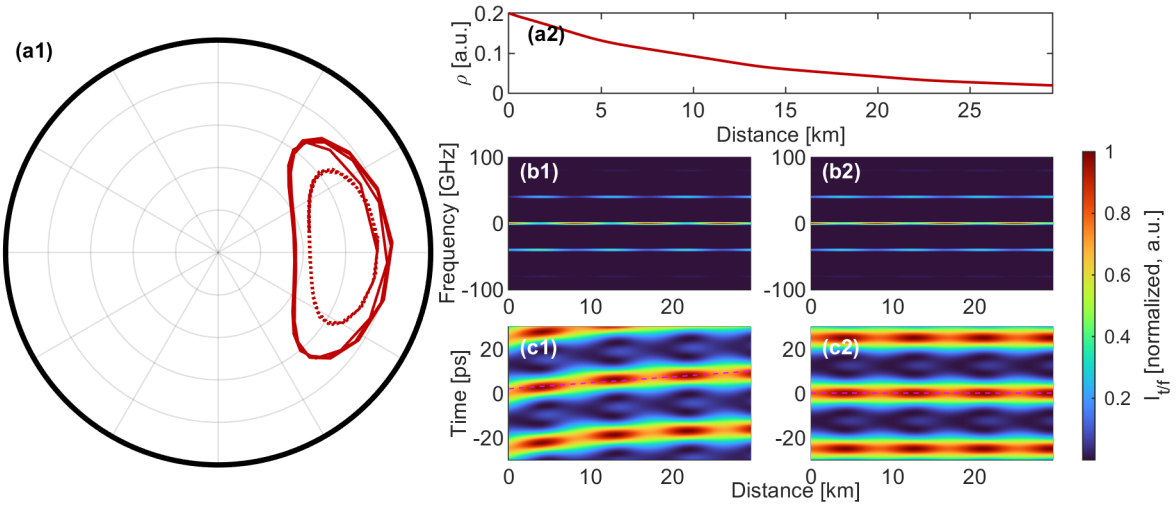

FIGURE 3.10: (a1) Phase-space portrait with segmented propagation (idealized FWM) at $\eta_0 = 0.75, \phi_0 = 0$ and $\rho = 0.20$ (red solid line) or $\rho = 0$ (red dashed line). (a2) Evolution of the asymmetry parameter ρ. The corresponding spectral amplitudes and temporal profiles longitudinal evolution is displayed in (b) and (c) with panels 1 and 2 dedicated to $\rho = 0.20$ and $\rho = 0$, respectively.

First, the asymmetry between the lines is neither preserved nor reversed by analogy with the ideal FWM and the full NLSE, respectively. The difference in spectral amplitudes at $\pm f_m$ reduces with distance since the highest harmonic is reducing and the lowest is getting amplified (Figure 3.10 (b) and Figure 3.11 (a2)). In the end, the asymmetric propagation reaches the case of ideal FWM with $\rho = 0$ (Figure 3.11 (b)). This behavior could be explained by impact of the residual sidelobes generation: as within the segment the light goes through short NLSE evolution, the residual sidelobes are generated impacting the higher and the lower amplitude spectral lines differently. However, the correlation coefficient at $I_f(-2f_m)$ (equal to 0.053) does not reveal the link between the two parameters.

The highest correlation coefficient (equal to 0.923) corresponds to phase difference between the higher line and the central line $\Delta\phi_L$ (for $\rho < 0$ it would be $\Delta\phi_R$) which means that the dephasing between the asymmetric spectral lines can be atributed to decreasing ρ. Similarly to the full NLSE propagation temporal profiles resulting from the segmented approach are shifted (Figure 3.10 (c1)), and difference $\phi_{-1} - \phi_1$ is growing with distance.

The main feature of the segmented approach is the periodic cutting the residual sidelobes and the subsequent recycling of three lines with reamplification of the signal. In general, this effects can be compared to dissipation and amplification in the NLSE propagation that were discussed in [68, 69, 86] in a context of wave propagation in hydrodynamics, where even a weak dissipation can impact the FPUT recurrence [14]. The authors investigate the effects of forcing and viscous damping on water waves that are described by the higher-order NLSE - the

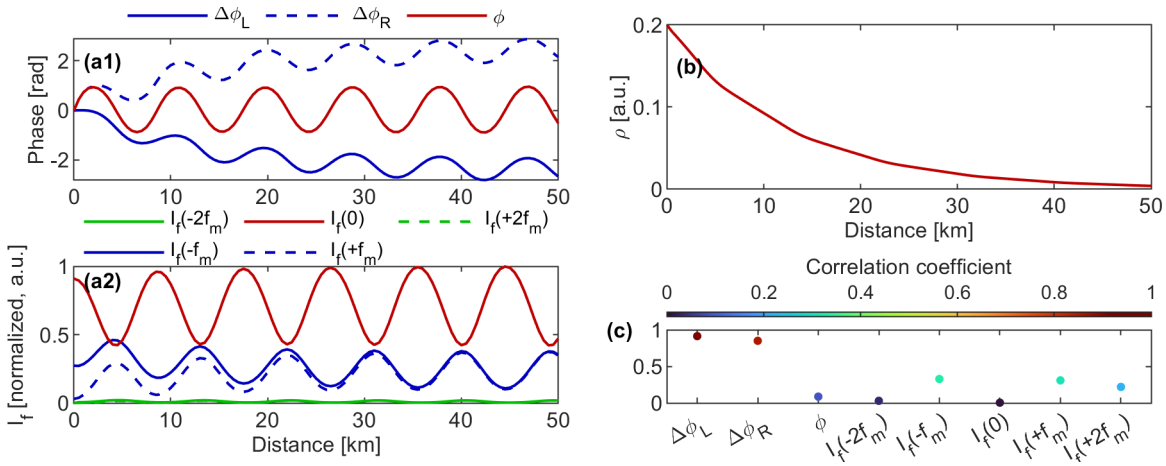

FIGURE 3.11: Longitudinal evolution of (a1) relative phases $\Delta\phi_L = \phi_{-1} - \phi_0$, $\Delta\phi_R = \phi_1 - \phi_0$, $\phi = \phi_1 + \phi_{-1} - 2\phi_0$ and (a2) spectral amplitudes for the segmented propagation with $\eta_0 = 0.75, \phi_0 = 0$ and $\rho = 0.20$. (b) Evolution of the asymmetry parameter ρ. (c) Correlation coefficient when comparing ρ with listed values.

Dysthe equation. Changes in wave dynamics caused by damping or forcing are projected on the phase-space plane, and the authors observe an attraction to the phase-shifted solutions (left side of the separatrix) in case of damping, and an attraction towards non-shifted solutions (right side) in case of wind forcing [68, 69]. Also, the asymmetry of the $\pm f_m$ lines is amplified in case of forcing and diminished in case of damping which also reflects in shifts of temporal profiles. These effects are qualitatively similar to spiraling and amplitude changes observed numerically and experimentally in the segmented approach. Of course, a continuous linear damping or forcing is far from being equivalent to changes induced in the idealized FWM, however, a qualitative behavior can be discussed, it is interesting to compare these two systems. In [69] a new set of three-waves equations are

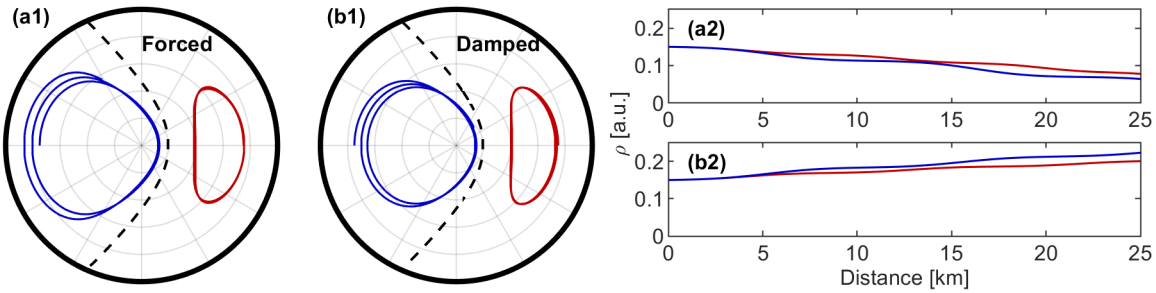

FIGURE 3.12: Phase-space maps for $\eta_0 = 0.75, \phi_0 = 0/\pi, \rho = 0.15$ with forcing $\delta_0 = 0.009, \delta_1 = 0.009$ (a1) and damping $\delta_0 = -0.009, \delta_1 = -0.009$ (b1). The corresponding variation of the asymmetry parameter ρ.

derived where the effects of forcing and damping are included. The δ_0 and δ_1 correspond to zero and first order terms, respectively, denoting forcing if $\delta > 0$ and damping if $\delta < 0$. Neglecting higher-order nonlinear terms

we write three-waves equations as (compare to Eq. 1.43):

$$\begin{aligned}
\tfrac{d\Psi_0}{\gamma P_0 dz} &= i\left(|\Psi_0|^2 + 2|\Psi_{-1}|^2 + 2|\Psi_1|^2\right)\Psi_0 + 2i\Psi_{-1}\Psi_1\Psi_0^* + +\delta_0\Psi_0 \\
\tfrac{d\Psi_{-1}}{\gamma P_0 dz} - i\tfrac{1}{2}\kappa\Psi_{-1} &= i\left(|\Psi_{-1}|^2 + 2|\Psi_1|^2 + 2|\Psi_0|^2\right)\Psi_{-1} + i\Psi_1^*\Psi_0^2 + \delta_0\Psi_{-1} + \sqrt{|\kappa|}\delta_1\Psi_{-1}, \\
\tfrac{d\Psi_1}{\gamma P_0 dz} - i\tfrac{1}{2}\kappa\Psi_1 &= i\left(|\Psi_1|^2 + 2|\Psi_{-1}|^2 + 2|\Psi_0|^2\right)\Psi_1 + i\Psi_{-1}^*\Psi_0^2 + \delta_0\Psi_1 - \sqrt{|\kappa|}\delta_1\Psi_1.
\end{aligned} \tag{3.1}$$

Previously the damping and forcing was discussed in a context of separatrix crossing for solutions that start near $\eta \neq 1$ and $\phi = 0$, however in our case the dynamics is reconstructed over the whole phase-space plane, so it is important to know what the impact and the consequences forcing and damping on these solutions is. We simulate propagation of wave with $\eta_0 = 0.75$ and asymmetry parameter $\rho = 0.15$ in cases when forcing of $\delta_0 = 0.009, \delta_1 = 0.009$ (panels (a)) and damping $\delta_0 = -0.009, \delta_1 = -0.009$ (panels (b) in Figure 3.12) dominate the system. Here the choice of values and combination of signs of the parameters is arbitrary, and they are selected to highlight qualitative behavior for two distinct regimes. In case of the waves amplified due to forcing, we observe spiraling outside of the initial point that has a high rate on the left side, while in the damped system with energy dissipation the solution spirals down. It agrees with predictions in [68] where the forced system had a tendency to move towards the solutions with non-shifted phase, and the reverse.

The asymmetry ρ between the sidebands is neither conserved as in case of ideal FWM nor oscillates as in the full NLSE propagation : it changes gradually depending on sign of initial unbalance and applied forces. The forcing amplifies the absolute value of $\rho < 0$, while the damping amplifies $\rho > 0$. So the decrease in ρ in case of the segmented approach can be attributed to periodic effects of energy dissipation and reamplification (hence, forcing), where energy dissipation dominates the system and should be understood as an energy flow outside of the three-waves system.

3.4.2. Experimental demonstration

To demonstrate the presented features experimentally we first must address two issues : the phase measurements and the working points.

As it is seen in Figure 3.11 (a1) the relative phase between the lateral harmonics and the central one differs for two sides $\pm f_m$. In the experimental setup, we are able to calibrate the phase offset directly related to the relative phase ϕ, so the individual offsets for left and right harmonics cannot be defined. Therefore, the recycling of initial conditions is made by imprinting $\phi/2$ on $\pm f_m$ lines. In Figure 3.13 (a) the phase at each $i-$cycle is updated by $\phi_i/2$ (unlike in Figure 3.11, where the recycled phases are defined from absolute phases of each spectral line), and, for comparison, the $\Delta\phi_L$ and $\Delta\phi_R$ are measured from the electric field. The relative phase difference between left and right sides, so pronounced before, is reduced, and shift of temporal profile becomes almost negligible (one can see the pattern asymmetry in between the two peaks). However, the values of η and ϕ are reconstructed correctly since only the relative dephasing between three lines defines the dynamics.

Experimentally we reconstruct the temporal profiles from measurements of η and ϕ, therefore, we assume $\Delta\phi_L = \Delta\phi_R = \phi/2$ as presented in Figure 3.13 (b1). Hence, the shift of the temporal intensity profile cannot be reconstructed from experimental measurements. Nevertheless, the dynamic still demonstrates the recurrence profile (Figure 3.13 (b2)).

Knowing the relative errors of the setup, measurement of slowly decaying asymmetry factor can become challenging : if the change from one iteration to another is less then 1% of the relative spectral amplitude,

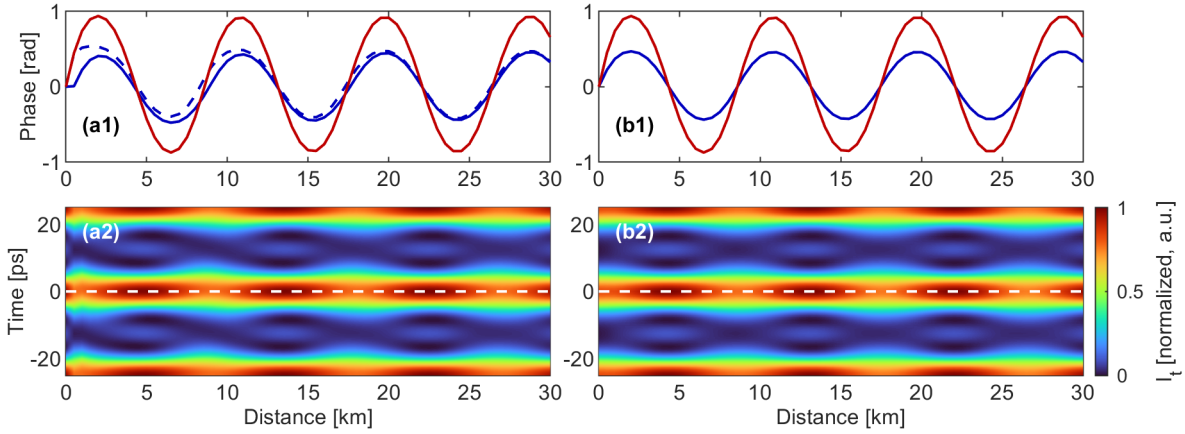

FIGURE 3.13: (a1) Evolution of relative phases $\Delta\phi_L$ (blue solid line) and $\Delta\phi_R$ (blue dashed line) extracted from the electric field directly when the phase recycling assumes equal phase difference on the sidelobes $\phi/2$. The relative phase ϕ is denoted in red solid line. (b1) The corresponding temporal intensity profile. (b1) Relative phases assuming that $\Delta\phi_L = \Delta\phi_R = \phi/2$, and the resulting temporal intensity evolution (b2). The latter case is equivalent to the one used in the experimental measurements.

then the measurement errors may mask the effect. Keeping in mind that generation of higher-order harmonics "helps" the asymmetry to decay faster, the 24 dBm working power was selected ($\kappa = -1.2$).

The experimental measurements were taken at $\eta = 0.75$ on both sides of the separatrix $\phi = 0, \pi$ for $\rho = \pm 0.15$. All experimental results show good agreement with numerical simulations of segmented approach, and the phase-space portraits agree well with the ideal FWM model, though the spiraling is present (panels (a) in Figures 3.14-3.17).

The decay rate of ρ is stronger for the orbits with bounded phases (right side of the separatrix). The asymmetry is decreasing with propagation length that is visible in spectral measurements and agrees with behavior present in numerical simulations (compare panels (b) and (c) in Figures 3.14-3.15).

For the other type of solutions with unbounded phase (left side) the ρ parameter experiences oscillations and decays slower in general. Since the relative change in ρ from one iteration to another is small, the experiment does not follow numerical predictions so precisely (compare panels (b) and (c) in Figures 3.16-3.17). Moreover, the spiraling of trajectories becomes more pronounced, and the asymmetry is slightly reversed in Figure 3.17. It can be explained by accumulation of experimental errors and stronger spiraling effects that are pronounced on the left side at high power. To characterize the strength of the spiraling we introduce colored markers in panels (b1) and (c1) of Figures 3.14-3.17 denoting value of Hamiltonian (Eq. 1.57) at this point. In ideal FWM it is seen as one of the invariants, however in the experimental system it's value changes due to cutting of residual sidelobes and reamplification at each iteration. One can see that Hamiltonian variation is more pronounced on the left side for the experimental measurements that can cause deviations of ρ.

3.5 Hamiltonian conservation

The numerical and experimental results provided in Section 3.4 have risen a question of invariants conservation that is fulfilled in the ideal FWM but not in case of the segmented approach. Another conserved quantity that

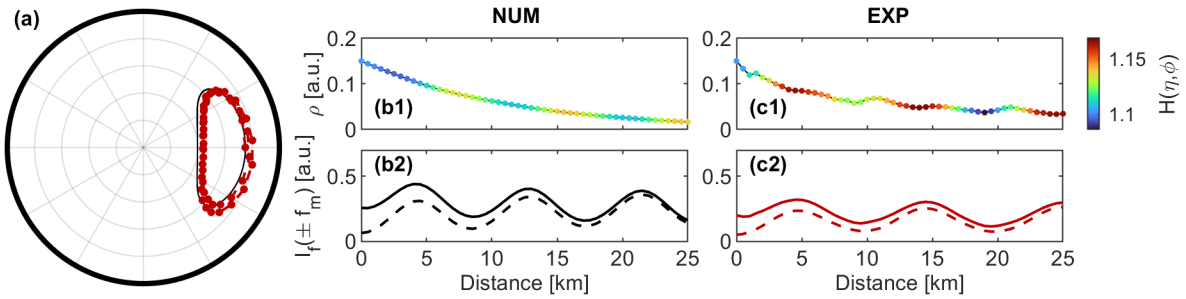

FIGURE 3.14: (a) Experimental phase-space portrait (red dashed line with markers) for $\eta = 0.75, \phi = 0, \alpha = 0.15$ is compared with ideal FWM. The corresponding evolution of ρ (panels 1) and spectral harmonics (panels 2) for numerical simulations of segmented approach and experiment. Colored markers represent the value of the Hamiltonian (Eq. 1.57).

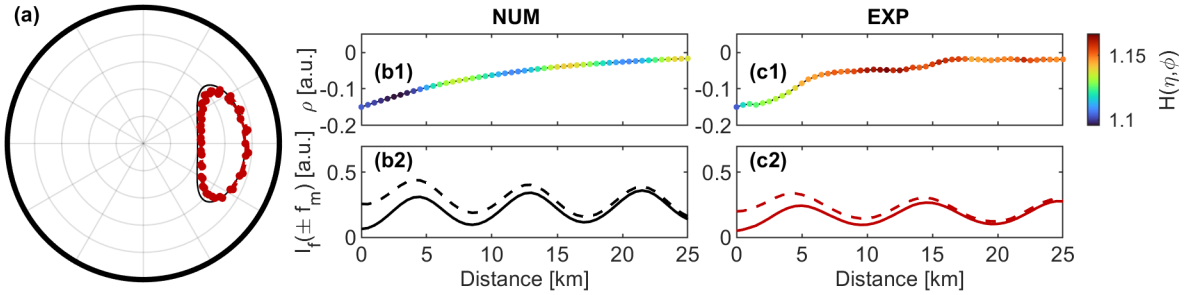

FIGURE 3.15: Same as Figure 3.14 but $\alpha = -0.15$.

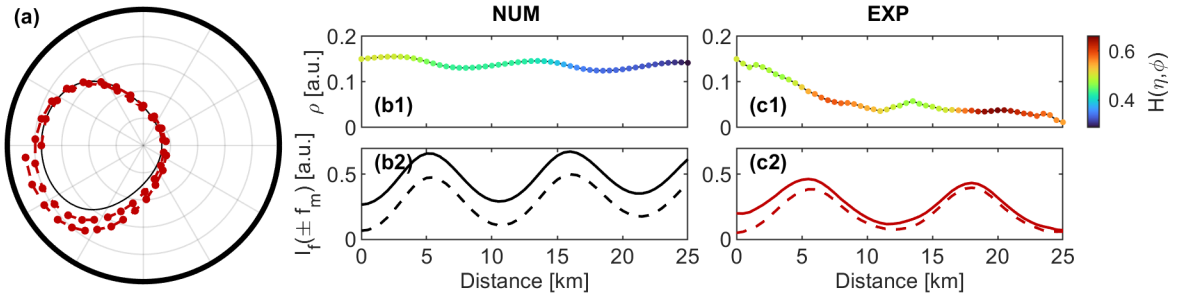

FIGURE 3.16: Same as Figure 3.14 but $\phi = \pi, \alpha = 0.15$.

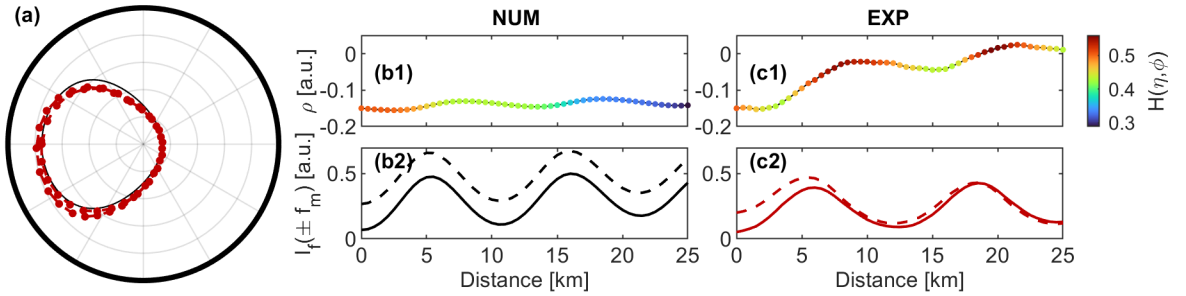

FIGURE 3.17: Same as Figure 3.14 but $\phi = \pi, \alpha = -0.15$.

ensures a conservation of energy is the Hamiltonian provided by Eq. 1.57. It has been already observed that

the spiraling of trajectories is caused not by the experimental inaccuracies, but it is a fundamental property of the system. Therefore, a question is related to the limits of the segmented approach where the Hamiltonian is nearly conserved. And whether the spiraling leads to instabilities or chaotic behavior for a very long propagation distances (well above the studied 50 km) similar to system where the signal is amplified periodically [115,116].

To estimate variation of the Hamiltonian in the segmented system and determine whether spiraling has any point of attraction, we simulate propagation over long distance of initial conditions equally sampled all over the phase-space map. Two system's states were considered : $\kappa = -2$ and $\kappa = -0.8$ with propagation distances of 2000 km and 1000 km, respectively. With such a long propagation we make sure that the spiraling has enough distance to converge to a given point. Each set of κ and initial conditions was tested for different segment lengths : 250, 500, 750 , 1000 and 2000 m. This allows to estimate how the full NLSE development over the given segment length would impact the dynamics.

3.5.1. Low power, $\kappa = -2$

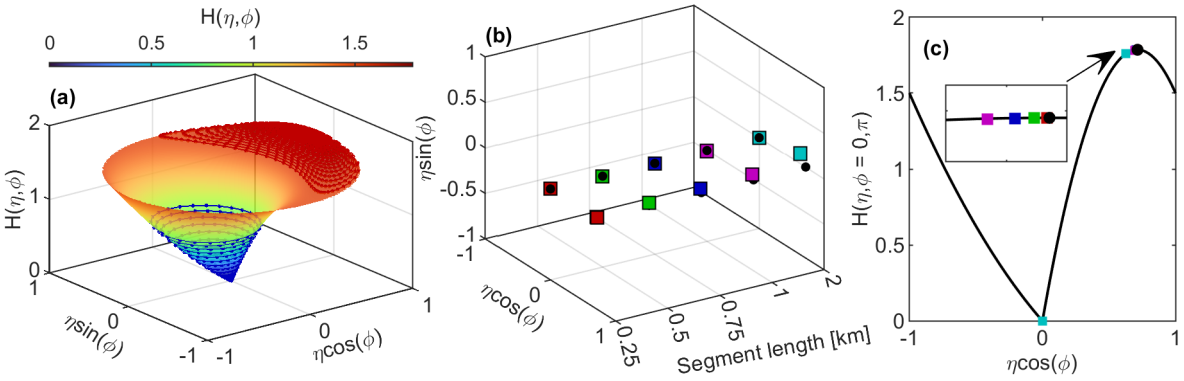

FIGURE 3.18: $\kappa = -2$. (a) Hamiltonian distribution of a phase-space map with examples of two trajectories : $\eta_0 = 0.99, \phi_0 = 0$ (red line) and $\eta_0 = 0.67, \phi_0 = \pi$ (blue line). The segment length is 500 m, no asymmetry is imprinted. Positions of attraction points derived for each segment length are compared to the fixed points of the system : (b) on the phase-space plane and (c) on the Hamiltonian curve taken as a cross-section of (a) at $\eta \sin\phi = 0$. The red, green, blue, magenta and cyan markers correspond to the segment lengths of $250, 500, 750, 1000, 2000$ m.

The Hamiltonian profile on the phase-space plane coordinates is depicted in Figure 3.18) (a). It has two extreme points located at $\eta_{fp} = 0.71, \phi_{fp} = 0$ and $\eta_0 = 0$ which correspond to eigensolutions of the system (noted as well in 3.18) (c) by black dots). In the ideal FWM, the trajectories move on orbits following a constant Hamiltonian. That creates "energy levels" that can characterize each close orbit. In the segmented case, the trajectories move on the phase-space plane with continuous energy transfer (namely, either dissipation or gain depending on the location) occurring after each segment length and resulting in spiraling on the Hamiltonian surface. From the ensemble of statistical data we can conclude that trajectories whose initial conditions belong to the right side of the separatrix are attracted towards the fixed point $\eta_{fp} = 0.71, \phi_{fp} = 0$, while the ones on the left are attracted to $\eta_0 = 0$. Examples of the trajectories is depicted in red ($\eta_0 = 0.99, \phi_0 = 0$) and blue ($\eta_0 = 0.67, \phi_0 = \pi$), respectively, in Figure 3.18) (a) for the fiber segment of 500 m.

The segment length defines how long the initial conditions propagate according to the full NLSE before the residual sidelobes are cut, and the system is reamplified (without corrections of the energy flow outside of three

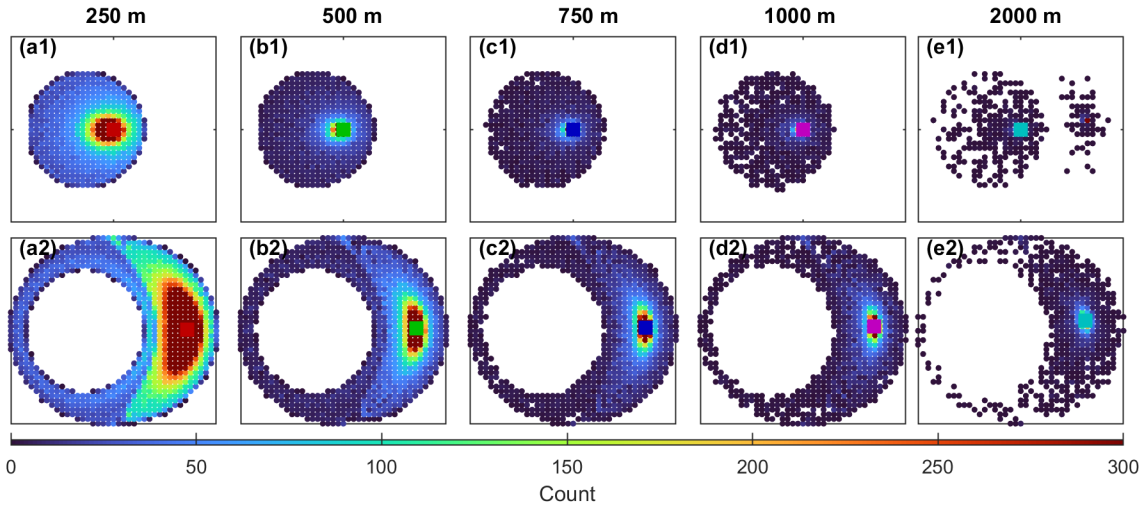

FIGURE 3.19: Ranges of attraction to fixed points on the left and the right sides of the separatrix (panels 1 and 2, respectively). Segment length is increasing from panels (a) to (e) from 250 m to 2 km (the colorcode for each marker is denoted in Figure 3.18). Here we consider 80 starting points evenly distributed on the phase-space map, where each propagates over 1000 km.

waves). Such a system is similar to a concept of reamplified fiber links, where a wave propagates with linear losses that are compensated by periodically spaced amplifiers [117]. This creates sidebands instabilities along with narrow parametric gain peaks located outside the MI band [115]. In the ideal three-waves interaction, stable fixed point attractors exist, where a balance between the parametric gain and the losses is achieved [116]. The field evolution in this case represents a spiraling trajectory towards such a focus point. If this balance is not achieved, for instance, because of the limited bandwidth amplification, the nonlinear propagation is destabilized, and the chaotic behavior is observed [116].

In case of the segmented approach, the spiraling to the focus points located near the fixed point solution (but not exactly) is observed after 2000 km for all segment lengths. Figure 3.18 (b) and (c) displays positions of the attractors on the phase-space map for each segment length. The focus points were defined from statistics gathered for all trajectories sampled on the phase-space plane. The radius of curvature and its corresponding center were defined for the last 200 points of the trajectory. Gathering statistics on the center position for all points, we define the attractor point more precisely, that allows to reach a better convergence.

In general, the longer the segment is, the farther the attractors are located from the fixed points defined from the ideal model (inset in panel (c) of Figure 3.18). It can be explained by longer NLSE propagation and, hence, stronger deviation from the model until the spectrum is recycled.

Since there exist two attraction points, it is interesting to know what is their range of attraction : an area on the phase-space map where statistically the trajectories tend to fall to the focus point. To define the attraction region, we split the phase-space map into a grid, and then analyze each of 80 simulated trajectories point by point. Each segmented output of the trajectory is affiliated to a cell on the phase-space map grid. Then, after defining to which attractor the trajectory falls, this cell is getting an increment each time new segment is passing through. After treating all trajectories, we obtain a density of points, which characterizes how being at a certain position on the phase-space map, impacts the attraction to one or another focus point. This way we can build a statistical map and define attraction regions.

The results are presented in Figure 3.19. There are two well-defined regions of attraction: the points with $\eta < 0.85$ on the left side of the separatrix spiral down to $\eta_0 = 0$ (panels 1), while the rest tends to be attracted by the fixed point η_e (panels 2). The ranges of attraction are strongly related to position of the separatrix, the trajectories passing near have a tendency to be unstable and cross it making a transition to another type of solutions. Here, for the small signal amplification (stating, with $\eta \neq 1$), the trajectories always converge to the right attractor. So the points with high η one the left side may fall into the opposite attractor.

As the segment length increases, the system deviates stronger from the ideal case, so $H(\eta, \phi)$ decays faster, and the separatrix border becomes "blurry" as after a few segments of NLSE propagation one may end up on the opposite side of the separatrix. That's why the attraction regions are more confined in case of longer propagation lengths (for instance, 1 or 2 km). Another point is that the spiraling with longer segments is more abrupt, so there is not enough statistics to cover the whole grid evenly. Interestingly, at 2 km segment length there exist trajectories that pass near the attraction point on the right side but still don't fall into it (Figure 3.19 (e1)) ending up on the left side.

3.5.2. High power, $\kappa = -0.80$

Knowing that not only the segment length but also the average input power impacts the dynamics, the same analysis was repeated for another case of $\kappa = -0.80$.

For $-1 < \kappa < 0$, there actually exist two fixed points satisfying $\eta_{fp} = (3 - \kappa)/7, \phi = 0$ and $\eta_{fp} = 1 + \kappa, \phi = \pi$. At $\kappa = -0.80$ the Hamiltonian profile (Figure 3.20 (a)) is steeper with two extreme points located at $\eta_{fp} = 0.54, \phi = 0$ and $\eta_{fp} = 0.20, \phi = \pi$. Similar to the previous case, it was expected that the trajectories would fall into these two points, however, they all tend to spiral down to the fixed point located on the left side of the separatrix. On examples displayed in Figure 3.20 (a) (red $\eta_0 = 0.99, \phi_0 = 0$ and blue $\eta_0 = 0.67, \phi_0 = \pi$ trajectories at segment length 500 m), the trajectory starting on the right side crosses the separatrix after a few propagation cycles. It happens because the system becomes so highly-nonlinear that the idealized FWM conditions are no longer fulfilled, and dynamics has a strong impact of the full NLSE propagation over even small segment length.

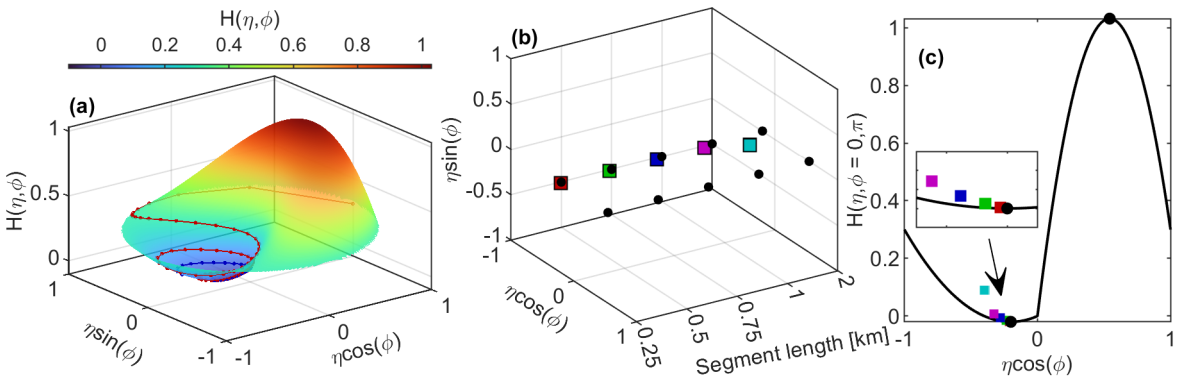

FIGURE 3.20: Same as Figure 3.18 but for $\kappa = -0.8$.

The statistical treatment reveals only one attraction point for each segment length that is located on the left side of the separatix (Figure 3.20 (b) and (c)). The attraction regions displayed in Figure 3.21 show that even at low segment length of 250 m the trajectories passing near the fixed point on the right side of the separatrix never fall into it. Even when the initial conditions are set in a vicinity of the fixed point on the right side, and

the small segment length is used (the values of 20 m and 50 m have been tested), the trajectories converge to the left side. Opposite to the "low power" in section 3.5.1, the trajectories only converge to the attractor on the left side of the separatrix. In fact, the trajectories that start on the right side tend to spiral outwards so they end up falling to the left attractor, and the segment length defines speed and steepness of trajectory movement. Such a behavior at higher nonlinearity can be explained by stronger impact of full NLSE propagation and; hence, the effects of periodic damping and forcing in the system discussed in the previous section.

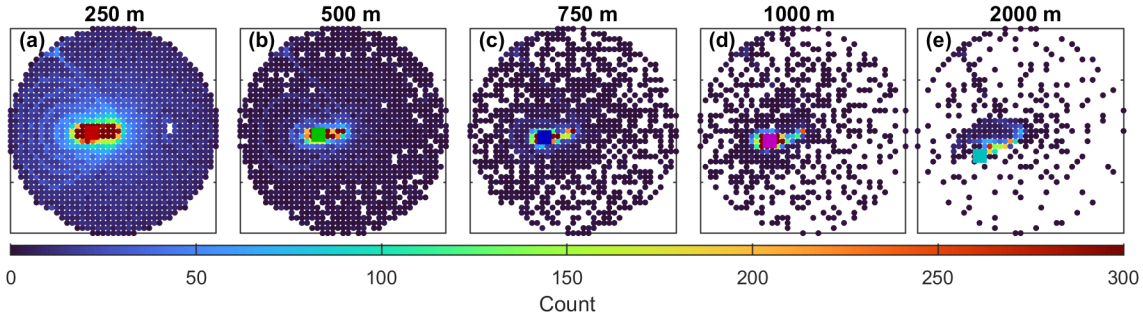

FIGURE 3.21: Same as Figure 3.19 but for $\kappa = -0.8$.

3.6 Conclusion

In the result of experimental demonstration of a fundamental FWM, we show that the recurrences and orbit dynamics can be retrieved with the results close to ideal theoretical modes. The trajectories are recurrent, and typical features of the phase-space plane such as two types of dynamics, separatrix and existence of a stationary wave are reproduces. The dependence of orbits shapes on the gain value is reproduced and consistent with theory.

Propagation of asymmetric initial conditions in the experimental setup reveals differences between different models. Unlike the ideal FWM where the asymmetry is conserved, and the full NLSE propagation where the asymmetry is recursive, the experiment shows different behavior : the difference in amplitudes is reduced with propagation until it reaches zero, and then the asymmetry is not growing. This behavior can be explained by a mixture of different propagation types, where light evolves according to the NLSE in the fiber segment, and then the residual harmonics are brutally cut and no longer participate in the process. In a sense, it can be compared to effects of damping or forcing where the asymmetry is not conserved.

Finally, we discuss a Hamiltonian conservation which is a fundamental property in the FWM. We numerically demonstrate that, in the segmented approach, the trajectories converge to states close to the fixed points of the ideal FWM. The exact positions depend on the fiber segment length and the input power. This behavior demonstrates additional effects of energy dissipation in the developed approach that should be interpreted as cutting out some parts of the signal that participated in dynamics without any compensation.

Chapter 4

Advanced numerical tools

Recent years have seen the rapid growth and development of machine learning : a set of statistical techniques and numerical algorithms for performing tasks without explicitly programmed instructions. It has found the use in computer vision, speech recognition, natural language processing, robot control, and other applications [118]. In science the interest of machine learning lies in analyzing the data to mimic the behavior of complex systems, however the machine learning extracts the knowledge out of data, and the resulting models can be opaque for understanding or missing prediction of new phenomena [119].

The use of machine learning application to the field of the ultrafast optics is quite new, and it has emerged less than a decade ago [120,121]. It can be used to predict the ultrafast dynamics [122,123] or light evolution in the NLSE [124], to optimize the lasers or control coherent structures parameters [120], and in many other fields including both fundamental and technical applications [120, 125]. In the context of a modulationally-unstable process in fiber, a neural network was used to correlate spectrum with time-domain intensity peaks resulting from propagation of a noise-like pulse laser [126] or a CW impaired by a random noise [127]. Overall the machine learning copes well with complex systems controlled or impacted by many parameters.

The previous chapter has demonstrated that there are limitations on the ideal FWM demonstration, and that the segmented approach can be placed in between the full NLSE propagation and the FWM. Derivation of an analytical model that would describe the idealized FWM is challenging, however the artificial intelligence methods can be applied to either distinguish the nonlinear dynamics itself from the experimental errors or to formulate the model that drives the experimental system. This chapter is dedicated to implementation of artificial intelligence methods to experimental data obtained from the idealized FWM demonstration.

4.1 Neural network : black-box dynamics

Machine learning includes different types of algorithms, one of which is neural network (NN). It is a powerful tool that can perform characterization, dynamics reconstruction, prediction or analysis. It relies on training the nonlinear structure underlying the NN against a big dataset. Depending on the problem, different NN configuration and strategies of training can be used. Here we focus on application of the NN tools in reconstruction of the experimental dynamics described in the previous chapter. The next section will provide the basics of the NNs operation.

4.1.1. Fundamentals of neural networks

A concept of an artificial NN was first proposed by McCulloch and Pitts [128] and then reinvented and popularized by Hopfield [129] in 1982 along with invention of the back-propagation algorithm. The main idea behind the artificial NNs is to mimic a brain function by creating artificial neurons that are linked to each other. In biology, a neuron is a special cell that processes information (Figure 4.1 (a)). It is composed of a body and two types of branches : the axon and the dendrites, which act as transmitters and receivers, respectively, of impulses [130]. At the terminals of these branches are the synapses, whose role is to release certain chemicals when an impulse is passing through. The amount of these chemicals determines the neuron's ability to emit electrical signals and depends on the synapses' types. The neurons are interconnected forming a complex and dense network. When a brain participates in an activity, the effectiveness of the synapses is adjusted during the learning process, as the signals are passing through the network.

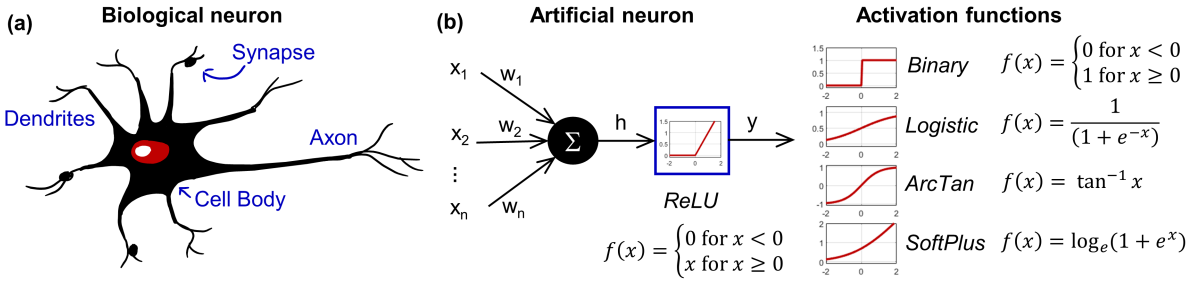

FIGURE 4.1: A sketch of (a) a biological neuron and (b) its artificial interpretation.

The artificial neuron, inspired by a biological one, can be represented as a function:

$$y = f(x) = f\left(\sum_{i=1}^{n} w_i x_i + h\right), \tag{4.1}$$

where w_i are the weights representing the synapse functionality, h is the bias, and $f(x)$ is a nonlinear activation function. The weights and the biases of each neuron composing the NN are free parameters to be chosen to approximate the relationships between the input $X = [x_1 ... x_n]$ and the output y in a dataset to be fitted. The gathered inputs from all the connected neurons then pass through a nonlinear function, that is known as the activation function. It allows to adjust the response of the neuron depending on the input and to switch it on or off.

The individual neurons are then composed to a structure with a certain connection pattern - the architecture. All NN can be divided into two main groups : feed-forward networks, where graphs have no recirculating loops, and recurrent networks in which neurons have feedback connections [130] (panels (a1) and (a2), respectively, in Figure 4.2). The NN architecture and size are quite flexible and shall be adjusted to the problem to be solved. For example, if one needs to simulate an input to output mapping of a single pass (for instance, a pulse propagation through a nonlinear system), a multi-layered feed-forward NN is the best candidate. If the output is expected to depend on both current and past data, the recurrent network are more suitable solutions [120].

The most common family of the NNs is a multi-layered feed-forward NNs, where the neurons are grouped into layers with unidirectional connections between them (Figure 4.2 (b)) [131]. The intermediate layers are called hidden layers, since the information between the inputs and the outputs is buried inside the NN. The total number of layers describe the NN's depth and, hence, there is an interest in the deep learning - construction of many-layer NNs which outperform simple shallow structures.

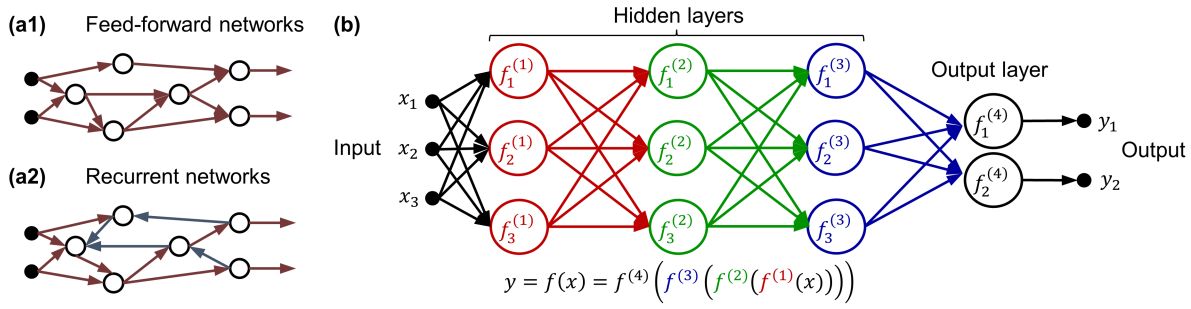

FIGURE 4.2: Sketches of (a1) a feed-forward and (a2) a recurrent NN. (b) A scheme of a multi-layer feed-forward NN.

Consider a feed-forward NN composed of three hidden layers as displayed in Figure 4.2 (b). Here to each neuron composing the layers is associated an activation function $f_i^{(j)}$ where i is a neuron's index and j is a layer number. An activation function can be any continuous but nonlinear function defined on a compact subset, for instance, bounded functions such as hyperbolic tangent or sigmoid, or rectifier-based functions (ReLU-family functions), or even trainable (adjustable or parameterized) functions [132]. Figure 4.1 (b) displays some frequently used activation functions. In a nutshell, a NN can be understood as the cascade of stages, each consisting of nonlinear operations, followed by a linear mixing. In case of recurring NN, the direct time feedback creates a nonlinearity in its own, so that each linear activation function may be used.

Taking into account the connections between the neurons in the NN displayed in Figure 4.2 (b) and neurons' structure, the output can be written as [133]:

$$Y = f(X) = f^{(4)}\left(H^{(4)} + W^{(4)} f^{(3)}\left(H^{(3)} + W^{(3)} f^{(2)}\left(H^{(2)} + W^{(2)} f^{(1)}\left(H^{(1)} + W^{(1)} X\right)\right)\right)\right), \quad (4.2)$$

where $H^{(j)} = [h_1^{(j)} ... h_n^{(j)}]$, $W^{(j)} = [w_1^{(j)} ... w_n^{(j)}]$ are biases and weights assigned to each neuron in a hidden layer j.

Now, as an architecture of the NN is defined, one has to train it by adjusting the weights and the biases to produce the desired output. The learning methods can be split into several categories. A supervised learning assumes a direct comparison between the NN's output and the desired data, where during the training the NN tries to predict the output by minimizing an error between the two. An unsupervised learning uses only the inputs to extract hidden patterns or common characteristics, which is suitable for big data analysis or clustering. Finally, a reinforcement learning is used to explore available parameter space to tailor the behavior of the system relying only of an evaluative feedback, referred to as the reward [125].

In ultrafast photonics, and in science, in general, the feed-forward NN has found strong applications since they are able to reconstruct or predict the nonlinear dynamics. However, to open a full potential of the NNs one requires quite often a large set of data, which can be problematic and/or time consuming in case of experimental or numerical data generation. If one knows approximately or assumes some properties of the system, it is possible to include physical constraints to the model for better accuracy, improved generalization and faster training [134]. For instance, one can imply boundary conditions in predicting pulse propagation in the NLSE system [135, 136]. However, putting constrains means that one assumes physical properties, which may not be present in reality but forced during the training. Therefore, such methods can be applied only for well-known systems.

After the training is finished, in order to characterize the accuracy one may use a root-mean-square error (RMSE) in case of the supervised learning. However, a low value of errors does not always mean good pre-

diction ability : the NN can fit the training data "too well" and miss a general behavior of the system. In this case, one has to discuss an overfitting and an underfitting. Overfitting happens when the selected model is too complex for the problem, so that the NN reproduced not only the features of the dynamics but also random deviations including noise. It also happens when the dataset to train is too small, which can be often the case in experimental physics. It results in poor generalization - the model fails to predict the outputs for new inputs. In case of underfitting, the selected model is too simple to capture important features of the dynamics, which gives poor training results in general. To evaluate the NN's performance correctly, a generalization error is computed. Some amount of input data that do not participate in training are used to compute the generalization error once the training is finished. This gives an idea whether the NN did manage to capture the dynamics and filter out the noise.

Overall, a NN is a good tool to perform complex tasks of dynamics characterization and prediction. However, the network's type and architecture should be specialized to the task taking into account the amount and availability of input data, noise level and assumptions regarding the underlying model. Next chapter describes selection and training process of the idealized FWM system.

4.1.2. Phase-space dynamics reconstruction by a neural network

A NN may seem an easy tool allowing to perform almost any kind of task. However, if one wants to achieve a fine result, an adaptation of a NN to the specified task is required. We want to train a NN on the experimental data in order to estimate and reduce the experimental errors, to reconstruct a full phase-space on area not available (or too impaired by noise) experimentally and to have an available on-demand tool to get the experimental results for extra tests. Even though a model that governs ideal FWM is known, we would like to avoid implementation of strict constrains with physics-informed NNs keeping in mind that there still exist fundamental differences between the experimental approach and the FWM. Instead we would like to use a feed-forward NN as it is well-suited for one-direction propagation of a nonlinear system.

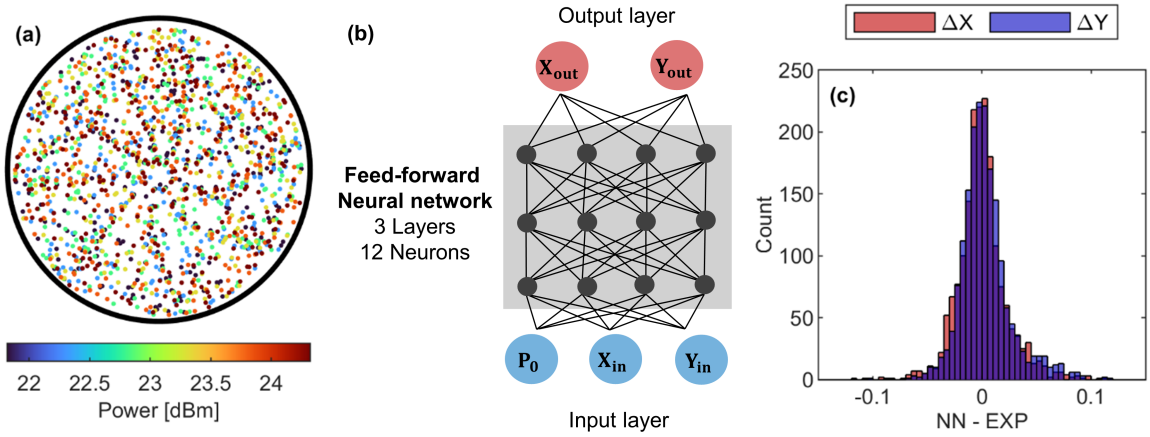

FIGURE 4.3: (a) Training data (outputs) : randomly sampled 300 points at discrete powers $P_0 = [21.2 : 0.5 : 23.7]$ dBm - 1800 points in total. (b) Architecture of used feed-forward NN. (c) Errors distribution comparing the NN with experimental data $\Delta X = X_{out}^{NN} - X_{out}^{EXP}$ (ΔY, respectively).

The main limitation in a wide use of NN is the amount of data required for good training. Since we want to use a NN as a universal interpolator over the whole phase-space, we have decided to train it on non-connected

segments randomly sampled over the $(\eta\cos\phi;\eta\sin\phi)$ plane instead of using the closed loop approached deployed in the previous Chapter. Since the trajectories' overall dynamics and shape depend strongly on the relative amplitude and phase (hence, on a position of the phase-space plane), the points should cover evenly the whole space. Also, due to the fixed segment length, a relative change in parameters would result in longer or shorter segments depending on a position on the phase-place plane (for instance, compare the outer and the inner segments in Figure 2.13 (b)). We have tested an approach with predefined values of η, ϕ sampled evenly over the space as well as randomly selected η, ϕ and X, Y coordinates. The optimal sampling strategy, covering the phase-space plane evenly, was to use a normal distribution of η with a peak value around 0.95 (in order to balance out the dense middle and the sparse outer parts of the space), and a uniform distribution of ϕ.

In this case, after the training we can reconstruct any orbit by iterating the outputs of the NN after each segments, hence mimicking the experiment. For the training data, we have measured 6 sets of 300 random points each for the input average power $P_0 = [21.2 : 0.5 : 23.7]$ dBm, so 1800 points in total. The points at each selected power were measured over a single non-interrupted run, hence, their number was limited to the stability of the calibrated phase, which was discussed in more details in Section 2.4.2., and is equal to about an hour. With time of each measurement taken into account, we can record up to 300 points without the need to recalibrate the phase offset. Figure 4.3 (a) displays the input points covering the whole phase-space plane.

The choice of the NN architecture remains largely empirical even if some guidelines can be found in the literature [137]. Since the dataset we have is quite limited, to avoid the overfitting, we select a rather simple structure of the NN : three layers with 4 neurons each (Figure 4.3 (b)). As inputs we use the coordinates $(X_{in}, Y_{in}) = (\eta_{in}\cos\phi_{in}, \eta_{in}\sin\phi_{in})$ and the average power in dBm. The NN is trained to predict the propagation results $(X_{out}, Y_{out}) = (\eta_{out}\cos\phi_{out}, \eta_{out}\sin\phi_{out})$ over a single segment for the given power. From the recorded data it is impossible to determine the nature of the trajectories for longer propagation distances or to draw conclusions on the existence of closed orbits. Therefore, ideally the NN shall be able to draw the nonlinear dynamics behind the disconnected segments.

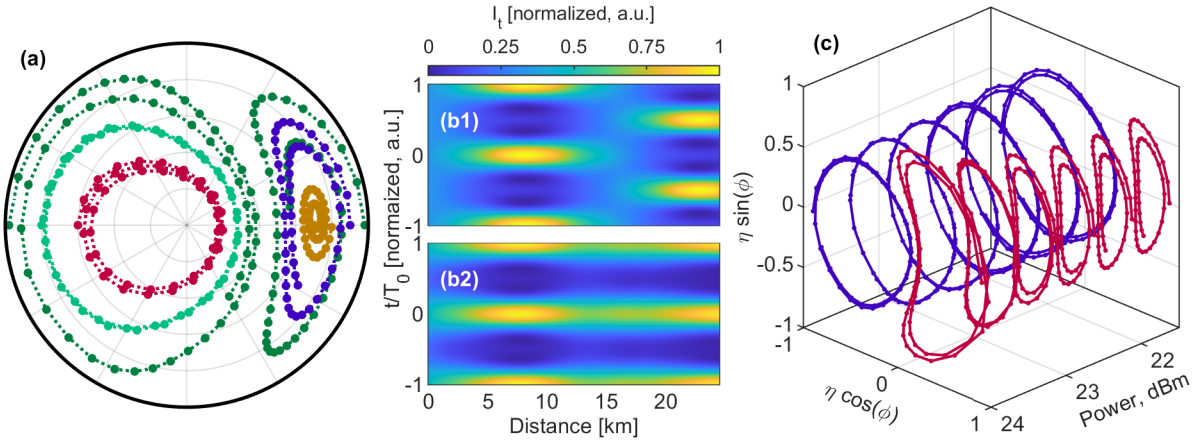

FIGURE 4.4: (a) Phase-space portrait reconstructed by the NN trained on the experimental data for $\eta_0 = 0.98, \phi_0 = 0, \pi$ (dark green), $\eta_0 = 0.80, \phi_0 = \pi$ (light green), $\eta_0 = 0.60, \phi_0 = \pi$ (red), $\eta_0 = 0.90, \phi_0 = 0$ (blue), $\eta_0 = 0.70, \phi_0 = 0$ (orange) over 50 iterations (25 km). Reconstructed temporal profiles for $\eta_0 = 0$ and (b1) $\phi_0 = \pi$ and (b2) $\phi_0 = 0$. (c) Trajectories with $\eta_0 = 0.90$ and $\phi_0 = 0, \pi$ (red and blue lines, respectively) generated at different power levels over 50 iterations (25 km).

The training relies on the Matlab Deep Learning toolbox (version 14.4) where we have used the Levenberg-Marquardt regularization back-propagation algorithm [138]. Note that, a conversion to other languages can be straightforward. Using 70% of our experimental data for training, the network converged in a few hundreds of epochs achieving a mean-square error (MSE) of $2.5 \cdot 10^{-4}$. This value of error ensures that the NN can reproduce the results without any overfitting. We also benchmark our NN by comparing its predictions with the results of direct numerical simulations of ideal FWM over a single fiber segment. In this case, an MSE of $2 \cdot 10^{-4}$ is achieved for a sampling of 10 000 randomly generated inputs. This level of error remains reasonable but suggests that residual deviations exist between the experiments and the ideal model.

A graphical way to confirm the NN accuracy is to reconstruct the complete trajectory in the phase-portrait plane. This can be easily achieved by concatenating the results obtained: the prediction of the NN obtained after 500 m propagation is used as input for the next step. The results are presented in Figure 4.4 (a) for different values of η_0, ϕ_0 at a maximum gain power 21.7 dBm where the NN predicts propagation over 50 iterations (25 km) [23]. These results yield immediate insight into the phase-space topology. The orbits are in qualitative agreement with the predictions from the ideal system, assessing both the robustness of the NN and the quality of the experimental data. The fundamental features of the ideal FWM dynamics are retrieved from these results. The trajectories are nearly closed orbits and do not intersect. The spiraling effect can be attributed to a mix between the finite size of the NN we choose, the measurement errors and deviations from the ideal framework. The NN captures correctly the phase features typical for left and right sides of the separatrix, namely, the decreasing phase translated to period-shifted recurrence (Figure 4.4 (b1)) and the bounded phase with the respective normal recurrence pattern in the temporal domain (Figure 4.4 (b2)).

As the NN is trained with data including various input average powers, it can also be used to explore unstable dynamics for other values of gain. Phase-space portraits predicted by the NN for a fixed initial value of $\eta_0 = 0.90$ and phase offsets $\phi_0 = 0, \pi$ for average values between 21.5 and 24 dBm are depicted in Figure 4.4 (c). Once again, the NN-based trajectories are in agreement with the theoretical predictions. We note how the dynamics at higher gain are associated with the change of the shape of the trajectories and the displacement of the separatrix. With increasing powers the separatrix progressively shifts: the intersection point between the separatrix and the horizontal axis continuously decreases. Consequently, the phase-space available for the evolution of initial conditions $\phi_0 = 0$ becomes larger, whereas orbits at $\phi_0 = \pi$ evolve in more restricted areas.

Here we demonstrated that a NN can be used to predict nonlinear dynamics of the FWM **relying on the experimental measurements**. One of the strongest limitations in the NN's training is the data availability and the level of experimental inaccuracies. To counterbalance these detrimental factors we then apply a different strategy described further.

4.1.3. Application of dithering technique

As it was discussed before, the main limitation we have faced in training of the NN is lack of experimental data. It is true that in general NN requires big datasets and complex architecture to produce a reliable result. In our case, training of a many-layers NN would quickly face an overfitting. In computer science it is quite a common problem, which is solved by a regularization - set of techniques that target to improve a generalization [139]. One of these methods is dithering which consists in adding an artificial noise over the training data. In this case the added noise acts as smoothing for the data masking their intrinsic noise, hence preventing the possibility for overfitting. This technique is widely used in image and sound processing to randomize a quantization error, including applications in image and speech recognition [140, 141]. In [141] the authors reuse same images with

different random noise, which allows to generalize the training and make the NN performance more robust.

Use of dithering in the case of experimental FWM can be completely justified : imagine a perfect FWM orbit that is approximated by segments. In previous chapters it was shown that even small deviations from the ideal FWM would result in strong accumulated effects and drift from the model (Chapter 3.5). In case of experimental demonstration the system is impaired, on top of that, by experimental inaccuracies and noise. Then by adding a bigger noise on both input and output we could smooth each segment, as depicted in sketch in Figure 4.5 (a), that would allow better reconstruction of the recurrence dynamics (red line).

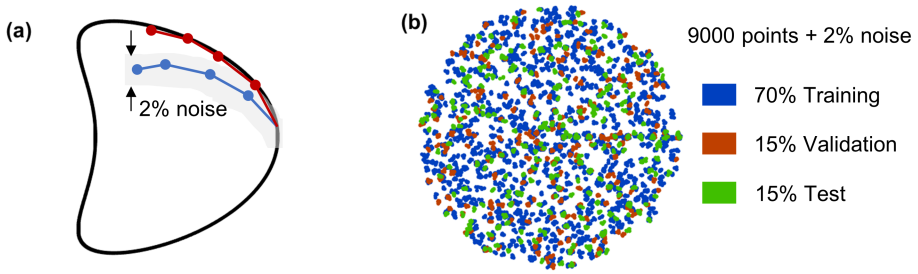

FIGURE 4.5: (a) A sketch depicting the segmented system impaired by noise (blue) which able to reproduce the FWM dynamics (red and black lines) is the noise constraint (gray) is relaxed. (b) Dataset splitting.

To apply the dithering, we have used the following strategy: the initial dataset was repeated 5 times with random 2% added noise to both input and output. Usually the data for training and validation are selected by the toolbox automatically, however in our implementation it may cause poor generalization : let consider, that the same point with just different level of noise was selected for both training and validation, in this case, since it's the same initial data, the NN may target a very precise fitting, causing poor generalization of the nonlinear dynamics. To avoid that, we split the initial dataset to three parts : 70 $\%$ training, 15 $\%$ validation and 15 $\%$ test data, and then we multiply and add noise to these sets. An example of such a set is depicted in Figure 4.5 (b).

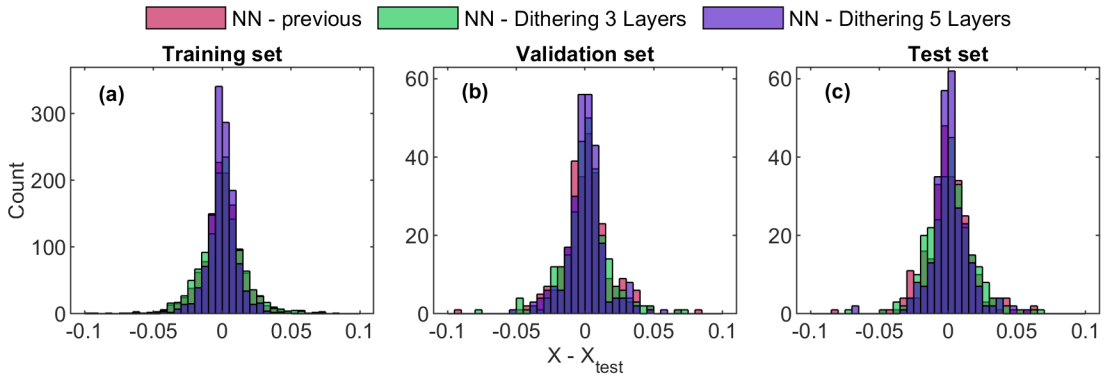

FIGURE 4.6: Statistics of errors when comparing results of NNs to the (a) training, (b) validation and (c) test data. Three different networks are tested : previously trained with no dithering (red), NN with added noise of 2% and 3 layers $[4, 4, 4]$-neurons (green), and 5 layers $[4, 10, 10, 10, 4]$-neurons (blue).

Firstly, the structure of the NN was kept the same as in the previous example : 3 layers with 4 neurons on each level. The training gives good results and provides some slight improvement, however, does not greatly

	σ			Skewness			Extreme events		
	Train	Valid	Test	Train	Valid	Test	Train	Valid	Test
NN-previous	0.016	0.018	0.018	0.023	0.016	0.102	0.018	0.011	0.022
NN-Dith-3	0.017	0.018	0.018	-0.205	-0.096	0.142	0.017	0.015	0.019
NN-Dith-5	0.010	0.014	0.014	-0.025	0.129	-0.197	0.028	0.022	0.019

TABLE 4.1: Main statistical characteristics of distributions presented in Figure 4.6

surpass the previous case. To give a figure of merit, we compare the NN's predictions with the experimental results plotting error distributions for x-coordinate (the y-coordinate comparison gives similar results). The red and the green distributions in Figure 4.6 denote, respectively, the previous NN and the NN with same architecture but with dithering applied. The main characteristics of these distributions : the standard deviation σ, the skewness $\frac{1}{n}\sum_{i=1}^{n}(X-\bar{X})^3/(\frac{1}{n-1}\sum_{i=1}^{n}(X-\bar{X})^2)^{3/2}$, and the probability of extreme events, denoted as the proportion of high errors occurring outside the main Gaussian peak defined as $3\cdot\sigma$ [142], are displayed in Table 4.1. Both previous and the three-layered NN with dithering give about the same σ and probability of extreme events. However, the skewness of the latter is more pronounced and not systematic depending on the used datasets.

Since we have increased (artificially) the initial dataset, now other more complex architectures of NN can be tested. So secondly, we test the NN composed of 5 layers with $[4, 10, 10, 10, 4]$ neurons on each, respectively (note that, this example was not optimized but rather selected arbitrary). Note that the training of such NNs simply fails when no dithering is applied. In this case we observe improvement of the result without overfitting : the error distribution for both training and test sets are less spread than in previous cases which shrinks the σ by 30 $\%$ in average. The output, however, becomes more skewed as in the previous case, and the probability of extreme events increases too. Note that here we compare the NN results with experimental data, which are, by default, impaired by noise and deviate from the ideal model. So the increased skewness and events outside of a Gaussian, may not indicate poor NN estimation but to give a hint regarding experimental errors and offsets or to provide a better generalization of a nonlinear model behind. The dynamics reconstructed by the NNs with dithering captures correctly the FWM features as well as deviations from the ideal model depending on the input power. The dynamics on the right side of the separatrix is reproduced less accurately, while the left side fits almost perfectly, which would explain a trade-off between small σ and failing of other characteristics.

We demonstrate that the dithering technique can be applied to the NN training. Using repeated datasets with different levels on noise it is possible to train a more complex NN without an overfitting. This study can be used to boost the performance of NNs based on limited set of training data.

4.2 Data-driven approach : sparse identification of nonlinear dynamics (SINDy)

The downside of the NNs' use is the fact that it works as a black box : the nonlinear dynamics is not reconstructed in a readable way, proposing instead a complex landscape of connected neurons. This limits an understanding and interpretation of the obtained results. And since the network is trained to reproduce well the desired data, it cannot be used to demonstrate a new phenomena. Therefore we consider other machine learning methods that would help to open a discussion what is a model behind the experimental demonstration of the

idealized FWM.

One particular approach of data-driven methods targets to determine the smallest number of terms from a large library of potential candidate functions that can accurately describe a system by a set of coupled differential equations [143, 144]. The method, introduced and popularized by S.L. Brunton and J.N. Kutz [145] who has implemented it on several nonlinear systems, is based on an observation that even highly-complex systems are often governed by interaction of smaller physical processes. This allows to use a sparse regression to determine a model that consists of the smallest number of terms without an overfitting. This technique is referred to as sparse identification of nonlinear dynamics (SINDy). Its successful application in chaotic system, in hydrodynamics and plasma physics [145–147], as well as in soliton dynamics reconstruction in the context of supercontinuum generation and higher order NLSE [148], opens up possibilities to use this technique in other complex nonlinear systems. In Besançon, Andrei Ermolaev has focused using SINDy starting from a set of ideal FWM trajectories generated by numerical simulations, potentially impaired by noise [24].

Our starting point is different : in this study we target to discover differential equations governing **the experimental system**. We assume that the dynamics would have the terms of the ideal FWM system and extra components that would describe deviations from the ideal model.

4.2.1. Fundamentals of SINDy

First, we give the basics of SINDy technique [145]. Consider a general dynamical system :

$$\frac{d}{dt}\boldsymbol{x}(t) = \boldsymbol{f}(\boldsymbol{x}(t)), \tag{4.3}$$

where $\boldsymbol{x}(t) = [x_1(t), x_2(t), ...x_n(t)]$ denotes a state of a system at time t, and the function $\boldsymbol{f}(\boldsymbol{x}(t))$ represents the dynamic constraints that define equations of the system. The key idea here, is that the $\boldsymbol{f}$ consists of only a few terms, which makes it sparse in the space of all possible functions. A progress in sparse regression now makes it possible to find the nonzero terms without the need of a brute-force search.

To find the function $\boldsymbol{f}$ from data, we gather the temporal evolution of $\boldsymbol{x}(t)$ and its derivative $\frac{d}{dt}\boldsymbol{x}(t)$ (or we approximate it numerically from $\boldsymbol{x}(t)$). The data sampled at different times $t_1, t_2, \cdots, t_m$ are arranged into matrices :

$$\boldsymbol{X} = \begin{bmatrix} \boldsymbol{x}(t_1) \\ \boldsymbol{x}(t_2) \\ \vdots \\ \boldsymbol{x}(t_m) \end{bmatrix} = \begin{bmatrix} x_1(t_1) & x_2(t_1) & \cdots & x_n(t_1) \\ x_1(t_2) & x_2(t_2) & \cdots & x_n(t_2) \\ \vdots & \vdots & \ddots & \vdots \\ x_1(t_m) & x_2(t_m) & \cdots & x_n(t_m) \end{bmatrix}, \tag{4.4}$$

$$\frac{d}{dt}\boldsymbol{X} = \begin{bmatrix} \frac{d}{dt}\boldsymbol{x}(t_1) \\ \frac{d}{dt}\boldsymbol{x}(t_2) \\ \vdots \\ \frac{d}{dt}\boldsymbol{x}(t_m) \end{bmatrix} = \begin{bmatrix} \frac{d}{dt}x_1(t_1) & \frac{d}{dt}x_2(t_1) & \cdots & \frac{d}{dt}x_n(t_1) \\ \frac{d}{dt}x_1(t_2) & \frac{d}{dt}x_2(t_2) & \cdots & \frac{d}{dt}x_n(t_2) \\ \vdots & \vdots & \ddots & \vdots \\ \frac{d}{dt}x_1(t_m) & \frac{d}{dt}x_2(t_m) & \cdots & \frac{d}{dt}x_n(t_m) \end{bmatrix}. \tag{4.5}$$

Then we construct a library of candidate functions $\boldsymbol{\Theta}(\boldsymbol{X})$ which may consist of constant, polynomials, and trigonometric terms:

$$\boldsymbol{\Theta}(\boldsymbol{X}) = \begin{bmatrix} | & | & | & & | & | & \\ 1 & \boldsymbol{X} & \boldsymbol{X}^{p2} & \cdots & \sin(\boldsymbol{X}) & \cos(\boldsymbol{X}) & \cdots \\ | & | & | & & | & | & \end{bmatrix}, \tag{4.6}$$

where $\boldsymbol{X}^{pi}$ denotes different polynomials of the i-order, for instance, for the 2-order it reads: $\boldsymbol{x}_1^2(t)$, $\boldsymbol{x}_1(t)\boldsymbol{x}_2(t)$, $\cdots$, $\boldsymbol{x}_2^2(t)$, $\cdots$, $\boldsymbol{x}_n^2(t)$. Each column of $\boldsymbol{\Theta}(\boldsymbol{X})$ represents a candidate function for the Eq. 4.3. Now one may find the sparse vector of coefficients $\boldsymbol{\Xi} = [\boldsymbol{\xi}_1, ...\boldsymbol{\xi}_n]$ that define which nonlinear functions are active:

$$\frac{d}{dt}\boldsymbol{X} = \boldsymbol{\Theta}(\boldsymbol{X})\boldsymbol{\Xi}. \tag{4.7}$$

Now each column of Eq. 4.7 requires an optimization to find the sparse vector of coefficients $\boldsymbol{\xi}_i$. The least absolute shrinkage and selection operator (LASSO) [149] is a regression adding an absolute value as a penalty (l_1-regression) that promotes sparsity. An alternative algorithm can be the least-angle regression (LARS) [150] that is also suitable for high-dimensional data.

Once the coefficients are found, the governing equations can be reconstructed as:

$$\frac{d}{dt}\boldsymbol{x}_i = \boldsymbol{f}_i(\boldsymbol{x}) = \boldsymbol{\Theta}(\boldsymbol{x})\boldsymbol{\xi}_i. \tag{4.8}$$

Note that now, knowing the differential equations, the reconstruction is made from an arbitrary input $\boldsymbol{x}$ (not

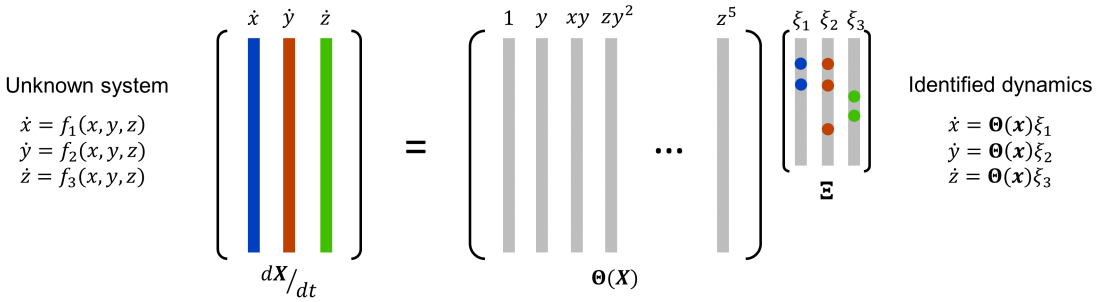

FIGURE 4.7: Schematic of the SINDy algorithm. The data and its derivatives are collected from the system composing the input $\frac{d}{dt}\boldsymbol{X}$, then the library of candidate functions $\boldsymbol{\Theta}(\boldsymbol{X})$ is generated. The sparse coefficients $\boldsymbol{\Xi}$ allow to identify the system's decomposition.

limited to the generated matrix $\boldsymbol{\Theta}(\boldsymbol{X})$). The idea of the algorithm is illustrated in Figure 4.7, where an arbitrary set of differential equations $\dot{x}, \dot{y}, \dot{z}$ can be reconstructed from $\boldsymbol{\Theta}(\boldsymbol{x})$ and $\boldsymbol{\xi}_{1:3}$.

A result of the SINDy method depends, of course, on the choice of data, its quality and, of course, on the selected functions basis. The approximated knowledge of physics behind the system (for instance, a presence of $\psi|\psi|^2$ terms in the NLSE or $\eta\cos(\phi)$ in the ideal FWM dynamics) may provide a reasonable choice of the candidate functions and the variables.

4.2.2. Methodology and reconstruction of ideal dynamics

The ultimate goal of the SINDy implementation is a reconstruction of differential equations that govern the experimental segmented dynamics. However, to test the method first, we apply it on the ideal FWM. Following guidelines in [145], we developed the home-made scripts in Matlab.

The FWM can be described by evolution of fields given by Eq. 1.43 or in terms of reduced coordinates η, ϕ (Eq. 1.59). The choice is arbitrary, however, in case of electric fields Ψ_i, it is useful to separate real and imaginary parts and then reconstruct a set of 6 differential equations [24]. For the current discussion we select to reconstruct the Eq. 1.59 with η, ϕ, assuming symmetric sidebands ($\rho = 0$).

For training we select evolution of η, ϕ with distance z over 50 km at different initial conditions : $\eta = [0.50 : 0.05 : 0.95]$ for $\phi = 0, \pi$ - 18 trajectories. Note that here we do not include a dependence of dynamics on the nonlinear mismatch parameter κ and target reconstruction of equations only at $\kappa = -2$. It is possible to include κ is form of a control parameter taking advantage from similarities of SINDy with a dynamical mode decomposition [151]. However, it would produce different sets of equations depending on value of κ, and since it is a constant in the Eq. 1.59, it may be difficult to extract it if the derivatives are normalized.

The derivatives $d\eta(z)/dz, d\phi(z)/dz$ are computed numerically from $\eta(z)$ and $\phi(z)$. Quite often, if the input data are noisy, it is difficult to estimate the derivatives numerically, since noise creates large differentiation error. If the data are impaired by noise, one may use smoothing functions, such as approximation by a high order polynomial with a shifting window [152]. Note that the input data are noiseless, so the derivatives can be computed directly.

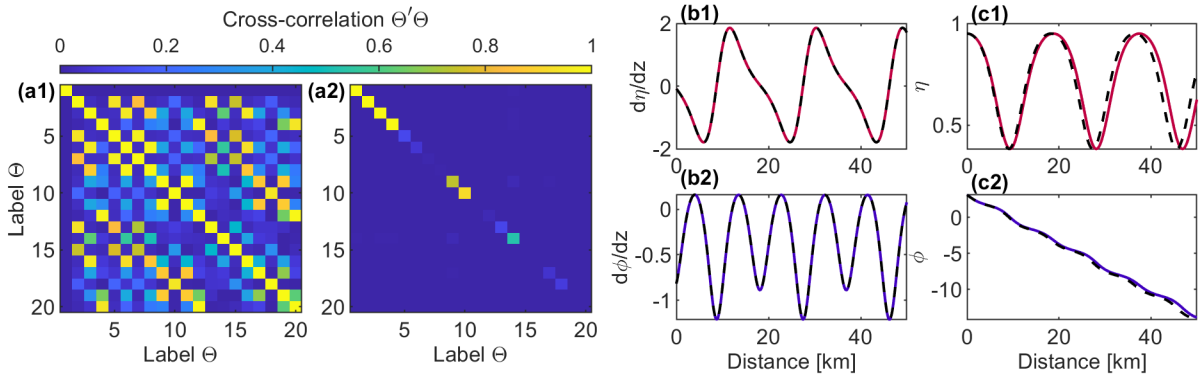

FIGURE 4.8: (a) Cross-correlation $\boldsymbol{\Theta}(\boldsymbol{X})'\boldsymbol{\Theta}(\boldsymbol{X})$ of initial candidate functions (panel 1) and only orthonormalized vectors (panel 2). (b) The derivatives $d\eta(z)/dz, d\phi(z)/dz$ (panels 1 and 2, respectively) computed directly from the ideal FWM (black dashed line) and from the SINDy model trained on it (blue and red solid lines). (c) Same but for integrated variables $\eta(z), \phi(z)$.

Another potential issue in the SINDy implementation, is that for the best fitting, the input variables should be normalized. In case if the inputs are given in real physical values, the optimization of sparse coefficients may fail because of numerical inaccuracies. For instance, consider an evolution of pulse width of an order of picosecond with distance, then the second-order polynomial would have an order of magnitude 10^{-24} that hits a numerical "zero", hence a coefficient in front of it would be poorly optimized. To avoid this issue we normalize both the input variables $\eta(z), \phi(z)$ and its derivatives, and the candidate nonlinear functions : $\bar{x} = (x - < x >)/\sigma(x)$ with x being a selected variable and σ - the standard deviation. This is extremely common in machine learning and the same processing is also implicitly realized during the training of the NN by Matlab toolboxes. In case of normalized variables, the differential equations will have different coefficients in front of the candidate functions, so during the dynamics reconstructions the variables must be translated back to the real units.

For the candidate nonlinear functions we select polynomial combinations of $\eta(z), \cos(\phi(z)), \sin(\phi(z))$ up to the 3$^{\text{rd}}$ order as presented in the first column of Table 4.2. Since the candidate functions contain a lot of trigonometrical functions, one may be expressed as a linear combination of others, hence, the sparse vector may contain equivalent candidate functions so the optimization is not efficient. To avoid this issue we check the cross-correlation matrix $\boldsymbol{\Theta}(\boldsymbol{X})'\boldsymbol{\Theta}(\boldsymbol{X})$ and keep the vectors that are non-orthogonal to each other. First, we compute the cross-correlation of initial library (all entries of column 1 in Table 4.2), that results in a colormap

Θ	Ξ			
	$d\eta(z)/dz$	ERR	$d\phi(z)/dz$	ERR
1				
$\sin(\phi)$	-2.80·10^{-5}	3		
$\cos(\phi)$			-1.229	10^{-4}
η			0.517	10^{-4}
$\eta\sin(\phi)$	-2.901	10^{-4}		
$\eta\cos(\phi)$			1.704	10^{-4}
$\eta^2\sin(\phi)$	2.085	10^{-4}		
$\eta^2\cos(\phi)$			1.67·10^{-5}	3
$\sin^2(\phi)$			2.85·10^{-6}	3
$\sin(\phi)\cos(\phi)$				
$\cos^2(\phi)$				
η^2	2.24·10^{-4}	0.415	6.78·10^{-6}	3
$\sin^3(\phi)$	-1.11·10^{-5}	3		
$\cos(\phi)\sin^2(\phi)$			4.31·10^{-6}	3
$\cos^2(\phi)\sin(\phi)$				
$\cos^3(\phi)$				
$\eta\sin^2(\phi)$				
$\eta\cos(\phi)\sin(\phi)$				
$\eta\cos^2(\phi)$				
η^3				

TABLE 4.2: Library of candidate functions and SINDy results for the ideal FWM. Here the colored cells in the Θ column represent the orthonormalized basis. Red cells denote the terms present in the ideal FWM model. The ERR is defined as a maximal increment that can be imprinted on the coefficient without increasing the MSE. Hence, the higher it is, the less reliable is the coefficient, and it can be omitted. Non-colored cells in the $d\eta(z)/dz$ and $d\phi(z)/dz$ columns are the filtered out coefficients based on errors estimation.

depicted in Figure 4.8 (a1), from here we see that many vectors can be expressed as linear combination of others. Then we use the Gram-Schmidt process to find a basis of candidate functions orthogonal to each other [153]. Starting from set of vectors $v_{1:N}$, we first set $u_1 = v_1$ and then for each $k = 1 : N$ we define $u_k = v_k - \sum_{j=1}^{k-1} \frac{<v_k,u_j>}{<u_j,u_j>} u_j$. The obtained $u_{1:N}/||u_{1:N}||$ is the required set of orthonormalized vectors. The result of cross-correlation of newly built vectors are presented in Figure 4.8 (a2). From here we keep only vectors whose norm is greater than 0.01. This procedure filters out 5 entries, so the resulting basis is marked by blue and red in Table 4.2. However, knowing that the system should include components of Eq. 1.59, we keep them in any case (red cells in Table 4.2).

The library functions list is now in a proper format, so then we use the LASSO algorithm (from the Statistics and Machine Learning Matlab Toolbox version 12.2) in order to find the sparse coefficients. Unlike the ridge regression, where the non-zero coefficients are penalized based on the l_2-norm, the LASSO penalizes the l_1-norm with regularization parameter λ_L that defines strength of the penalty. In the Matlab toolbox it is possible to combine both squared coefficients and absolute values penalty with α_L parameter: $\frac{1-\alpha_L}{2} l_2$ and

$\alpha_L l_1$, respectively. If $\alpha_L = 0$, the regression is done by ridge optimization, and if $\alpha_L = 1$ it's purely LASSO algorithm. For our implementation we select $\alpha_L = 0.10$, $\lambda_L = 0.10$, so the system has quite relaxed constraints in terms of zeroing the matrix.

The optimized coefficients for nonlinear terms for the ideal FWM system are presented in Table 4.2 (for the normalized variables, hence the exact values do not match). In the same table we present the error that is defined as a maximum amount of relative changes that can be imprinted on each coefficient without increasing the initial MSE. We increment each Ξ by $\nu = (1/2^{10} : 4)$ and stop when error exceeds the initial one. With this procedure we can sort out the coefficients that have no characteristic impact on the dynamics. For instance, if a parameter can be increased by a factor 3 without increase of the MSE, it means that we can remove this parameter from the equations. In the end, we can filter out small coefficients that were not zeroed by the regression algorithm. For example, the coefficient in front of $\sin^3(\phi)$ equals to $-1.11 \cdot 10^{-5}$ with an error of 3, which means that we can increase this coefficient by 3 times without any impact on the system. Hence, the coefficients with a 100% error and larger are not essential to the dynamics (non-colored cells in Table 4.2).

Overall, the SINDy is able to find back the ideal FWM equations that results in perfect fitting of $d\eta(z)/dz$, $d\phi(z)/dz$ example of which is presented in Figure 4.8 (b) and (c). Note that the $\eta(z), \phi(z)$ are reconstructed by numerical integration of the differential equations that results in small accumulated deviations in the end of the dynamics. The SINDy has found an extra term η^2 with a small coefficient and 40% relative error, so it can be excluded from the dynamics.

Here we have trained the SINDy on the ideal data without noise, but the system impaired by $2.5 - 7.5\%$ noise can be also reconstructed by the method as it was shown by Andrei Ermolaev with independently carried numerical simulations [24].

4.2.3. Reconstruction of experimental dynamics

Now we want to retrieve a nonlinear model from the experimental results with the SINDy method. For input dataset we select experimental orbits for the same inputs as for the ideal FWM : $\eta = [0.50 : 0.05 : 0.95]$ for $\phi = 0, \pi$ - 18 trajectories over 50 km. The data treatment and the procedure is kept the same as described in the previous section.

The resulting coefficients are presented in Table 4.3 (column L+R). The final model contains ideal FWM term (red cells) and extra functions (non-colored cells), here we have already filtered out the entries with high errors. The additional terms have smaller coefficients than the ideal FWM, which indicates that the experiment indeed follows the FWM dynamics with deviations that can be attributed to fundamental differences between the segmented, ideal and the full NLSE approaches.

The reconstructed curves are presented in Figure 4.9 where they are compared to the training data, and tested with arbitrary inputs on the phase-space map. The derivatives are well-fitted by the model, and the reconstruction of $\eta(z), \phi(z)$ fits well for the first period and then the numerical errors impact the reconstruction. The main difficulty here is that the derivatives are computed with $dz = 500$ m which is poor and not smooth approximation for the $d\eta(z)/dz, d\phi(z)/dz$, so the dynamics reconstruction can be impaired by it. Nevertheless, the equations reproduce well the experimental behavior : two distinct families of solutions with spiraling down orbits. All trajectories have the same speed of spiraling, so we observe how they spiral down with the consequent merging of the curves, which does not happen experimentally and numerically in the segmented approach. So the different rate of dissipation is, apparently, difficult to catch, or we need to include other terms in the library of candidate functions to reconstruct it correctly.

Θ	Ξ					
	L+R		L		R	
	$d\eta(z)/dz$	$d\phi(z)/dz$	$d\eta(z)/dz$	$d\phi(z)/dz$	$d\eta(z)/dz$	$d\phi(z)/dz$
1						
$\sin(\phi)$			0.032		-0.774	
$\cos(\phi)$	0.118	-1.156	0.020	-0.903		-0.091
η	-0.107	0.546	-0.100	0.952	-0.060	0.568
$\eta\sin(\phi)$	-2.798		-2.563		-2.399	
$\eta\cos(\phi)$		1.327	0.092	0		0.174
$\eta^2\sin(\phi)$	2.001		1.730		2.216	
$\eta^2\cos(\phi)$	-0.080	0.155		0.907		0.339
$\sin^2(\phi)$		-0.055				
$\sin(\phi)\cos(\phi)$			-0.020		0.062	
η^2	0.048		0.139			
$\sin^3(\phi)$			0.029			
$\cos(\phi)\sin^2(\phi)$						
$\eta\sin^2(\phi)$	0.038					
$\eta\cos(\phi)\sin(\phi)$			0.025			

TABLE 4.3: SINDy experimental results. Here L and R denote the cases where the system was trained only on the left-side (non-bounded phase) or the right-side (bounded phase) trajectories. The L+R denotes that both types of solutions were used for the training. The red-colored cells mark the terms present in the ideal FWM model. Note that the coefficients were already filtered based on the error.

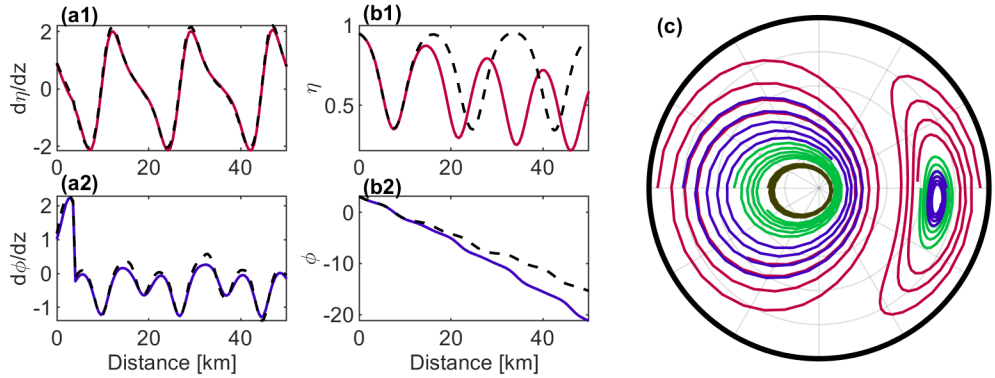

FIGURE 4.9: SINDy trained on the experimental data. (a) Derivatives $d\eta(z)/dz, d\phi(z)/dz$ computed from the experimental (black dashed line) and the SINDy model (red and blue solid lines) and (b) the integrated variables $\eta(z), \phi(z)$, respectively. (c) Phase-space maps reconstructed from SINDy for $\eta_0 = 0.95, \phi_0 = 0, \pi$ (red), $\eta_0 = 0.80, \phi_0 = \pi$ and $\eta_0 = 0.75, \phi_0 = 0$ (blue), $\eta_0 = 0.50, \phi_0 = \pi$ and $\eta_0 = 0.60, \phi_0 = 0$ (green), $\eta_0 = 0.30, \phi_0 = \pi$ (dark green).

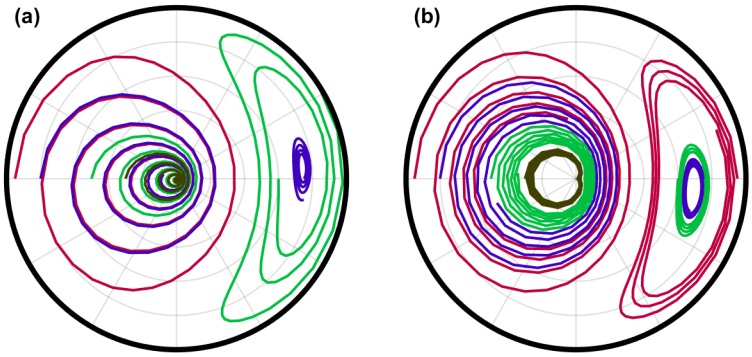

FIGURE 4.10: Phase-space map for initial values as in Figure 4.9 (c) reconstructed from SINDy trained only on the left part (a) and on the right part (b) of the experimental data.

Since SINDy does not require as large dataset as for the NNs training, we can try to extract the dynamics from the curves located just on the left or right side of the separatrix. For the training we use the same experimental data : $\eta = [0.50 : 0.05 : 0.95]$, $\phi = 0$ for the right (R), and $\eta = [0.50 : 0.05 : 0.95]$, $\phi = \pi$ for the left (L) side. The results of the SINDy reconstruction are presented in Table 4.3. Similarly to the previous training, the ideal FWM dynamics terms are included to both models, however, some terms are reduced, for instance in L and R the $\eta\cos(\phi)$ terms is almost excluded. The training on the left side includes more components with low amplitudes that may indicate poor reconstruction. While for the right side training, number of terms is more limited.

In terms of the phase-space reconstruction, both types of models are able to reconstruct the existence of two types of solutions and position of the separatrix even if the training was done on a single side. However, training on the left side is less successful : while features of the unbounded phase are reconstructed, the right side training fails and exhibits a qualitatively different dynamics, pronounced phase growth and consequent spiraling outwards (note that the solution at $\eta_0 = 0.95, \phi_0 = 0$). Training on the right side reproduces the complete dynamics better, even different rate of spiraling for the orbits is reconstructed. The only failure is reconstruction of the inner orbits on the left side : the shape is too rounded and η goes to negative values near

the $(0, 0)$ point. This may indicate that the dynamics on the right side encompasses the left one, while the left side dynamics is only a restricted subspace of the whole dynamics.

Overall, the SINDy approach shows promising results when applied to experimental data of an unknown system. The noise is not detrimental to the analysis. With correct data treatment and training procedures the dynamics can be extracted even from limited dataset. In the context of the segmented approach, it is interesting to see that the dynamics of a complete system can be retrieved just from one type of the solutions. The presented results prove that the underlying dynamics of the segmented approach indeed the ideal FWM which is impaired by small additional terms, which can be attributed to dissipation and deviations from the model.

4.3 Conclusion

We demonstrate two applications of the advanced numerical methods to the experimental FWM reconstruction. With training of a NN we are able to reproduce the experimental dynamics with its unique features. We also show that application of dithering techniques can reduce noise in the system and improve the training. So this method can be applied to NN trained on limited set of noisy data which is a general case for experimental datasets.

Application of SINDy method allows to retrieve a model behind the experimental data, which represent an interplay between the full NLSE dynamics and the ideal FWM. The final equation includes terms responsible for the FWM and extra components with low amplitudes that are responsible for extra effects such as spiraling and deviations from the model. This study confirms that the base of the experimental dynamics is the ideal FWM, and demonstrates that the method can be still applied to limited set of noisy experimental data.

Chapter 5

Control of trajectories

The dynamics of FWM follows unique orbits both in the segmented and in the ideal cases, where the interaction is restricted to three waves. These orbits do not intersect or flow one into another. Hence, naturally it is impossible to link two states unless they belong to the same orbit. We seek to remove this fundamental limitation by introducing a method to control the trajectories by modifying properties of the guiding media. In the Chapter 3 we have shown that the asymmetry parameter ρ (introduced in Section 3.4) can change the trajectory's appearance. However, the induced changes are not so significant, so within the present chapter we consider only symmetric conditions. In principle, the shape and the path of each orbit are strictly defined by $\kappa = sgn(\beta_2)\frac{|\beta_2|\omega_m^2}{\gamma P_0}$ (with $sgn(x) = x/|x|$) that includes fiber and wave parameters (β_2 - second-order dispersion coefficient, γ - nonlinear coefficient, ω_m - modulation frequency) and the input average power P_0. In principle, the trajectory shape can be changed with variation of one of these values. Therefore, we adapt the system's parameters to meet the required transition. We introduce a simple and general approach based on a discrete change in one of the system properties, namely the average power. Abruptly changing the propagation conditions allows us to switch from one orbit to another, and thus to connect any two points of the phase portrait.

5.1 Wave dynamics in varying conditions

Modifications of a nonlinear wave under varying conditions (periodic or not) has been a subject of many works, especially in a context of control of dynamics of coherent structures [154]. Propagation of a soliton in a medium with varying parameters has resulted in new phenomena. For instance, an observation of a cascade of phase-matched resonant radiations has been observed during soliton propagation in a fiber with longitudinally varying dispersion [155]. Also in fibers, in [156], the use of longitudinally tailored dispersion allowed to freeze the Akhmediev breather (AB) at a point of maximal compression. The experimental demonstration based on cut-back measurements has proven feasibility of the method, and the evolution in the dispersion varying fiber clearly differs from a uniform fiber case.

The nonuniformity of the medium has also been used as an advantage in development of autoresonant wave mixing schemes. In [157], the idea is based on resonant interaction between two pump waves and a weak signal propagating in a weakly nonuniform fiber which results in a complete pump depletion. After the stage of initial phase-locking, the signal enters a stage of autoresonant interaction, where variation of a propagation constant is balanced by the nonlinearity, and small oscillating modulations of power help to make the resonance stable.

A unique feature of this process is that the exact shape of the fiber's nonuniformity (tapering, in this case) is not important as long as it is sufficiently adiabatic. This leads to development of adiabatic frequency conversion schemes [158, 159] inspired by adiabatic control developed in quantum physics (the adiabatic processes are described in more details on the example of coupled waveguides in Appendix B.2).

Therefore, the variation or nonuniform changes in the system's parameters can be used as control tools to obtain a desired dynamics. However, some methods may require optimization or transition near certain conditions. As an example, in [160], a soliton conservation can be maintained when two different pieces of fibers are concatenated and their parameters meet optimal conditions.

In [161], the authors have shown that the AB solutions are robust by themselves, so they cannot be destroyed by perturbations of the shape, however, to transform them, the NLSE governing equation should be modified. The simplest modification of the NLSE is to include linear gain or losses, which makes an impact on the FWM dynamics.

Both in optics [85] and in hydrodynamics [14] it has been demonstrated that a weak linear damping alters the FPUT recurrence. Conversion from one type of dynamics is prevented by the Hamiltonian conservation, but in presence of losses, the recurrences can undergo changes from one type to another. And, eventually, the system can experience a loss-induced separatrix crossing when level of loss becomes significant. Indeed, in presence of losses, the average power experiences fluctuations which modify the shapes of the orbits and shift position of the separatrix, so it becomes "blurry". The trajectories are not closed orbits anymore, so the losses can break the FPUT recurrence cycles.

Overall, dissipation should not be considered as a detrimental effect that has to be systematically counteracted : if properly tailored, a longitudinal loss or gain profile may open additional possibilities as it leads to a continuous change of the κ, which can be seen as a control parameter. Nevertheless, more advanced optimization tools that go well beyond the scope of this present research are required to make out the optimum strategy on a case-by-case basis.

If one, however, wants to "freeze" or transform a coherent structure to stable periodic pulse trains, simple gain or losses are not enough for these transformations - they cause falling from the separatrix either to normal or phase-shifted recurrences. However, if higher order dissipation and the gain terms are included into the NLSE, transforming it into the Ginzburg-Landau equation, the AB converges into two distinct stationary solutions [161], hence it is possible to transform a breather into a stable solution. However, this transformation requires rather long propagation distance (it is, in fact, more a statistical property of the system), therefore, another methods to control the dynamics are required.

To control the system, one can combine the discussed strategies. In [76], the authors consider propagation of a water-wave over a bottom with a gradually varying depth. The selected model describes the dynamics as an interaction between three waves (similar to ideal FWM in the degenerate case). The depth variation is selected based on the theory of autoresonance [157], which results in linear variation of the bottom's depth. The dynamics is composed of the following transitions : first, system evolves linearly, then it crosses the separatrix and phase-locks in a close proximity of an equilibrium, which is a stable solution of the three-wave mixing. In the end, it allows to transform the initial state into a stationary wave.

Another strategy relies on abrupt perturbation of the system. In [162], the authors propagate the AB solution and then perturb the system by an abrupt change of the water depth, hence, changing the dispersion and the nonlinearity of the system. It results in modification of the phase-space portrait, so the AB orbit changes accordingly. Consequently, the trajectory falls into the center of the orbit to the stationary wave described by a dnoidal solution, therefore, the FPUT recurrence becomes blocked. This process reflects a controlled

transformation of a breather solution into a stable periodic train of pulses.

Similar strategy was applied to stabilize a breather [163] : the breathing state is frozen by destroying its recurrent characteristic when a suitable dispersive medium is applied. The medium change can be done by longitudinal adjustment of fiber characteristic, tapering or replacement of a fiber. Here the stabilization is proposed by cascading two pieces of fiber with different dispersion and nonlinearity which disrupts the recurrence at a selected point, therefore, freezing the AB envelope.

5.2 Trajectory control by an abrupt change

In our case, we target to control transitions between two different states that do not belong to the same orbit. Unlike in [14, 85], the losses and gain in our system cannot be evaluated thoroughly and used as a control method to reach the desired task. So we address to works [160, 162, 163] where an abrupt change in the system parameters allowed to convert the dynamics. We consider κ as a control parameter of our system, hence, by changing nonlinearity, dispersion or the input average power, we could reshape the phase-space plane and force the state to propagate in a different environment, that, eventually, changes the dynamics, similar to cases of the AB freezing in [162, 163].

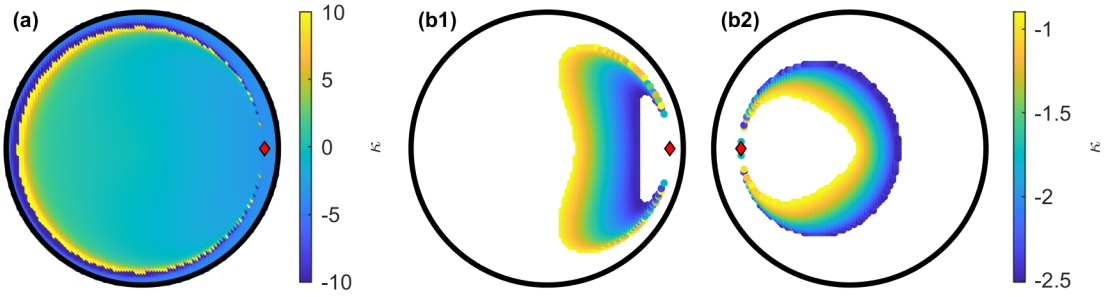

FIGURE 5.1: (a) Set of reachable points on the phase-space plane from $\eta_{in} = 0.90, \phi_{in} = 0$. Color defines value of κ required to reach a given point on the map. (b) Same as (a) but with limited $\kappa = [-2.50 : -0.90]$ for input points $\eta_{in} = 0.90, \phi_{in} = 0$ and $\eta_{in} = 0.80, \phi_{in} = \pi$ (panels 1 and 2, respectively).

The states through which the orbits go are determined by the value of κ and the input coordinates on the phase-space diagram. If there exists no limitation in possible values of κ, any two points on the phase-space plane can be connected. For instance, panel (a) in Figure 5.1 depicts states that belong to the same orbit as $\eta_{in} = 0.90, \phi_{in} = 0$ (red diamond) and the corresponding values of κ required to draw the orbit. The depicted points belong to the same trajectory, hence they share the same values of κ and H. It is therefore possible to derive a value of κ that would connect two arbitrary states η_1, ϕ_1 and η_2, ϕ_2. Assuming a conservation of the Hamiltonian (eq. 1.57) we obtain:

$$\begin{aligned}\kappa =& 2\left[1-(\eta_1+\eta_2)\right]\cos\left(\frac{\phi_1+\phi_2}{2}\right)\cos\left(\frac{\phi_2-\phi_1}{2}\right)+1-\frac{3}{2}(\eta_1+\eta_2)\\ &-2\sin\left(\frac{\phi_1+\phi_2}{2}\right)\sin\left(\frac{\phi_2-\phi_1}{2}\right)\frac{\eta_1+\eta_2-\eta_1^2-\eta_2^2}{\eta_2-\eta_1}\end{aligned} \tag{5.1}$$

Except for the case $\eta_1 = \eta_2$, where no solution exists except for the trivial case where $\phi_1 = \pm\phi_2$, we see that two arbitrary points can indeed be connected. If we replace η_2, ϕ_2 by sampled grid over the whole phase-space, we obtain a graph depicted in Figure 5.1 (a) giving a set of reachable points.

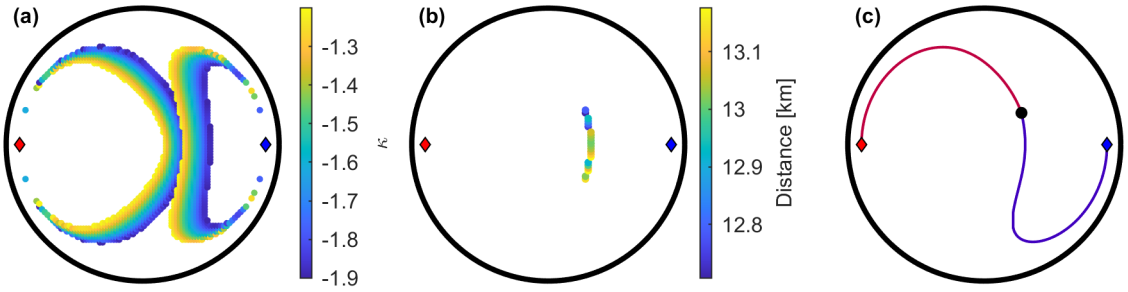

FIGURE 5.2: (a) Set of reachable phase-space map points for $\eta_{in} = 0.90, \phi_{in} = \pi$ (red diamond) and $\eta_{out} = 0.90, \phi_{out} = 0$ (blue diamond) with implemented experimental limits $\kappa = [-1.90 : -1.20]$. (b) Set of points that connect η_{in}, ϕ_{in} and η_{out}, ϕ_{out} with the respective propagation distance. (c) The optimal connection trajectory with $P_{in} = 22.07$ dBm and $P_{out} = 23.98$ dBm.

However, one has to take into account several strong restrictions regarding the accessible values of κ : the dispersion regime limits, for a given fiber, κ to positive or negative values, while the ratio β_2/γ is not fully flexible either, and moreover the total power P_0 has to be limited so as to remain in the framework of the ideal FWM. Therefore the approach based on Eq. 5.1 only cannot in practice be applied in a straightforward manner. Consequently, when $\kappa_{min} < \kappa < \kappa_{max}$, a different strategy has to be developed. For example, if we want to connect two points located on different sides of the separatrix : $\eta_{in} = 0.90, \phi_{in} = 0$ and $\eta_{in} = 0.80, \phi_{in} = \pi$, when the limits on κ are implemented (for instance, $\kappa = [-2.50 : -0.90]$), we cannot find a direct solution, since the values do not belong to the same orbit. Instead we obtain a set of reachable state for each point (Figure 5.1 (b) and (c)), hence we can imagine a transition from one state to another though an intermediate point. In order to switch from one κ to another we rely on a change of the average power P_0.

As the power can be selected on a continuous range, the number of possible switching points can be high. In order to find more systematically all the switching points (η_S, ϕ_S) that are available for $\kappa_{min} < \kappa < \kappa_{max}$, we scan the full space to obtain a set of reachable points for both input η_{in}, ϕ_{in} and output η_{out}, ϕ_{out}. And the we cross-check points on the phase-space map that are available to both sets, and they form possible switching points (η_{tmp}, ϕ_{tmp}). Figure 5.2 (a) shows these two sets of reachable points and the crossing between them. Here we use the experimental limits $\kappa = [-1.90 : -1.20]$ corresponding to power variation from 22 to 24 dBm for a fiber having the same parameters as the fiber in the previously detailed experiments.

Then the question is, how to select an optimal switching point out of (η_{tmp}, ϕ_{tmp}). Here, we define this optimal path as the solution leading to the shortest propagation distance, but other criteria can be chosen. To answer this, we performed numerical simulations of the system to evaluate the physical distance of propagation to link η_{in}, ϕ_{in} to η_{out}, ϕ_{out} with a single power change in between. The ensemble of switching points and the corresponding propagation distances are presented in Figure 5.2 (b). The optimal solution corresponds to $\eta_S = 0.36, \phi_S = 0.71$ with switching from $\kappa_{in} = -1.87$ ($P_{in} = 22.07$ dBm) to $\kappa_{out} = -1.20$ ($P_{out} = 23.98$ dBm) giving the shortest distance of 12.7 km. The resulting trajectory is plotted in Figure 5.2 (c) in red (when the power is P_{in}) and in blue (when the power is P_{out}). The location η_S, ϕ_S at which the power switching occurs is highlighted on the phase plane by a black dot.

Therefore, with this technique it is possible to control the trajectory dynamics by connecting two arbitrary states with a single abrupt change in the input average power.

5.3 Experimental control of dynamics

We implement the developed method to control the dynamics experimentally in the segmented approach extensively described before. The setup is identical to the one described in Chapter 2. Note that given the discreteness of the propagation distances under investigation (the distances being multiples of the 500 m length of the fiber segment), we cannot carry out the change in power at the exact distance predicted by the numerical analysis. We therefore monitor when η_{i+1}, ϕ_{i+1} approaches η_S, ϕ_S by checking the distance D_{i+1} (when plotted on the phase plane) between the state $i+1$ and the switching point. When we operate in the vicinity of the switching coordinates and when $D_{i+1} > D_i$, we update the state back to η_i, ϕ_i and carry out the power change. By doing so we take into account possible deviations from the theoretical model, and we approach the switching position at the nearest.

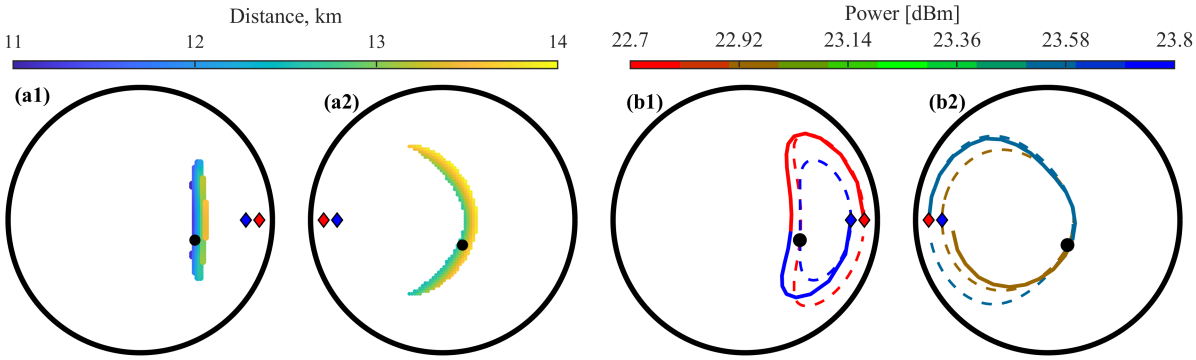

FIGURE 5.3: (a) Set of connection points and the corresponding propagation lengths for $\eta_{in} = 0.90, \phi_{in} = 0$ (red diamond) $\eta_{out} = 0.80, \phi_{out} = 0$ (blue diamond) and $\eta_{in} = 0.90, \phi_{in} = \pi$ (red diamond) and $\eta_{out} = 0.80, \phi_{out} = \pi$ (blue diamond) (panels 1 and 2, respectively), where the switching point is depicted in black dot. (b) Experimental transitions between the given points (solid lines) and the ideal FWM points (dashed lines). Color depicts the input average powers for each part of the trajectory.

Let us first discuss the case where the input and output states lie on the same side of the separatrix. We have considered here two examples summarized in Figure 5.3, with panels (1) and (2) corresponding to cases where the two states lie on the right and left sides of the separatrix, respectively. The input and output states have been chosen with the same phase ($\phi = 0$ or π), but similar results could be obtained with different values. The target is to connect $\eta_{in} = 0.90, \phi_{in} = 0$ with $\eta_{out} = 0.80, \phi_{out} = 0$ (case 1), and $\eta_{in} = 0.90, \phi_{in} = \pi$ with $\eta_{out} = 0.80, \phi_{out} = \pi$ (case 2). Panels (a) are obtained from numerical simulations and show the area where the power switch should be achieved when the average power available ranges between 22 and 24 dBm. Note that the higher the range of power available is, the broader this area is. The optimal combination is marked with a black circle and corresponds to a power change from $P_{in} = 22.7$ dBm to $P_{out} = 23.8$ dBm (case 1) and from $P_{in} = 23.5$ dBm to $P_{out} = 22.9$ dBm (case 2). Whereas in the case 1, one has to increase the power in order to reach a point in an inner orbit, this is the contrary in the second case. The corresponding switching propagation distance predicted by numerical simulations occurs at 6.5 km and 11.5 km, for cases 1 and 2, respectively [26].

The resulting trajectories mapped on the phase-space portraits are reported in panels (b) where color notes the corresponding total power. Given the granularity of the distances involved in the experiment as well as some sources of errors in the measurements of the wave parameters, some deviations would appear with respect to the

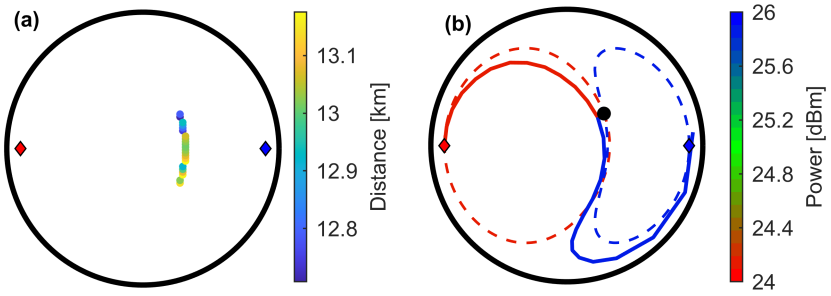

FIGURE 5.4: (a) Set of connection points and the corresponding propagation lengths for $\eta_{in} = 0.90, \phi_{in} = \pi$ (red diamond) and $\eta_{out} = 0.90, \phi_{out} = 0$ (blue diamond). (b) Experimental transition between the given points (solid lines) and the ideal FWM points (dashed lines). Color depicts the input average powers for each part of the trajectory.

ideal orbits. However, those discrepancies remain very slight so that, for these two cases, we can convincingly validate the numerical predictions and conclude on the efficient control of the trajectory.

In a second set of experiments, we investigate the connection between two states that are located on different sides of the separatrix, $\eta_{in} = 0.90, \phi_{in} = \pi$ and $\eta_{out} = 0.90, \phi_{out} = 0$. Following an analysis similar to the one reported in the previous section, we found numerically the optimum switching point. The experimental validation is summarized in Figure 5.4 and further validates our approach to this challenging target. Once again, a single change of average power by less than 2dB imprinted at a distance of 6.5 km was required to efficiently reach the output. The slight mismatch between the experimental output state and the target is mainly due to the finite length of 500 m of the fiber segment (as the power involved here is quite significant, the discreteness of the states that are accessed becomes more visible).

We have demonstrated here that the four-wave mixing interaction in optical fiber can be efficiently manipulated by using a control parameter such as the total power. A single local and abrupt change of the average power after a well-chosen propagation distance enables one to manipulate the trajectories and to jump from one orbit to another. This allows us to connect two states even if they lie on different sides of the separatrix. A simple and general methodology to select the suitable switching states has been presented, and experiments taking advantage of iterated programmed initial conditions confirm this approach. Three examples have been discussed, but we have also successfully tested many other combinations of input and output states.

Although we have focused our investigation here on the use of a single change of power in a focusing nonlinearity where the input and output average powers are the degree of freedom, this work can be further extended in many directions. First, one may choose to fix the input and output powers. In that case, if the input and output orbits do not cross, a third power level will have to be involved as an intermediate stage. Another strategy can be to generate an optimal power variation using path-finding algorithms on a 3D-plane that includes both state positions and power.

5.4 Conclusion

In this Chapter we considered a method to connect two arbitrary states that do not belong to the same trajectory. We abruptly change the control parameter κ by changing the input average power. This allows to reshape the orbits of the phase-space plane, so the dynamic continues to follow transformed path, hence, reaching the target point. The position of the power switch one the longitudinal coordinate is optimally chosen based on theoretical

predictions originating from the ideal FWM theory. Here the criteria of the optimal solution is the length of the total transition. Numerical predictions are confirmed with experimental demonstrations. We observe controlled crossing of the separatrix and transitions from one orbit to another on the same par of the phase-space plane. We believe that our study can help in understanding processes of phase matching and the consequent state transitions relevant for parametric or phase-sensitive amplification [31, 32].

Conclusions and Perspectives

Optical systems are well-known to be flexible testbeds to study diverse nonlinear phenomena. With a novel experimental technique relying on iterative propagation in a small segment of fiber we mitigate the effects of losses and growth of high-order sidebands, that enables us to demonstrate a fundamental FWM process experimentally. This study bridges a gap between the purely theoretical discussions and the experimental demonstrations of the cascaded FWM, that allows to fully examine fundamental properties of the idealized FWM.

In order to become closer experimentally to the ideal FWM, and avoid detrimental effects such as Raman and Brillouin scattering, generation of higher order sidebands, we constructed a new type of the setup. It is based on idea of the iterative propagation of three waves in a small segment of fiber : if the fiber is sufficiently short, higher order sidebands generation is kept to a minimum. Hence, when we measure the output properties of the wave, we can virtually reinject them in the fiber by tuning the input conditions accordingly. As such, we increase the virtual propagation length up to dozens of kilometers. In the end, we are limited by errors of the measurements and shaping that are gradually accumulated and does not allow to reach an infinite propagation length. The setup is built out of telecommunication components, which makes it easily reproducible and a good test platform.

In this thesis we demonstrate experimentally nonlinear dynamics of the FWM that results in periodic orbits on the phase-space plane manifesting the FPUT recurrence. We observe an existence of two types of solutions : with bounded and unbounded phases, that results in normal and period-shifted recurrence during the longitudinal propagation of the temporal intensity. The two families of solutions with different properties are divided by the separatrix whose position is accurately predicted by the experimental curves. We demonstrate an emergence of stationary wave solutions at different values of gain. Input conditions of the stationary waves - fixed point - depend on a value of normalized mismatch parameter κ, which we control by varying the input average power. This dependence is reproduced experimentally and follows well the theoretical predictions. Also with changing κ, we investigate how shape of orbits varies at different input power levels, and confirm growth and squeezing of trajectories depending on their position with respect to the separatrix. The discrepancies between the experimental demonstration and the ideal model can be assigned to generation of small residual sidebands and error accumulations that is manifested in a form of spiraling of the orbits. That said, considering the overall very good agreement between the model and our experimental investigations, it proves formally that the ideal FWM model is not a pure theoretical/mathematical model that describes the actual dynamics of the FWM process (as long as the cascading does not appear).

The study of asymmetrical spectrum propagation and the Hamiltonian conservation brings up a discussion about fundamental differences between the experimental approach and the ideal FWM. In the asymmetric spectrum propagation we observe a behavior that is different from both the full NLSE model and the ideal FWM : the asymmetry decreases with propagation distance until the spectrum becomes symmetric. This feature is

similar to systems with dissipation and forcing, however, in our case it is hard to assign it unambiguously since the segmented approach is a mixture between the NLSE propagation and the ideal FWM. The Hamiltonian, defined in the framework of the ideal FWM, is not exactly conserved in the experimental dynamics. The spiraling leads, over very large propagation distances, to attraction to the areas near the eigensolutions of the ideal FWM system. Exact attraction regions and points depend strongly on the segment length and the input power, that can be explained by increasing impact of the NLSE dynamics and generation of the higher-order sidebands during propagation in a segment of fiber. Finally, we interpret deviations from the ideal model as energy transformations inside of the system, which results from brutal cuts of small high-order harmonics generated in the NLSE propagation in a short segment of fiber after each iteration.

With the use of advanced numerical tools we are able to complete the analysis. The NN trained on the experimental data helps to reconstruct the FWM dynamics observed experimentally. Use of dithering technique helps to improve the training, which opens up a valuable discussion for the community on how to train a NN on limited and noisy dataset. The SINDy approach allows to retrieve a set of differential equations that govern the experimental dynamics. They include the terms of the ideal FWM system, and extra entries with smaller coefficients, which confirms that the experimental system follows the fundamental FWM dynamics with small deviations. The differential equations reproduce the spiraling orbits on both sides of the separatrix, however, the different speed of rotation is poorly fitted. Nevertheless, data-driven approaches show promising results in experimental analysis.

The revised methods of dynamics reconstruction in Chapter 4, represent general tools to analyze and reconstruct the nonlinear dynamics. The SINDy method can be a powerful tool to be applied in experimental systems where the model is not known in advance. We have tested this approach to reconstruct the movement of a soliton-molecule (SM) in a fiber-laser cavity recorded with the Dispersive Fourier Transform (DFT) technique [164]. In the results, we not only reconstruct an equation with just seven parameters, but also evaluate noise impact by constructing a Langevin's model where noise distribution is extracted from the experimental data. Therefore, we infer how the SM would respond to external perturbations, how stable the limit attractor is.

The observed FWM orbits are uniquely defined on the phase-space plane depending on the fiber and the signal characteristics (value of the second order dispersion, nonlinearity, input power and modulation frequency), therefore they do not intersect, so no transition between the states is possible. We have removed this fundamental restriction by using the input average power as a control parameter. Using an abrupt power change at an optimal point found theoretically, we are able to connect two arbitrary states on the phase-space map. Experimental results agree well with theoretical predictions even taking into account the accumulated inaccuracies. These results contribute to methods of control of nonlinear dynamics investigated recently.

The developed experimental technique can be adapted to many tasks. The setup is constructed out of readily available telecommunication components, that makes it a universal testbed which can be reproduced in any optical lab. The calibration of the setup and its accuracy allows detailed demonstration of the FWM process covering the whole phase-space plane. Here we've focused on the degenerate FWM case [11], however, the setup can be adapted to the non-degenerate FWM [13] operating with 4 spectral components. Here, only the phase calibration and measurement should be reworked : to avoid polarization dependent phase, we could use a single channel connected to the sampling oscilloscope, and change the filter position selecting each pair of frequencies. This would allow to compare all phases and deduce the ϕ phase mismatch correctly.

Another application of the developed setup can be a test of different fibers and their FWM dynamics. For instance, normal dispersion fibers [13, 165], fourth-order dispersion [166] or dispersion oscillating profiles weather structured [167, 168] or dispersion-managed [169].

Since we have a recurrence step that appears at a fixed periodicity, we can also test a system with random kicks [170] which could be induced or imprinted in the end of each propagation by a WaveShaper, noise or power fluctuations. This feature can also help the extend the study to chaotic systems. The NLSE which is subject to perturbations, can make a transition to chaotic regimes [171, 172]. Here, we can induce such perturbations experimentally, and, since the process is automatized, we can gather statistics on the wave behavior and conclude on the chaotic regimes.

In the context of dynamics control, we can imagine more complex profiles or strategies such as resonant interactions [157] or adiabatic transitions [76]. The parametric nonlinear FWM [173] can be experimentally investigated as well which help a discussion about frequency conversion schemes and phase-sensitive amplifiers [31, 32].

Another powerful method of data-driven dynamics reconstruction is Dynamic mode decomposition (DyMD) [174, 175]. The principle of the technique consists in decomposing the signal into a set of orthogonal modes and coefficients that reflect modes evolution in time. We have applied this technique to study behavior of SM in the fiber-laser cavity in a similar system described above which is detailed in the Appendix C [25]. This method has allowed to greatly compress and denoise the raw data, and demonstrated that the oscillatory pattern of the SMs results from the interplay of individual modes. The technique complements the general analysis of the SMs behavior in the cavity, and can be a universal tool for characterization of dynamics in other experiments. At the current stage of its development, this technique still appears less suitable for FWM than the NN or the SINDy approach.

The FWM can be regarded as the nonlinear diffraction of a signal and an idler by a temporal grating. We have seen in Chapter 5 that this process can be controlled to some extend by a change of the propagation conditions. Still it may not be possible to control directly the shape of the temporal grating. If we now consider the analogy that exist between the temporal propagation of light and its spatial propagation in an array of waveguides, we can imagine that modulating spatially the conditions of propagation in a multimode system could become a good analogy to the FWM process. In particular, nanophotonics would allow nowadays the possibility to tune exactly the conditions of propagation of light in a way that is not possible with fibers. Therefore, I have also worked during my PhD on the development of tools so that the experiments carried here in the temporal domain can be translated in the spatial one.

Considering the less degree of maturity of these new developments, and that they would require an expertise very different from the one involved in the study of the FWM, I decided not to submit these results to the evaluation of the jury, but still to present them in the Appendix.

In the Appendix A we discussed a way to improve the perturbative methods for computation of coupling and propagation constants in a system of coupled waveguides. Inclusion of the local field effect (LFE) and the effective background allows to retrieve and acceptable accuracy. The LFE results from a divergence of a Green function in a source region, and a concept of the effective background allows to take into account impact of the substrate's geometry and configuration of the system. We show that with rather simple implementation of these two effects we improve performance of perturbative methods.

The Appendix B is devoted to design of light transitions in a system of coupled waveguides. We show that the light transfer can be controlled with a non-adiabatic method which controls an interaction between the supermodes. We investigate, first, a case of perturbative modulation of the waveguides' parameters and show that when the propagation constant matching condition is fulfilled, the transition can be achieved. Then we obtain an expression to model an optimal shape - the variation of parameters that allows to couple the supermodes outside of the perturbative regime. The non-adiabatic theory is well adapted for coupling of asymmetric

waveguides in a controlled manner with low cross-talk, which opens up a new approach in design of densely packed photonic switches.

Once developed theoretically, we seek to test the non-adiabatic transition in practice. The SiN waveguides should provide a sufficient level of coupling, since the light is less confined in the core. In principle, the perturbations, implemented in our case as a change of the waveguides width and the inter-waveguide spacing, can be induced by different methods. For instance, the use of phase-changing materials [176, 177] can provide a variation of a refractive index in presence of heat, which, combined with non-adiabatic periodic pattern, can be a method to design an active photonic switch.

A topological photonics has emerged in the last few years. Topology is a property of a photonic material (or a periodic structure such as photonic crystal, or array of waveguides [178, 179]) that is characterized by a quantized behavior of the function on its entire dispersion band [180]. The band should necessarily have a gap, so the topological transition is observed when a (topological) phase accumulated during propagation closes this gap. In photonics it results in unexpected properties, such as transmission with no back-reflection allowing to construct perfect insulators. We believe that the properties of non-adiabatic system can be extended to topological transitions : by tuning a frequency of the perturbation we can create and destroy topological states in array of coupled waveuigdes. We've seen as well that the anti-symmetric operator $\frac{\partial V^{\dagger}(x)}{\partial x}V(x)$ contains the off-diagonal terms responsible for coupling of the supermodes, and the diagonal terms contain the Berry phase [181] which reflect topological properties of the system. Therefore, by introducing a transition operator σ, that is now diagonal and imaginary, we could create topological properties in two coupled waveguides. Also, the non-adiabatic transitions allow to construct non-symmetric systems (for instance, the designs of chip in Figures B.5, B.6) which, therefore, can be described by imaginary Bloch modes. Since Bloch bands are characterized by a set of topological invariants, it can be an evidence of topological behavior. Therefore, we believe that theory of non-adiabatic transitions can be characterized or extended to the field of topological systems.

Another perspective application can be inclusion of nonlinearity to the non-adiabatic light switch. Indeed, nonlinear directional couplers are important in design of power-sensitive switches: for low power input light oscillates between the waveguides, while for higher power it stays confined in one [182]. Also, if one waveguide experiences losses and the other - equal amount of gain, it is possible to realize a parity-time($\mathcal{PT}$)-symmetric system [183, 184], which results in a non-symmetrical dynamics [185] or even chaotic regimes [186]. The non-adiabatic transition can already construct non-symmetric systems, and the asymmetric coupling is non-Hermitian by construction which is a requirement to observe the , so the impact of nonlinearity and/or losses can result in new phenomena.

A similarity between quantum physics and guided optics has been developed in the context of optical fibers too. The adiabatic frequency conversion and autoresonances were demonstrated in [158, 159], which shows that similar Hamiltonian formalism shown in Appendix B can be developed in fibers. The main difference is in the nonlinear term - the processes considered in Appendix B are purely linear, while the adiabatic processes in fibers include nonlinearity. Nevertheless, an interesting discussion can brought by connecting the two subjects. The definition of supermodes and controlled transition between them can be a promising subject for : (a) fundamental discussions and establishment of links with quantum processes, (b) development of new type of frequency conversion devices.

Glossary

AB	Akhmediev Breather
ASE	Amplified Spontaneous Emission
CMT	Coupled-mode theory
GVD	Group-velocity dispersion
CW	Continuous wave
DFT	Dispersive Fourier Transform
DyMD	Dynamic Mode Decomposition
EDFA	Erbium-doped fiber amplifier
FWM	Four-wave mixing
FPU	Fermi-Pasta-Ulam (recurrence)
$\mathcal{F}.\mathcal{T}.$	Fourier transform
GF	Green Function
HNLF	Higly-nonlinear fiber
LASSO	Least absolute shrinkage and selection operator
LARS	Least-angle regression
LFE	Local-field effect
MI	Modulation instability
MSE	Mean-square error
NLS (NLSE)	Nonlinear Schrödinger equation
NN	Neural network
OBPF	Optical band-pass filter
OSA	Optical spectrum analyzer
PD	Photodiode
PM	Phase modulator
PMD	Polarization-mode dispersion
QNM	Quasi-normal Modes
RF	radiofrequency
RMSE	Root mean-square error
SINDy	Sparse identification of nonlinear dynamics
SM	Soliton molecule
SMF	Single-mode fiber
SPM	Self-phase modulation
TL	TeraLight

Appendix A

Local Field and Effective background effects in coupled integrated photonic waveguides systems

Two waveguides placed near each other become coupled, hence light can flow from one to another. Optical couplers are essential building block in design of photonic integrated chips, understanding of which is important in control of complex systems such as : nonlinear waveguide arrays [187–190], realization of optical analogue to quantum effects [36, 191–193], topological systems [194–196] and the dispersion engineering [197, 198].

The estimation of the coupling strength is a critical feature in photonics. A modern approach is to describe the waveguides array in terms of its supermodes that are shaped according to the inter-modes coupling constants. The coupling constant between the two waveguides is derived from the perturbative theory applied to Maxwell's equations. However, these formula fail to provide reliable results as soon as the index contrast between the waveguide's core and its cladding become large. In this chapter we demonstrate that the inclusion of the local field effect (LFE) allows to retrieve a good accuracy. Moreover, in case of structured inhomogeneous cladding, an effective background index should be also taken into account so the LFE correction remains accurate [199].

A.1 Perturbative method in guided optics

A.1.1. Hamiltonian formulation of problems in perturbative photonics

First, let us rewrite the Maxwell's equations introduced in Eq. 1.1 in a form adapted directly for a dielectric:

$$\begin{aligned} \bigtriangledown \cdot \varepsilon_0 \varepsilon \boldsymbol{E} = 0 \quad \bigtriangledown \times \boldsymbol{E} = -\mu_0 \frac{\partial \boldsymbol{H}}{\partial t} \\ \bigtriangledown \cdot \mu_0 \boldsymbol{H} = 0 \quad \bigtriangledown \times \boldsymbol{H} = \varepsilon \varepsilon_0 \frac{\partial \boldsymbol{E}}{\partial t} \end{aligned} \tag{A.1}$$

We first deduce from the translation invariance along the waveguide direction **x** that the optical mode can be decomposed as:

$$\begin{bmatrix} \boldsymbol{E}(x,y,z,t) \\ \boldsymbol{H}(x,y,z,t) \end{bmatrix} = \begin{bmatrix} \boldsymbol{E}(y,z) \\ \boldsymbol{H}(y,z) \end{bmatrix} e^{i\beta x - i\omega t} \tag{A.2}$$

Moreover, the longitudinal components of the field $\{E_x, H_x\}$ can be expressed from its transverse components $\{\boldsymbol{E}_\perp, \boldsymbol{H}_\perp\}$, so that the Maxwell's equations A.1 can be expressed using only the latter. After some math, and following the guidelines in [200], we can define a generalized propagation equation where $|\psi\rangle = [\boldsymbol{E}_\perp(y,z); \boldsymbol{H}_\perp(y,z)]$

$$\frac{\partial}{\partial x}\hat{B}\,|\psi\rangle = \imath\frac{\omega}{c}\hat{A}\,|\psi\rangle \tag{A.3}$$

The corresponding eigenvalue problem with value β_0 and eigenvector $|\psi_0\rangle = [\boldsymbol{E}_{\perp 0}(y,z); \boldsymbol{H}_{\perp 0}(y,z)]$ is then:

$$\beta_0\hat{B}\,|\psi_0\rangle = \frac{\omega}{c}\hat{A}\,|\psi_0\rangle \tag{A.4}$$

The hermitian operators $\hat{A}$ and $\hat{B}$ are

$$\hat{B} = \begin{bmatrix} 0 & -\vec{x}\times \\ \vec{x}\times & 0 \end{bmatrix}$$
$$\hat{A} = \begin{bmatrix} \sqrt{\frac{\varepsilon_0}{\mu_0}}\left[\varepsilon - \frac{c^2}{\omega^2}\bigtriangledown_t \times \left\{\vec{x}\cdot\left[\frac{1}{\mu}\vec{x}\cdot(\bigtriangledown_t\times)\right]\right\}\right] & 0 \\ 0 & \sqrt{\frac{\mu_0}{\varepsilon_0}}\left[\mu - \frac{c^2}{\omega^2}\bigtriangledown_t \times \left\{\vec{x}\cdot\left[\frac{1}{\varepsilon}\vec{x}\cdot(\bigtriangledown_t\times)\right]\right\}\right] \end{bmatrix} \tag{A.5}$$

Knowing an eigensolution $|\psi_0\rangle$, the corresponding propagation constant β_0 is simply the Rayleigh quotient:

$$\beta_0 = \frac{\omega}{c}\frac{\langle\psi_0|\,\hat{A}\,|\psi_0\rangle}{\langle\psi_0|\,\hat{B}\,|\psi_0\rangle} \tag{A.6}$$

These equations are the starting point to construct a perturbative theory [35, 200, 201]. We now consider a system of coupled waveguides, where the second one is considered as a perturbation which modifies the field of the first (and vice versa), resulting in new optical modes $\left|\psi^{(t)}\right\rangle$. Using the Hamiltonian formulation developed previously we separate the parts corresponding to the isolated single waveguides equations $\hat{A}_0$ and its corrections $\Delta\hat{A}$:

$$\beta\hat{B}\left|\psi^{(t)}\right\rangle = \frac{\omega}{c}\left(\hat{A}_0 + \Delta\hat{A}\right)\left|\psi^{(t)}\right\rangle \tag{A.7}$$

By projecting Eq. A.7 on the eigenmodes of the isolated basis, the equation can be further simplified, namely by exploiting the hermitian property of $\hat{A}$ and $\hat{B}$. In this case the eigenvalue propagation equation becomes:

$$\left(\beta - \beta_0^{(i)}\right)\left\langle\psi_0^{(i)}\right|\hat{B}\left|\psi^{(t)}\right\rangle = \frac{\omega}{c}\left\langle\psi_0^{(i)}\right|\Delta\hat{A}^{(i)}\left|\psi^{(t)}\right\rangle \tag{A.8}$$

The index $i = \{1,2\}$ indicates whether the first or second isolated waveguide is considered. Following the conventional coupled-mode theory (CMT) [202, 203] the eigenmode supported by the waveguides array (with the respective propagation constant β) is then approximated as a combination of the isolated waveguides' modes, hence:

$$\left|\Psi^{(t)}\right\rangle = \left(a_1\left|\psi^{(1)}\right\rangle + a_2\left|\psi^{(2)}\right\rangle\right)e^{i\beta x} \tag{A.9}$$

After substituting $\left|\Psi^{(t)}\right\rangle$ to Eq. A.8 and rearranging the terms we obtain the two-unknown set of equations:

$$B^{-1}\begin{bmatrix}\beta - \beta_0^{(1)} & 0 \\ 0 & \beta - \beta_0^{(2)}\end{bmatrix}B\begin{bmatrix}a_1 \\ a_2\end{bmatrix} = \frac{\omega}{c}B^{-1}\Delta A\begin{bmatrix}a_1 \\ a_2\end{bmatrix} \tag{A.10}$$

where $\Delta A, B$ are matrices with elements expressed as:

$$B_{ij} = \iint_S \boldsymbol{x} \cdot (\boldsymbol{E}^{(i)*} \times \boldsymbol{H}^{(j)} - \boldsymbol{H}^{(i)*} \times \boldsymbol{E}^{(j)}) \tag{A.11}$$

$$\Delta A_{ij} = \sqrt{\frac{\varepsilon_0}{\mu_0}} \iint_S [E_x^{(i)*} E_x^{(j)} \frac{\varepsilon_i \Delta\varepsilon_i}{\varepsilon_t} + D_y^{(i)*} D_y^{(j)} \frac{\Delta\varepsilon_i}{\varepsilon_i \varepsilon_{\ j}} + E_z^{(i)*} E_z^{(j)} \Delta\varepsilon_i] \tag{A.12}$$

Here $\boldsymbol{E}(y,z)^{(i)}$ is the eigen-field of the i^{th} waveguide, and ε_i its dielectric constant. Correspondingly $\Delta\boldsymbol{\varepsilon}_i$ is a perturbation introduced to the i^{th} waveguide by the other one; $\boldsymbol{\varepsilon}_t = \boldsymbol{\varepsilon}_i + \Delta\boldsymbol{\varepsilon}_i$ is then the total dielectric portrait of the system, varying in the transverse (y,z) plane. If we assume $\beta_0^{(1)} = \beta_0 + \frac{\Delta\beta}{2}$ and $\beta_0^{(2)} = \beta_0 - \frac{\Delta\beta}{2}$, then Eq. A.10 turns into:

$$(\beta - \beta_0) \begin{bmatrix} a_1 \\ a_2 \end{bmatrix} = B^{-1} \left(\frac{\Delta\beta}{2} \begin{bmatrix} -1 & 0 \\ 0 & 1 \end{bmatrix} B + \frac{\omega}{c} \Delta A \right) \begin{bmatrix} a_1 \\ a_2 \end{bmatrix} \tag{A.13}$$

For identical waveguides $\Delta\beta = 0$, Eq. A.13 can be further simplified as:

$$(\beta - \beta_0) \begin{bmatrix} a_1 \\ a_2 \end{bmatrix} = \frac{\omega}{c} B^{-1} \Delta A \begin{bmatrix} a_1 \\ a_2 \end{bmatrix} \tag{A.14}$$

The $\{i,j\}$ off-diagonal elements of $B^{-1}\Delta A$ correspond to the coupling κ_{ij} between the i^{th} and the j^{th} waveguides. The case of different waveguides, namely how the mismatch between the waveguides impacts their effective coupling [204], will be discussed in another work. Note that the propagation equation is constructed such that the flux of the Poynting vector (hence $\langle\Psi|\,\hat{B}\,|\Psi\rangle$) is preserved throughout propagation. If applied to the case of moderate modifications of an isolated waveguide, Eq. A.8 produces a good quantitative estimate. It can cope in particular with moving boundaries and polarization issues in high index problems [35, 200]. More details regarding the underlying mathematics and the corresponding electromagnetic Hamiltonian formulation of such theory can be found in [35].

The coupling between two adjacent waveguides is ascribed to the evanescent tail of the optical mode which extends far away from the core region of the waveguide and interacts with the neighboring waveguides. For negligibly overlapping waveguides modes ($B_{ij} = \delta_{ij}$) [205], and neglecting both the longitudinal component of the Electric field ($E_x = 0$) and the polarization effects caused by the dielectric interface, Eq. A.14 admits a simple analytical form, that is [206]:

$$\kappa_{ij} = \frac{\omega\varepsilon_0 \iint_S \Delta\boldsymbol{\varepsilon}_i \boldsymbol{E}^{(i)*} \cdot \boldsymbol{E}^{(j)}}{\iint_S \boldsymbol{x} \cdot (\boldsymbol{E}^{(i)*} \times \boldsymbol{H}^{(j)} - \boldsymbol{H}^{(i)*} \times \boldsymbol{E}^{(j)})} \tag{A.15}$$

Eq. A.15 is identical to the formulation derived in seminal works [205–207]. The relative impacts of the polarization of the electromagnetic field - including the impact of the longitudinal $\boldsymbol{E}_x$ component - [35], or the non-orthogonality of the isolated waveguide basis [205, 207] (hence $B_{ij} \neq 0$ for $i \neq j$) result in about minor changes. The data in Figure A.2 (c,d) labeled as "Previous works" can be separated to three methods: data obtained from a simplified approach Eq. A.15 [203, 205]; perturbative method Eq. A.10 with longitudinal field included [207]; perturbative method with $\boldsymbol{E}_x$ and $\boldsymbol{E}_y \rightarrow \frac{\boldsymbol{D}_y}{\varepsilon}$ (black line, yellow diamonds and blue circles in Figure A.1, respectively) [35]. The presented methods result in approximately the same results; and they deviate substantially from the results of direct simulations.

Therefore for sake of clarity, only one of these curves will be for the figures, and simply labeled as "previous works". As seen in Figure A.2, Eq. A.15, or any other similar derivations, actually fails to provide an accurate estimate of the coupling constant (for the high index contrast systems).

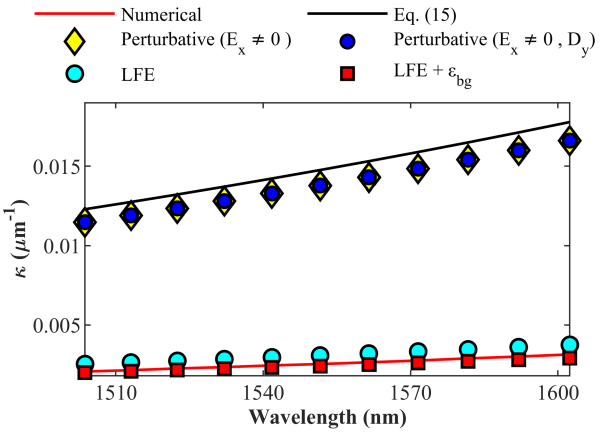

FIGURE A.1: (a) Coupling constant κ for two silicon waveguides separated by $G_1 = 220$ nm, as a function of the wavelength. Red line: numerical simulation. Black line: simplified analytical, from Eq. A.15. Yellow diamonds: coupling constant resulting from the perturbative method (Eq. A.10) with longitudinal field $\boldsymbol{E}_x$ included. Blue circles: same as previous but continuity of y-field is preserved. Cyan circles: theory including the Local Field Effect (LFE). Red squares: theory including the LFE complemented by the concept of the effective background (ε_{bg})

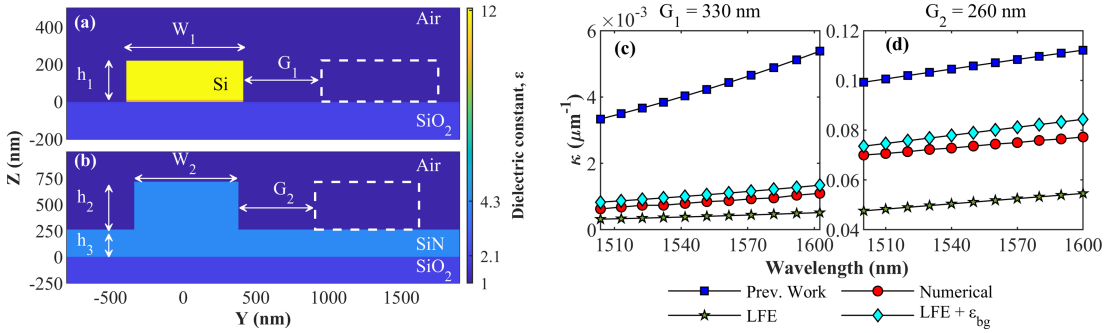

FIGURE A.2: (a) Dielectric map of the silicon ridge waveguide considered in this work. ($W_1 = 803$ nm , $h_1 = 220$ nm). (b) Dielectric map of the silicon-nitride rib-waveguide ($W_2 = 715$ nm , $h_2 = 455$ nm , $h_3 = 260$ nm). (c) Coupling constant κ for two silicon waveguides separated by $G_1 = 330$ nm, as a function of the wavelength. Squares: previous works. Red circles: Numerical simulation. Green stars: theory including the Local Field Effect (LFE). Cyan diamonds: Theory including the LFE complemented by the concept of the effective background (ε_{bg}). (d) Same as (c), but for the SiN rib waveguides, considering an inter-waveguide spacing of $G_2 = 260$ nm.

A.1.2. Waveguides configuration

Here we consider two configurations that would help to access the accuracy of the perturbative theory and the applied concepts.

First we consider a silicon on insulator design composed of two 220 nm high and 803 nm wide waveguides (Figure A.2-(a)). This geometry can be considered as a standard in current integrated photonics industry. It exhibits one of the largest confinement and index contrast between the core of the waveguide and its cladding. As such, nearly all the light remains confined within the core of the waveguide, and the evanescent tail decays very sharply.

The second system under investigation is composed of two silicon-nitride (SiN) rib waveguides that are partially etched, leaving out a 260 nm silicon-nitride membrane on insulator (Figure A.2-(b)). The index contrast provided by SiN ($n = 1.6$ up to 2.2) is quite similar to what is found for emerging material like TiO_2 ($n = 2.5$) and Ta_2O_5. To provide indicative numbers, the contrast between the core of the waveguide and its silica substrate is about $\Delta\varepsilon = 2.4$, hence nearly 50% smaller than the contrast with the air cladding $\Delta\varepsilon = 3.5$. Moreover, the presence of a high-index thin SiN layer on top of the silica substrate helps extending the evanescent tail of the optical mode farther away from the waveguide. Therefore, despite the index contrast being formally large $\Delta\varepsilon > 1$, the optical mode is actually weakly confined in the core of the waveguide, like this is the case for low contrast systems. Furthermore, we can also expect that the properties of this system also depend strongly on the exact structure of the air-SiN-Silica stack. This study is thus the occasion to explore the fundamental differences between fully etched and rib-waveguides. These systems would constitute a good benchmark to test the robustness and accuracy of perturbative theory in photonics.

The results of Eq. A.14 and Eq. A.15 are compared against direct simulation of the coupled waveguide system. The electromagnetic field distribution of the isolated waveguides is obtained by simulation using the same plane wave expansion simulation method, namely the MIT Photonics Band package (MPB) [208].

For Si waveguides we have used the following parameters : Global scaling factor of $a = 440\ nm$, Pixelsize 11 nm/pixel, Meshsize 12, Resolution 40, Tolerance 10^{-9}, Range of eigenvalues $k = [0.57 : 1.1334]$ (normalized in $2\pi/a$ unit), Simulation geometry width $= 24$, height $= 12$ (in a-units).

For SiN waveguides we have used the following parameters : Global scaling factor of $a = 650\ nm$, Pixelsize 65 nm/pixel, Meshsize 12, Resolution 40, Tolerance 10^{-9}, Range of eigenvalues $k = [0.5871 : 0.8890]$ (normalized in $2\pi/a$ unit), Simulation geometry width $= 18$, height $= 10$ (in a-units).

Waveguides' widths and separations are chosen to match precisely the discretisation grid, as to minimize smoothing errors. Since the chromatic dispersion in waveguides for nanophotonics is mostly dominated by the geometry, we assume a dispersionless material.

A.2 Local field effect

In general, the corrective models of the first order consider small modifications to the initial problem. The perturbative and standard modes expansion models assume that the system can be described in terms of solutions of the unmodified one. However, these few modes are usually not enough to enforce the divergence free of the electric field in presence of large index contrast perturbation. To solve this issue one may, for instance, complete the mode basis by a few "unphysical" modes that are pure mathematical non-divergence-free solutions of the Helmholtz equation [209, 210] or by the Quasi-Normal-Modes (QNMs) [211, 212]. However, the main disadvantage of these strategies is that it is required to know the properties of the system after the modifications, hence the final properties cannot be inferred $a\ proiri$. The solution in our case is to modify the nominal optical modes so that the mode expansion becomes more accurate, while number of included modes os minimal. This is done by inclusion of the LFE complemented by the effective background theory.

We ascribe the difference between the Eq. A.11 and the numerical results (Figure A.2 (c,d)) to the fact that the first order perturbative theory assumes no modification in nominal field shape, hence the mode basis is unchanged even though a dielectric perturbation has been introduced to the system. This assumption fails explicitly in large contrast systems ($\Delta\varepsilon$), where the resulting dipole $\Delta\varepsilon \boldsymbol{E}^{(i)}$ created by the perturbation becomes

larger than the nominal electric field itself. Under the influence of this perturbation the electric field becomes :

$$\boldsymbol{E} = \boldsymbol{E}_0 + \iint_{\boldsymbol{r}\neq\boldsymbol{r}'} \left(\overleftrightarrow{\boldsymbol{G}}_0(\boldsymbol{r},\boldsymbol{r}') k_0^2 \Delta\varepsilon(\boldsymbol{r}') \boldsymbol{E}(\boldsymbol{r}') d\boldsymbol{r}' \right) - \frac{L\Delta\varepsilon}{\varepsilon_{\text{bg}}} \boldsymbol{E}, \tag{A.16}$$

where $\boldsymbol{E}_0$ denotes the initial field before the perturbation is introduced, and $\overleftrightarrow{\boldsymbol{G}}_0$ is the Green function (GF) of the unperturbed system. Here the convolution term (the second term in Eq. A.16) is the contributions of the Green function which reflects : the change in electromagnetic fields even outside of the perturbed region; includes effects of multiple scattering impacted by presence of dielectric surfaces.

The optical field propagates in a waveguide in the x direction with n_{eff} which is greater than a dielectric permittivity of the cladding, hence the GF is evanescent function that is tightly localized. Consider the GF's decay rate as $\alpha = 2\pi/\lambda\sqrt{n_{eff}^2 - \varepsilon}$, which gives $\alpha = 9.7\ \mu m^{-1}$ and $\alpha = 6.2\ \mu m^{-1}$ for Si and SiN waveguides, respectively. When comparing α^{-1} ($= 100$ nm and $= 160$ nm for Si and SiN, respectively) to the waveguides width (803 and 715 nm) and the inter-waveguides separations (ranging from 100 to 1200 nm), we can conclude that the multiple scattering will be of second-order, and the changes in the electric field can be approximated by $\Delta\boldsymbol{E} = \boldsymbol{E} - \boldsymbol{E}_0$ (at least not in the vicinity of the dielectric perturbation).

The third term of Eq. A.16 reflects the impact of the LFE, which origin lies in divergence of GF in the source region : the derivation and the integration operators cannot be interchanged [213]. When the dielectric background is different from vacuum, the defect polarization $\delta\varepsilon(\boldsymbol{r})$ should be corrected by a dyadic factor $L\Delta\varepsilon\boldsymbol{E}(\boldsymbol{r})/\varepsilon_{\text{bg}}$ [213–215]. Here the ε_{bg} is the background permittivity at the source point. The L-factor depends on shape of the principal volume, in general - geometry of the problem. For a square grid considered here $L = 1/3$.

In the absence of multiple scattering the LFE term dominates the system, so the modified electric field can be expressed as [216]:

$$\boldsymbol{E} = \frac{\boldsymbol{E}_0}{1 + \frac{L\Delta\varepsilon}{\varepsilon_{\text{bg}}}} \tag{A.17}$$

The reduced polarizability can be interpreted in terms of the LFE as the feedback action of a single and isolated dipole on itself. The screening effect of Eq. A.17 would apply to estimate the defect polarization induced by a dielectric perturbation which is then not simply $\Delta\varepsilon\boldsymbol{E}_0$ anymore.

The result of inclusion of the LFE in the Eq. A.2 is shown in green-stars line in Figure A.2 (c,d). The developed Eqs A.10-A.14 rely on reducing the dimensionality of the problem by selecting a basis test functions $\left\langle \psi_0^{(i)} \right|$, which reduces the accuracy. If now we modify the test functions by injecting Eq. A.17 to Eq. A.9, we can improve the accuracy. For the Si waveguide, the result is notably improved (Figure A.2 (c)), while for SiN/SiO_2 the comparison is less striking. It can be explained by difference in index contrast : the Si has the highest index contrast so the perturbative theory fails. On the other side, the field shape for Si is simpler, and there is no long-distance contribution from the GF as in case of weaker confined SiN.

Another discrepancy can be attributed to a fact that we assume that each waveguide supports only one mode. The higher order modes with different polarizaton actually exist in waveguides, however, for a fairer comparison and clearer physics-oriented discussion, we select to consider only one mode which may impact the accuracy.

A.3 Effective background

The remaining error can be attributed to an inadequate choice of the background dielectric : it is equal to ε_{air} which may lead to an over-estimation of the LFE impact. The seminal theory of the LFE has considered only the case of a homogeneous background, so in a case when the perturbation occurs at a dielectric interface, the background permittivity is uncertain. In our case, even though the second waveguide occupies the space filled with air, the dielectric substrate is located a few hundreds nanometers away, which can have an impact on the radiation properties in the source region.

In order to get a better understanding of the impact of the substrate geometry and the dielectric value we directly estimate the resulting perturbed field. The dielectric permittivity ε_{bg} stated in the LFE effect is intrinsically linked to the Green function, so one needs to estimate how the GF is modified by a dielectric inhomogeneity. When the problem stated in Eq. A.16 is solved numerically over a finite grid in the limit of small volume around the source region, the solution provides a correct response for both LFE and other GF induced scattering included. Hence, we cannot distinguish the two terms in the solution. Therefore, we solve the GF response to the dielectric perturbation $\Delta\varepsilon$ assuming an $\{x, y\}$ invariant medium with an air-dielectric interface along the z-direction (more precisely, air-Silica interface for Si waveguides and air-SiN-Silica for the considered SiN structure). Considering in Eq. A.2 that the electromagnetic field propagates along x-direction with phasor $\beta = \frac{\omega}{c} n_{eff}$, the equation to solve is :

$$\bigtriangledown \times \bigtriangledown \times \overleftrightarrow{\boldsymbol{G}}_0 + 2\imath\frac{\omega}{c} n_{eff}\vec{x} \times (\bigtriangledown \times \overleftrightarrow{\boldsymbol{G}}_0) \quad + \quad \left(\frac{\omega}{c}\right)^2 n_{eff}^2 \vec{x} \cdot (\vec{x}.\overleftrightarrow{\boldsymbol{G}}_0) + \left(\frac{\omega}{c}\right)^2 (\varepsilon(y,z) - n_{eff}^2)\overleftrightarrow{\boldsymbol{G}}_0 = \overleftrightarrow{\delta}(y - y_0, z - z_0). \tag{A.18}$$

The Eq. A.19 is solved using the Fourier modal expansion (with a grid size of 10 nm), assuming a purely y-polarized electric field. The results are displayed in Figure A.3. In contrast to the first order perturbation theory which assumes no modifications in the electric field (Figure A.3 (c1-2,f1-2)), the new displacement field is now divergence-free (cyan line in Figure A.3 (h1-2)). A strong modification of the dielectric is compensated by a corresponding decrease in the electric field to minimize a discontinuity of the displacement field, the residual discontinuity on edges is compensated by a gradient. The generalized LFE reduces the value of the electric field, however, cannot take into account these gradients, hence the effective background shall act as a crude approximation of the exact field. The accuracy of the LFE can be linked to the evanescent nature of the field outside of the waveguide's core. In the case of SiN waveguides, where the dielectric pattern is more complex, and the confinement is not so strong, the assumption of purely y-polarized field works a bit worse, which leaves small discontinuity in the displacement field. Nevertheless, the concept of effective background still allows to compensate the field difference in presence of a complex pattern.

As comparison, we also show in Figure A.4 the case of a waveguide embedded in a homogeneous background. This confirms the excitation of the LFE in any case, and demonstrates that the effective background is now matching the value of the cladding, as predicted by the nominal theory of LFE.

Of course, to avoid complex calculations, the ε_{bg} can be chosen as a fitting parameter that matches the best result of Eq. A.16. However, the concept of the effective background is deeply rooted to the properties of the optical mode.

The value of the effective background is well approximated as an average permittivity felt by the optical mode away from the weveguide's core : $\varepsilon_{\text{bg}} = \int \varepsilon(r)|\boldsymbol{E}|^2 / \int |\boldsymbol{E}|^2$. It can be linked to a fact that the coupling constant evolves similarly as the evanescent tail of the mode outside of the waveguide. Then, if the mode

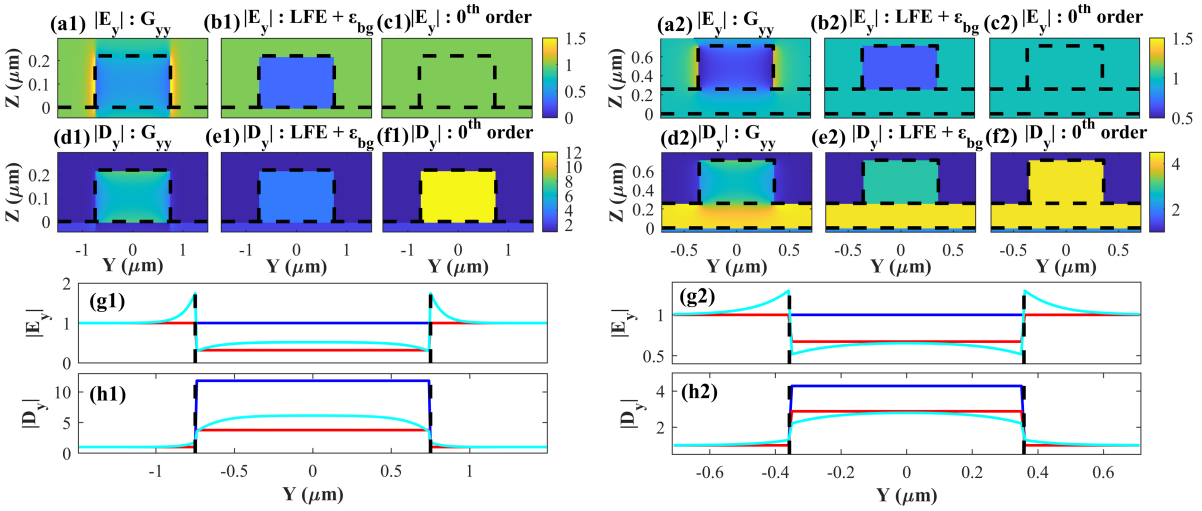

FIGURE A.3: Cases of silicon and silicon nitride waveguides are displayed in panels 1 and 2, respectively. (a-c) y-component of the Electric Field resulting from the perturbation of an initial homogeneous $\boldsymbol{E} = 1\boldsymbol{y}$ field by a dielectric perturbation $\Delta\varepsilon$ which corresponds to the presence of the second waveguides. (a) is the solution of Eq. A.16 restricted to the y-component of the field. (b) the result of the LFE assuming an effective background $\varepsilon_{\text{bg}} = 1.7$ for Si and $\varepsilon_{\text{bg}} = 2.7$ for SiN. (c) Initial Coupled mode formulation where no changes of the Electric field are assumed (i.e. 0^{th} order theory). Black-dashed lines indicate the position of the dielectric perturbation. (d-f) y-component of the displacement field. (g-h) Variation of the electric Field (resp. Displacement Field) along y, for an altitude of 110 nm for Si and 230 nm for SiN (Half the waveguide's height). Dark blue: zeroth order theory (no changes in the nominal electric field). Red: LFE theory assuming an effective background. Light Blue: Solution of Eq. A.19.

propagates with effective index n_{eff}, the coupling constant decays with a rate $\alpha = k_0\sqrt{n_{\text{eff}}^2 - \varepsilon_{\text{bg}}}$, where k_0 is the vacuum wave-vector. Therefore, with the knowledge of one coupling constant, the values for other separations can be extrapolated.

The use of the nominal vacuum permittivity $\varepsilon_{bg} = 1$ results in large overestimation of the decay rate. For the SiN (blue squares in Figure A.5 (b)), it can be explained from the fact that the mode decays both in the cladding and in the substrate, so the actual decay rate is a mixture between the two. If the effective background is computed correctly $\varepsilon_{bg} = 2.7$ (cyan diamonds in Figure A.5 (b)), the decay factor matches the numerical simulation. For the Si waveguides, the effective index is way larger than the background permittivity, hence, the slope is not so affected.

To summarize, we can conclude that the effective background is intrinsically included in the LFE and in the natural decay of the optical mode away from the waveguide. The ε_{bg} is, in this case, uniquely defined and is a fundamental property of the optical mode. To avoid complex estimations of the Green function presented in this chapter, one can rely on the decay of the optical mode. The discussed effects allow to estimate the coupling at different distances with better accuracy, especially for large gaps, where numerical simulations do not provide accurate estimations.

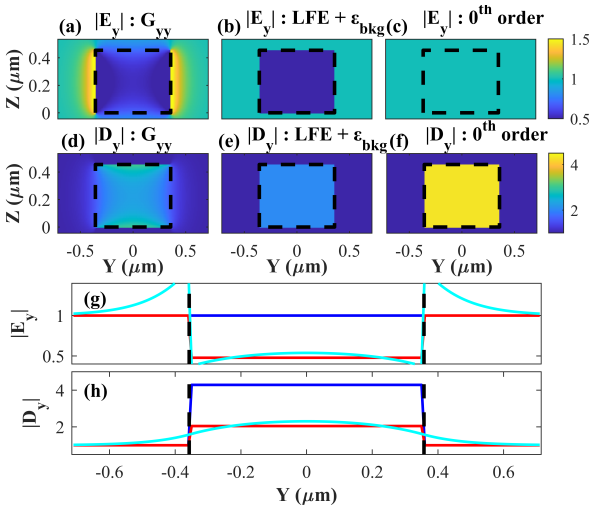

FIGURE A.4: Case of silicon nitride waveguides in air cladding, hence $\varepsilon_{\text{bg}} = 1$. (a-c) y-component of the Electric Field resulting from the perturbation of an initial homogeneous $E_y = 1$ field by a dielectric perturbation $\Delta\varepsilon$ which correspond to the presence of the second waveguides. (a) is the solution of Eq. A.16 restricted to the y-component of the field. (b) the result of the Local Field Effect assuming an effective background $\varepsilon_{\text{bg}} = \varepsilon_{\text{air}} = 1.00$. (c) Initial Coupled mode formulation where no changes of the Electric field are assumed (i.e. 0^{th} order theory). Black-dashed lines indicate the position of the dielectric perturbation and the limit with the air cladding. (d-f) y-component of the displacement field. (g-h) Variation of the electric Field (resp. Displacement Field) along y, for an altitude of 230 nm (Half the waveguide's height). Dark blue: zeroth order theory (no changes in the nominal electric field). Red: LFE theory assuming an effective background. Light Blue: Solution of Eq. A.19.

A.4 Conclusion

We demonstrate that compared to previous models, the LFE allows to improve the estimation of the coupling constant by nearly an order of magnitude. The remaining discrepancies can be linked to presence of higher order modes in the system, which we neglect for simpler discussion. In fact, higher order modes and modes of different polarization can be coupled in a presence of the second waveguide. This effect is stronger if the modes have the similar propagation constants, for instance, in large waveguides. In principle, our approach is general and the other modes can be included in Eq. A.9-A.10.

The LFE is always present, its magnitude may vary depending on exact geometry, the index contrast and the initial permittivity at position of the perturbation. The LFE is not symmetric if one adds a dielectric on a low index background or subtracts a dielectric on a high index material. And modification of a core of the waveguide would have a reduced LFE contribution compared to modification of a cladding.

Overall, we demonstrate how the interplay between the cladding and the substrate impacts the optical mode. Even though the coupling constants can be easily accessed with modern computing capability, the discussion around the physics and precise description of the system is valuable.

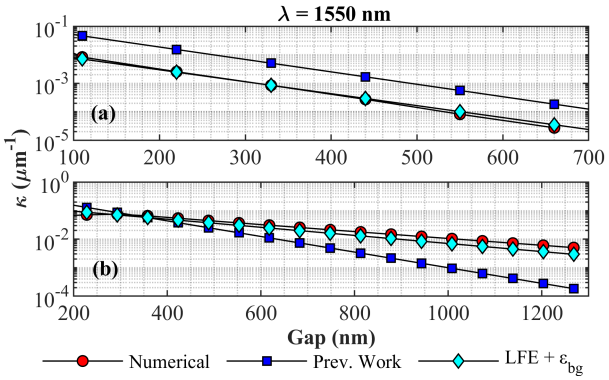

FIGURE A.5: (a-b) Evolution of the coupling constant κ as function of the inter-waveguide spacing (Gap). The results obtained from perturbation theories for a Gap of 300 nm are assumed to vary with a decay rate $\alpha = k_0\sqrt{n_{\text{eff}}^2 - \varepsilon_{\text{bg}}}$. Red circles: results from direct simulations. Blue squares: previous perturbative theory where ε_{bg} is assumed to be equal to the cladding permittivity, namely $\varepsilon_{\text{bg}} = \varepsilon_{\text{air}} = 1$. Cyan diamonds: New formulation considering an effective background. (a) Case of silicon waveguides, $\varepsilon_{\text{bg}} = 1.7$. (b) Case of silicon nitride waveguides, $\varepsilon_{\text{bg}} = 2.7$

Appendix B

Non-adiabatic light control

The ever-increasing use of integrated photonics for application and fundamental research is motivating a search for fundamentally new design strategies, so that optical phenomena can be controlled -or observed- more easily. The intensive use of computer optimization in photonics does not provide much insight into new principles and properties of light manipulation, hence it is limited in adaptability and scalability of the solutions. Here we propose a framework that relies on fundamental properties of coupled waveguides systems, so that interpretable and optimal solution for manipulating the light can be obtained. Analogies between quantum physics and optics have given rise to many useful applications and strategies in both domains. In this work, we demonstrate a photonic transition in a system of coupled waveguides which is analogous to excitation of energy states in atoms. We demonstrate that arrays of integrated coupled waveguides can be operated in the non-adiabatic regime, which also gives a way to control these systems in the reciprocal space. With an optimal shape that is obtained from direct solving of a set of equations, we can achieve efficient non-adiabatic light coupling; and consequently the adiabatic evolution restriction that was imposed thus far on the design of integrated photonic systems does not hold anymore.

On a more general, or more exactly mathematical view, this Appendix is devoted to the control (and the transfer of energy) between asymmetric optical modes. Besides, the spatial control provides, here in microphotonics, more degrees of freedom when it comes to varying the propagation parameters compared to what is possible to do either in fiber, or in the time domain.

B.1 Propagation equation in coupled waveguides

B.1.1. Propagation equations in direct and reciprocal spaces

Now we are interested in how light propagates in a system of coupled waveguides. For a general discussion we consider two waveguides with varying parameters in the longitudinal direction x (for instance, width, height, interwaveguide spacing, refractive index, etc.). We consider an instantaneous snapshot mode $|\psi_{x_0}(x,y,z)\rangle$ at position x_0 which is adapted to the given parameters according to equation :

$$\hat{B}\frac{\partial}{\partial x}\left|\psi_{x_0}(x,y,z)\right\rangle = i\frac{\omega}{c}\hat{A}(x_0)\left|\psi_{x_0}(x,y,z)\right\rangle . \tag{B.1}$$

Note that for eigen-solution of Eq. B.1 with associated β_k eigenvalue, the x dependence of $|\psi_k(x,y,z)\rangle$ is simply $|\psi_k(y,z)\rangle \exp(i\beta_k(x_0)x)$. Eq. B.1 has several solutions that form a complete basis so that the total field

at position x can be expressed as a linear combination of the modes with varying coefficients $a(x)$. Hence, the anzats (Eq. A.9) is modified as:

$$|\mathbf{\Psi}\rangle = \sum_{k=1}^{2} a_k(x) \, |\psi_{k,x_0=x}(x,y,z)\rangle \, . \tag{B.2}$$

For simplicity, we will hereafter omit the $x = x_0$ index. k represent the different solutions of Eq. B.1. For sake of simplicity, we will consider 2 mono-mode waveguides, hence there exist only two supermodes (eigen-modes) $k = \{1, 2\}$. After substituting Eq. B.2 to the general propagation equation A.3 one receives:

$$\hat{B}\left(\sum_{k=1}^{2} \frac{\partial a_k(x)}{\partial x} |\psi_k\rangle + \sum_{k=1}^{2} a_k(x) \frac{\partial |\psi_k\rangle}{\partial x}\right) = i\frac{\omega}{c}\hat{A}\sum_{k=1}^{2} a_k(x) \, |\psi_k\rangle \, . \tag{B.3}$$

The Eq. B.3 is projected on $\langle\psi_k|$. Similar to derivation in the previous chapter, the resulting equation can be represented in a matrix form with each element defined by (here we sum over j) :

$$\langle\psi_k| \hat{B} \frac{\partial a_j(x)}{\partial x} |\psi_j\rangle + \langle\psi_k| \hat{B} a_j(x) \frac{\partial |\psi_j\rangle}{\partial x} = i\frac{\omega}{c} \langle\psi_k| \hat{A} a_j(x) \, |\psi_j\rangle \, . \tag{B.4}$$

We separate the varying coefficients from the modes

$$\frac{\partial a_j(x)}{\partial x} = \left[-\frac{\langle\psi_k| \hat{B} \left|\frac{\partial}{\partial x}\psi_j\right\rangle}{\langle\psi_k| \hat{B} |\psi_j\rangle} + i\frac{\omega}{c}\frac{\langle\psi_k| \hat{A} |\psi_j\rangle}{\langle\psi_k| \hat{B} |\psi_j\rangle}\right] a_j(x). \tag{B.5}$$

if we normalize $|\psi_k\rangle$ such that $\langle\psi_k| \hat{B} |\psi_k\rangle = 1$, we have the equality

$$\left\langle \frac{\partial}{\partial x}\psi_k \right| \hat{B} |\psi_k\rangle + \langle\psi_k| \hat{B} \left| \frac{\partial}{\partial x}\psi_k \right\rangle = 0 \tag{B.6}$$

that leads to :

$$\frac{\partial a_j(x)}{\partial x} = \left[\frac{\left\langle \frac{\partial}{\partial x}\psi_k \right| \hat{B} |\psi_j\rangle}{\langle\psi_k| \hat{B} |\psi_j\rangle} + i\frac{\omega}{c}\frac{\langle\psi_k| \hat{A} |\psi_j\rangle}{\langle\psi_k| \hat{B} |\psi_j\rangle}\right] a_j(x). \tag{B.7}$$

Now we construct a system of coupled equations. We denote $(a_1(x), a_2(x))$ as $\tilde{\mathbf{\Psi}}$. The combination of the first terms of Eq. B.7 can be denoted in compact form as $\frac{\partial \boldsymbol{V}^\dagger(x)}{\partial x}\boldsymbol{V}(x)$ that represents normalized eigen modes. From Eq. A.6, the second term can be replaced by $\frac{\omega}{c}\langle\psi_k| \hat{A} |\psi_j\rangle = \delta_{kj}\beta_{k0}\langle\psi_k| \hat{B} |\psi_j\rangle$ which results in a diagonal matrix containing eigenvalues $\boldsymbol{\beta}_k(x)$.

$$\frac{\partial \tilde{\mathbf{\Psi}}(x)}{\partial x} = \left[\frac{\partial \boldsymbol{V}^\dagger(x)}{\partial x}\boldsymbol{V}(x) + i\begin{pmatrix}\beta_1(x) & 0\\ 0 & \beta_2(x)\end{pmatrix}\right]\tilde{\mathbf{\Psi}}(x). \tag{B.8}$$

The Eq. B.8 is the propagation equation in the reciprocal space : it operates with the eigen-modes of the system. This presentation of arrays of coupled waveguides differs from what is usually found in textbooks. Indeed, coupled waveguides are often presented as the result of coupled equations involving the individual waveguides.

Similar equation can be derived for the direct space, which operates in terms of field distribution in each waveguide. If we assume that the super-modes $\tilde{\mathbf{\Psi}}$ can be expressed as linear combinations of the individual waveguides, hence $\mathbf{\Psi} = \boldsymbol{V}\tilde{\mathbf{\Psi}}$ where $\mathbf{\Psi}$ is light in each waveguide, then using $\frac{\partial \tilde{\mathbf{\Psi}}}{\partial x} = \frac{\partial \boldsymbol{V}^\dagger}{\partial x}\mathbf{\Psi} + \boldsymbol{V}^\dagger\frac{\partial \mathbf{\Psi}}{\partial x}$ the Eq. B.8 is transformed

$$\frac{\partial \boldsymbol{V}^\dagger(x)}{\partial x}\mathbf{\Psi}(x) + \boldsymbol{V}^\dagger(x)\frac{\partial \mathbf{\Psi}(x)}{\partial x} = \frac{\partial \boldsymbol{V}^\dagger(x)}{\partial x}\boldsymbol{V}(x)\boldsymbol{V}^\dagger(x)\mathbf{\Psi}(x) + i\boldsymbol{\beta}_0(x)\boldsymbol{V}^\dagger(x)\mathbf{\Psi}(x), \tag{B.9}$$

$$\frac{\partial \boldsymbol{\Psi}(x)}{\partial x} = i\boldsymbol{V}(x)\boldsymbol{\beta}_0\boldsymbol{V}^{\dagger}(x)\boldsymbol{\Psi}(x). \tag{B.10}$$

Here we can use the diagonalization of the matrix $\boldsymbol{M}(x) = \boldsymbol{V}(x)\boldsymbol{\beta}_0(x)\boldsymbol{V}^{\dagger}(x)$. Then the propagation equation for the direct (namely, per waveguide) space is :

$$\frac{\partial \boldsymbol{\Psi}(x)}{\partial x} = i\boldsymbol{M}(x)\boldsymbol{\Psi}(x) = i\begin{bmatrix} k_1(x) & \kappa_{12}(x) \\ \kappa_{21}(x) & k_2(x) \end{bmatrix}\boldsymbol{\Psi}(x). \tag{B.11}$$

Both equations for direct $\boldsymbol{\Psi}(x)$ and reciprocal $\tilde{\boldsymbol{\Psi}}(x)$ variables can be of course extended to N waveguides :

$$\frac{\partial \boldsymbol{\Psi}(x)}{\partial x} = i\begin{bmatrix} k_1(x) & \kappa_{12}(x) & \ddots \\ \kappa_{21}(x) & k_2(x) & \ddots \\ \ddots & \ddots & \ddots \end{bmatrix}\boldsymbol{\Psi}(x) = i\boldsymbol{V}(x)\begin{bmatrix} \beta_1(x) & 0 & \ddots \\ 0 & \beta_2(x) & \ddots \\ \ddots & \ddots & \ddots \end{bmatrix}\boldsymbol{V}^{\dagger}(x)\boldsymbol{\Psi}(x), \tag{B.12}$$

$$\frac{\partial \tilde{\boldsymbol{\Psi}}(x)}{\partial x} = \left(\frac{\partial \boldsymbol{V}^{\dagger}(x)}{\partial x}\boldsymbol{V}(x) + i\begin{bmatrix} \beta_1(x) & 0 & \ddots \\ 0 & \beta_2(x) & \ddots \\ \ddots & \ddots & \ddots \end{bmatrix}\right)\tilde{\boldsymbol{\Psi}}(z). \tag{B.13}$$

To find how the light propagates between the waveguides we solve the propagation equations: first we compute eigen modes and eigen values of the $\boldsymbol{M}(x)$ matrix. Then we select the initial energy distribution either in the direct or the reciprocal space (hence, we excite either the waveguide or the supermode). To compute propagation, we project the direct basis on the supermode basis $\boldsymbol{V}(x)$ and compute propagation of the supermode, and then reproject on the direct basis by $\boldsymbol{V}^{\dagger}(x)$.

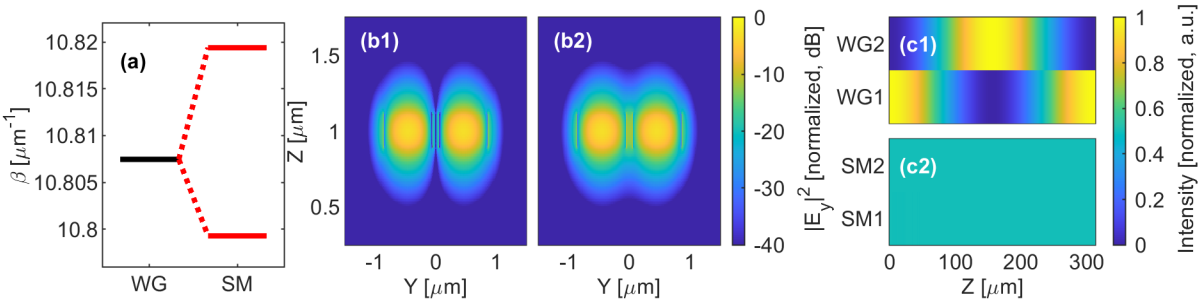

FIGURE B.1: (a) Propagation constants of modes of the individual symmetric waveguides (black) and the supermodes of the coupled waveguides (red). (b) Shape of the odd and even supermodes (panels 1 and 2, respectively). (c) Propagation of light in coupled waveguides in the direct (panel 1) and the reciprocal (panel 2) spaces. For all examples we consider two coupled Si waveguides (the dimensions are presented in Figure A.2 (a)) at inter waveguide spacing of 110 nm and 1550 nm wavelength.

When two waveguides are coupled, the excited supermodes have propagation constants β different from the ones of individual waveguides. On a diagram in Figure B.1 (a), this is reflected as a splitting of the propagation constants, where the difference between the levels shows the coupling strength. Consider an example of two coupled waveguides made of Si with width and height of 803 and 220 nm, respectively, put on a SiO_2 substrate

(Figure A.2 (a)). At the inter waveguide spacing of 110 nm and the wavelength of 1550 nm, the coupling constants are $\kappa_{12} = \kappa_{21} = 1.004 \cdot 10^{-2}\ \mu\text{m}^{-1}$, and the respective propagation constants of the supermodes are 10.819 and 10.799 μm^{-1}. When comparing to $\beta_0 = 10.8075\ \mu\text{m}^{-1}$ of individual waveguides (black line in Figure B.1 (a)) we observe a typical level splitting (red lines in Figure B.1 (a)).

If the coupled waveguides are symmetric (identical), the two excited supermodes are odd and even combinations of the individual electric fields of each waveguides. The Figure B.1 (b) shows an example of these modes approximating that individual modes contain only E_y field (the main direction of polarization in our configuration). The strength of both lobes in the field distribution is the same, so if we allow the light propagate in this configuration we observe the light beating in the direct space (Figure B.1 (c1)) that results from interference between the dephased supermodes. The periodicity of the transition $2\pi/\kappa_{12}$ corresponds in our case to 312.9 μm. Since both supermodes are excited equally, and the system parameters are kept constant, no difference in energy distribution between each SM is observed (Figure B.1 (c2)). This configuration of an optical coupler is the simplest and the most robust to change of the wavelength or fabrication roughness. However, it offers little control and the length of transition may be nonoptimal.

B.1.2. Asymmetric waveguides : non-Hermitian systems

In codirectional couplers, the modes carry electromagnetic power in the same direction, so the power carried by modes $\mathbf{\Psi}_1(x)$ and $\mathbf{\Psi}_2(x)$ (in the 2-waveguides configuration) should be conserved along the longitudinal direction. This condition is fulfilled if $\kappa_{12}(x) = \kappa_{21}^*(x)$ [217], which is true only for identical waveguides with $\Delta\beta(x) = \beta_1(x) - \beta_2(x) = 0$. However, light propagation in asymmetric waveguides is not only an interesting fundamental problem but also a subject that can bring up new strategies and phenomena, for instance, adiabatic elimination [38, 218, 219], switching based on refractive index engineering [220].

The conventional CMT implicitly assumes orthogonality of the optical modes, which is not supported in case of the asymmetric waveguides : the modes are nonorthogonal, which results in violation of the power conservation law. To enforce the correct power flow, Hardy and Streifer [203] propose to modify the mode formulations to counterbalance their nonorthogonality and to better evaluate propagation and coupling constants where $\kappa_{12}(x) \neq \kappa_{21}(x)$. In such a situation, the propagation matrix $\boldsymbol{M}(x)$ (Eq. B.11) is not Hermitian anymore. However, this approach does not enforce the power conservation low in a self-consistent manner. Another approach consists in using a modified CMT [207, 221] where perturbation-correction terms are introduced to the propagation matrix elements. However, the supermodes of this theory are still not perfectly orthogonal to each other, which leads to inaccuracies in the power conservation [207]. Finally, Haus et al. [205] have proposed a method for orthogonalization of the modes, giving a general (non unique) way to obtain a Hermitian propagation matrix with reworked modes definitions. Here we follow guidelines in [205] and propose a detailed approach in orthogonalization of the asymmetric system and compare it with other approximations.

The issue related to the conservation of power is deeply rooted in the seminal description of the array as the result of couplings between the waveguides. In fact, the framework used in Eq. B.11 corresponds to the evolution in terms of optical modes (associated to the isolated waveguides), and not in terms of energy per waveguide. Furthermore, the coupling between optical modes originates from their overlap. This means that the optical mode associated to a waveguide has actual part of its energy propagating inside the neighboring ones (due to overlaps over them). Missing this key point would correspond to the use of wrong projection basis (like a misoriented polarizer when trying to separate two orthogonal polarizations) : modulation occurs then as a result of the interference between the asymmetric (i.e. different) optical modes. The solution to this problem

consist then in redefining the correct propagation basis.

Consider a system of coupled Si waveguides on a SiO_2 substrate with widths of 759 and 649 nm spaced by 110 nm. For simplicity, consider an instantaneous distance x_0 so that there is no dependence on position. The propagation constants at 1550 nm wavelength of individual waveguides are equal to 10.725 and 10.436 μm^{-1}. The waveguides are strongly asymmetric, so to confirm the discussed features we first compute the propagation constants of the supermodes.

In the conventional CMT, if the asymmetry is not taken into account, the eigenvalues of the asymmetric coupled waveguides is computed as:

$$k_{1,2} = eig\left(\frac{\omega}{c}B^{-1}A\right) \pm \frac{\Delta\beta}{2} \tag{B.14}$$

where $\Delta\beta = \beta_1 - \beta_2$ is a difference of propagation constants, and matrices B^{-1} and A are defined according derivations in Chapter A.1. The Eq. B.14 gives the result depicted in cyan squares in Figure B.2 (a). The approach fails to reproduce the numerical results, the resulting propagation constants are symmetric which is not true in the numerics.

Another approach is to use Eq. A.13, where the difference in two waveguides is taken into account correctly :

$$k_{1,2} = eig\left(B^{-1}\frac{\Delta\beta}{2}\begin{bmatrix}-1 & 0\\ 0 & 1\end{bmatrix}B + \frac{\omega}{c}B^{-1}\Delta A\right) = eig(H). \tag{B.15}$$

This equation provides good estimation of propagation constants that fits well the numerical results (yellow diamonds in Figure B.2 (a)). However, the H matrix is non-Hermitian, that would violate the power conservation law.

To "hermitize" H, first let search for the matrix C such as $C = C^\dagger$ and $HC = CH^\dagger$. Using the eigendecompostion of $H = V\lambda V^{-1}$ and the previous expression, we search for C such as : $V\lambda V^{-1}C = C(V^{-1})^\dagger\lambda V^\dagger$. Here, $\lambda \in \Re$, which is similar to the case considered for the $\mathcal{PT}-$ symmetric system. Then the value of C that fulfills this expression is $C = VV^\dagger$ which is Hermitian. Now we use the Cholesky decomposition to transform C into a product of lower and upper triangular matrices $W^\dagger$ and W, respectively. For this, we apply the following strategy:

$$\begin{aligned} C &= VV^\dagger = VUU^{-1}V^\dagger = W^\dagger W \\ W^\dagger &= VU \\ \begin{bmatrix}A & 0\\ B & C\end{bmatrix} &= \begin{bmatrix}V_{11} & V_{12}\\ V_{21} & V_{22}\end{bmatrix}\begin{bmatrix}\cos\Theta & -\sin\Theta\\ \sin\Theta & \cos\Theta\end{bmatrix} \\ \Theta &= \tan^{-1}(V_{12}/V_{11}) \end{aligned} \tag{B.16}$$

U can be any unitary transformation (i.e. rotation by an angle Θ), therefore, according to [205] the orthonormalized version of H reads :

$$H_H = (W^\dagger)^{-1}HW^\dagger. \tag{B.17}$$

Note that this procedure is very general and works for any nonsymmetric system. The eigenvalues of the modified version of the matrix and the initial H are equal, while the eigenvectors are non invariant. That confirms the correct formulation of the problem : we modify the basis of the system now using the new orthogonal supermodes, while the propagation constants are conserved.

To define the new shape of the supermodes (instantaneous), we follow:

$$\begin{aligned}
\frac{\partial \mathbf{\Psi}}{\partial x} &= iH\mathbf{\Psi} \\
\frac{\partial \mathbf{\Psi}}{\partial x} &= iW^{\dagger}(W^{\dagger})^{-1}HW^{\dagger}(W^{\dagger})^{-1}\mathbf{\Psi} \\
\frac{\partial (W^{\dagger})^{-1}\mathbf{\Psi}}{\partial x} &= iH_H(W^{\dagger})^{-1}\mathbf{\Psi} \\
\frac{\partial (W^{\dagger})^{-1}\mathbf{\Psi}}{\partial x} &= iV_H\lambda_H V_H^{\dagger}(W^{\dagger})^{-1}\mathbf{\Psi} \\
\frac{\partial V_H^{\dagger}(W^{\dagger})^{-1}\mathbf{\Psi}}{\partial x} &= i\lambda_H V_H^{\dagger}(W^{\dagger})^{-1}\mathbf{\Psi} \\
\frac{\partial \tilde{\tilde{\mathbf{\Psi}}}}{\partial x} &= i\lambda_H \tilde{\tilde{\mathbf{\Psi}}},
\end{aligned} \tag{B.18}$$

hence, the $\tilde{\tilde{\mathbf{\Psi}}} = V_H^{\dagger}(W^{\dagger})^{-1}\mathbf{\Psi}$ define the supermodes of the orthonormalized system.

The resulting shape the field in the SM representation is depicted in Figure B.2 (b) for non-hermitian matrix H ($\tilde{\mathbf{\Psi}} = V^{-1}\mathbf{\Psi}$) and (c) for hermitian matrix H_H ($\tilde{\tilde{\mathbf{\Psi}}} = V_H^{\dagger}(W^{\dagger})^{-1}\mathbf{\Psi}$) which are compared to (d) results of direct numerical simulations. We see that the modified supermodes reproduce the shape better, however, the details of the second waveguide impact do not fit precisely. It may be explained by the fact that the selected basis is incomplete : since we take into account only the first fundamental mode of each waveguide, some inaccuracies can be present.

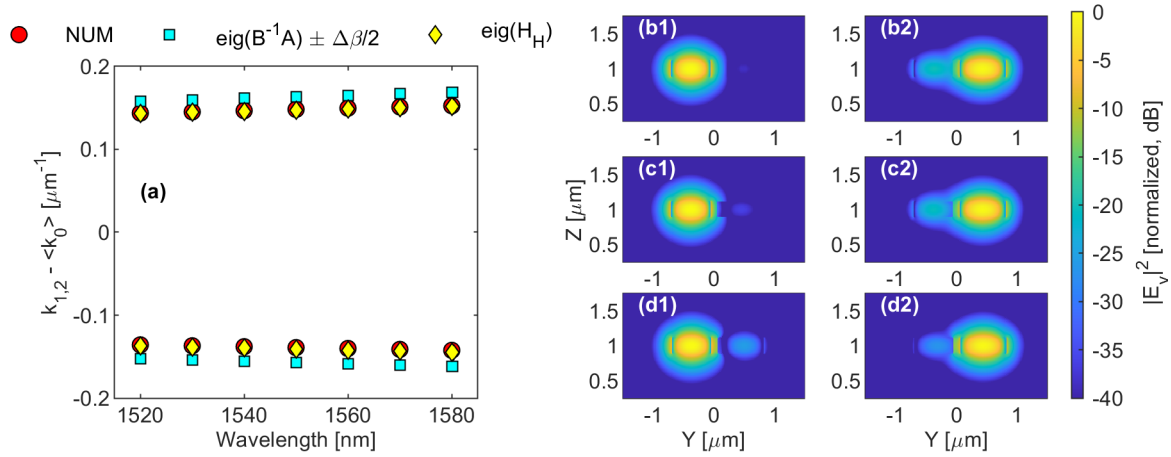

FIGURE B.2: (a) Propagation constants of the supermodes computed from Eq. B.17 (yellow diamonds), Eq. B.15 (cyan squares) compared to numerical simulations (red circles). Supermodes according to (b) the non-hermitian basis $\tilde{\mathbf{\Psi}} = V^{-1}\mathbf{\Psi}$, (c) the orthonormalized basis $\tilde{\tilde{\mathbf{\Psi}}} = V_H^{\dagger}(W^{\dagger})^{-1}\mathbf{\Psi}$, (d) numerical simulations.

If now one includes a dependence of the parameters on the longitudinal direction : $H_H(x), V_H(x)$ and $W(x)$, then the propagation equations read :

$$\frac{\partial \mathbf{\Psi}(x)}{\partial x} = iW^{\dagger}(x)H_H(x)(W^{\dagger}(x))^{-1}\mathbf{\Psi}(x) \tag{B.19}$$

for the direct space and

$$\frac{\partial \tilde{\tilde{\mathbf{\Psi}}}(x)}{\partial x} = \left(\frac{\partial V_H(x)^{\dagger}(W^{\dagger}(x))^{-1}}{\partial x}W^{\dagger}(x)(V_H^{\dagger}(x))^{-1} + i\lambda_H(x)\right)\tilde{\tilde{\mathbf{\Psi}}}(x) \tag{B.20}$$

for the reciprocal space. These equations, respectively, reproduce Eq. B.11 and B.13, so the general propagation equations hold for the orthonormalized modes.

If the actual propagation can always be described by a Hermitian (symmetric) operator (once the correct basis has been defined), one must pay attention that the corresponding modes can the exhibit a strong asymmetry as seen in Figure B.1. The eventual non-Hermitian character of the system would then be moved to the conditions of excitation : is it possible to address one of these supermodes using a continuous (and adiabatic) transformation from a pure symmetric case? Without answering completely this question, we will present next a general procedure about how the flow of light can be controlled in a non-continuous, non-adiabatic manner.

B.2 Strategies for light coupling

Light flow between the waveguides can be achieved if the waveguides are simply put in proximity of each other. However, this method does not allow a control of the coupling distance, interacting modes, robustness to the wavelength variation and etc. If we want to achieve a customized power distribution between the waveguides, we can dephase the two modes by introducing a difference of optical paths [222]. This strategy is robust, but the design can be long and poorly selective. To design a complex photonic chip that would generate tailored outputs depending on the inputs, one may combine building blocks of coupled waveguides, however, the system is not protected from a cross-talk (interaction between unwanted waveguides) and the final design may seem bulky. Moreover, this method doesn't work well in asymmetric waveguides. Therefore, there is a need in development of new methods of selective light control flowing in array of waveguides.

B.2.1. Quantum-inspired adiabatic methods

Quantum control methods for driving a system from an initial to a target state is a base for existing applications of quantum physics. The strategies to transfer a population from one state to another or to excite a molecule are in the heart of the quantum control [223, 224]. There exist techniques to find an optimal external field shape that allows robust and efficient state transfer. Usually, these techniques are of adiabatic nature : the changes acting on a system are slow enough, so it has time to adapt and the system ends in the directly corresponding eigenstate of the final Hamiltonian. In the adiabatic regime, there is no transitions between the system's states, so the supermodes coupling $\frac{\partial V^{\dagger}(x)}{\partial x} V(x)$ term is either null or compensated [225].

Analogies between quantum and guided optics have inspired many theoretical and practical investigations [36] including a concept of adiabatic light transition. The Hamiltonian formulation allows to apply the same techniques as in quantum control. In the result, the tailored variations of coupling and propagation constants allow a broadband and robust light transition [37, 226]. This method can operate in several waveguides configuration and the shape can be scaled up or down depending on the waveguides' parameters. However, since adiabaticity implies slow variation of parameters, the final design may end up lengthy. More generally, the requirement for adiabaticity limits the types of structures that can be implemented, and restricts the vision/understanding we may have about coupled waveguides.

That said, the analogy with quantum systems already resulted in successful strategies. A typical example inspired from quantum mechanics is the adiabatic elimination. In the conventional scheme we consider a system of three waveguides where the middle one is different from the outer ones (different width, refractive index, etc.), which allows to view the waveguides as a three-level quantum system where one level corresponding to the middle waveguide is separated from the others [38] as it is depicted in example in Figure B.3 (b). In

this case, light flows between two outer waveguides without accumulation in the middle one which serves as an intermediate 'weakly populated' level (Figure B.3 (c,d)). This concept corresponds to 'light tunneling' in optical waveguides. Note the absence of energy maximum in the middle waveguide.

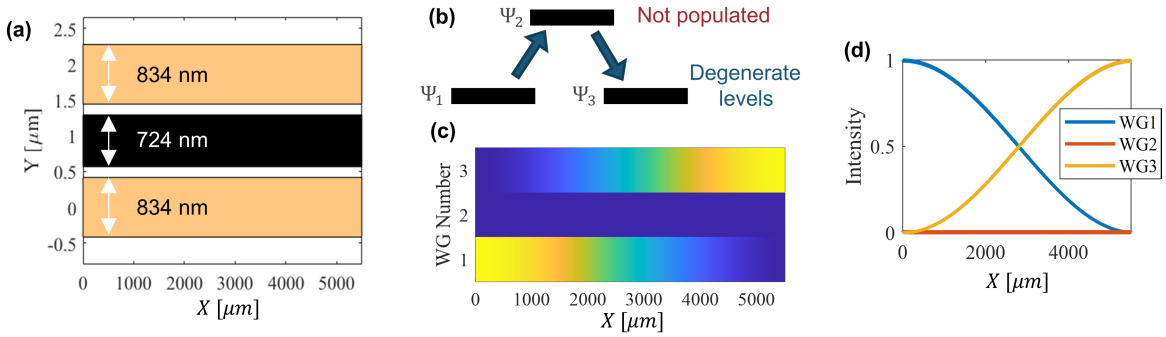

FIGURE B.3: (a) Three-coupled waveguides where the middle one has a different width. (b) The corresponding scheme of 'energy levels', where the middle waveguide has a different propagation constant. (c,d) Light transition that corresponds to adiabatic elimination (normalized, a.u.).

The adiabatic elimination concept can be extended to several waveguides [227] or it can be combined with changes in waveguide separation which allows to achieve a custom energy distribution between the outputs [218, 219]. It has shorter length and dimensions that the adiabatic methods, robust to wavelength variations, and the structures have good tolerance to fabrication imperfections. However, the possibilities to design a complex photonic chip with this concept are limited.

From the photonics point of view, the adiabatic elimination can be understood as modification of the effective coupling constant, so the system can be transformed to a two-mode coupler with the respective effective coupling between them [38]. Similar idea was implemented in [228, 229] where a subwavelength Si strips were placed in between waveguides in an asymmetric manner to reduce a cross-talk by modification of coupling constants. This results in a more compact structure with well-isolated light propagation. If instead of modifications of the coupling constants, waveguides with periodically varying width (in the paraxial direction, while the longitudinal width of each waveguide is constant) can be combined, resulting in various effects of self-splitting, self-induced Talbot effect and effective negative coupling [230, 231].

Overall, adiabatic light control provides robust and scalable techniques, however, the design of a big photonic chip with complex transitions ends up bulky and long, different waveguides cannot be coupled, and the transitions are symmetric.

B.2.2. Non-adiabatic transition of light

The drawbacks of the adiabatic methods stimulate a research for new design strategies able to cope with asymmetric waveguides in densely packed arrays.

Systems composed of different waveguides can indeed take advantage of the unique properties created by the asymmetry. For instance, in [232] the authors develop two grating assisted waveguides with asymmetric inputs and symmetric outputs, which allowed to obtain a coupler with asymmetric transitions. Waveguides of different width have been used also to selectively couple the TM modes : in a three-waveguides configuration presented in [233] the middle waveguide is wider and supports a TM_1 mode, that allows to make a transition

$TM_0 \rightarrow TM_1 \rightarrow TM_0$ between the waveguides. Such strategies can be useful in design of mode multiplexers and demultiplexers [234] or polarization splitters and rotators [28]. In [220, 235] the poor coupling of asymmetric waveguides is used as a switch : with thermo-optic phase shift materials it is possible to control the difference in propagation constants of the coupled waveguide. As a result, the coupling between the waveguides of identical geometry can switched 'on' and 'off' on demand. However, similarly to adiabatic transitions in the systems of asymmetric waveguides just mentioned, there is no energy conversion between the supermodes.

In order to trigger the transition of light between two modes, their inherent phase mismatch must be compensated. This can be done through modulation of the propagation parameters [236]. In guided optics, the concept was proposed in [237] where a high energy pump power was producing a spatial modulation of the refractive index in an optical fiber. If the periodicity of the created grating matches a difference in propagation constants of two modes, the transition between the modes is observed. In waveguides, a light transition was demonstrated in two-waveguides system which was modulated with a sinus-shape perturbation of the refractive index [238]. This approach has demonstrated a good selectivity : if the modulation frequency slightly differs from the difference of propagation constants, the transition efficiency sharply drops.

These first proposals assumed very simple systems (2 modes); and the control was also defined by simple physic oriented reasoning, without relying on any consistent theory. The fact that the proposed modulation did indeed result in the desired effect was considered as enough justification. This approach would unfortunately not allow the control of more complex system, and cannot provide any indication regarding the optimality of the solution. In particular, on top of the frequency of modulation, the excitation must also break a given symmetry (selection rules) in order to couple two modes that have by definition different geometry/symmetry.

Indeed, in principle, the perturbations can be induced not only by the refractive index change but also by variation of other parameters. Correspondingly, we see in Eq. B.13 that the non-trivial evolution of the light is constructed by the $\frac{\partial V^{\dagger}(x)}{\partial x} V(x)$ operators. This operator can have any form, the only requirement being that it must be antisymmetric. In that, the diagonal components correspond to the Berry phase - a parameter reflecting topological properties of the system [181]. Meanwhile the off-diagonal terms correspond to a transfer of energy between supermodes, namely the photonic bands supported by the photonic system. By essence, these terms control the non-adiabatic evolution of the photonic system.

In the following chapter we describe a principle of non-adiabatic transition and demonstrate its light routing properties.

B.3 Non-adiabatic control

B.3.1. Sinusoidal modulation

We focus on the non-adiabatic light control, hence where a transition is produced due to excitation of the supermodes. As it was demonstrated in Figure B.1 (a), coupling of waveguides creates a splitting between propagation constants of two supermodes. Hence, following [237,238] a perturbation with periodicity matching this difference between levels would bring two modes in interaction and would make a transition between the supermodes. In case of two identical waveguides as in Figure B.1, the energy splitting is small, so the oscillations shall be rapid, and in the end, an interference between the odd and the even mode would mask the non-adiabatic transition. Therefore, we consider a system of different waveguides.

We assume a system of three coupled partially etched SiN waveguides (Figure A.2 (b)) of different widths which are placed at 150 nm inter-waveguide spacing each as depicted in Figure B.4 (a). Even though the

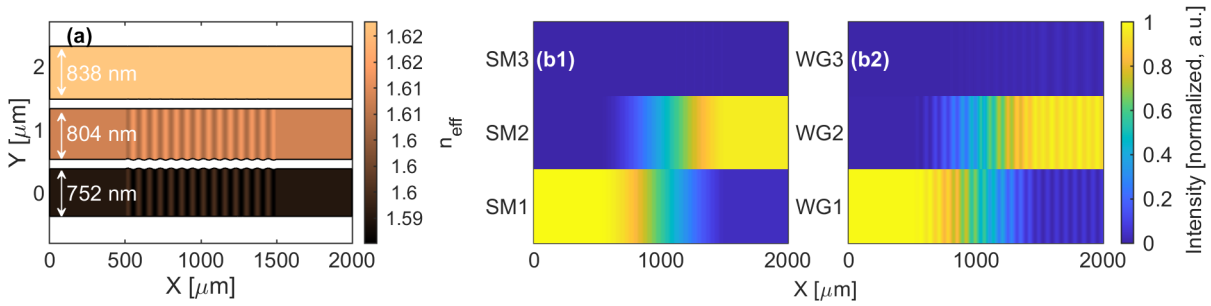

FIGURE B.4: (a) Dielectric structure of SiN waveguides coupled non-adiabatically. (b) Energy transitions in the reciprocal space and in the direct space (panels 1 and 2, respectively) which corresponds to initial excitation of the first supermode.

coupling constant is equal to $0.0073\ \mu\text{m}^{-1}$ (that would correspond to a transition length of 860 μm), the differences in propagation constants of $\Delta k_{12} = 0.088, \Delta k_{13} = 0.14\ \mu\text{m}^{-1}$ (with respect to the 1st waveguide) make the waveguides isolated. In order to couple the supermodes, one must apply a perturbation that matches the difference in propagation constants of the modes. In our case, we select to change geometrical parameters of the waveguides, namely the width of the waveguides, hence we modify the $\beta(x)$ along the propagation direction, which would result in perturbation of the effective index (colorscale in Figure B.4 (a)). It is also possible to vary the inter-waveguide spacing, however, taking into account the fabrication restrictions related to a minimal gap that can be opened (150 nm), we decide to not overstep this limit. Therefore, we apply a modulation on the propagation constants (hence, waveguides width) that reads as $\alpha_\beta \sin \Delta\beta_{ij} x$ with α_β being the modulation amplitude and $\Delta\beta_{ij}$ the difference in propagation constant between the supermodes i and j. In order to be in the perturbative regime, the α_β should be small. In the given configuration, we wand to couple supermodes 1 and 2 applying the perturbation of the strength of $\alpha_\beta = 0.01\ \mu\text{m}^{-1}$ in the middle of the system over a length of 1000 μm. The periodicity of the modulation is $2\pi/\Delta\beta_{12}$ 71.33 μm.

Note that although we formally drive the light in the non-adiabatic regime, this does not require abrupt changes; and light can make an even smoother transition over a rather long length ($\neq$ 500 μm here). The key point is that by applying the right periodicity, it is possible to accumulate coherently infinitely small transitions that would results into a macroscopic change of the light distribution.

The results of the propagation in the reciprocal and direct spaces are depicted in Figure B.4 (b) (panels 1 and 2, respectively). We start with excitation of the first supermode. Since the waveguides are well-isolated at first, the supermode representation correspond directly to excitation of each waveguide in the direct space as it was shown in Figure B.2 (d). Light transition appears only at the perturbation position, while the cross-talk is kept to minimum, and the third waveguide stays isolated. So we can conclude that the main effect causing energy flow is indeed the non-adiabatic transition.

B.3.2. Photonic chip design and optimization

The non-adiabatic coupling allows to design a transition with good selectivity and isolation of transitions, hence, it is beneficial to use in design of complex densely packed photonics chips with minimized cross-talk [239, 240]. In these systems light must be routed efficiently through multiple input and output ports, using a minimal footprint on the chip. Since there are many degrees of freedom that should be optimized in order to design a photonic integrated circuit, a computer optimization can be applied. All optimization strategies can be

classified into two approaches.

The first one operates with a small set of building blocks each performing a specific function, where an assembly of these individual blocks gives a global design [241]. A major advantage of this technique is that each design can then be easily reemployed and adapted to other problems. However, the final design may end up bulky. And since the initial set of the building blocks is limited, the optimality of the final solution is compromised.

The second technique, on the other hand, benefits from extensive use of techniques developed in computer optimization. The inverse design can cope with an extremely large number of degrees of freedom to be optimized [242,243], which results in the design with the smallest footprints and the best performances [244]. The inverse design combined with machine learning techniques allow to boost the efficiency even further [245,246]. However, the drawback of this approach lies in a fact that it is very hard to interpret the geometrical features of the design. Therefore, it is impossible to adapt the existing design to any other even slightly different problem.

So here we propose a combination of these two approaches : with the help of the non-adiabatic transition we can reduce a number of degrees of freedom describing the system, so we can use the computer optimization strategies to find the best design. The advantage of the non-adiabatic approach is that the transition appears in the reciprocal space, so we transform the parameter's space in which the system is optimized. As a result, we simplify the problem by reducing a number of degrees of freedom without simplifying the final solution. With a few parameters, we're still able to form complex shapes and variations of parameters. Note that, later in Section B.4, we provide details on how to obtain an exact optimal shape that allows to perfectly couple the supermodes in the reciprocal space. This leads to non-trivial solutions; and furthermore the perturbations can be combined to give rise to new functionalities. And since we understand the physics underlying the transitions, the system can be easily analyzed and adapted to different situation.

To demonstrate how non-adiabatic transition can be used in design of a complex photonic chip, we target the optimization of a 5-waveguide system where we want to meet the transitions depicted in Figure B.5 (a) [39]. We impose no restrictions on the width of the waveguides, only the inter-waveguide spacing must not be less than 150 nm. And we limit the number of perturbations to 5 and the total length of the device to 1500 μm.

First we present a general strategy to design a photonic meeting the aforementioned objectives. In order to minimize the cross-talk, we use waveguides with different propagation constants, hence, widths. The supermodes propagation constants can be assigned as in 'energy ladder' (Figure B.5 (b2)). As the width of each waveguide proportionally increases, the propagation constants differ by a constant value of $\Delta\lambda$. Note that, the design and optimization are done on the effective propagation parameters, we design and optimize first the propagation matrix, and the physical structure of the waveguides' array (Figure B.5 (b1)) is then reconstructed using a semi-empirical formula developed in the lab.

The connecting individual transitions are placed strategically, so light flows sequentially between the waveguides meeting all the required objectives. However, even though the width of the device does not exceed 6 μm, the structure seems bulky, and the transitions require the full length of the device. So there is a room for optimization of the design.

Next, we challenge this human-made design against the use of a genetic algorithm to generate a computer-optimized solution. By describing the system in term of a maximum of 5-non-adiabatic transitions, we reduce the number of degrees of freedom to be optimized to 34 : 5 initial propagation constants, 4 coupling constants, 5 perturbation each described by their starting position, their length, their amplitudes of modulation α_β and α_κ, and the indices of the two supermodes that they must couple. This massive decrease of the number of parameters to be optimized is also called dimensionality reduction.

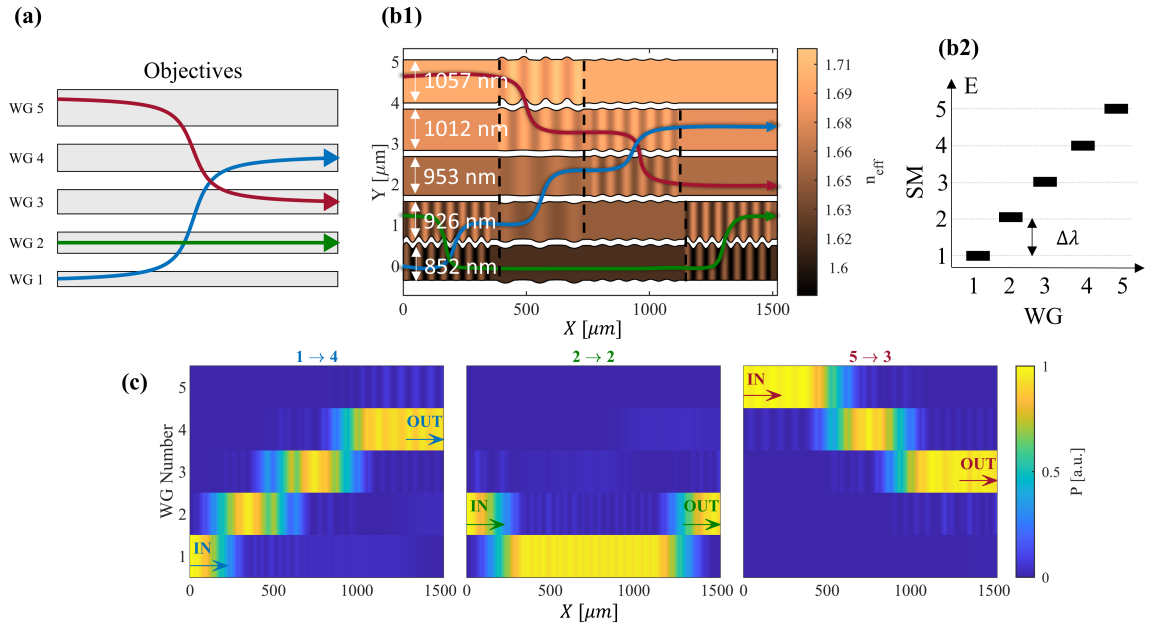

FIGURE B.5: (a) The target transition to be fulfilled on a single photonics chip. (b) The resulting design optimized by a human (panel1) and the corresponding scheme of 'energy levels' of the supported supermodes and light distribution in waveguides (panel 2). (c) Light transition in the direct space.

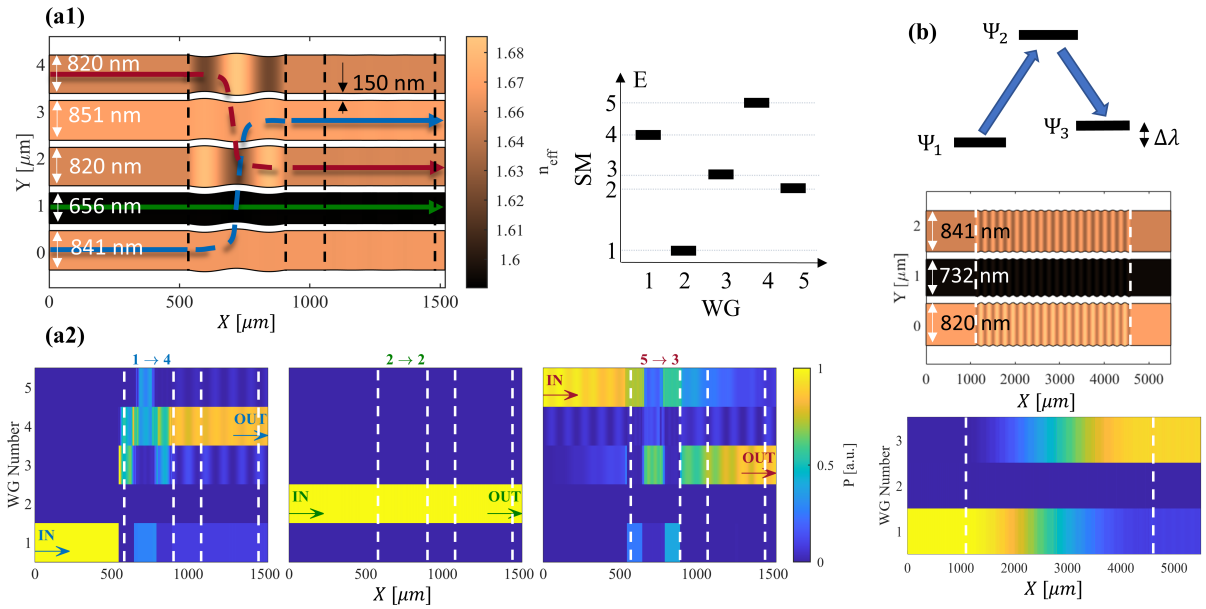

FIGURE B.6: (a1) The GA optimized structure of the photonic chip and a scheme of 'energy levels'. (a2) Light transitions in the direct space. (b) Transition $1 \rightarrow 4$ explained by combination of the adiabatic elimination and the non-adiabatic transition.

The optimization was completed by a genetic algorithm in 5 hours on a regular laptop : Intel I5-7300HQ 2.50 GHz, population size - 300, number of epochs - 100. Score function was defined as a weighted sum of different constraints related to each objectives of the design: correct routing of the light, low cross-talk, minimal

size. The computer started from a random initial guess, so it is a true computer design. This differs greatly from the strategies that most often consist in the computer optimization starting from an initial human-made solution.

The result of the optimization is displayed in Figure B.6 (a1).

Reading the optimized gene, we can analyze the structure and interpret the strategy taken by the computer. The supermodes' 'energy levels' differ from the ladder of consecutive transitions in the human-made design, instead they form an alternate ladder. Such design allows to use each waveguide as an isolation shield and as a transmission channel, simultaneously. This strategy opens up a possibility to design arrays of waveguides with greater density.

The computer solution contains only 3 perturbations instead of allowed 5 : two of them are combined in the middle of the structure between 500 and 1000 μm and are responsible for light routing, while the third one dephases the light and eliminates the residual cross-talk. The combination of two perturbations enhances the functionality and now the light transitions are made concomitantly on a 500 μm scale, which is three times shorter than a solution offered by the hand-made design.

Looking in details into the transition region, we discover that the waveguide 2, which has a different width from the two outer waveguides, prevents light leaks without self-elimination from the light routing (compare transitions $1 \rightarrow 4$ and $2 \rightarrow 2$ in Figure B.6 (a2)). This transition can be interpreted as a combination of the adiabatic elimination [38, 227] and the nonadiabatic transition. Unlike the general adiabatic elimination with degenerate levels (Figure B.3) where transition is done between the degenerate levels, our system has a small energy offset in between these levels (as depicted in example in Figure B.6 (b)). Therefore, when non-adiabatic transition matches this energy gap, the light is routed without accumulation in the middle waveguide.

We demonstrated that non-adiabatic strategy can be used in design of a complex photonic chip. Operation with asymmetric waveguides allows to develop densely packed arrays of the waveguides with little cross-talk. Reduction of degrees of freedom used to describe the system allows an efficient computer optimization of the whole design and not its individual blocks. The formulation of the problem in the reciprocal space allows combination of functionalities and physics-based reading of the design.

B.4 Optimal shape

B.4.1. Derivation and assumptions

Even though the developed approach proved that exact matching of the periodicity the difference of propagation constants allows the supermodes coupling, since we know which term in the propagation equation is responsible for the state excitation, we derive a formalism under which it is possible to obtain an optimal shape. Here the term "optimal" refers to a configuration that allows to couple two supermodes.

We start from the propagation equation in the reciprocal space Eq. B.9, where we denote the eigenvalues as $\boldsymbol{\lambda}(x)$:

$$\frac{\partial \tilde{\boldsymbol{\Psi}}(x)}{\partial x} = \left[\frac{\partial \boldsymbol{V}^{\dagger}(x)}{\partial x} \boldsymbol{V}(x) + i\boldsymbol{\lambda}(x) \right] \tilde{\boldsymbol{\Psi}}(x). \tag{B.21}$$

We separate the phasor term in the supermodes by denoting $\breve{\boldsymbol{\Psi}}(x) = \mathrm{e}^{-i\int_0^x \lambda(x')dx'} \tilde{\boldsymbol{\Psi}}(x)$, and after translation

to this rotating basis we obtain:

$$\frac{\partial \breve{\boldsymbol{\Psi}}(x)}{\partial x} = -i\mathrm{e}^{-i\int_0^x \lambda(x')dx'}\boldsymbol{\lambda}(x)\mathrm{e}^{i\int_0^x \lambda(x')dx'}\breve{\boldsymbol{\Psi}}(x) + i\mathrm{e}^{-i\int_0^x \lambda(x')dx'}\boldsymbol{\lambda}(x)\mathrm{e}^{i\int_0^x \lambda(x')dx'}\breve{\boldsymbol{\Psi}}(x) + \mathrm{e}^{-i\int_0^x \lambda(x')dx'}\frac{\partial \boldsymbol{V}^\dagger(x)}{\partial x}\boldsymbol{V}(x)\mathrm{e}^{i\int_0^x \lambda(x')dx'}\breve{\boldsymbol{\Psi}}(x), \tag{B.22}$$

$$\frac{\partial \breve{\boldsymbol{\Psi}}(x)}{\partial x} = \mathrm{e}^{-i\int_0^x \lambda(x')dx'}\frac{\partial \boldsymbol{V}^\dagger(x)}{\partial x}\boldsymbol{V}(x)\mathrm{e}^{i\int_0^x \lambda(x')dx'}\breve{\boldsymbol{\Psi}}(x), \tag{B.23}$$

$$\frac{\partial \breve{\boldsymbol{\Psi}}(x)}{\partial x} = \boldsymbol{\sigma}(x)\breve{\boldsymbol{\Psi}}(x). \tag{B.24}$$

Here we have removed the phasor terms $i\lambda$ from the propagation equation, and only the supermodes coupling term $\boldsymbol{\sigma}(x)$, which takes into account the phase changes between the supermodes, is left. In this formulation, the $\frac{\partial \boldsymbol{V}^\dagger(x)}{\partial x}\boldsymbol{V}(x)$ term responsible for the supermodes coupling reads:

$$\frac{\partial \boldsymbol{V}^\dagger(x)}{\partial x}\boldsymbol{V}(x) = \mathrm{e}^{i\int_0^x \lambda(x')dx'}\boldsymbol{\sigma}(x)\mathrm{e}^{-i\int_0^x \lambda(x')dx'} = \boldsymbol{\alpha}(x). \tag{B.25}$$

If we start from a basis with orthogonal modes (hence, a hermitian system), then $\boldsymbol{V}^\dagger\boldsymbol{V} = \boldsymbol{V}\boldsymbol{V}^\dagger = \mathbb{1}$ and $\frac{\partial \boldsymbol{V}^\dagger(x)}{\partial x}\boldsymbol{V}(x) = -\boldsymbol{V}^\dagger(x)\frac{\partial \boldsymbol{V}(x)}{\partial x} = -\left(\frac{\partial \boldsymbol{V}^\dagger(x)}{\partial x}\boldsymbol{V}(x)\right)^\dagger$ or $\boldsymbol{\alpha}^\dagger(x) = -\boldsymbol{\alpha}(x)$. This condition is fulfilled only when the diagonal part of $\boldsymbol{\alpha}(x)$ is imaginary, and the off-diagonal terms are of opposite signs : $\alpha_{jj} \in \Im$, $\alpha_{ij}^* = -\alpha_{ji}$.

Similarly, since $\boldsymbol{\alpha}^\dagger(x) = -\boldsymbol{\alpha}(x)$:

$$\left(\mathrm{e}^{i\int_0^x \lambda(x')dx'}\boldsymbol{\sigma}(x)\mathrm{e}^{-i\int_0^x \lambda(x')dx'}\right)^\dagger = -\mathrm{e}^{i\int_0^x \lambda(x')dx'}\boldsymbol{\sigma}(x)\mathrm{e}^{-i\int_0^x \lambda(x')dx'}, \tag{B.26}$$

hence, the same conditions are true for the $\boldsymbol{\sigma}^\dagger(x) = -\boldsymbol{\sigma}(x)$, so $\sigma_{jj} \in \Im$, $\sigma_{ij}^* = -\sigma_{ji}$.

To know, how the parameters should vary with propagation in order to obtain the optimal coupling, we compute the derivative of the propagation matrix :

$$\frac{\partial \boldsymbol{M}(x)}{\partial x} = \frac{\partial \boldsymbol{V}(x)}{\partial x}\boldsymbol{\lambda}(x)\boldsymbol{V}^\dagger(x) + \boldsymbol{V}(x)\frac{\partial \boldsymbol{\lambda}(x)}{\partial x}\boldsymbol{V}^\dagger(x) + \boldsymbol{V}(x)\boldsymbol{\lambda}(x)\frac{\partial \boldsymbol{V}^\dagger(x)}{\partial x}, \tag{B.27}$$

$$= (\boldsymbol{V}(x)\boldsymbol{V}^\dagger(x))\frac{\partial \boldsymbol{V}(x)}{\partial x}(\boldsymbol{V}^\dagger(x)\boldsymbol{V}(x))\boldsymbol{\lambda}(x)\boldsymbol{V}^\dagger(x) + \boldsymbol{V}(x)\frac{\partial \boldsymbol{\lambda}(x)}{\partial x}\boldsymbol{V}^\dagger(x) + \boldsymbol{V}(x)\boldsymbol{\lambda}(x)(\boldsymbol{V}^\dagger(x)\boldsymbol{V}(x))\frac{\partial \boldsymbol{V}^\dagger(x)}{\partial x}(\boldsymbol{V}(x)\boldsymbol{V}^\dagger(x)). \tag{B.28}$$

Using $\boldsymbol{\alpha}(x) = \frac{\partial \boldsymbol{V}^\dagger(x)}{\partial x}\boldsymbol{V}(x)$, $-\boldsymbol{\alpha}(x) = \boldsymbol{V}^\dagger(x)\frac{\partial \boldsymbol{V}(x)}{\partial x}$ and the eigen decomposition of $\boldsymbol{M}(x)$, we transform this equation to :

$$\frac{\partial \boldsymbol{M}(x)}{\partial x} = \boldsymbol{V}(x)\frac{\partial \boldsymbol{\lambda}(x)}{\partial x}\boldsymbol{V}^\dagger(x) + \boldsymbol{M}(x)\boldsymbol{V}(x)\boldsymbol{\alpha}(x)\boldsymbol{V}^\dagger(x) - \boldsymbol{V}(x)\boldsymbol{\alpha}(x)\boldsymbol{V}^\dagger(x)\boldsymbol{M}(x). \tag{B.29}$$

Now we can solve this Eq. B.29 and obtain the optimal configuration of the system where the supermodes transition is maximized. In order to define the supermodes transition, we must define the supermodes coupling term $\boldsymbol{\alpha}(x)$ which can be interpreted as a transition control parameter. We know that $\boldsymbol{\alpha}^\dagger(x) = -\boldsymbol{\alpha}(x)$ and

$\boldsymbol{\sigma}^{\dagger}(x) = -\boldsymbol{\sigma}(x)$ must be fulfilled. So for a 2 by 2 system we have found the following Pauli matrices that satisfy these conditions :

$$\boldsymbol{\alpha}(x) = \mathrm{e}^{i\int_0^x \lambda(x')dx'}\left[i\sigma^{(0)}\begin{pmatrix}1 & 0\\ 0 & -1\end{pmatrix} + i\sigma^{(1)}\begin{pmatrix}1 & 0\\ 0 & 1\end{pmatrix} + \sigma^{(2)}\begin{pmatrix}0 & -1\\ 1 & 0\end{pmatrix} + \sigma^{(3)}\begin{pmatrix}0 & i\\ i & 0\end{pmatrix}\right]\mathrm{e}^{-i\int_0^x \lambda(x')dx'}. \tag{B.30}$$

Here we split the coupling matrices and the strength of interaction denoted as $\sigma^{(i)}$. Therefore, to obtain an optimal shape of the propagation and coupling constants (combined in $\boldsymbol{M}(x)$), we solve Eq. B.29 with Eq. B.30. The diagonal operators with $\sigma^{(0)}, \sigma^{(1)}$ imply changes of only phase. These terms are the Berry phase that characterize the topological nature of the evolution, but do not cause transition of light. The terms $\sigma^{(2)}$ and $\sigma^{(3)}$, which maximize the supermodes coupling, are the terms responsible for transition. Interestingly, we see that there exist potentially two means of equivalent efficiency in order to couple two supermodes.

B.4.2. Results and properties

As an example, we consider a two coupled waveguides system with initial propagation constants $k_{01} = 10.8113$ $\mu\mathrm{m}^{-1}$, $k_{02} = 10.7287$ $\mu\mathrm{m}^{-1}$ ($\Delta k = 0.0826$ $\mu\mathrm{m}^{-1}$) and a coupling constant $\kappa_{12} = \kappa_{21} = 0.0754$ $\mu\mathrm{m}^{-1}$. If the parameters of the system are kept constant, light propagates uncoupled both in direct and reciprocal spaces since two waveguides are asymmetric. To trigger the light transition, we now want to vary the parameters and obtain $\beta_{1,2}(x), \kappa_{12,21}(x)$ that allow to couple the supermodes.

We solve Eq. B.29 choosing the strength of modulation as multiple of the difference in supermodes propagation constants, first, for the $\begin{pmatrix}0 & -1\\ 1 & 0\end{pmatrix}$ transition $\sigma^{(2)} = 0.2\Delta\lambda$, second, for the $\begin{pmatrix}0 & i\\ i & 0\end{pmatrix}$ coupling type with $\sigma^{(3)} = 0.2\Delta\lambda$. Both cases are displayed in Figure B.7 (a) and (b), respectively.

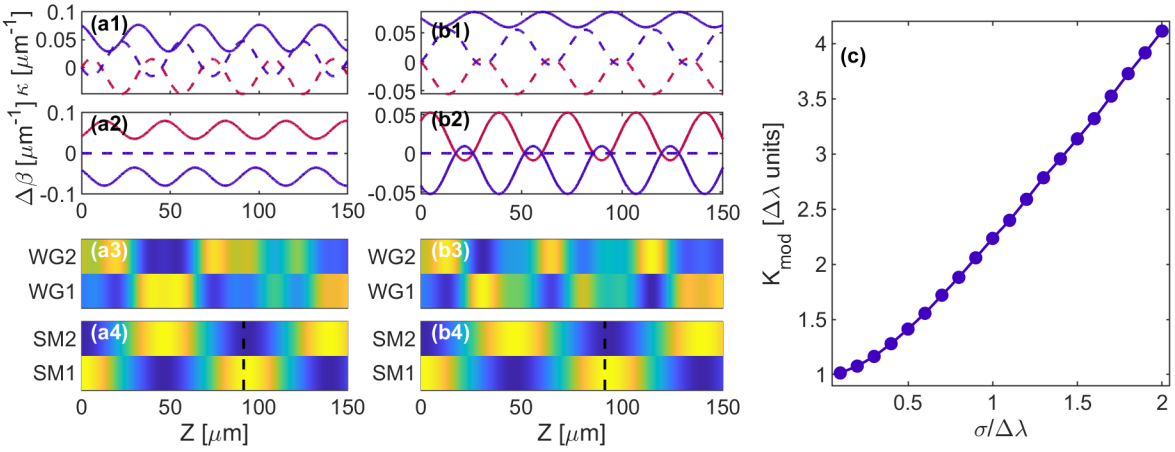

FIGURE B.7: Optimal shape and light transitions for non-adiabatic coupling in a system with $\beta_{01} = 10.8113$ $\mu\mathrm{m}^{-1}$, $\beta_{02} = 10.7287$ $\mu\mathrm{m}^{-1}$, $\kappa_{12} = \kappa_{21} = 0.0754$ $\mu\mathrm{m}^{-1}$ initial parameters. Panels (a) and (b) correspond to $\sigma^{(2)} = 0.2\Delta\lambda$ and $\sigma^{(3)} = 0.2\Delta\lambda$, respectively. Panels 1-2 display the resulting parameters with solid and dashed lines denoting real and imaginary parts, respectively; and panels 3-4 light transitions in the direct and reciprocal spaces (a.u., normalized). Black dashed line marks period of modulation defined as π/σ (c) Periodicity of parameters modulation depending on its strength $\sigma^{(2)}$.

The resulting $\beta(x)$ and $\kappa(x)$ vary periodically with distance following a shape resembling -but no exactly equal to- the sinusoidal modulation. Note that, modulations of $\sigma^{(2)}$ and $\sigma^{(3)}$ produce different solutions, but the modulation period is the same, and the $\kappa(x)$ contains an imaginary part while $\kappa_{12} = \kappa_{21}$. Here we did not implement any constraints on the parameters being real or fitting in into the fabrication constraints. The imaginary coupling can be tailored in a system with losses and gain [247], however, in our applications it is better to put constrains on the parameters.

The modulation period of coupling and propagation constants is the same, however, unlike the previous case, it is not approximated by a difference in propagation constants of the supermodes. In fact, it holds a more complex dynamics : in a small modulation, hence perturbation, regime, the conservation of wavevectors is fulfilled, and the periodicity matches $\Delta\lambda$ (which is consistent with assumptions in [237, 238]). However, as soon as the modulation strength grows, the periodicity increases too. This property is depicted in Figure B.7 (c). This nonlinear dependence of the modulation frequency with the modulation amplitude is clearly a non trivial property that may only be accessed through the theory we just demonstrated.

For the waveguides modulated with the optimal pattern we observe an energy exchange and periodic excitation of the supermodes, and the consequent light transition between the waveguides in the direct space (Figure B.7 (a,b 3-4)). The beating periodicity is controlled by the modulation strength so that $L_{per} = 2\pi/\sigma$. That allows to reach short propagation distances in an optimized manner.

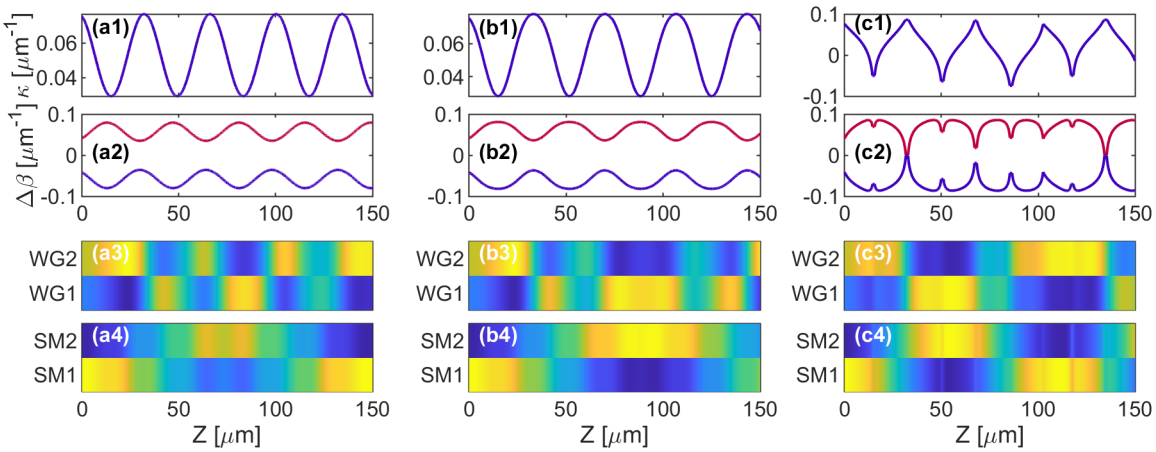

FIGURE B.8: System parameters and the respective light propagation for the same coupled waveguides as in Figure B.7 with (a) keeping only real part of solution displayed in panels (a) in Figure B.7; (b) forcing real $\boldsymbol{M}(x)$ matrix when solving Eq. B.30; (c) compensating imaginary part by $\sigma^{(3)}$.

Since imaginary coupling constant is not easy to obtain for simple coupled dielectric waveguides, we seek for ways to obtain real solutions for the optimal shape. If we simply keep only the real part of the previous parameters (Figure B.8 (a1-2)), then the light flow is not so efficient : in the reciprocal space, Figure B.8 (a4), poor light transfer is achieved, so the state transition is not complete, which results in complex light patterns in the direct space.

One strategy could be to enforce the $\boldsymbol{M}(x)$ being real while solving the Eq. B.30. To do so, we keep only real part of the matrix at each step of the derivation. The resulting shapes are displayed in Figure B.8 (b1-2). Now the parameters modulation differs more from a sinus shape, and its periodicity does not match the previous results. However, supermodes coupling is achieved with a better efficiency (Figure B.8 (b3-4)). The period of

the transition differs from the $L_{per} = 2\pi/\sigma$ value too.

Since the modulation associated with $\sigma^{(3)}$ is imaginary, another strategy could be to use this matrix to compensate for a growing imaginary part of the solution. In this case we expect to overlap two complex modulations, and the resulting modulation could be of only real-values. To implement this in practice, we adapt the $\sigma^{(3)}$ to the imaginary part of the off-diagonal terms of the propagation matrix. Since by construction, the coefficient attributes to the imaginary part itself, we rescale it to match precisely the required compensation : $\sigma^{(3)} = -\sigma^{(2)} \frac{\Im(\delta M_{12}^{(2)})}{\Im(\delta M_{12}^{(3)})}$, here $\delta M_{12}^{(i)}$ denote the Eq. B.29 with keeping only coupling terms associated to $\sigma^{(i)}$.

The resulting parameters are displayed in Figure B.8 (c1-2). The shape of the modulation forms indeed a complex pattern. But that still remains within realistic bounds. Light coupling in both direct and reciprocal spaces (B.8 (c3-4)) has good efficiency, the discontinuities in light propagation should be referred to numerical inaccuracies from interpolation of the shapes (to speed up the calculation we interpolate the parameters over a coarser grid).

Overall, the optimal shape for non-adiabatic transitions gives promising results to be applied in densely packed array of waveguides. It offers shorter solutions with limited cross-talk, and the distance of coupling can be tailored to ones needs.

B.4.3. Bloch modes

The waves traveling through a periodic structure can be described in terms of Bloch modes, defined as : $\mathbf{\Psi}_B(x) = \boldsymbol{u}(x)\mathrm{e}^{ik_B x}$ with $\boldsymbol{u}(x)$ being a periodic function that matches the periodicity of the structure, and k_B is the Bloch wave vector [248]. Then light behavior can be analyzed in the reciprocal space of Bloch modes, so the patterns in the direct space can be seen as an interference between these modes which results in light beating [249]. In a sense, it is similar to a simple beating in symmetric waveguides when even and odd modes are excited in the reciprocal space (an example is displayed in Figure B.1 (c)). While here we are looking at a "reciprocal space of a reciprocal space" where we find odd and even Bloch modes and observe their interference resulting in transition between the supermodes.

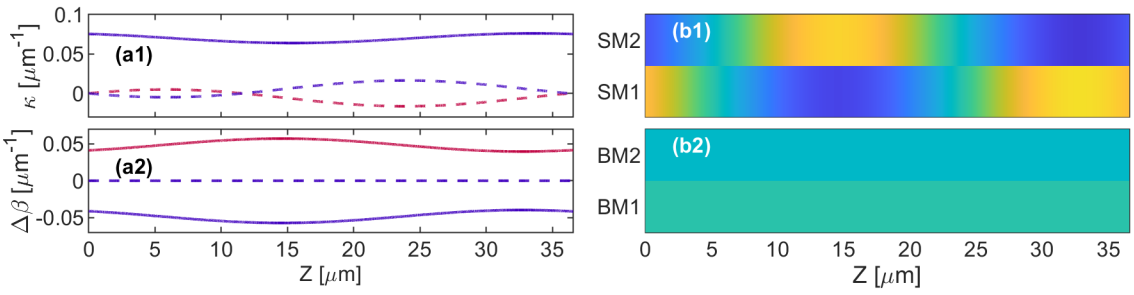

FIGURE B.9: (a) One period of changes in coupling (panel 1) and propagation (panel 2) constants. (b) Evolution of Bloch Modes (panel 2) and the respective transitions in the reciprocal space (panel 1).

By definition, Bloch modes must be periodic, so that $\boldsymbol{u}(0) = \boldsymbol{u}(L_{per})$, therefore, they shall fulfill the

following propagation equation :

$$\begin{aligned} \rho_{out} &= [\boldsymbol{T}]\rho_{in} \\ \begin{pmatrix} \rho_1^{(1)} & \rho_1^{(2)} \\ \rho_2^{(1)} & \rho_2^{(2)} \end{pmatrix} &= [\boldsymbol{T}] \begin{pmatrix} 1 & 0 \\ 0 & 1 \end{pmatrix}. \end{aligned} \tag{B.31}$$

Here ρ_{in} and ρ_{out} are the input and the respective outputs distribution between the supermodes (in $\rho_j^{(i)}$, j are the output supermode and i the excited supermode index), and $[\boldsymbol{T}]$ represents an arbitrary change between the supermodes energy distribution. In the Bloch modes basis, $[\boldsymbol{T}]$ is diagonal with eigenvalues equals to $\boldsymbol{k}_B$. Then if we use the diagonalization of $\rho_{out} = [\boldsymbol{T}] = \boldsymbol{V}_b \boldsymbol{k}_B \boldsymbol{V}_b^{\dagger}$, the definition of $[\boldsymbol{T}]$ is satisfied.

Therefore, in our system, the Bloch modes are defined as eigenvectors of the output matrix. As an example, consider the system described in the previous chapter with $k_1 = 10.8113\ \mu\text{m}^{-1}$, $k_2 = 10.7287\ \mu\text{m}^{-1}$ ($\Delta k = 0.0826\ \mu\text{m}^{-1}$) and $\kappa_{12} = \kappa_{21} = 0.0754\ \mu\text{m}^{-1}$. The optimal shape of parameters is obtained for a case of $\sigma^{(2)} = 2^{-4}\Delta\lambda, \sigma^{(3)} = 0$ with no constraints on the parameters being real applied (one period is displayed in Figure B.9 (a)).

After calculation of Bloch modes according to the presented method, we find even and odd combinations of the supermodes. After one Bloch mode is excited, it propagates unchanged as displayed in panel (b2) of Figure B.9. In the supermode basis, in the meantime, we observe an interference between these modes dephased with propagation distance (panel (b1) of Figure B.9). The light evolution is periodic and the final state is identical to the input which confirms the properties of the Bloch modes.

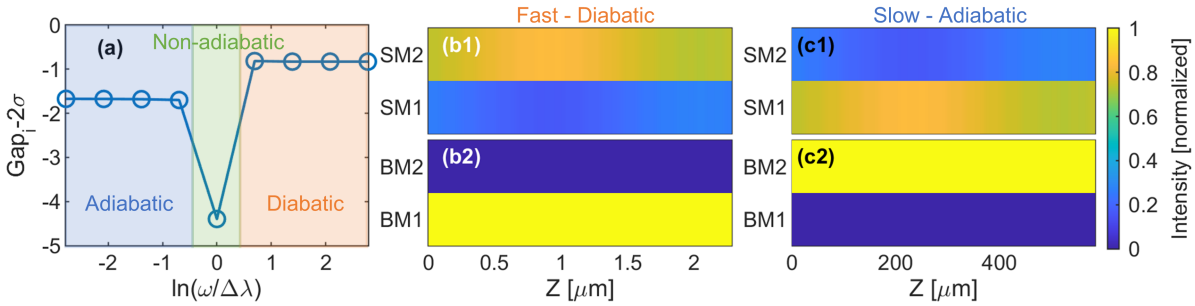

FIGURE B.10: (a) Relative evolution of the Bloch mode splitting versus the frequency of modulation ω (log scale). Colors indicate different propagation regimes depending on modulation frequency. Propagation of Bloch and supermodes for (b) the shorter period of 2.29 μm^{-1} and (c) longer period of 585 μm^{-1}, which corresponds to diabatic (fast) and adiabatic (slow) evolution, respectively. For the non-adiabatic transition refer to Figure B.9.

As the supermode coupling must occur at a rate 2σ, then this number must correspond to the Bloch modes frequency splitting at resonance. To verify this hypothesis, we rescale the periodicity of modulation (with keeping the amplitude of modulation unchanged) and compute the Bloch modes for each case. Then we check the difference between Bloch modes eigenvalues and compare it with $2\sigma^{(2)}$. The results displayed in Figure B.10 (a) show that gap matching is fulfilled only at the nominal periodicity, so that the non-adiabatic supermodes coupling is fulfilled (green region in Figure B.7 (a)). This feature reflects the efficiency of supermodes coupling. The cases where the periodicity is not matched can be split into two types of dynamics : the longer periodicity results in slow variation of parameters, hence, adiabatic dynamics (blue region in Figure B.7 (a)); while the shorter periodicity corresponds to diabatic transition (orange region in Figure B.7 (a)) where the parameters evolve fast and (relatively) high, and the system has no time to adapt. These two borderline cases are

displayed in Figure B.10 (b) and (c). In both cases, the Bloch modes do not combine the supermodes equally, which results in isolated propagation of the supermodes with no interference. Hence, no coupling between the supermodes is triggered, and the modulation then only acts as an effective medium.

Note that, here we select a low modulation amplitude $\sigma^{(2)} = 2^{-4}\Delta\lambda$, so that periodicity of light transition and modulation nearly matches (check Figure B.7 (c)). In other cases, when the frequency of transition depends nonlinearly on the modulation amplitude (discussed in the previous subsection), the dynamics is more complex and even though the Bloch modes can be found, the gap splitting doesn't match the modulation amplitude.

Here we demonstrate another interpretation of supermodes coupling and light propagation in the non-adiabatic regime. We believe that this discussion can stimulate a better understanding of light coupling. The formation of Bloch mode, and the subsequent apparition of photonic bandgap.

B.5 Conclusion

We demonstrate a new type of light control in a coupled waveguides system. Instead of relying on adiabatic transition, we maximize the non-adiabatic coupling that exchanges the energy between the supermodes - eigen solutions of the system. This method has an analogy with quantum mechanics : we fulfill a frequency matching condition between two states and excite one, as it is done in excitation of atoms. Thus we control light flow in the reciprocal space by bringing in interaction the supermodes, which results in light transition in the direct space. This method allows to couple asymmetric waveguides by applying localized perturbations.

We show that in the simplest case we should apply a small sinusoidal modulation of the waveguides' parameters with a frequency matching a difference in propagation constants of the supermodes. Following this approach, we reduce a number of parameters used to describe the system, which allows then to efficiently apply computer optimization strategies. The non-adiabatic coupling allows to combine several perturbations or even different strategies (for instance, adiabatic elimination) to obtain new functionalities and enhance device performance. The method allows to design complex photonic switches with low cross-talk and high efficiency. Hence, we believe that it can be useful in systems of densely packed arrays of waveguides.

From direct theoretical guidelines we develop expression for the optimal coupling shape. Here the interaction is guides by a more complex dynamics : the frequency of modulation depends on the modulation strength and it matches the difference in propagation constants only in perturbative regime. The transitions can be obtained at shorter propagation distances, which opens new possibilities in design.

Finally, we interpret a transition between the supermodes as a result of interference of the Bloch modes. When a periodicity matches the difference between two Bloch modes, a beating in the reciprocal space is observed. This bring up interesting discussions about interpretation of the modes interaction.

Appendix C

Analysis of Dispersive Fourier Transform dataset using Dynamic Mode Decomposition

We demonstrate that the Dynamic Mode Decomposition (DyMD) technique can effectively reduce the amount of noise in Dispersive Fourier Transform (DTF) dataset; and allow for finer quantitative analysis of the experimental data. We therefore show that the oscillation pattern of a soliton molecule actually results from the interplay of several elementary vibration modes.

C.1 DFT technique for investigating the laser cavity properties

Since its first demonstration, the DFT has been a key experimental technique to investigate ultrafast fiber ring laser cavities [250–254]. As a convenient way to observe the pulse evolution round-trip after round-trip, this technique allows indeed a better comprehension of the nonlinear phenomena governing these systems. If the main features of fiber ring laser cavities are now well understood, it appears that weaker effects are also of importance because they can build-up to the point where their contribution to the dynamics becomes also determinant [255, 256]. Correspondingly, DFT experiments would now require either very long record time - so that the long-term dynamics caused by the weaker effects can fully develop; and more acute measurements - so that minute phenomena can be observed [256]. Experimentally, the bottleneck would therefore come from the oscilloscope which records the DFT trace. Indeed, the electronic noise and the discretization granularity prevent recording the single shot spectra with utmost precision and the limited memory capacity hinders the observation of long timescale dynamics.

Using the example of a three-soliton molecule, we demonstrate that the DyMD allows minimizing experimental noise without compromising the quality of the information. We show in particular that this technique is more efficient than any other curve smoothing techniques, for instance, the Savitzky-Golay filter [257]. Namely, we fully characterize the oscillations of a 3-Soliton Molecule (SM) and demonstrate that it comprises two nonlinear oscillators of different timescales that are coupled to each other. On a more practical aspect, DyMD permits lossless compression of the DFT dataset by at least a 90 % factor.

This demonstration is the occasion to show that DyMD provides a fine qualitative analysis of the dynamics

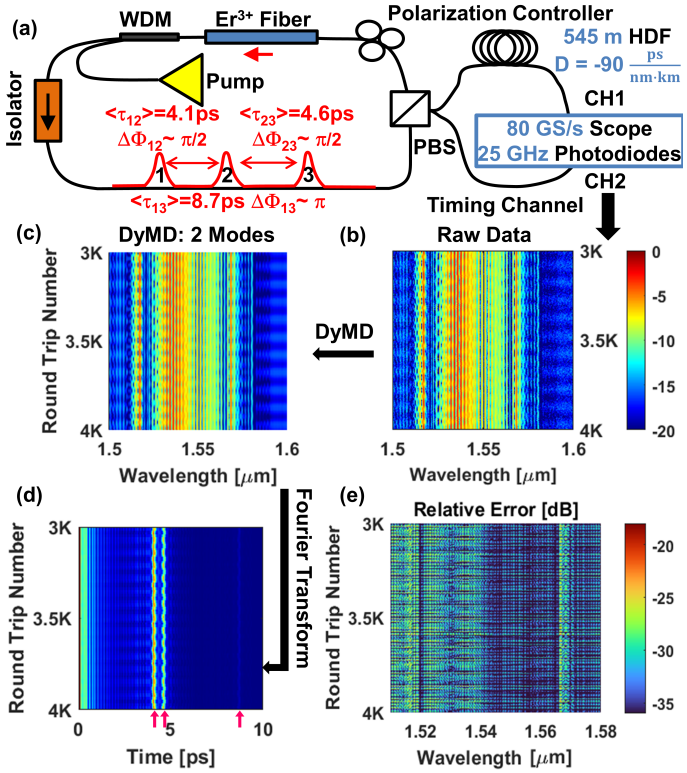

FIGURE C.1: (a) Experimental setup; PBS: polarization beam splitter; HDF: 545 m of Highly Dispersive Fiber; Pump: 980-nm laser diode; WDM: pump-signal multiplexer. (b) Single-shot spectra. (c) DFT Spectra after 2-Mode reduction by Dynamic Mode Decomposition. (d) Fourier Transform of (b) showing three characteristic inter-Soliton seperations of 4.1 ps 4.6 ps and 8.7 ps (pink arrows). (e) Error of the DyMD in (b). -3 dB corresponds to 1 Bit of precision (hence -24 dB is 8-Bit precision). Subpanels (b-e) are represented in logarithmic scale.

of SMs, which are bound states formed by dissipative solitons [258] traveling in close interaction around the laser cavity [259,260]. The large variety of mechanisms responsible for their existence, for instance, gain recovery dynamics, cross-phase modulation effect [261], laser noise [262, 263], emission of dispersive waves [264], or acoustic phenomena [265], results in the SMs exhibiting numerous distinct vibration patterns. In detail, we consider here a 5-m long fiber ring laser cavity comprising 3 meters of Erbium doped fiber and a polarizer (see Figure C.1-(a)). Mode-locking is ensured by nonlinear polarization rotation followed by discrimination through a polarization beam splitter, also acting as the output coupler. After dispersion of the laser output in a -50 ps/nm Highly Dispersive Fiber (HDF), the DFT spectra are recorded by an 80 GS/s, 40 GHz electrical bandwidth, 8-bit depth oscilloscope. The photodiode has a 25 GHz bandwidth, and acts as a low pass filter for higher frequencies. This laser architecture can support the propagation of a 3-SM, characterized by the distinct interferometric fringes seen on the DFT spectra (Figure C.1-(b)).

C.2 DMD analysis of the SM

As detailed later, this molecule can be described as two coupled oscillators. It exhibits in Figure C.2 a complex oscillatory pattern with a principal periodicity of about 71 round-trips (RTs). Note that the SM under investigation here is not a soliton crystal because the solitons do not have the same optical phase: the leading and

the trailing soliton are actually π-shifted, resulting in a more unstable interaction. Therefore, the separation between the middle and the last soliton is slightly larger than the one between the leading and middle soliton. Another consequence is that the soliton pairs have radically different properties and exhibit a very complex dynamics [266]. If the vibrations associated to the two closest pairs of solitons can be easily retrieved from the Fourier transform of the DFT spectra, the last oscillatory pattern created by the interaction of the two solitons located at each bound of the molecule clearly suffers from strong measurement noise (Figure C.2-(c,f), black dots) despite the noise level being already drastically reduced by the use of a Savitzky-Golay [257] filter (hence a 4^{th} order polynomial fit over a sliding window). This type of filtering does indeed reduce the amount of noise, but it cannot suppress low frequency noise (aka. drift), and furthermore filters out any fast-varying data. Consequently, this signal processing helps improving the precision of the measurement to some extent, but it leaves some residual artifacts that will ultimately limit the former. In brief, the main limitation of such a filtering originates from the fact that it is conducted independently on each single shot spectrum; and therefore it does not benefit from the knowledge of the whole evolution of the single-shot spectra in order to identify truly random features, namely noise. Therefore, we performed a DyMD [174, 267] on the DFT dataset (Figure C.1-(b)) in order to improve the quality of the data. It consists in decomposing the instantaneous snapshot spectra $S(\lambda, n)$ at round-trip n as $S(\lambda, n) = \sum_k \Re(\ Mode_k(\lambda) b_k(n)\ )$. The temporal dynamics of the laser system is then encoded in the b_k coefficients (Figure C.3-(c,d)), whereas the $Mode_k$ contains the information related to vibration modes (Figure C.3-(a-b)). This decomposition method uses the full DFT dataset, hence it is more accurate than any local filtering and fitting technique. As the DyMD relies on a round-trip-shifted covariance, we believe that it is very well suited for DFT data because the spectrum evolves non-chaotically round-trip after round-trip. The result of the DyMD performed with respectively 1, 2, and 4 modes is shown in Figure C.2.

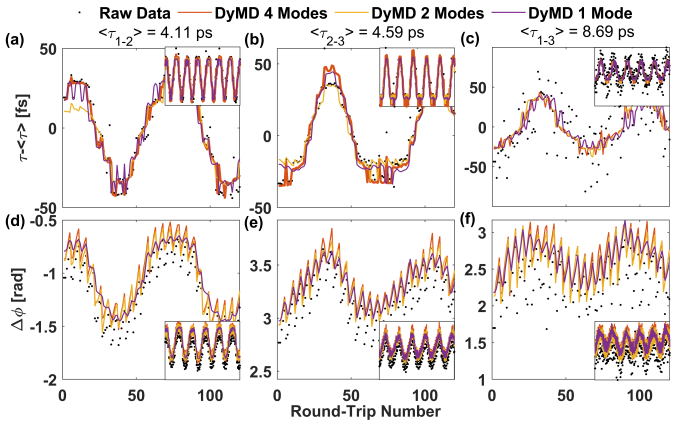

FIGURE C.2: (a-b-c). Evolution of the inter-soliton separation for different soliton pairs: $\{1-2\}$, $\{2-3\}$, and $\{1-3\}$, respectively. (d-e-f): Same as above, but for the optical phase difference between the solitons. The insets show the signal reconstruction over 400 round-trips. Black points stand for data processed using a Stavitzky-Golay filter. Orange: 4-Mode DyMD. Yellow: 2-Mode DyMD. Purple: 1-Mode DyMD.

First we see in Figure C.2 that the relative motion of the trailing and heading solitons is now retrieved correctly, whereas it suffers from very strong noise as seen for the raw data. In details, we see first that the vibration patterns reproduced by the 4-Mode decomposition (Figure C.2, orange lines) follow almost exactly the original data. The 2-mode decomposition (yellow lines in Figure C.2) reconstructs the experimental data

with an average error of 1 bit, and the maximal error never exceeds 2 bits. This validates the ability of the DyMD to investigate more complex soliton molecules that would remain hidden in the electronic noise. Note that center of the single-shot spectra is not known *a priori*, which results after Fourier Transform into a global phase slope (The reader may refer to Ref. [256] regarding how the time-offset vs. frequency-shift entanglement in the DFT can be further mitigated). As part of the DFT procedure, this phase slope must be corrected. Noise has of course an impact and results in a systematic offset in the phase difference as seen in Figure C.2-(d,f). A more quantitative comparisons between the original DFT data and the DyMD Figure C.1-(e) reveals a difference of about -24dB. Such a level corresponds to a lossless reconstruction for a full-scale signal, digitized on 8-bits. True lossless reconstruction is obtained for 8-mode decomposition (not shown here). As a side remark, the memory requirement for such a decomposition (2^{10} points per spectrum, 2^{14} Round-Trips, 32 bits resolution) would correspond to a compression of the experimental raw data by 93%. In contrast, the single-mode decomposition clearly misses a few important features, like the fast over-modulation in Figure C.2-(d) which is filtered out.

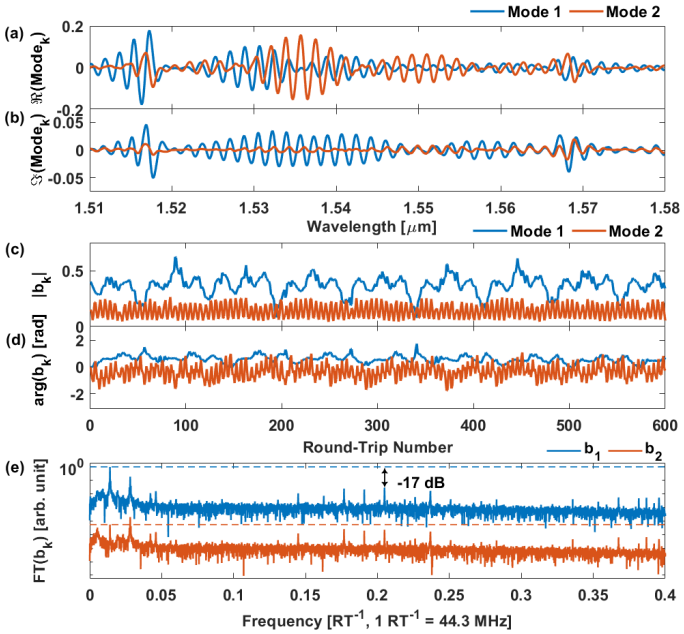

FIGURE C.3: (a-b) Representation of the 1^{st} and 2^{nd} modes of the 2-Mode DyMD (c-d) Evolution of the coefficients b_k, $k = \{1, 2\}$ used for the reconstruction. (e) Logarithmic Scale. Spectra of evolving vibration mode's amplitude b_k. Dashed lines mark the fundamental harmonic's amplitude allowing a comparison of the fast oscillations strength.

The 2-mode DyMD appears here to be the best choice; and the corresponding modes are shown in Figure C.3-(a,b). An important point is that this decomposition does not only reduce the amount of noise, it also allows a finer interpretation of the SM vibration pattern. The b_k coefficients (Figure C.3-(c,d)) are indeed completely correlated to the molecule oscillations shown in Figure C.2. We see that the weak over-modulation of 5.24 RTs periodicity that is imprinted on the main oscillation originates almost exclusively from the second mode, whose b_2 coefficient exhibits clearly fast varying features. In contrast b_1 evolves more slowly, following a periodic pattern with high harmonic content. Detailed Fourier analysis in Figure C.3-(e) confirms this relative distribution of fast and slow oscillations between the two modes. Statistically, independent oscillators are described by different modes; this is then the case here. It is actually the reason behind the failure of the

single-mode DyMD as it cannot reproduce concomitantly the dynamics of two independent modes.

Moreover, another advantage of the mode decomposition lies in the fact that knowing the modes' shape means that it is also possible visualize their associated molecule vibration pattern. They are depicted schematically in Figure C.4. This analysis contrasts with previous study were the vibration was only analyzed pair of solitons by pair of solitons, but the global picture was missing [268]. We see here that the first and dominant mode is actually anti-symmetric while the second mode is symmetric. The first vibration mode does not impact much the relative distance between the leading and trailing solitons. This fact does not change even if more modes are included in the DyMD. As a good approximation, the first mode involves the motion of the middle pulse, along with the corresponding dephasing of the first dissipative soliton. In the second mode, the middle pulse acts as an anchor, and the two other pulses move (and dephase) in an symmetric manner. We can conclude that each of the two fundamental vibration patterns encompasses the whole molecule and cannot be described as a combination of isolated soliton pairs movements. The two retrieved oscillators are independent entities, however, they interplay with each other. Indeed both b_1 and b_2 include modulations at high and low frequencies (Figure C.3-(e)), which is characteristic of an interaction between the two vibration modes. In detail b_2 encodes the fast oscillation of about 5 RTs periodicity, but exhibits at the same time a modulation at the main fundamental oscillation period (71 RTs). In Figure C.3-(e) the tone of the fast oscillation (located at about 0.2 RT^{-1}) is modulated by the main slow oscillation, which creates two equally spaced sidebands. This is the direct consequence of the slow oscillation modifying adiabatically the parameters of the fast oscillator.

We would like to stress that this phenomenon can only be clearly observed because the experimental noise has been reduced so that the small fast over-modulation takes over. As a consequence, the spectral comb that characterizes the modulation of one oscillator by another is only fully revealed by the DyMD approach. To allow a global comparison, the spectra of τ_{2-3} provided by the different types of data processing are presented in Figure C.5. The single mode DyMD misses the fundamental tone of the fast oscillation (peaks marked by purple dashed lines), and it is indeed not able to reproduce the signal correctly. The 2-Mode DyMD exhibits up to six harmonics, while only one is present in the raw data (first fundamental harmonics are denoted by dashed light blue lines in Figure C.5).

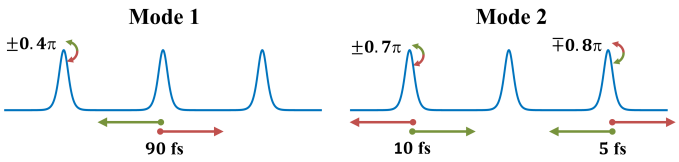

FIGURE C.4: Schematic representation of the two vibration modes, indicating the relative displacement of the dissipative solitons (arrows, with amplitude of the displacement), and the concomitant changes of optical phase. These representations are obtained by zeroing either the b_1 or b_2 coefficients during the DyMD reconstruction. For clarity, the numbers have been rounded up.

The DyMD technique also permits in-depth understanding of the molecule vibration through analysis of the b_k coefficients. In literature, vibrations of SMs are usually classified depending on how the optical phase between the solitons evolves [269], and a single oscillation pattern is usually assumed. Here the SM experiences a periodic evolution (71 RTs), set by the largest and strongest oscillator (b_1) that bounds the whole molecule. Still there exists a minor part of this oscillation caused by another oscillator, characterized by the coefficient b_2. Consequently the SM is under the influence of at least two limit-cycles of radically different nature. The fast oscillation is of much weaker amplitude and thus it is not strong enough to take over the dynamics. The

co-existence of several limit cycle attractors, and their range of attraction, is a fundamental question for a better understanding of the creation and the dissolution of SMs [270–273]. There exists mostly scarce information regarding the stability of the molecules' motion. Assessing the latter experimentally is usually tricky as it might involve actually the destruction of the SM as soon as one tries to alter forcefully its properties. Here we see that a finer analysis of the SM motion allows to get a better estimation of its stability by simply looking at its weak fluctuations. It provides also clear indication regarding how the destabilization of the SM would occur. Considering here that the optical phase relationship between the leading and trailing solitons is not favorable for the SM's stability, one hypothesis we could formulate is that a larger fast trembling could eventually result into the SM achieving a more stable conformation (metastability). The SM can thus switch between limit cycle attractors.

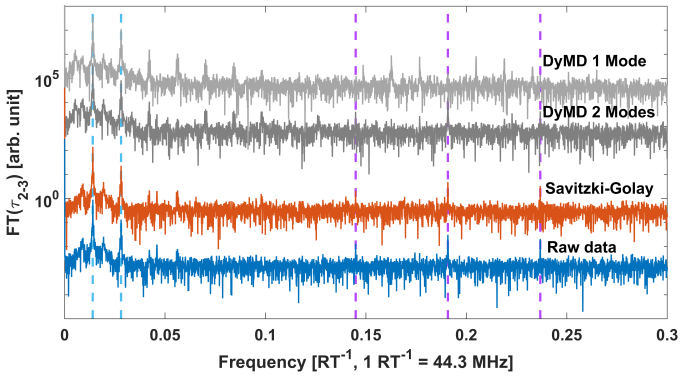

FIGURE C.5: Spectrum of the round-trip evolution of the inter-soliton separation τ_{2-3}. Blue: raw data. Red: Data processed by a 4^{th} order Savitzky-Golay filter. Dark and Light Grey: Results of 2- and single-Mode DyMD, respectively. Note the apparition of spurious harmonic tone (light blue dashed lines that show correct number of present harmonics), along with the disappearance of the fast oscillation's tone around 0.2 RT^{-1} (purple dashed lines).

C.3 Conclusion

To conclude, we demonstrated that Dynamic Mode Decomposition is a suitable method for the analysis of DFT data. By reducing the noise, it allows the observation of minute phenomena that would have otherwise remained hidden. Moreover, the DyMD decomposition can be used to compress the data efficiently, without loss of information. Depending on the denoising which is desired, the initial data set can be sequentially reconstructed using a different number of modes. Regarding the quantitative analysis of the experimental data, the DyMD reveals how a complex oscillation pattern of the SM is shared between its elementary constitutive components; and separate the temporal evolution of the individual vibration modes from their spatial distribution. We are then able to describe complex vibration patterns that involve more than two pulses, and this technique could be extended to complex solitonic systems [274].

As a practical example, we investigated the dynamics of a 3-Soliton molecule in an ultrafast fiber ring laser cavity. We showed that the solitons belonging to the same molecule may not experience the same vibration, and that limit cycles of different kind could co-exist inside the same laser cavity. Considering the optical phase difference of $\Delta\phi$ between the leading and the trailing soliton is known to create repulsion, this poses the

question regarding the meta-stability of some soliton molecules configurations. And it reinforces the interest in experiments (and data analysis) of acute precision as most transition phenomena start from weak instabilities.

For this first proof-of-principle demonstration about the opportunities offered by the DyMD, we implemented the DyMD on the raw DFT spectral data without performing any subsequent data treatment. The technique also has the denoising and compression capability. Regarding the analysis of the dynamics, the DyMD representation can be seen as a change of basis (or a projector, similar to a principal component analysis - PCA). Consequently, some DyMD decompositions could be more straightforward to interpret, depending on the system under study. For example, without changing the main conclusions, the DyMD could have been performed on the Fourier transformed data (Figure C.1-(d)) instead of the raw DFT data, or even on the resulting SM motion (Figure C.2). We believe that this work paves the way for more detailed analysis of the SM dynamics. In particular, we demonstrated that the oscillatory pattern of SMs results from the interplay of individual vibration modes and we were able to extract the round-trip evolution of each mode. It is then possible to investigate further how the modes interact by constructing a simpler nonlinear model that would reproduce the interplay that is observed between the b_k coefficients.

Bibliography

[1] B. Kibler, A. Chabchoub, A. Gelash, N. Akhmediev, and V. E. Zakharov. Superregular breathers in optics and hydrodynamics: Omnipresent modulation instability beyond simple periodicity. *Phys. Rev. X*, 5:041026, Nov 2015.

[2] Pallavi Jha, Punit Kumar, Gaurav Raj, and Ajay K. Upadhyaya. Modulation instability of laser pulse in magnetized plasma. *Physics of Plasmas*, 12(12):123104, 2005.

[3] V.E. Zakharov and L.A. Ostrovsky. Modulation instability: The beginning. *Physica D: Nonlinear Phenomena*, 238(5):540–548, 2009.

[4] Corentin Naveau, Pascal Szriftgiser, Alexandre Kudlinski, Matteo Conforti, Stefano Trillo, and Arnaud Mussot. Experimental characterization of recurrences and separatrix crossing in modulational instability. *Opt. Lett.*, 44(22):5426–5429, Nov 2019.

[5] Enrico Fermi, P Pasta, Stanislaw Ulam, and Mary Tsingou. Studies of the nonlinear problems. Technical report, Los Alamos National Lab.(LANL), Los Alamos, NM (United States), 1955.

[6] Akira Hasegawa. Generation of a train of soliton pulses by induced modulational instability in optical fibers. *Opt. Lett.*, 9(7):288–290, Jul 1984.

[7] Mikko Närhi, Benjamin Wetzel, Cyril Billet, Shanti Toenger, Thibaut Sylvestre, Jean-Marc Merolla, Roberto Morandotti, Frederic Dias, Goëry Genty, and John M. Dudley. Real-time measurements of spontaneous breathers and rogue wave events in optical fibre modulation instability. *Nature Communications*, 7(1):13675, 2016.

[8] J. M. Dudley, G. Genty, F. Dias, B. Kibler, and N. Akhmediev. Modulation instability, akhmediev breathers and continuous wave supercontinuum generation. *Opt. Express*, 17(24):21497–21508, Nov 2009.

[9] M. Erkintalo, G. Genty, B. Wetzel, and J.M. Dudley. Akhmediev breather evolution in optical fiber for realistic initial conditions. *Physics Letters A*, 375(19):2029–2034, 2011.

[10] K. Hammani, B. Wetzel, B. Kibler, J. Fatome, C. Finot, G. Millot, N. Akhmediev, and J. M. Dudley. Spectral dynamics of modulation instability described using akhmediev breather theory. *Opt. Lett.*, 36(11):2140–2142, Jun 2011.

[11] G. Cappellini and S. Trillo. Third-order three-wave mixing in single-mode fibers: exact solutions and spatial instability effects. *J. Opt. Soc. Am. B*, 8(4):824–838, Apr 1991.

[12] S. Trillo and S. Wabnitz. Dynamics of the nonlinear modulational instability in optical fibers. *Opt. Lett.*, 16(13):986–988, Jul 1991.

[13] S. Trillo, S. Wabnitz, and T. A. B. Kennedy. Nonlinear dynamics of dual-frequency-pumped multiwave mixing in optical fibers. *Phys. Rev. A*, 50:1732–1747, Aug 1994.

[14] O. Kimmoun, H. C. Hsu, H. Branger, M. S. Li, Y. Y. Chen, C. Kharif, M. Onorato, E. J. R. Kelleher, B. Kibler, N. Akhmediev, and A. Chabchoub. Modulation instability and phase-shifted fermi-pasta-ulam recurrence. *Scientific Reports*, 6(1):28516, 2016.

[15] Gang Xu, Amin Chabchoub, Dmitry E. Pelinovsky, and Bertrand Kibler. Observation of modulation instability and rogue breathers on stationary periodic waves. *Phys. Rev. Res.*, 2:033528, Sep 2020.

[16] G. Van Simaeys, Ph. Emplit, and M. Haelterman. Experimental demonstration of the fermi-pasta-ulam recurrence in a modulationally unstable optical wave. *Phys. Rev. Lett.*, 87:033902, Jun 2001.

[17] Corentin Naveau, Pascal Szriftgiser, Alexandre Kudlinski, Matteo Conforti, Stefano Trillo, and Arnaud Mussot. Full-field characterization of breather dynamics over the whole length of an optical fiber. *Opt. Lett.*, 44(4):763–766, Feb 2019.

[18] Guillaume Vanderhaegen, Pascal Szriftgiser, Alexandre Kudlinski, Matteo Conforti, Stefano Trillo, Maxime Droques, and Arnaud Mussot. Observation of four fermi-pasta-ulam-tsingou recurrences in an ultra-low-loss optical fiber. *Opt. Express*, 28(12):17773–17781, Jun 2020.

[19] Guillaume Vanderhaegen, Pascal Szriftgiser, Corentin Naveau, Alexandre Kudlinski, Matteo Conforti, Stefano Trillo, Nail Akhmediev, and Arnaud Mussot. Observation of doubly periodic solutions of the nonlinear schrödinger equation in optical fibers. *Opt. Lett.*, 45(13):3757–3760, Jul 2020.

[20] Anastasiia Sheveleva, Ugo Andral, Bertrand Kibler, Sonia Boscolo, and Christophe Finot. Temporal optical besselon waves for high-repetition rate picosecond sources. *Journal of Physics: Photonics*, 3(2):025001, feb 2021.

[21] Anastasiia Sheveleva and Christophe Finot. Nonlinear compression of besselon waves for high repetition-rate subpicosecond pulse trains. *IEEE Photonics Technology Letters*, 32(23):1493–1496, 2020.

[22] Anastasiia Sheveleva, Ugo Andral, Bertrand Kibler, Pierre Colman, John M. Dudley, and Christophe Finot. Idealized four-wave mixing dynamics in a nonlinear schrödinger equation fiber system. *Optica*, 9(6):656–662, Jun 2022.

[23] Anastasiia Sheveleva, Pierre Colman, John. M. Dudley, and Christophe Finot. Phase space topology of four-wave mixing reconstructed by a neural network. *Opt. Lett.*, 47(24):6317–6320, Dec 2022.

[24] Andrei V. Ermolaev, Anastasiia Sheveleva, Goëry Genty, Christophe Finot, and John M. Dudley. Data-driven model discovery of ideal four-wave mixing in nonlinear fibre optics. *Scientific Reports*, 12(1):12711, 2022.

[25] Anastasiia Sheveleva, Saïd Hamdi, Aurélien Coillet, Christophe Finot, and Pierre Colman. Analysis of the dispersive fourier transform dataset using dynamic mode decomposition: evidence of multiple vibrational modes and their interplay in a three-soliton molecule. *Opt. Lett.*, 48(11):3015–3018, Jun 2023.

[26] Anastasiia Sheveleva, Pierre Colman, John. M. Dudley, and Christophe Finot. Trajectory control in idealized four-wave mixing processes in optical fiber. *Optics Communications*, page 129472, 2023.

[27] Hao Hu, Hua Ji, Michael Galili, Minhao Pu, Christophe Peucheret, Hans Christian H. Mulvad, Kresten Yvind, Jørn M. Hvam, Palle Jeppesen, and Leif K. Oxenløwe. Ultra-high-speed wavelength conversion in a silicon photonic chip. *Opt. Express*, 19(21):19886–19894, Oct 2011.

[28] Yunhong Ding, Liu Liu, Christophe Peucheret, and Haiyan Ou. Fabrication tolerant polarization splitter and rotator based on a tapered directional coupler. *Opt. Express*, 20(18):20021–20027, Aug 2012.

[29] Francesco Da Ros, Kjeld Dalgaard, Lei Lei, Jing Xu, and Christophe Peucheret. Qpsk-to-2×bpsk wavelength and modulation format conversion through phase-sensitive four-wave mixing in a highly nonlinear optical fiber. *Opt. Express*, 21(23):28743–28750, Nov 2013.

[30] C. J. McKinstrie and S. Radic. Phase-sensitive amplification in a fiber. *Opt. Express*, 12(20):4973–4979, Oct 2004.

[31] Michel E. Marhic, Peter A. Andrekson, Periklis Petropoulos, Stojan Radic, Christophe Peucheret, and Mahmoud Jazayerifar. Fiber optical parametric amplifiers in optical communication systems. *Laser and photonics reviews*, 9:50–74, Jan 2015.

[32] Zhi Tong and Stojan Radic. Low-noise optical amplification and signal processing in parametric devices. *Adv. Opt. Photon.*, 5(3):318–384, Sep 2013.

[33] Joseph Kakande, Carl Lundström, Peter A. Andrekson, Zhi Tong, Magnus Karlsson, Periklis Petropoulos, Francesca Parmigiani, and David J. Richardson. Detailed characterization of a fiber-optic parametric amplifier in phase-sensitive and phase-insensitive operation. *Opt. Express*, 18(5):4130–4137, Mar 2010.

[34] Renyong Tang, Jacob Lasri, Preetpaul S. Devgan, Vladimir Grigoryan, Prem Kumar, and Michael Vasilyev. Gain characteristics of a frequency nondegenerate phase-sensitive fiber-optic parametric amplifier with phase self-stabilized input. *Opt. Express*, 13(26):10483–10493, Dec 2005.

[35] Steven G. Johnson, M. Ibanescu, M. A. Skorobogatiy, O. Weisberg, J. D. Joannopoulos, and Y. Fink. Perturbation theory for maxwell's equations with shifting material boundaries. *Phys. Rev. E*, 65:066611, Jun 2002.

[36] S. Longhi. Quantum-optical analogies using photonic structures. *Laser & Photonics Reviews*, 3(3):243–261, 2009.

[37] H. S. Hristova, A. A. Rangelov, S. Guérin, and N. V. Vitanov. Adiabatic evolution of light in an array of parallel curved optical waveguides. *Phys. Rev. A*, 88:013808, Jul 2013.

[38] Michael Mrejen, Haim Suchowski, Taiki Hatakeyama, Chihhui Wu, Liang Feng, Kevin O'Brien, Yuan Wang, and Xiang Zhang. Adiabatic elimination-based coupling control in densely packed subwavelength waveguides. *Nature Communications*, 6(1):7565, 2015.

[39] Anastasiia Sheveleva, Christophe Finot, and Pierre Colman. Dimensionality reduction for efficiency human and computer codesign in integrated photonics. In Roel G. Baets, Peter O'Brien, and Laurent Vivien, editors, *Integrated Photonics Platforms II*, volume 12148, page 1214808. International Society for Optics and Photonics, SPIE, 2022.

[40] Truong X Tran and Fabio Biancalana. An accurate envelope equation for light propagation in photonic nanowires: new nonlinear effects. *Optics Express*, 17(20):17934–17949, 2009.

[41] Marco Santagiustina, Carlo G Someda, Giovanni Vadala, Sylvain Combrie, and Alfredo De Rossi. Theory of slow light enhanced four-wave mixing in photonic crystal waveguides. *Optics Express*, 18(20):21024–21029, 2010.

[42] Robert W Boyd. *Nonlinear optics*. Academic press, 2020.

[43] M. Kolesik and J. V. Moloney. Nonlinear optical pulse propagation simulation: From maxwell's to unidirectional equations. *Phys. Rev. E*, 70:036604, Sep 2004.

[44] G. Agrawal. *Nonlinear Fiber Optics*. Elsevier Inc., 5th edition, 2013.

[45] M. Kolesik, J. V. Moloney, and M. Mlejnek. Unidirectional optical pulse propagation equation. *Phys. Rev. Lett.*, 89:283902, Dec 2002.

[46] Anastasiia Sheveleva and Christophe Finot. Temporal fresnel diffraction induced by phase jumps in linear and nonlinear optical fibres. *Results in Physics*, 19:103344, 2020.

[47] Anastasiia Sheveleva, Pierre Colman, and Christophe Finot. The temporal analogue of diffractive couplers. *Results in Optics*, 3:100059, 2021.

[48] Frédéric Chaussard, Hervé Rigneault, and Christophe Finot. Two-wave interferences space-time duality: Young slits, fresnel biprism and billet bilens. *Optics Communications*, 397:31–38, 2017.

[49] Christophe Finot, F. Chaussard, and Sonia Boscolo. Simple guidelines to predict self-phase modulation patterns. *J. Opt. Soc. Am. B*, 35(12):3143–3152, Dec 2018.

[50] K. Tai, A. Hasegawa, and A. Tomita. Observation of modulational instability in optical fibers. *Phys. Rev. Lett.*, 56:135–138, Jan 1986.

[51] Miro Erkintalo, Kamal Hammani, Bertrand Kibler, Christophe Finot, Nail Akhmediev, John M. Dudley, and Goëry Genty. Higher-order modulation instability in nonlinear fiber optics. *Phys. Rev. Lett.*, 107:253901, Dec 2011.

[52] Stefan Wabnitz. Modulational polarization instability of light in a nonlinear birefringent dispersive medium. *Phys. Rev. A*, 38:2018–2021, Aug 1988.

[53] G. Cappellini and S. Trillo. Bifurcations and three-wave-mixing instabilities in nonlinear propagation in birefringent dispersive media. *Phys. Rev. A*, 44:7509–7523, Dec 1991.

[54] G. Millot and S. Wabnitz. Nonlinear polarization effects in optical fibers: polarization attraction and modulation instability. *J. Opt. Soc. Am. B*, 31(11):2754–2768, Nov 2014.

[55] G. Millot, E. Seve, S. Wabnitz, and S. Trillo. Observation of a novel large-signal four-photon instability in optical wave mixing. *Phys. Rev. Lett.*, 80:504–507, Jan 1998.

[56] François Copie, Stëphane Randoux, and Pierre Suret. The physics of the one-dimensional nonlinear schrödinger equation in fiber optics: Rogue waves, modulation instability and self-focusing phenomena. *Reviews in Physics*, 5:100037, 2020.

[57] Xueming Liu, Xiaoqun Zhou, and Chao Lu. Multiple four-wave mixing self-stability in optical fibers. *Phys. Rev. A*, 72:013811, Jul 2005.

[58] Frédérique Vanholsbeeck, Philippe Emplit, and Stéphane Coen. Complete experimental characterization of the influence of parametric four-wave mixing on stimulated raman gain. *Opt. Lett.*, 28(20):1960–1962, Oct 2003.

[59] C.J. McKinstrie and G.G. Luther. Solitary-wave solutions of the generalised three-wave and four-wave equations. *Physics Letters A*, 127(1):14–18, 1988.

[60] Yijiang Chen and Allan W. Snyder. Four-photon parametric mixing in optical fibers: effect of pump depletion. *Opt. Lett.*, 14(1):87–89, Jan 1989.

[61] K. Inoue. Four-wave mixing in an optical fiber in the zero-dispersion wavelength region. *Journal of Lightwave Technology*, 10(11):1553–1561, 1992.

[62] Andrea Armaroli and Stefano Trillo. Modulational instability due to cross-phase modulation versus multiple four-wave mixing: the normal dispersion regime. *J. Opt. Soc. Am. B*, 31(3):551–558, Mar 2014.

[63] Joshua E. Rothenberg. Modulational instability for normal dispersion. *Phys. Rev. A*, 42:682–685, Jul 1990.

[64] E. Infeld. Quantitive theory of the fermi-pasta-ulam recurrence in the nonlinear schrodinger equation. *Phys. Rev. Lett.*, 47:717–718, Sep 1981.

[65] Peter A. E. M. Janssen. Modulational instability and the fermi-pasta-ulam recurrence. *The Physics of Fluids*, 24(1):23–26, 1981.

[66] D. Pierangeli, M. Flammini, L. Zhang, G. Marcucci, A. J. Agranat, P. G. Grinevich, P. M. Santini, C. Conti, and E. DelRe. Observation of fermi-pasta-ulam-tsingou recurrence and its exact dynamics. *Phys. Rev. X*, 8:041017, Oct 2018.

[67] Hie Tae Moon. Homoclinic crossings and pattern selection. *Phys. Rev. Lett.*, 64:412–414, Jan 1990.

[68] D. Eeltink, A. Armaroli, C. Luneau, H. Branger, M. Brunetti, and J. Kasparian. Separatrix crossing and symmetry breaking in nlse-like systems due to forcing and damping. *Nonlinear Dynamics*, 102(4):2385–2398, 2020.

[69] Andrea Armaroli, Debbie Eeltink, Maura Brunetti, and Jérôme Kasparian. Nonlinear stage of benjamin-feir instability in forced/damped deep-water waves. *Physics of Fluids*, 30(1):017102, 2018.

[70] Arnaud Mussot, Corentin Naveau, Matteo Conforti, Alexandre Kudlinski, Francois Copie, Pascal Szriftgiser, and Stefano Trillo. Fibre multi-wave mixing combs reveal the broken symmetry of fermi-pasta-ulam recurrence. *Nature Photonics*, 12(5):303–308, 2018.

[71] S. Trillo and S. Wabnitz. Self-injected spatial mode locking and coherent all-optical fm/am switching based on modulational instability. *Opt. Lett.*, 16(20):1566–1568, Oct 1991.

[72] Sonia Boscolo and Christophe Finot. *Shaping light in nonlinear optical fibers*. John Wiley & Sons, 2017.

[73] M. Erkintalo, Y. Q. Xu, S. G. Murdoch, J. M. Dudley, and G. Genty. Cascaded phase matching and nonlinear symmetry breaking in fiber frequency combs. *Phys. Rev. Lett.*, 109:223904, Nov 2012.

[74] M. Baillot, M. Gay, C. Peucheret, J. Michel, and T. Chartier. Phase quadrature discrimination based on three-pump four-wave mixing in nonlinear optical fibers. *Opt. Express*, 24:26930–26941, 2016.

[75] Stefan Wabnitz and Nail Akhmediev. Efficient modulation frequency doubling by induced modulation instability. *Optics Communications*, 283(6):1152–1154, 2010.

[76] Andrea Armaroli, Alexis Gomel, Amin Chabchoub, Maura Brunetti, and Jéröme Kasparian. Stabilization of uni-directional water wave trains over an uneven bottom. *Nonlinear Dynamics*, 101(2):1131–1145, 2020.

[77] J. Bromage. Raman amplification for fiber communications systems. *Journal of Lightwave Technology*, 22(1):79–93, 2004.

[78] Stefan Wabnitz and Benjamin Wetzel. Instability and noise-induced thermalization of fermi-pasta-ulam recurrence in the nonlinear schrodinger equation. *Physics Letters A*, 378(37):2750–2756, 2014.

[79] Guillaume Vanderhaegen, Pascal Szriftgiser, Alexandre Kudlinski, Matteo Conforti, Andrea Armaroli, and Arnaud Mussot. Observation of the noise-driven thermalization of the fermi-pasta-ulam-tsingou recurrence in optical fibers. *Phys. Rev. A*, 106:033519, Sep 2022.

[80] Xiaoyang Hu, Wei Chen, Yang Lu, Zhijie Yu, Mo Chen, and Zhou Meng. Distributed measurement of fermi-pasta-ulam recurrence in optical fibers. *IEEE Photonics Technology Letters*, 30:47–50, 2018.

[81] A. Bendahmane, A. Mussot, A. Kudlinski, P. Szriftgiser, M. Conforti, S. Wabnitz, and S. Trillo. Optimal frequency conversion in the nonlinear stage of modulation instability. *Opt. Express*, 23(24):30861–30871, Nov 2015.

[82] Gaetan Van Simaeys, Philippe Emplit, and Marc Haelterman. Experimental study of the reversible behavior of modulational instability in optical fibers. *J. Opt. Soc. Am. B*, 19(3):477–486, Mar 2002.

[83] Jan-Willem Goossens, Hartmut Hafermann, and Yves Jaouen. Experimental realization of fermi-pasta-ulam-tsingou recurrence in a long-haul optical fiber transmission system. *Scientific Reports*, 9(1):18467, 2019.

[84] Matteo Conforti, Arnaud Mussot, Alexandre Kudlinski, Stefano Trillo, and Nail Akhmediev. Doubly periodic solutions of the focusing nonlinear schrödinger equation: Recurrence, period doubling, and amplification outside the conventional modulation-instability band. *Phys. Rev. A*, 101:023843, Feb 2020.

[85] Guillaume Vanderhaegen, Pascal Szriftgiser, Alexandre Kudlinski, Andrea Armaroli, Matteo Conforti, Arnaud Mussot, and Stefano Trillo. Multiple symmetry breaking induced by weak damping in the fermi-pasta-ulam-tsingou recurrence process, 2022.

[86] C. Kharif, R. A. Kraenkel, M. A. Manna, and R. Thomas. The modulational instability in deep water under the action of wind and dissipation. *Journal of Fluid Mechanics*, 664:138–149, 2010.

[87] Juan Diego Ania-Castañón, Tim J. Ellingham, R. Ibbotson, X. Chen, L. Zhang, and Sergei K. Turitsyn. Ultralong raman fiber lasers as virtually lossless optical media. *Phys. Rev. Lett.*, 96:023902, Jan 2006.

[88] Miro Erkintalo, Goëry Genty, Benjamin Wetzel, and John M. Dudley. Limitations of the linear raman gain approximation in modeling broadband nonlinear propagation in optical fibers. *Opt. Express*, 18(24):25449–25460, Nov 2010.

[89] R. H. Stolen, J. P. Gordon, W. J. Tomlinson, and H. A. Haus. Raman response function of silica-core fibers. *J. Opt. Soc. Am. B*, 6(6):1159–1166, Jun 1989.

[90] K.J. Blow and D. Wood. Theoretical description of transient stimulated raman scattering in optical fibers. *IEEE Journal of Quantum Electronics*, 25(12):2665–2673, 1989.

[91] Q. Lin and Govind P. Agrawal. Raman response function for silica fibers. *Opt. Lett.*, 31(21):3086–3088, Nov 2006.

[92] A. S. Y. Hsieh, G. K. L. Wong, S. G. Murdoch, S. Coen, F. Vanholsbeeck, R. Leonhardt, and J. D. Harvey. Combined effect of raman and parametric gain on single-pump parametric amplifiers. *Opt. Express*, 15(13):8104–8114, Jun 2007.

[93] N. Bloembergen. The stimulated raman effect. *American Journal of Physics*, 35(11):989–1023, 1967.

[94] Andrey Kobyakov, Michael Sauer, and Dipak Chowdhury. Stimulated brillouin scattering in optical fibers. *Adv. Opt. Photon.*, 2(1):1–59, Mar 2010.

[95] Y. Aoki, K. Tajima, and I. Mito. Input power limits of single-mode optical fibers due to stimulated brillouin scattering in optical communication systems. *Journal of Lightwave Technology*, 6(5):710–719, 1988.

[96] D. Cotter. Stimulated brillouin scattering in monomode optical fiber. *Journal of Optical Communications*, 4(1):10–19, 1983.

[97] S. P. Smith, F. Zarinetchi, and S. Ezekiel. Narrow-linewidth stimulated brillouin fiber laser and applications. *Opt. Lett.*, 16(6):393–395, Mar 1991.

[98] X.S. Yao. Brillouin selective sideband amplification of microwave photonic signals. *IEEE Photonics Technology Letters*, 10(1):138–140, 1998.

[99] Marc Niklès, Luc Thévenaz, and Philippe A. Robert. Simple distributed fiber sensor based on brillouin gain spectrum analysis. *Opt. Lett.*, 21(10):758–760, May 1996.

[100] Mitsunobu Miyagi and Shigeo Nishida. Pulse spreading in a single-mode fiber due to third-order dispersion. *Appl. Opt.*, 18(5):678–682, Mar 1979.

[101] Kai Choong Chan and Hai Feng Liu. Effect of third-order dispersion on soliton-effect pulse compression. *Opt. Lett.*, 19(1):49–51, Jan 1994.

[102] A. Mussot, E. Louvergneaux, N. Akhmediev, F. Reynaud, L. Delage, and M. Taki. Optical fiber systems are convectively unstable. *Phys. Rev. Lett.*, 101:113904, Sep 2008.

[103] M. Droques, B. Barviau, A. Kudlinski, M. Taki, A. Boucon, T. Sylvestre, and A. Mussot. Symmetry-breaking dynamics of the modulational instability spectrum. *Opt. Lett.*, 36(8):1359–1361, Apr 2011.

[104] C Finot, F Chaussard, and S Boscolo. Impact of a temporal sinusoidal phase modulation on the optical spectrum. *European Journal of Physics*, 39(5):055303, aug 2018.

[105] U. Andral, J. Fatome, B. Kibler, and C. Finot. Triangular spectral phase tailoring for the generation of high-quality picosecond pulse trains. *Opt. Lett.*, 44(19):4913–4916, Oct 2019.

[106] Coherent, finisar, waveshaper 4000a multiport optical processor, https://ii-vi.com/product/waveshaper-4000a-multiport-optical-processor/.

[107] Nam Quoc Ngo and Yufeng Song. On the interrelations between an optical differentiator and an optical hilbert transformer. *Opt. Lett.*, 36(6):915–917, Mar 2011.

[108] Yokogawa, optical spectrum analyze aq6370, https://tmi.yokogawa.com/solutions/discontinued/aq6370-optical-spectrum-analyzer/.

[109] Keysight, 86100d infiniium dca-x wide-bandwidth oscilloscope, https://www.keysight.com/zz/en/product/86100d/infiniium-dca-x-wide-bandwidth-oscilloscope-mainframe.html.

[110] Andrea Galtarossa, Luca Palmieri, Marco Schiano, and Tiziana Tambosso. Measurement of birefringence correlation length in long, single-mode fibers. *Opt. Lett.*, 26(13):962–964, Jul 2001.

[111] Q. Lin and G.P. Agrawal. Impact of polarization-mode dispersion on measurement of zero-dispersion wavelength through four-wave mixing. *IEEE Photonics Technology Letters*, 15(12):1719–1721, 2003.

[112] Guy Millot, Alexandre Sauter, John M. Dudley, Laurent Provino, and Robert S. Windeler. Polarization mode dispersion and vectorial modulational instability in air–silica microstructure fiber. *Opt. Lett.*, 27(9):695–697, May 2002.

[113] Corentin Naveau, Guillaume Vanderhaegen, Pascal Szriftgiser, Gilbert Martinelli, Maxime Droques, Alexandre Kudlinski, Matteo Conforti, Stefano Trillo, Nail Akhmediev, and Arnaud Mussot. Heterodyne optical time domain reflectometer combined with active loss compensation: A practical tool for investigating fermi pasta ulam recurrence process and breathers dynamics in optical fibers. *Frontiers in Physics*, 9:637812, 2021.

[114] Darlene L. Hart, Arthur Judy, T. A. Brian Kennedy, Rajarshi Roy, and Kroum Stoev. Conservation law for multiple four-wave-mixing processes in a nonlinear optical medium. *Phys. Rev. A*, 50:1807–1813, Aug 1994.

[115] F. Matera, A. Mecozzi, M. Romagnoli, and M. Settembre. Sideband instability induced by periodic power variation in long-distance fiber links. *Opt. Lett.*, 18(18):1499–1501, Sep 1993.

[116] S. Trillo and S. Wabnitz. Modulational chaos in periodically amplified fiber links and in fiber lasers. In *Nonlinear Guided-Wave Phenomena*, page TuD.6. Optica Publishing Group, 1993.

[117] Akira Hasegawa and Yuji Kodama. Guiding-center soliton in optical fibers. *Opt. Lett.*, 15(24):1443–1445, Dec 1990.

[118] M. I. Jordan and T. M. Mitchell. Machine learning: Trends, perspectives, and prospects. *Science*, 349(6245):255–260, 2015.

[119] Giuseppe Carleo, Ignacio Cirac, Kyle Cranmer, Laurent Daudet, Maria Schuld, Naftali Tishby, Leslie Vogt-Maranto, and Lenka Zdeborová. Machine learning and the physical sciences. *Rev. Mod. Phys.*, 91:045002, Dec 2019.

[120] Göery Genty, Lauri Salmela, John M. Dudley, Daniel Brunner, Alexey Kokhanovskiy, Sergei Kobtsev, and Sergei K. Turitsyn. Machine learning and applications in ultrafast photonics. *Nature Photonics*, 15(2):91–101, 2021.

[121] Pedro Freire, Egor Manuylovich, Jaroslaw E. Prilepsky, and Sergei K. Turitsyn. Artificial neural networks for photonic applications—from algorithms to implementation: tutorial. *Adv. Opt. Photon.*, 15(3):739–834, Sep 2023.

[122] Mikko Närhi, Lauri Salmela, Juha Toivonen, Cyril Billet, John M. Dudley, and Goëry Genty. Machine learning analysis of extreme events in optical fibre modulation instability. *Nature Communications*, 9(1):4923, 2018.

[123] Sonia Boscolo and Christophe Finot. Artificial neural networks for nonlinear pulse shaping in optical fibers. *Optics and Laser Technology*, 131:106439, 2020.

[124] Sonia Boscolo, John M. Dudley, and Christophe Finot. Predicting nonlinear reshaping of periodic signals in optical fibre with a neural network. *Optics Communications*, 542:129563, 2023.

[125] Francesco Musumeci, Cristina Rottondi, Avishek Nag, Irene Macaluso, Darko Zibar, Marco Ruffini, and Massimo Tornatore. An overview on application of machine learning techniques in optical networks. *IEEE Communications Surveys and Tutorials*, 21(2):1383–1408, 2019.

[126] Mehdi Mabed, Fanchao Meng, Lauri Salmela, Christophe Finot, Goëry Genty, and John M. Dudley. Machine learning analysis of instabilities in noise-like pulse lasers. *Opt. Express*, 30(9):15060–15072, Apr 2022.

[127] Mehdi Mabed, Lauri Salmela, Andrei Ermolaev, Christophe Finot, GoÃ«ry Genty, and John M. Dudley. Neural network analysis of unstable temporal intensity peaks in continuous wave modulation instability. *Optics Communications*, 541:129570, 2023.

[128] Warren S. McCulloch and Walter Pitts. A logical calculus of the ideas immanent in nervous activity. *The bulletin of mathematical biophysics*, 5(4):115–133, 1943.

[129] J J Hopfield. Neural networks and physical systems with emergent collective computational abilities. *Proceedings of the National Academy of Sciences*, 79(8):2554–2558, 1982.

[130] A.K. Jain, Jianchang Mao, and K.M. Mohiuddin. Artificial neural networks: a tutorial. *Computer*, 29(3):31–44, 1996.

[131] Christophe Finot and Sonia Boscolo. Exploring fresnel diffraction at a straight edge with a neural network. *European Journal of Physics*, 43(3):035306, apr 2022.

[132] Andrea Apicella, Francesco Donnarumma, Francesco Isgrö, and Roberto Prevete. A survey on modern trainable activation functions. *Neural Networks*, 138:14–32, 2021.

[133] Brian K. Spears, James Brase, Peer-Timo Bremer, Barry Chen, John Field, Jim Gaffney, Michael Kruse, Steve Langer, Katie Lewis, Ryan Nora, Jayson Luc Peterson, Jayaraman Jayaraman Thiagarajan, Brian Van Essen, and Kelli Humbird. Deep learning: A guide for practitioners in the physical sciences. *Physics of Plasmas*, 25(8):080901, 2018.

[134] George Em Karniadakis, Ioannis G. Kevrekidis, Lu Lu, Paris Perdikaris, Sifan Wang, and Liu Yang. Physics-informed machine learning. *Nature Reviews Physics*, 3(6):422–440, 2021.

[135] M. Raissi, P. Perdikaris, and G.E. Karniadakis. Physics-informed neural networks: A deep learning framework for solving forward and inverse problems involving nonlinear partial differential equations. *Journal of Computational Physics*, 378:686–707, 2019.

[136] Xiaotian Jiang, Danshi Wang, Qirui Fan, Min Zhang, Chao Lu, and Alan Pak Tao Lau. Physics-informed neural network for nonlinear dynamics in fiber optics. *Laser & Photonics Reviews*, 16(9):2100483, 2022.

[137] D. Stathakis. How many hidden layers and nodes? *International Journal of Remote Sensing*, 30(8):2133–2147, 2009.

[138] Donald W. Marquardt. An algorithm for least-squares estimation of nonlinear parameters. *Journal of the Society for Industrial and Applied Mathematics*, 11(2):431–441, 1963.

[139] Reza Moradi, Reza Berangi, and Behrouz Minaei. A survey of regularization strategies for deep models. *Artificial Intelligence Review*, 53(6):3947–3986, 2020.

[140] Michal Borsky, Petr Mizera, Petr Pollak, and Jan Nouza. Dithering techniques in automatic recognition of speech corrupted by mp3 compression: Analysis, solutions and experiments. *Speech Communication*, 86:75–84, 2017.

[141] H.I. Avi-Itzhak, T.A. Diep, and H. Garland. High accuracy optical character recognition using neural networks with centroid dithering. *IEEE Transactions on Pattern Analysis and Machine Intelligence*, 17(2):218–224, 1995.

[142] Varun Chandola, Arindam Banerjee, and Vipin Kumar. Anomaly detection: A survey. *ACM Comput. Surv.*, 41(3), jul 2009.

[143] Michael Schmidt and Hod Lipson. Distilling free-form natural laws from experimental data. *Science*, 324(5923):81–85, 2009.

[144] Josh Bongard and Hod Lipson. Automated reverse engineering of nonlinear dynamical systems. *Proceedings of the National Academy of Sciences*, 104(24):9943–9948, 2007.

[145] Steven L. Brunton, Joshua L. Proctor, and J. Nathan Kutz. Discovering governing equations from data by sparse identification of nonlinear dynamical systems. *Proceedings of the National Academy of Sciences*, 113(15):3932–3937, 2016.

[146] Alan A. Kaptanoglu, Jared L. Callaham, Aleksandr Aravkin, Christopher J. Hansen, and Steven L. Brunton. Promoting global stability in data-driven models of quadratic nonlinear dynamics. *Phys. Rev. Fluids*, 6:094401, Sep 2021.

[147] Kai Fukami, Takaaki Murata, Kai Zhang, and Koji Fukagata. Sparse identification of nonlinear dynamics with low-dimensionalized flow representations. *Journal of Fluid Mechanics*, 926:A10, 2021.

[148] Jared L. Callaham, James V. Koch, Bingni W. Brunton, J. Nathan Kutz, and Steven L. Brunton. Learning dominant physical processes with data-driven balance models. *Nature Communications*, 12(1):1016, 2021.

[149] Robert Tibshirani. Regression shrinkage and selection via the lasso. *Journal of the Royal Statistical Society: Series B (Methodological)*, 58(1):267–288, 1996.

[150] Bradley Efron, Trevor Hastie, Iain Johnstone, and Robert Tibshirani. Least angle regression. *The Annals of Statistics*, 32(2):407 – 499, 2004.

[151] Joshua L. Proctor, Steven L. Brunton, and J. Nathan Kutz. Dynamic mode decomposition with control. *SIAM Journal on Applied Dynamical Systems*, 15(1):142–161, 2016.

[152] William H. Press and Saul A. Teukolsky. Savitzky-golay smoothing filters. *Computers in Physics*, 4(6):669–672, 1990.

[153] Å. Björck. Numerics of gram-schmidt orthogonalization. *Linear Algebra and its Applications*, 197-198:297–316, 1994.

[154] Sergei K. Turitsyn, Brandon G. Bale, and Mikhail P. Fedoruk. Dispersion-managed solitons in fibre systems and lasers. *Physics Reports*, 521(4):135–203, 2012. Dispersion-Managed Solitons in Fibre Systems and Lasers.

[155] A. Bendahmane, F. Braud, M. Conforti, B. Barviau, A. Mussot, and A. Kudlinski. Dynamics of cascaded resonant radiations in a dispersion-varying optical fiber. *Optica*, 1(4):243–249, Oct 2014.

[156] A. Bendahmane, A. Mussot, P. Szriftgiser, O. Zerkak, G. Genty, J. M. Dudley, and A. Kudlinski. Experimental dynamics of akhmediev breathers in a dispersion varying optical fiber. *Opt. Lett.*, 39(15):4490–4493, Aug 2014.

[157] O. Yaakobi and L. Friedland. Autoresonant four-wave mixing in optical fibers. *Phys. Rev. A*, 82:023820, Aug 2010.

[158] Haim Suchowski, Gil Porat, and Ady Arie. Adiabatic processes in frequency conversion. *Laser & Photonics Reviews*, 8(3):333–367, 2014.

[159] Gil Porat and Ady Arie. Efficient, broadband, and robust frequency conversion by fully nonlinear adiabatic three-wave mixing. *J. Opt. Soc. Am. B*, 30(5):1342–1351, May 2013.

[160] Christian Agger, Simon T. Sørensen, Carsten L. Thomsen, Søren R. Keiding, and Ole Bang. Nonlinear soliton matching between optical fibers. *Opt. Lett.*, 36(13):2596–2598, Jul 2011.

[161] J. M. Soto-Crespo, N. Devine, and N. Akhmediev. Adiabatic transformation of continuous waves into trains of pulses. *Phys. Rev. A*, 96:023825, Aug 2017.

[162] Alexis Gomel, Amin Chabchoub, Maura Brunetti, Stefano Trillo, Jérôme Kasparian, and Andrea Armaroli. Stabilization of unsteady nonlinear waves by phase-space manipulation. *Phys. Rev. Lett.*, 126:174501, Apr 2021.

[163] Zhixiang Deng, Jin Zhang, Dianyuan Fan, and Lifu Zhang. Manipulation of breather waves with split-dispersion cascaded fibers. *New Journal of Physics*, 24(6):063018, jun 2022.

[164] Anastasiia Sheveleva, Said Hamdi, Aurélien Coillet, Christophe Finot, and Pierre Colman. Langevin's model for soliton molecules in ultrafast fiber ring laser cavity. In *Optica Advanced Photonics Congress 2022*, page NpTh1G.3. Optica Publishing Group, 2022.

[165] A. Barthelemy and R. De La Fuente. Unusual modulation instability in fibers with normal and anomalous dispersions. *Optics Communications*, 73(5):409–412, 1989.

[166] Xiankun Yao, Chong Liu, Zhan-Ying Yang, and Wen-Li Yang. Heteroclinic-structure transition of the pure quartic modulation instability. *Phys. Rev. Res.*, 4:013246, Mar 2022.

[167] M. Conforti, A. Mussot, A. Kudlinski, S. Rota Nodari, G. Dujardin, S. De Biévre, A. Armaroli, and S. Trillo. Heteroclinic structure of parametric resonance in the nonlinear schrödinger equation. *Phys. Rev. Lett.*, 117:013901, Jun 2016.

[168] N. J. Smith and N. J. Doran. Modulational instabilities in fibers with periodic dispersion management. *Opt. Lett.*, 21(8):570–572, Apr 1996.

[169] Jared C. Bronski and J. Nathan Kutz. Modulational stability of plane waves in nonreturn-to-zero communications systems with dispersion management. *Opt. Lett.*, 21(13):937–939, Jul 1996.

[170] G. Dujardin, A. Armaroli, S. Rota Nodari, A. Mussot, A. Kudlinski, S. Trillo, M. Conforti, and S. De Bièvre. Modulational instability in optical fibers with randomly kicked normal dispersion. *Phys. Rev. A*, 103:053521, May 2021.

[171] Min Li, Lei Wang, and Feng-Hua Qi. Nonlinear dynamics of a generalized higher-order nonlinear schrödinger equation with a periodic external perturbation. *Nonlinear Dynamics*, 86(1):535–541, 2016.

[172] John R. Thompson and Rajarshi Roy. Statistical fluctuations in multiple four-wave mixing in a single-mode optical fiber. *Phys. Rev. A*, 44:7605–7614, Dec 1991.

[173] Trillo S. and Wabnitz S. Hamiltonian dynamics of parametric nonlinear wave mixing 132-134. (speech presented at the). In *Nonlinear Dynamics in Optical Systems conference, Alpbach, Austria*, 1992.

[174] Peter J. Schmid. Dynamic mode decomposition of numerical and experimental data. *Journal of Fluid Mechanics*, 656:5–28, 2010.

[175] J. Nathan Kutz, Steven L. Brunton, Bingni W. Brunton, and Joshua L. Proctor. *Dynamic Mode Decomposition*. Society for Industrial and Applied Mathematics, Philadelphia, PA, 2016.

[176] Kevin J. Miller, Kent A. Hallman, Richard F. Haglund, and Sharon M. Weiss. Silicon waveguide optical switch with embedded phase change material. *Opt. Express*, 25(22):26527–26536, Oct 2017.

[177] Matthias Stegmaier, Carlos Ríos, Harish Bhaskaran, C. David Wright, and Wolfram H. P. Pernice. Nonvolatile all-optical 1 Ã— 2 switch for chipscale photonic networks. *Advanced Optical Materials*, 5(1):1600346, 2017.

[178] Sebabrata Mukherjee, Alexander Spracklen, Manuel Valiente, Erika Andersson, Patrik Ã–hberg, Nathan Goldman, and Robert R. Thomson. Experimental observation of anomalous topological edge modes in a slowly driven photonic lattice. *Nature Communications*, 8(1):13918, 2017.

[179] Martin Wimmer, Hannah M. Price, Iacopo Carusotto, and Ulf Peschel. Experimental measurement of the berry curvature from anomalous transport. *Nature Physics*, 13(6):545–550, 2017.

[180] Ling Lu, John D. Joannopoulos, and Marin Soljačić. Topological photonics. *Nature Photonics*, 8(11):821–829, oct 2014.

[181] M. V. Berry. Quantal phase factors accompanying adiabatic changes. *Proceedings of the Royal Society of London. Series A, Mathematical and Physical Sciences*, 392(1802):45–57, 1984.

[182] Allan W. Snyder and Yijiang Chen. Nonlinear fiber couplers: switches and polarization beam splitters. *Opt. Lett.*, 14(10):517–519, May 1989.

[183] S. K. Özdemir, S. Rotter, F. Nori, and L. Yang. Parity-time symmetry and exceptional points in photonics. *Nature Materials*, 18(8):783–798, 2019.

[184] Christian E. Rüter, Konstantinos G. Makris, Ramy El-Ganainy, Demetrios N. Christodoulides, Mordechai Segev, and Detlef Kip. Observation of parity-time symmetry in optics. *Nature Physics*, 6(3):192–195, 2010.

[185] Hamidreza Ramezani, Tsampikos Kottos, Ramy El-Ganainy, and Demetrios N. Christodoulides. Unidirectional nonlinear $\mathcal{PT}$-symmetric optical structures. *Phys. Rev. A*, 82:043803, Oct 2010.

[186] N. V. Alexeeva, I. V. Barashenkov, K. Rayanov, and S. Flach. Actively coupled optical waveguides. *Phys. Rev. A*, 89:013848, Jan 2014.

[187] A.V. Yulin, D.V. Skryabin, and A.G. Vladimirov. Modulational instability of discrete solitons in coupled waveguides with group velocity dispersion. *Opt. Express*, 14(25):12347–12352, Dec 2006.

[188] I. Babushkin, A. Husakou, J. Herrmann, and Yuri S. Kivshar. Frequency-selective self-trapping and supercontinuum generation in arrays of coupled nonlinear waveguides. *Opt. Express*, 15(19):11978–11983, Sep 2007.

[189] Arash Joushaghani, Rajiv Iyer, Joyce K. S. Poon, J. Stewart Aitchison, C. Martijn de Sterke, Jun Wan, and Marc M. Dignam. Quasi-bloch oscillations in curved coupled optical waveguides. *Phys. Rev. Lett.*, 103:143903, Oct 2009.

[190] Yoav Lahini, Eugene Frumker, Yaron Silberberg, Sotiris Droulias, Kyriakos Hizanidis, Roberto Morandotti, and Demetrios N. Christodoulides. Discrete x-wave formation in nonlinear waveguide arrays. *Phys. Rev. Lett.*, 98:023901, Jan 2007.

[191] S. Longhi, M. Marangoni, M. Lobino, R. Ramponi, P. Laporta, E. Cianci, and V. Foglietti. Observation of dynamic localization in periodically curved waveguide arrays. *Phys. Rev. Lett.*, 96:243901, Jun 2006.

[192] G. Lenz, I. Talanina, and C. Martijn de Sterke. Bloch oscillations in an array of curved optical waveguides. *Phys. Rev. Lett.*, 83:963–966, Aug 1999.

[193] N. Chiodo, G. Della Valle, R. Osellame, S. Longhi, G. Cerullo, R. Ramponi, P. Laporta, and U. Morgner. Imaging of bloch oscillations in erbium-doped curved waveguide arrays. *Opt. Lett.*, 31(11):1651–1653, Jun 2006.

[194] R. El-Ganainy, K. G. Makris, D. N. Christodoulides, and Ziad H. Musslimani. Theory of coupled optical pt-symmetric structures. *Opt. Lett.*, 32(17):2632–2634, Sep 2007.

[195] Nikolaos K. Efremidis. Topological photonic su-schrieffer-heeger-type coupler. *Phys. Rev. A*, 104:053531, Nov 2021.

[196] Natalia Malkova, Ivan Hromada, Xiaosheng Wang, Garnett Bryant, and Zhigang Chen. Observation of optical shockley-like surface states in photonic superlattices. *Opt. Lett.*, 34(11):1633–1635, Jun 2009.

[197] Yingwen Liu, Chao Wu, XiaoGang Qiang, Junjie Wu, Xuejun Yang, and Ping Xu. Evanescent-wave coupling phase-matching for ultrawidely tunable frequency conversion in silicon-waveguide chips. *Opt. Express*, 27(20):28866–28878, Sep 2019.

[198] Bodong Liu, Huakang Yu, Zhi yuan Li, and Limin Tong. Phase-matched second-harmonic generation in coupled nonlinear optical waveguides. *J. Opt. Soc. Am. B*, 36(10):2650–2658, Oct 2019.

[199] Anastasiia Sheveleva, Mathieu Leonardo, Christophe Finot, and Pierre Colman. Local-field and effective-background effects in coupled integrated photonic waveguide systems. *Phys. Rev. A*, 107:063502, Jun 2023.

[200] Maksim Skorobogatiy, Mihai Ibanescu, Steven G. Johnson, Ori Weisberg, Torkel D. Engeness, Marin Soljačić, Steven A. Jacobs, and Yoel Fink. Analysis of general geometric scaling perturbations in a transmitting waveguide: fundamental connection between polarization-mode dispersion and group-velocity dispersion. *J. Opt. Soc. Am. B*, 19(12):2867–2875, Dec 2002.

[201] M. Skorobogatiy, Steven A. Jacobs, Steven G. Johnson, and Yoel Fink. Geometric variations in high index-contrast waveguides, coupled mode theory in curvilinear coordinates. *Opt. Express*, 10(21):1227–1243, Oct 2002.

[202] Wei-Ping Huang. Coupled-mode theory for optical waveguides: an overview. *J. Opt. Soc. Am. A*, 11(3):963–983, Mar 1994.

[203] A. Hardy and W. Streifer. Coupled mode theory of parallel waveguides. *Journal of Lightwave Technology*, 3(5):1135–1146, 1985.

[204] Saeed Ghadirli, K. Thyagarajan, and Arun Kumar. Band stop filter characteristics of non identical waveguides directional couplers; a comparison of three methods. *Optics Communications*, 84(3):144–148, 1991.

[205] H. Haus, W. Huang, S. Kawakami, and N. Whitaker. Coupled-mode theory of optical waveguides. *Journal of Lightwave Technology*, 5(1):16–23, 1987.

[206] Katsunari Okamoto. Chapter 4 - coupled mode theory. In Katsunari Okamoto, editor, *Fundamentals of Optical Waveguides (Second Edition)*, pages 159–207. Academic Press, Burlington, second edition edition, 2006.

[207] Niharika Kohli, Sangeeta Srivastava, and Enakshi K. Sharma. Orthogonal solutions for asymmetric strongly coupled waveguide arrays: an elegant, analytical approach. *J. Opt. Soc. Am. B*, 31(11):2871–2878, Nov 2014.

[208] Steven G. Johnson and J. D. Joannopoulos. Block-iterative frequency-domain methods for maxwell's equations in a planewave basis. *Opt. Express*, 8(3):173–190, Jan 2001.

[209] S. V. Lobanov, W. Langbein, and E. A. Muljarov. Resonant-state expansion applied to three-dimensional open optical systems: Complete set of static modes. *Phys. Rev. A*, 100:063811, Dec 2019.

[210] J. E. Sipe. Vector $k \cdot p$ approach for photonic band structures. *Phys. Rev. E*, 62:5672–5677, Oct 2000.

[211] Parry Y. Chen, David J. Bergman, and Yonatan Sivan. Generalizing normal mode expansion of electromagnetic green's tensor to open systems. *Phys. Rev. Appl.*, 11:044018, Apr 2019.

[212] Sravya Rao, Guillaume Le Saux, Yonatan Sivan, and Parry Y. Chen. Generalized normal mode expansion method for open and lossy periodic structures. *J. Opt. Soc. Am. B*, 39(5):1338–1347, May 2022.

[213] A.D. Yaghjian. Electric dyadic green's functions in the source region. *Proceedings of the IEEE*, 68(2):248–263, 1980.

[214] Olivier J. F. Martin and Nicolas B. Piller. Electromagnetic scattering in polarizable backgrounds. *Phys. Rev. E*, 58:3909–3915, Sep 1998.

[215] S. G. Johnson, M. L. Povinelli, M. Soljačić, A. Karalis, S. Jacobs, and J. D. Joannopoulos. Roughness losses and volume-current methods in photonic-crystal waveguides. *Applied Physics B*, 81(2):283–293, 2005.

[216] L. Ramunno and S. Hughes. Disorder-induced resonance shifts in high-index-contrast photonic crystal nanocavities. *Phys. Rev. B*, 79:161303, Apr 2009.

[217] H.F. Taylor and A. Yariv. Guided wave optics. *Proceedings of the IEEE*, 62(8):1044–1060, 1974.

[218] Xi Chen, Rui-Dan Wen, Jie-Long Shi, and Shuo-Yen Tseng. Compact beam splitters in coupled waveguides using shortcuts to adiabaticity. *Journal of Optics*, 20(4):045804, mar 2018.

[219] Jheng-Yi Sie, Hung-Ching Chung, Xi Chen, and Shuo-Yen Tseng. Robust arbitrary ratio power splitter by fast quasi-adiabatic elimination in optical waveguides. *Opt. Express*, 27(26):37622–37633, Dec 2019.

[220] Yanxian Wei, Junwei Cheng, Yilun Wang, Hailong Zhou, Jianji Dong, Dongmei Huang, Feng Li, Ming Li, Ping Kong Alexander Wai, and Xinliang Zhang. Strategy for low-loss optical devices when using high-loss materials. *Advanced Photonics Research*, 3(9):2200120, 2022.

[221] Hosung Chang and Je-Myung Jeong. A modified coupled-mode analysis for asymmetric coupled waveguides. *Microwave and Optical Technology Letters*, 13(5):277–280, 1996.

[222] Matteo Cherchi. Design scheme for mach-zehnder interferometric coarse wavelength division multiplexing splitters and combiners. *J. Opt. Soc. Am. B*, 23(9):1752–1756, Sep 2006.

[223] V. Dorier, M. Gevorgyan, A. Ishkhanyan, C. Leroy, H. R. Jauslin, and S. Guérin. Nonlinear stimulated raman exact passage by resonance-locked inverse engineering. *Phys. Rev. Lett.*, 119:243902, Dec 2017.

[224] S. Guérin, M. Gevorgyan, C. Leroy, H. R. Jauslin, and A. Ishkhanyan. Efficient adiabatic tracking of driven quantum nonlinear systems. *Phys. Rev. A*, 88:063622, Dec 2013.

[225] Shuo-Yen Tseng. Robust coupled-waveguide devices using shortcuts to adiabaticity. *Opt. Lett.*, 39(23):6600–6603, Dec 2014.

[226] Hung-Ching Chung, Chih-Hsien Chen, Guan-Xun Lu, Yung-Jr Hung, and Shuo-Yen Tseng. Adiabaticity engineered silicon polarization independent 3-db coupler for the o-band. *IEEE Photonics Journal*, 15(3):1–6, 2023.

[227] Michael Mrejen, Haim Suchowski, Taiki Hatakeyama, Yuan Wang, and Xiang Zhang. Experimental realization of two decoupled directional couplers in a subwavelength packing by adiabatic elimination. *Nano Lett.*, 15(11):7383–7387, November 2015.

[228] Cheng Chen, Xianmeng Zhao, Shengjie Tang, Xiaoping Liu, and Haibin Lv. Realization of low-crosstalk half-wavelength pitch waveguide array on a silicon-on-insulator platform. *Opt. Lett.*, 47(12):2955–2958, Jun 2022.

[229] Liping Wang, Ze Chen, Hongfei Wang, Ang Liu, Peng Wang, Tianying Lin, Xiaoping Liu, and Haibin Lv. Design of a low-crosstalk half-wavelength pitch nano-structured silicon waveguide array. *Opt. Lett.*, 44(13):3266–3269, Jul 2019.

[230] Nikolaos K. Efremidis and Kyriakos Hizanidis. Bandgap lattices: low index solitons and linear properties. *Opt. Express*, 13(26):10571–10588, Dec 2005.

[231] Nikolaos K. Efremidis, Peng Zhang, Zhigang Chen, Demetrios N. Christodoulides, Christian E. Rüter, and Detlef Kip. Wave propagation in waveguide arrays with alternating positive and negative couplings. *Phys. Rev. A*, 81:053817, May 2010.

[232] Han Yun, Lukas Chrostowski, and Nicolas A. F. Jaeger. Ultra-broadband 2x2 adiabatic 3â€‰db coupler using subwavelength-grating-assisted silicon-on-insulator strip waveguides. *Opt. Lett.*, 43(8):1935–1938, Apr 2018.

[233] Daoxin Dai. Silicon polarization beam splitter based on an asymmetrical evanescent coupling system with three optical waveguides. *Journal of Lightwave Technology*, 30(20):3281–3287, 2012.

[234] Yunhong Ding, Jing Xu, Francesco Da Ros, Bo Huang, Haiyan Ou, and Christophe Peucheret. On-chip two-mode division multiplexing using tapered directional coupler-based mode multiplexer and demultiplexer. *Opt. Express*, 21(8):10376–10382, Apr 2013.

[235] Hirohito Yamada, Tao Chu, Satomi Ishida, and Yasuhiko Arakawa. Si photonic wire waveguide devices. *IEEE Journal of Selected Topics in Quantum Electronics*, 12(6):1371–1379, 2006.

[236] Yoshiaki Teranishi and Hiroki Nakamura. Control of time-dependent nonadiabatic processes by an external field. *Phys. Rev. Lett.*, 81:2032–2035, Sep 1998.

[237] H. G. Park, S. Y. Huang, and B. Y. Kim. All-optical intermodal switch using periodic coupling in a two-mode waveguide. *Opt. Lett.*, 14(16):877–879, Aug 1989.

[238] Y. Chen. Coupling of periodic modes. *Journal of Lightwave Technology*, 9(7):859–863, 1991.

[239] Nicholas C. Harris, Jacques Carolan, Darius Bunandar, Mihika Prabhu, Michael Hochberg, Tom Baehr-Jones, Michael L. Fanto, A. Matthew Smith, Christopher C. Tison, Paul M. Alsing, and Dirk Englund. Linear programmable nanophotonic processors. *Optica*, 5(12):1623–1631, Dec 2018.

[240] Mingye Fu, Guangyao Liu, Yichi Zhang, Roberto Proietti, and S. J. Ben Yoo. Monolithic silicon photonic 32x32 thin-clos awgr for all-to-all interconnections. *Opt. Express*, 31(10):16623–16633, May 2023.

[241] Wim Bogaerts and Lukas Chrostowski. Silicon photonics circuit design: Methods, tools and challenges. *Laser & Photonics Reviews*, 12(4):1700237, 2018.

[242] Rasmus E. Christiansen and Ole Sigmund. Inverse design in photonics by topology optimization: tutorial. *J. Opt. Soc. Am. B*, 38(2):496–509, Feb 2021.

[243] Fengwen Wang, Jakob Søndergaard Jensen, Jesper Mørk, and Ole Sigmund. Systematic design of loss-engineered slow-light waveguides. *J. Opt. Soc. Am. A*, 29(12):2657–2666, Dec 2012.

[244] Guowu Zhang, Dan-Xia Xu, Yuri Grinberg, and Odile Liboiron-Ladouceur. Efficient mode exchanger-based silicon photonic switch enabled by inverse design. *Opt. Express*, 30(12):20543–20553, Jun 2022.

[245] Simei Mao, Lirong Cheng, Caiyue Zhao, Faisal Nadeem Khan, Qian Li, and H. Y. Fu. Inverse design for silicon photonics: From iterative optimization algorithms to deep neural networks. *Applied Sciences*, 11(9), 2021.

[246] Christopher Yeung, David Ho, Benjamin Pham, Katherine T. Fountaine, Zihan Zhang, Kara Levy, and Aaswath P. Raman. Enhancing adjoint optimization-based photonic inverse design with explainable machine learning. *ACS Photonics*, 9(5):1577–1585, May 2022.

[247] Shaolin Ke, Dong Zhao, Qingjie Liu, Shun Wu, Bing Wang, and Peixiang Lu. Optical imaginary directional couplers. *J. Lightwave Technol.*, 36(12):2510–2516, Jun 2018.

[248] Marko Lončar, Dušan Nedeljković, Thomas P Pearsall, Jelena Vučković, Axel Scherer, Sergey Kuchinsky, and Douglas C Allan. Experimental and theoretical confirmation of bloch-mode light propagation in planar photonic crystal waveguides. *Applied physics letters*, 80(10):1689–1691, 2002.

[249] P. St. J. Russell. Optics of floquet-bloch waves in dielectric gratings. *Applied Physics B*, 39(4):231–246, 1986.

[250] Tomasz Jannson. Real-time fourier transformation in dispersive optical fibers. *Optics Letters*, 8(4):232, April 1983.

[251] K. Goda and B. Jalali. Dispersive fourier transformation for fast continuous single shot measurements. *Nature Photonics*, 7:102, January 2013.

[252] Ata Mahjoubfar, Dmitry V. Churkin, Stéphane Barland, Neil Broderick, Sergei K. Turitsyn, and Bahram Jalali. Time stretch and its applications. *Nature Photonics*, 11(6):341–351, June 2017.

[253] Yunzheng Wang, Cong Wang, Feng Zhang, Jia Guo, Chunyang Ma, Weichun Huang, Yufeng Song, Yanqi Ge, Jie Liu, and Han Zhang. Recent advances in real-time spectrum measurement of soliton dynamics by dispersive fourier transformation. *Reports on Progress in Physics*, 83(11):116401, October 2020.

[254] Thomas Godin, Lynn Sader, Anahita Khodadad Kashi, Pierre-Henry Hanzard, Ammar Hideur, David J. Moss, Roberto Morandotti, Goery Genty, John M. Dudley, Alessia Pasquazi, Michael Kues, and Benjamin Wetzel. Recent advances on time-stretch dispersive fourier transform and its applications. *Advances in Physics: X*, 7(1), May 2022.

[255] Jae K. Jang, Miro Erkintalo, Stuart G. Murdoch, and Stéphane Coen. Ultraweak long-range interactions of solitons observed over astronomical distances. *Nature Photonics*, 7(8):657–663, July 2013.

[256] Said Hamdi, Aurélien Coillet, Benoit Cluzel, Philippe Grelu, and Pierre Colman. Superlocalization reveals long-range synchronization of vibrating soliton molecules. *Physical Review Letters*, 128(21):213902, May 2022.

[257] Abraham. Savitzky and M. J. E. Golay. Smoothing and differentiation of data by simplified least squares procedures. *Analytical Chemistry*, 36(8):1627–1639, July 1964.

[258] Coraline Lapre, Cyril Billet, Fanchao Meng, Piotr Ryczkowski, Thibaut Sylvestre, Christophe Finot, Göery Genty, and John M. Dudley. Real-time characterization of spectral instabilities in a mode-locked fibre laser exhibiting soliton-similariton dynamics. *Scientific Reports*, 9(1), September 2019.

[259] M. Stratmann, T. Pagel, and F. Mitschke. Experimental observation of temporal soliton molecules. *PRL*, 95(14):143902, September 2005.

[260] N. Akhmediev, A. Ankiewicz, and J. Soto-Crespo. Multisoliton solutions of the complex ginzburg-landau equation. *Physical Review Letters*, 79(21):4047–4051, November 1997.

[261] Luca Nimmesgern, Cornelius Beckh, Hannes Kempf, Alfred Leitenstorfer, and Georg Herink. Soliton molecules in femtosecond fiber lasers: universal binding mechanism and direct electronic control. *Optica*, 8(10):1334, October 2021.

[262] Rafi Weill, Alexander Bekker, Vladimir Smulakovsky, Baruch Fischer, and Omri Gat. Noise-mediated casimir-like pulse interaction mechanism in lasers. *Optica*, 3(2):189–192, Feb 2016.

[263] Mengjie Zhou, Jiangyong He, Caiyun Li, Yan-Ge Liu, Yang Yue, Ruijin He, Siyu Chen, Luhe Zhang, Longfei Zhu, Kaiyan Zhu, Kun Chang, and Zhi Wang. Oscillatory self-organization dynamics between soliton molecules induced by gain fluctuation. *Optics Express*, 29(11):16362, May 2021.

[264] J. M. Soto-Crespo, Nail Akhmediev, Ph. Grelu, and F. Belhache. Quantized separations of phase-locked soliton pairs in fiber lasers. *Opt. Lett.*, 28(19):1757–1759, Oct 2003.

[265] Yves Jaouën and Laurent du Mouza. Transverse brillouin effect produced by electrostriction in optical fibers and its impact on soliton transmission systems. *J. of Stat. Mech.*, 7(3):141–169, July 2001.

[266] J. Igbonacho, K. Nithyanandan, K. Krupa, P. Tchofo Dinda, P. Grelu, and A. B. Moubissi. Dynamics of distorted and undistorted soliton molecules in a mode-locked fiber laser. *Phys. Rev. A*, 99:063824, Jun 2019.

[267] Peter J. Schmid. Application of the dynamic mode decomposition to experimental data. *Experiments in Fluids*, 50(4):1123–1130, February 2011.

[268] G. Herink, F. Kurtz, B. Jalali, D. R. Solli, and C. Ropers. Real-time spectral interferometry probes the internal dynamics of femtosecond soliton molecules. *Science*, 356(6333):50, April 2017.

[269] Katarzyna Krupa, K. Nithyanandan, Ugo Andral, Patrice Tchofo-Dinda, and Philippe Grelu. Real-time observation of internal motion within ultrafast dissipative optical soliton molecules. *Phys. Rev. Lett.*, 118:243901, Jun 2017.

[270] Philippe Grelu and Nail Akhmediev. Dissipative solitons for mode-locked lasers. *Nature Photonics*, 6:84, February 2012.

[271] Thomas Schreiber, Bülend Ortaç, Jens Limpert, and Andreas Tünnermann. On the study of pulse evolution in ultra-short pulse mode-locked fiber lasers by numerical simulations. *Opt. Express*, 15(13):8252–8262, June 2007.

[272] Aleksandr Zavyalov, Rumen Iliew, Oleg A Egorov, and Falk Lederer. Dissipative soliton molecules with independently evolving or flipping phases in mode-locked fiber lasers. *Physical Review A: Atomic, Molecular and Optical Physics*, 80, 2009.

[273] Aleksandr Zavyalov, Rumen Iliew, Oleg Egorov, and Falk Lederer. Discrete family of dissipative soliton pairs in mode-locked fiber lasers. *Phys. Rev. A*, 79:053841, May 2009.

[274] Xiuqi Wu, Junsong Peng, Sonia Boscolo, Ying Zhang, Christophe Finot, and Heping Zeng. Intelligent breathing soliton generation in ultrafast fiber lasers. *Laser and Photonics Reviews*, 16(2):2100191, December 2021.

List of publications

Publications in peer-reviewed journals

- **Sheveleva A**, Leonardo M, Finot C, Colman P Local-field and effective-background effects in coupled integrated photonic waveguide systems, Phys. Rev. A 107, 063502 - 2023

- **Sheveleva A**, Hamdi S, Coillet A, Finot C, Colman P Analysis of the dispersive Fourier transform dataset using dynamic mode decomposition: evidence of multiple vibrational modes and their interplay in a three-soliton molecule, Optics Letters Vol. 48, Issue 11, pp. 3015-3018 - 2023

- **Sheveleva A**, Colman P, Dudley J M, Finot C Trajectory control in idealized four-wave mixing processes in optical fiber, Optics Communications, 10.1016/j.optcom.2023.129472 - 2023

- **Sheveleva A**, Colman P, Dudley J M, Finot C Phase space topology of four wave mixing reconstructed by a neural network, Optics Letters, 10.1364/OL.472039 - 2022

- **Sheveleva A**, Andral U, Kibler B, Colman P, Dudley J M, Finot C Ideal Four Wave Mixing Dynamics in a Nonlinear Schrödinger Equation Fibre System, Optica, 10.1364/OPTICA.445172 - 2022

- Ermolaev A, **Sheveleva A**, Genty G, Finot C, Dudley J M, Data-driven model discovery of ideal four-wave mixing in nonlinear fibre optics, Scientific Reports, 10.1038/s41598-022-16586-5 - 2022

- **Sheveleva A**, Finot C Ultrashort pulse generation from binary temporal phase modulation, Microwave and Optical Technology Letters, 10.1002/mop.32807 - 2021

- **Sheveleva A**, Colman P, Finot C The temporal analogue of diffractive couplers, Results in Optics, 10.1016/j.rio.2021.100059 - 2021

- **Sheveleva A**, Andral U, Kibler B, Boscolo S, Finot C Temporal optical besselon waves for high-repetition rate picosecond sources, J. Phys. Photonics 3 025001 - 2021

- **Sheveleva A**, Finot C, Nonlinear compression of Besselon waves for high repetition-rate subpicosecong pulse trains, IEEE Photonics Technology Letters, 10.1109/LPT.2020.3037786 - 2020

- **Sheveleva A**, Finot C Temporal Fresnel diffraction induced by phase jumps in linear and nonlinear optical fibres, Results in Physics, 10.1016/j.rinp.2020.103344 - 2020

Publications in conference proceedings

- **Sheveleva A**, Finot C, Colman P, Dimensionality reduction for efficiency human and computer codesign in integrated photonics, Integrated Photonics Platforms II, vol. 12148, p 1214808, International Society for Optics and Photonics, SPIE, 10.1117/12.2620510 - 2022

Invited orals at international conferences

- Experimental investigation of phase-space portraits of ideal four-wave mixing, **A Sheveleva**[1], A Ermolaev, P Colman, J M Dudley, C Finot *ICTON - Bucharest, Romania* (2023)

- Phase-space topology of fiber four-wave mixing, **A Sheveleva**, P Colman, J M Dudley, C Finot *ICLO - Saint-Petersburg, Russia* (2022)

Orals at international conferences

- Control of light in the non-adiabatic regime in integrated optical waveguides, **A Sheveleva**, M Leonardo, C Finot, P Colman *ICTON - Bucharest, Romania* (2023)

- Langevin's model for soliton molecules in ultrafast fiber ring laser cavity: investigating the interplay between noise and inertia, A Sheveleva, S Hamdi, A Coillet, C Finot, **P Colman** *CLEO - San Jose, California, USA* (2023)

- Existence of nested oscillators in soliton molecules revealed by Mode Decomposition, A Sheveleva, S Hamdi, A Coillet, C Finot, **P Colman** *CLEO - San Jose, California, USA* (2023)

- Reconstruction of idealized phase-space topology of four-wave mixing observed in nonlinear fiber, **A Sheveleva**, U Andral, B Kibler, P Colman, J M Dudley, C Finot *Advanced Photonics Congress - Maastricht, Netherlands* (2022)

- Langevin's model for soliton molecules in ultrafast fiber ring laser cavity, A Sheveleva, S Hamdi, A Coillet, C Finot, **P Colman** *Advanced Photonics Congress - Maastricht, Netherlands* (2022)

- Complete measurement of the phase-space topology of fiber four-wave mixing using iterated initial conditions, **A Sheveleva**, U Andral, B Kibler, P Colman, J M Dudley, C Finot *CLEO - San Jose, California, USA* (2022) - Online

- Recent advances in Dispersive Fourier Transform techniques , S Hamdi, **A Sheveleva**, A Coillet, P Grelu, P Colman *ICLO - Saint-Petersburg, Russia* (2022) - Online

- Reduced set of descriptors for experimental analysis of nonlinear optics phenomena, **A Sheveleva**, C Finot, P Colman *ICLO - Saint-Petersburg, Russia* (2022) - Online

- Machine learning for ultrafast nonlinear photonics, **C Finot**, A Sheveleva, J Peng, J M Dudley, S Boscolo *ICLO - Saint-Petersburg, Russia* (2022) - Online

[1] The presenting author is marked in bold.

- Accurate fiber-optic emulator of fundamental four-wave mixing theory, **A Sheveleva**, U Andral, B Kibler, P Colman, J M Dudley, C Finot *SPIE Photonics Europe - Strasbourg, France* (2022)

- Dimensionality reduction for efficiency human and computer codesign in integrated photonics, **A Sheveleva**, C Finot, P Colman *SPIE Photonics Europe - Strasbourg, France* (2022)

- Nonlinear temporal Fresnel diffraction induced by phase jumps in fiber optics, **A Sheveleva**, C Finot *EOS Annual Meeting (EOSAM 2020)* (2022) - Online

- All-fibered high-quality 40-GHz to 200 GHz pulse sources based on nonlinear compression of besselons, **A Sheveleva**, C Finot *EOS Annual Meeting (EOSAM 2020)* (2022) - Online

Orals at national conferences

- Reconstruction of phase-space topology in fiber four-wave mixing, **A Sheveleva**, P Colman, J M Dudley, C Finot *Journées du GDR ELIOS - Marseille, France* (2022) (given in French)

- Data-driven Discovery of the Ideal Four Wave Mixing Modelin Nonlinear Fiber Optics, **A Ermolaev**, A Sheveleva, L Salmela, G Genty, C Finot, J M Dudley *Journées du GDR ELIOS - Marseille, France* (2022)

- Temporal analogue of the Fresnel diffraction by a phase plate in linear and nonlinear optical fibers, **A Sheveleva**, C Finot *Journées du GDR ELIOS - Marseille, France* (2020) - Online

Posters at international conferences

- Temporal analogue of the Fresnel diffraction by a phase plate in linear and nonlinear optical fibers, **A Sheveleva**, C Finot *CLEO Europe - Munich, Germany* (2021) - Online

- Design and control of NxN microphotonics switch array based on non-adiabatic theory, **A Sheveleva**, P Colman *CLEO Europe - Munich, Germany* (2021) - Online

- All-fibered high-quality 28-GHz to 112 GHz pulse sources based on nonlinear compression of optical temporal besselons, **A Sheveleva**, C Finot *CLEO Europe - Munich, Germany* (2021) - Online

- All-fibered high-quality low duty-cycle 40-GHz picosecond pulse source based on nonlinear compression of besselons, **A Sheveleva**, C Finot *OSA Advanced Photonics Congress - Washington, DC United States* (2020) - Online

- Temporal Arago spot in nonlinear optical fibers, **A Sheveleva**, H Rigneault, C Finot *OSA Advanced Photonics Congress - Washington, DC United States* (2020) - Online

Posters at national conferences

- Non-adiabatic control in NxN integrated photonic switch, **A Sheveleva**, C Finot, P Colman *Optique - Dijon, France* (2021)

- Source optique a très haut débit basée sur la compression non linéaire de besselons optiques, **A Sheveleva**, C Finot *Optique - Dijon, France* (2021)
- Génération de doublets d'impulsions picosecondes a très haut débit, **A Sheveleva**, C Finot *Optique - Dijon, France* (2021)
- La tache d'Arago temporelle en optique fibrée non-linéaire, **A Sheveleva**, H Rigneault, C Finot *Optique - Dijon, France* (2021)